

## AVERTISSEMENT

Ce document est le fruit d'un long travail approuvé par le jury de soutenance et mis à disposition de l'ensemble de la communauté universitaire élargie.

Il est soumis à la propriété intellectuelle de l'auteur. Ceci implique une obligation de citation et de référencement lors de l'utilisation de ce document.

D'autre part, toute contrefaçon, plagiat, reproduction illicite encourt une poursuite pénale.

➤ Contact SCD Nancy 1 : [theses.sciences@scd.uhp-nancy.fr](mailto:theses.sciences@scd.uhp-nancy.fr)

## LIENS

Code de la Propriété Intellectuelle. articles L 122. 4

Code de la Propriété Intellectuelle. articles L 335.2- L 335.10

[http://www.cfcopies.com/V2/leg/leg\\_droi.php](http://www.cfcopies.com/V2/leg/leg_droi.php)

<http://www.culture.gouv.fr/culture/infos-pratiques/droits/protection.htm>

U.F.R Sciences et Technologie  
Ecole doctorale RP2E (Ressources, Produits, Procédés et Environnements)

**THESE en COTUTELLE**  
Présentée pour l'obtention du titre de  
Docteur de l'Université Henri Poincaré, NANCY I  
en **Géosciences**

**PHILOSOPHICAL DOCTORAL THESIS**

Defended for the title of  
Doctor of Nanjing University in Earth Sciences

by **Junying DING**

The pH determination of palaeofluids:  
experimental and thermodynamic approach

Defended the 12<sup>th</sup> of November 2010 at Nanjing University

Members of the committee:

Rapporteur:	Michel DUBOIS	Professeur, USTL, Lille
Referee:	Hongrui FAN	Researcher, Institute of Geology and Geophysics, CAS, Beijing
Directeur de thèse:	Jean DUBESSY	Directeur de Recherche CNRS, G2R, Nancy
Advisor:	Pei NI	Professor, State Key Laboratory for Mineral Deposit Research, Nanjing
Représentant UHP:	Anne-Sylvie ANDRE	Maître de Conférences, HDR, G2R, Nancy
Examinator:	Kun SHEN	Professor, Institute of Geological Sciences of Shandong, Jinan
Invited:	Rucheng WANG	Professor, School of Earth Sciences and Engineering, NJU, Nanjing
Invited:	Shaoyong JIANG	Professor, State Key Laboratory for Mineral Deposits Research, Nanjing

UMR 7566 - Géologie et Gestion des Ressources Minérales et Energétiques  
Faculté des Sciences & Techniques, BP239, 54501 Vandoeuvre-lès-Nancy

State Key Laboratory for Mineral Deposits Research,  
School of Earth Sciences and Engineering, Nanjing University, 210093, Nanjing



## Abstract

The aim of this study is to develop the methodology to get the pH values of the palaeo-circulation in the system  $\text{H}_2\text{O}-\text{CO}_2-\text{HCO}_3^--\text{NaCl}$  in the P-T conditions of circulation. It combines the use of an experimental approach for calibrating the analytical method, Raman spectrometry, and numerical modelling for the quantitative interpretation of phase and chemical species equilibria. The routine analytical techniques for fluid inclusions are used to carry out the experimental analyses, such as microthermometry and micro-Raman spectroscopy. Experiments are based both on the use of synthetic fluid inclusions produced in quartz crystal and a new method to make synthetic fluids in fused-silica glass capillary. The synthetic fluid in silica glass capillary can be applied to a wide range of pressure (up to 2 to 3 kbar) at room temperature and temperature (as high as at least 673 K). The experimental protocol of capillary loading with different chemical species in the system  $\text{H}_2\text{O}-\text{CO}_2-\text{HCO}_3^--\text{NaCl}$  and the methods to quantify their amount are elaborated and validated.

Numerical modelling is based on the use of the Pitzer model to describe the liquid aqueous phase, especially the activity coefficients of each chemical species in the liquid aqueous phase. The Duan equation of state is used for the P-V-T-X properties of the liquid and vapour phases in the simplified subsystem  $\text{H}_2\text{O}-\text{CO}_2-\text{NaCl}$ . The application pressure and temperature ranges of the model are respectively 273 to 523 K, and 0 to 2000 bar. Range of NaCl concentration is between 0 and 5 molal and corresponds to the range of ice melting temperature ( $T_{\text{mice}}$ ). The determination of the concentration of aqueous species  $\text{HCO}_3^-$  and  $\text{CO}_2$  is performed by using micro-Raman spectrometry and is calibrated with using the standards of synthetic fluid inclusion and silica glass capillary. A software program based on the Pitzer and Duan models has been done for the interpretation of i) ice melting temperature ( $T_{\text{mice}}$ ) and bicarbonate concentration in terms of NaCl concentration, and ii) total homogenisation temperature in terms of bulk molar volume and pressure at homogenisation temperature. Then speciation of the fluid is calculated along the isochore till the trapping temperature if lower than 250 °C. A first application to the Mokrsko gold deposit in Bohemian Massif is done and discussed.

**Key words:** pH, system  $\text{H}_2\text{O}-\text{CO}_2-\text{HCO}_3^--(\text{NaCl})$ , fluid inclusion, silica capillary, Raman spectroscopy, Pitzer model

## Résumé

Le but de cette étude est de développer une méthodologie permettant d'obtenir le pH des paléo fluides du système  $\text{H}_2\text{O}-\text{CO}_2-\text{HCO}_3^--\text{NaCl}$  dans leurs conditions P-T de circulation. Ceci combine une approche expérimentale pour le calibrage d'une méthode analytique, la spectrométrie Raman et une modélisation numérique pour l'interprétation quantitative des équilibres de phase ou d'espèces chimiques. Les techniques analytiques utilisées en routine pour l'étude des inclusions fluides, comme la microthermométrie et la micro-spectrométrie Raman sont utilisées pour la détermination des concentrations. Les expériences sont basées à la fois sur l'utilisation d'inclusions fluides synthétiques fabriquées dans des cristaux de quartz et sur une nouvelle méthode de synthèse de fluides dans des capillaires de silice pure. La technique des fluides contenus dans des capillaires de silice pure peut être appliquée dans une gamme de pressions, jusqu'à 2 ou 3 kbar à température ambiante, et de températures au moins jusqu'à 400 °C sous 2 kbar de pression. Le protocole expérimental de chargement des fluides du système  $\text{H}_2\text{O}-\text{CO}_2-\text{HCO}_3^--\text{NaCl}$  et les méthodes de quantification sont élaborées et validées.

La modélisation numérique est basée sur le modèle de Pitzer pour décrire la phase liquide aqueuse, en particulier les coefficients d'activité de chaque espèce chimique des espèces présentes dans la phase aqueuse. L'équation d'état de Duan est utilisée pour le calcul des propriétés P-V-T-X des phases liquide et vapeur dans le sous-système  $\text{H}_2\text{O}-\text{CO}_2-\text{NaCl}$ . Les conditions d'application du modèle de Pitzer dans le champ température-pression sont respectivement comprises entre 273 et 523 K et 0 et 2000 bar. La gamme de concentration en NaCl de notre modèle est comprise entre 0 et 5 molal, gamme qui correspond aux températures de fusion de la glace ( $T_{m_{ice}}$ ) comme dernière phase. La détermination de la concentration des espèces  $\text{HCO}_3^-$  et  $\text{CO}_2$  est réalisée à l'aide de la micro-spectrométrie Raman et est calibrée grâce à l'utilisation des standards que sont les inclusions fluides synthétiques et la technique des capillaires de silice fondue. Un programme de calcul utilisant les modèles de Pitzer et de Duan est réalisé afin d'interpréter i) la température de fusion de la glace et la concentration en bicarbonate en termes de concentration de NaCl et ii) la température d'homogénéisation globale en termes de volume molaire global et de pression à la température d'homogénéisation. Ensuite, la spéciation du fluide est calculée le long de l'isochore à la température de piégeage si celle-ci est inférieure à 250 °C. Une première application au gisement d'or de Mokrsko dans le massif de Bohême est discutée.

**Mots clés:** pH, système  $\text{H}_2\text{O}-\text{CO}_2-\text{HCO}_3^--(\text{NaCl})$ , inclusion fluide, capillaire de silice, spectroscopie Raman, modèle de Pitzer

## Acknowledgement

This thesis could not be finished without the help and support of many people who deserve to be greatly acknowledged here.

At the very first, I sincerely thank Université Henri Poincaré and Nanjing University for the agreement between two universities to develop my PhD thesis, and thank French lab (UMR Géologie et Gestion des Ressources Minérales et Energétiques) and Chinese lab (State Key Laboratory for Mineral Deposits Research) for their support to carry out my PhD thesis, and thank French government for the doctoral fellowship (3 x 6 months) and GREGU for the 6 last months fellowship in 2009 to financially support to complete my PhD thesis, and thank Université Henri Poincaré for the BQRI support, and I am honored to thank the members of the PhD dissertation defense committee.

I also would like to express my deepest gratitude to my two supervisors, Prof. Jean Dubessy and Prof. Pei Ni. With their guidance I could have worked out this thesis. They have offered me valuable ideas, suggestions with their profound knowledge and rich research experience. Their patience and kindness are greatly appreciated. I am very much obliged to their efforts of helping me complete the dissertation.

What's more, I wish to extend my thanks to peoples in French lab and Chinese lab and in School of Earth Sciences and Engineering for their support of this study. I owe special thanks to Pascal, Aurelien, Mathieu, Prof. Marie-Christine Boiron, Prof. Wang Rucheng and Prof. Jiang Shaoyong for their priceless helps on this study.

Thanks are also due to my friends in France and in China, who never failed to give me great encouragement and suggestions. Special thanks should go to Jérémy, Foxy, Michael, Rakim, Olivier, Antonin, Isa, Anne, Vancent, Emanuel, Maomao, Zhen, Xiaojun, Lifan, Sijie ..., so many friends, for their warmth and happiness brought to me to pass through the past four years and to arrive at the end of thesis.

At last, I would like to thank my family for their support all the way from the very beginning of my study. I am thankful to all my family members for their thoughtfulness and encouragement.

Thank you all of people who give me a hand or a smile!!



# Contents

<b>INTRODUCTION</b>	17
1. A survey of the main crustal fluids	18
2. Parameters controlling mass transport by fluids	21
3. PH of present day geological fluid	25
3.1. Definition of pH	25
3.2. Main acid-base equilibria	25
3.3. PH data and pH measurement of present-day geological fluids	28
3.4. PH of palaeo-fluids	29
3.4.1. Palaeo-fluid and fluid inclusions: a brief summary	29
3.4.2. Use of fluid inclusions for palaeo-pH estimation	30
<b>CHAPTER I: EXPERIMENTAL METHODS</b>	35
I.1. Microthermometric measurements	36
I.1.1. Linkam geology heating-freezing stage	37
I.1.2. USGS gas-flow heating-freezing stage	39
I.1.3. Calibration of Linkam and USGS stages	41
I.2. Raman measurements	42
I.2.1. Principles of Raman spectroscopy	42
I.2.2. Principles of Raman spectrometers	45
I.2.3. Micro-Raman spectrometers used in this work	46
I.2.3.1. Labram Raman spectrometer (Dilor/Jobin-Yvon/Horiba, USA)	46
I.2.3.2. Renishaw Raman spectrometer (Renishaw, UK)	47
I.3. Synthetic samples	48
I.3.1. Synthetic fluid inclusions	48
I.3.1.1. Autoclaves used for the synthesis of fluid inclusions	49
I.3.1.2. Methods for synthesizing fluid inclusions in cold sealed autoclaves	51
I.3.1.3. Samples of synthetic fluid inclusions	54
I.3.2. Pure silica capillary	54
I.3.2.1. Pure silica capillary tube	55
I.3.2.2. Adaptation of the system of I-Ming Chou (by J. Dubessy and P. Robert) and general procedure of capillary loading	55



I.3.2.3. Procedures for loading silica glass capillary with different gases, liquids and solids.....	59
I.3.2.4. Capillary samples.....	63
<b>CHAPTER II: THE SYSTEM <math>\text{H}_2\text{O}-\text{CO}_2-\text{NaCl}-\text{H}^+-\text{HCO}_3^-</math>: RESULTS OF EXPERIMENTS.....</b>	<b>65</b>
II.1. Objectives of the experimental part.....	66
II.2. Calibration of analysis of bicarbonates by Raman spectroscopy.....	66
II.2.1. Vibrational modes and bands of Raman active of related species in $\text{HCO}_3^-$ -bearing aqueous solution.....	66
II.2.2. Principles of calibration of $\text{HCO}_3^-$ analysis from Raman spectra at ambient temperature.....	70
II.2.2.1. Results obtained from synthetic fluid inclusion.....	73
II.2.2.2. Results obtained from silica glass capillaries.....	75
II.2.2.3. Comparison between the results from synthetic fluid inclusion and the results from silica glass capillary.....	77
II.2.3. Calibration as a function of temperature.....	78
II.2.3.1. Results obtained from synthetic fluid inclusions.....	78
II.2.3.2. Results obtained from capillary samples.....	82
II.3. Calibration of the analysis of $\text{CO}_2$ by Raman spectroscopy.....	85
II.3.1. Synthesis of fluid from the $\text{H}_2\text{O}-\text{CO}_2-(\text{NaCl})$ system in capillary.....	85
II.3.1.1. Method for loading pure $\text{CO}_2$ in silica glass capillary.....	85
II.3.1.2. Method for quantifying $\text{CO}_2$ condensed in capillary and the precision of the method.....	86
II.3.1.3. Validation of the approach and determinations the density of $\text{CO}_2$ .....	91
II.3.1.4. Results and discussion.....	92
II.3.1.5. Method for loading $\text{CO}_2$ with $\text{H}_2\text{O}$ liquid in silica glass capillary.....	94
II.3.2. Synthesis of $\text{CO}_2$ -bearing silica glass capillary by the thermal decomposition of organic acids: oxalic acid and formic acid.....	96
II.3.2.1. Oxalic acid as a source of $\text{CO}_2$ .....	96
II.3.2.2. Formic acid as a source of $\text{CO}_2$ .....	115
II.4. Conclusions and perspectives.....	117
<b>CHAPTER III: METHODOLOGY OF DETERMINATION OF PH APPLICATED TO FLUID INCLUSIONS.....</b>	<b>120</b>

III.1. Determination of pH in fluid inclusions.....	121
III.1.1. The thermodynamic models.....	122
III.1.1.1. Thermodynamic model of the aqueous phase: the Pitzer model.....	122
III.1.1.2. The equation of state: the Duan model.....	124
III.1.2. Theoretical principles.....	126
III.1.2.1. Calculation of the concentration of $\text{Na}^+$ and $\text{Cl}^-$ .....	127
III.1.2.2. Calculation of bulk composition and density.....	128
III.1.2.3. Calculation of molar volume.....	129
III.1.2.4. Calculation of pH.....	131
III.1.3. The algorithm of program.....	132
III.2. Application to natural case.....	134
III.2.1. Geology background of Mokrsko gold deposit.....	134
III.2.2. Experimental measurements of fluid inclusions.....	135
III.2.3. Calculation of pH.....	137
<b>CONCLUSIONS AND PERSPECTIVES.....</b>	<b>141</b>
1. Conclusions.....	142
1.1. A new method for synthesizing fluid inclusions by sealing material into fused-silica glass capillary tubing.....	142
1.2. Calibration of the concentration analysis of aqueous species $\text{HCO}_3^-$ and $\text{CO}_2$ using micro-Raman spectroscopy.....	142
1.3. Algorithm for the calculation of pH.....	143
1.4. The application on natural case.....	143
2. Perspectives.....	143
2.1. The calibration of $\text{CO}_2$ amount by controlling the loading materials in system $\text{H}_2\text{O}-\text{CO}_2$ in silica glass capillary.....	143
2.2. The quantification of $\text{CO}_2$ and $\text{H}_2\text{O}$ in system $\text{H}_2\text{O}-\text{CO}_2$ -salts systems should be fully investigated.....	144
2.3. The liquid-vapor isopleths of bicarbonate-rich fluids.....	144
2.4. The use of temperature of relevant phase equilibria other than $T_{\text{mice}}$ .....	144
2.5. Thermodynamic models above 250 °C.....	145
2.6. More applications to the natural cases are needed for verifying and improving the methodology.....	145
2.7. Other acido-base equilibria of interest.....	145

REFERENCES.....	146
-----------------	-----

## Listing of figures

Figure 0-1: Sketch of water cycle ( <a href="http://ga.water.usgs.gov/edu/watercycle.html">http://ga.water.usgs.gov/edu/watercycle.html</a> ) .....	19
Figure 0-2: Stability fields of gibbsite, diaspore, and corundum in the system $\text{Al}_2\text{O}_3\text{-H}_2\text{O}$ as a function of temperature and $\text{H}_2\text{O}$ pressure (Helgeson et al., 1978).....	22
Figure 0-3: Phase relations in the system $\text{HCl-H}_2\text{O-(FeO)-O}_2\text{-S}_2$ at 150 °C and 3.0 kbar (Bowers et al., 1984).....	22
Figure 0-4: Phase relations in the system $\text{HCl-H}_2\text{O-(CaO)-CO}_2\text{-H}_2\text{SO}_4$ at 25 °C and 0.001 kbar (Bowers et al., 1984).....	23
Figure 0-5: Solubility of Au(c) in water as a function of oxygen fugacity at 450 °C and 500 bar (Baranova et al., 1983).....	23
Figure 0-6: Dependence of wolframite solubility as a function of the concentration of NaCl, HCl, and HF at 400 °C, 1 kbar (Zaraisky, 1995).....	24
Figure 0-7: Activity diagram for the equilibria of principal mineral phases as a function of pH in the system $\text{Na}_2\text{O-K}_2\text{O-Al}_2\text{O}_3\text{-H}_2\text{O}$ at 250 °C at saturation pressure (Henley et al., 1984).....	24
Figure 0-8: Gold solubility and concentration thio-gold complexes as a function of pH at 225 °C and 1 kbar pressure (after Seward, 1973).....	25
Figure 0-9: Variation of equilibrium constants of acid-base equilibria as a function of temperature along the saturation curve of pure water ( $P = P_{\text{sat}}$ at T). Data are calculated from Program OrganoBioGeoTherm (V. 1.52) written by John J. Donovan.....	26
Figure 0-10: Difference of pH of fluids at $\text{pH} = \text{pK}_r$ of different acid-base equilibria versus temperature at water saturation pressure. $\Delta \text{pH} / \text{neutrality} = - (1/2) \text{pK}_w - \text{pK}_r$ .....	27
Figure 0-11: Diagram of temperature dependence of the association constants for the formation of weak acids and bases at the saturation vapour pressure of water to 300 °C. (Pitzer, 1991).....	32
Figure I-1: a. Photograph of the Linkam MDS600 heating-freezing stage; b. the cutaway view of the stage.....	38

Figure I-2: Sketch of silver lid and sample holder and carrier commonly used in Linkam geology heating-freezing stage. a, b and c are the sample hold and carrier with sample-placed glass in different size.....	39
Figure I-3: Sketch of modified silver lid and sample holder and carrier designed for capillary sample.....	39
Figure I-4: a. Photograph of the USGS gas-flow heating-freezing stage (taken from Instruction of U.S.G.S. ); b. the cutaway view of the stage.....	40
Figure I-5: Sketch of sample chamber of USGS stage.....	41
Figure I-6: Diagrammatic representation of an energy transfer model of Stokes Raman scattering, anti-Stokes Raman scattering and Rayleigh scattering.....	43
Figure I-7: Rayleigh and Raman spectra of CCl <sub>4</sub> (liquid) excited with 514.5nm laser light (printed from Kerkhof, 1988).....	44
Figure I-8: Photograph of Labram micro-Raman spectrometer (Dilor/Jobin-Yvon/Horiba, USA).....	46
Figure I-9: Photograph of micro-Raman spectrometer (Renishaw, UK).....	47
Figure I-10: Optical paths of the Renishaw micro-Raman spectrometer (Renishaw <sup>®</sup> , UK)...	48
Figure I-11: Sketch of fluid-pressure autoclave (simple autoclave for the synthesis of aqueous inclusion). a and b are section of flank and top of autoclave, respectively.....	50
Figure I-12: Sketch of gas-pressure autoclave (autoclave for the synthesis of gas-bearing aqueous inclusion).....	50
Figure I-13: Sketch of horizontal cold-seal pressure vessel (a) and a sealed golden capsule with samples (b).....	51
Figure I-14: Microphotographs of synthetic fluid inclusions. a. in system KHCO <sub>3</sub> -NaCl-H <sub>2</sub> O (KHCO <sub>3</sub> :NaCl = 1.0:0.0), b. in the system KHCO <sub>3</sub> -NaCl-H <sub>2</sub> O (KHCO <sub>3</sub> :NaCl = 1.0:1.0), c. is in the system CO <sub>2</sub> -H <sub>2</sub> O.....	54
Figure I-15: Sketch of cylindrical of flexible pure silica glass capillary tube coated with polyimide (PolymicroTechnology).....	55
Figure I-16: Schematic diagram showing the adaptation system of Chou I-Ming in G2R lab, France. For details, see text.....	57
Figure I-17: Silica capillary with samples sealed cryogenically to produce chemical systems in closed capillary.....	57
Figure I-18: Three special devices for the link between the stainless steel line (1/16 inch external diameter) and the silica glass capillary.....	58
Figure I-19: Photographs of special stainless metal connection.....	58
Figure I-20: Schematic diagram showing the procedure 1 to load solid to silica capillary.....	59

Figure I-21: Schematic diagram showing the procedure 2 to load solid to silica capillary.....	60
Figure I-22: Schematic diagram showing the procedure 2 to load solid to silica capillary.....	60
Figure I-23: Schematic diagram showing the procedure to load liquid to silica capillary. For details, see text.....	61
Figure I-24: Schematic diagram showing the procedure of gas loading in silica capillary. For details, see text.....	62
Figure I-25: Microphotographs of capillary samples. a. capillary with solid sample (oxalic acid solid), b. capillary sample in system $\text{KHCO}_3\text{-NaCl-H}_2\text{O}$ (binary phases: vapour and aqueous solution), c. capillary in pure $\text{CO}_2$ (monophase), d is capillary in system $\text{H}_2\text{O-CO}_2$ (ternary phases: $\text{CO}_2$ vapour ( $\text{VCO}_2$ ), $\text{CO}_2$ liquid ( $\text{LCO}_2$ ), $\text{H}_2\text{O}$ liquid ( $\text{LH}_2\text{O}$ )) and the detail of part in red circle is shown in e.....	63
Figure I-26: Photographs of micrometric stage ( $\text{MW}^{\text{®}}$ ) equipped with microscope. a and b. complete set, c. the capillary sample in stage display.....	64
Figure II-1: One possible geometry of bicarbonate ion $\text{C}_s(\sigma_h)$ .....	68
Figure II-2: Spectra collected from the aqueous solution in bicarbonate-bearing inclusion and from quartz near inclusion focusing on the same distance.....	70
Figure II-3: Spectra collected from the aqueous solution and from the vapour phase in bicarbonate-bearing capillary focusing on the same distance.....	71
Figure II-4: Two spectra collected from aqueous phase in fluid inclusion and from quartz crystal near inclusion, respectively.....	72
Figure II-5: Raman spectra collected from aqueous phase in fluid inclusion and in capillary, respectively.....	73
Figure II-6: Linear variations of ratio1 and ratio2 deduced from spectra collected from bicarbonate-bearing synthetic fluid inclusions with the concentration of bicarbonate.....	74
Figure II-7: Influence of the addition of 1.0 m NaCl in bicarbonate-bearing solution to the variations of ratio1 and ratio2. Anion $\text{Cl}^-$ decreases the area ratios between bands of bicarbonate and bending band of water in both inclusion samples.....	75
Figure II-8: Variations of ratio1 and ratio2 deduced from spectra collected from bicarbonate-bearing silica glass capillary samples versus concentration of bicarbonate.....	76
Figure II-9: Influence of the addition of 1.0 m NaCl in bicarbonate-bearing solution to the variations of ratio1 and ratio2. Anion $\text{Cl}^-$ decreases the area ratios between bands of bicarbonate and bending band of water in both capillary samples.....	76
Figure II-10: Spectra collected in the aqueous phase in fluid inclusion at different temperature. This fluid inclusion is homogenized at $256.6\text{ }^{\circ}\text{C}$ ( $\text{L+V}\rightarrow\text{L}$ ) .....	79

Figure II-11: Variation of $\nu_5(\text{A}')$ C-O-H and $\nu_3(\text{A}')$ C-O wavenumbers versus temperature. Spectra were collected from fluid inclusion.....	80
Figure II-12: Variations of intensity ratio1 and ratio2 deduced from spectra collected from bicarbonate-bearing fluid inclusion with the increasing of temperature.....	80
Figure II-13: Spectra collected in the vapor phase in fluid inclusion at different temperature.....	81
Figure II-14: Spectra collected in the aqueous phase in capillary at different temperature. This capillary sample is homogenized as $\text{L}+\text{V}\rightarrow\text{V}$ .....	82
Figure II-15: Spectra collected in the vapour phase in capillary sample at different temperature.....	83
Figure II-16: Variation of $\nu_5(\text{A}')$ C-O-H and $\nu_3(\text{A}')$ C-O wavenumbers versus temperature. Spectra were collected from capillary sample.....	84
Figure II-17: Linear variations of ratio1 and ratio2 deduced from spectra collected from bicarbonate-bearing capillary with the increasing of temperature.....	84
Figure II-18: The line of system for $\text{CO}_2$ loading in silica glass capillary. a and b are tow valves.....	87
Figure II-19: Sketch of capillary sample in pure $\text{CO}_2$ with two phases at $T_a$ . $\text{LCO}_2$ : liquid $\text{CO}_2$ ; $\text{VCO}_2$ : vapour $\text{CO}_2$ .....	92
Figure II-20: Sketch of diagram of T- $\rho$ in pure $\text{CO}_2$ .....	94
Figure II-21: Microphotograph of the capillary with the oxalic acid solid.....	97
Figure II-22: Microphotographs of the capillary at ambient temperature after heating in the oven. Phase 2 and Phase 3 are two non-colored liquid phases and Phase 1 is vapor phase.....	98
Figure II-23: Changes of interior surface of capillary at ambient temperature after heating in the oven.....	98
Figure II-24: Raman Spectra collected from the different phases in capillary after heating in the oven. a and b are the spectra of the liquid phase 3; c, d and e are the spectra of the vapor phase1.....	99
Figure II-25: Raman spectra at ambient temperature in the region of $2600 - 3800\text{cm}^{-1}$ collected on (a) solid of oxalic acid and (b) solution of oxalic acid (10g/100ml) and (c) solution of formic acid (1m) .....	100
Figure II-26: Raman Spectra in the region of $1000 - 2000\text{cm}^{-1}$ collected on solid of oxalic acid (a) and solution of oxalic acid (10g/100ml) (b) .....	100

- Figure II-27: Microphotographs of the capillary 47 at ambient temperature. a. before microthermometry, b. after microthermometry, c. after heating in the oven at 400 °C lasting 10 hours.....103
- Figure II-28: The changes of volume of each phase in the capillary. The volume of the liquid phase decreases after heating and the volume of the vapour phase increases after heating.....104
- Figure II-29: The Raman spectra of solution of oxalic acid at ambient temperature. 1057  $\text{cm}^{-1}$  and 1190  $\text{cm}^{-1}$ : silica glass. 1638  $\text{cm}^{-1}$ :  $\text{H}_2\text{O}$  bending mode. 1382  $\text{cm}^{-1}$ , 1410  $\text{cm}^{-1}$ , 1446  $\text{cm}^{-1}$ , and 1745  $\text{cm}^{-1}$ : the characteristics of the aqueous oxalic acid. 2800 - 3800  $\text{cm}^{-1}$  region: O-H stretching of molecular  $\text{H}_2\text{O}$ .....104
- Figure II-30: The Raman spectra of vapour phase in capillary after heating in the microthermometric stage. Bands 1284 $\text{cm}^{-1}$  and 1387  $\text{cm}^{-1}$ :  $\nu_1$ - $2\nu_2$  Fermi resonance of  $\text{CO}_2$ . Bands 1264  $\text{cm}^{-1}$  and 1408  $\text{cm}^{-1}$ : hot bands of  $\text{CO}_2$ . Bands 1368 $\text{cm}^{-1}$ : the isotopic splitting of  $\text{CO}_2$  due to the presence of  $^{13}\text{CO}_2$ . Bands 1241 $\text{cm}^{-1}$ : the characteristic of CO. Bands 4125  $\text{cm}^{-1}$ , 4143  $\text{cm}^{-1}$ , 4155  $\text{cm}^{-1}$  and 4161  $\text{cm}^{-1}$ : the characteristics of  $\text{H}_2$ .....105
- Figure II-31: The Raman spectra of the O-H stretching region of water collected on the vapour phase in capillary after heating in the microthermometric stage. Band at 3653  $\text{cm}^{-1}$ : intermolecular O-H stretching vibration of water. Band at 3672 $\text{cm}^{-1}$ : SiO-H stretching feature. Band at 3604 $\text{cm}^{-1}$ : one type of OH group.....106
- Figure II-32: The Raman spectra collected on the liquid phase in capillary after heating in the microthermometric stage at 400°C during 10-20 mn. Bands 1273  $\text{cm}^{-1}$  and 1381  $\text{cm}^{-1}$ : characteristic of  $\text{CO}_2$  dissolved in water. 1500  $\text{cm}^{-1}$ -1800  $\text{cm}^{-1}$ : bending mode of water. 2800  $\text{cm}^{-1}$ -3800  $\text{cm}^{-1}$ : stretching mode of water.....107
- Figure II-33: The Raman spectra collected on the vapour phase in capillary after heating in the oven at 400°C. In 1200-1500 $\text{cm}^{-1}$  region: characteristic of  $\text{CO}_2$ . In 2100-2200 $\text{cm}^{-1}$  region: no characteristic of CO. In 4100-4200 $\text{cm}^{-1}$  region: no characteristic of  $\text{H}_2$ .....108
- Figure II-34: Raman spectra of the vapor phase in capillary 36 (0.573 molal oxalic acid) after different heating times. With the increasing of heating time, the intensity of  $\text{CO}_2$  bands increases and the intensity of bands of CO and  $\text{H}_2$  (respectively in 2120-2160  $\text{cm}^{-1}$  region and 4110-4180  $\text{cm}^{-1}$  region) decreases versus heating time....109
- Figure II-35: The Raman spectra of  $\text{CH}_4$  collected at ambient temperature on the vapor phase in capillary 3 (1.175 molal oxalic acid) after heating in the oven. The intensity of band  $\text{CH}_4$  is enhanced with the increasing of heating duration (Blue line: the

duration of first heating is 64 hours, red line: the duration of second heating is 20 hours).....	109
Figure II-36: The Raman spectra collected on the liquid phase in capillary 36 after heating in the oven. Bands $1273\text{cm}^{-1}$ and $1381\text{cm}^{-1}$ : characteristic of $\text{CO}_2$ dissolved in water. $1500\text{cm}^{-1}$ - $1800\text{cm}^{-1}$ : bending mode of water. $2800\text{cm}^{-1}$ - $3800\text{cm}^{-1}$ : stretching mode of water.....	110
Figure II-37: Raman spectra of the aqueous phase in capillary 36 after different heating times. With the increasing of heating duration, the intensity of bands of dissolved $\text{CO}_2$ (in $1260$ - $1420\text{cm}^{-1}$ region) is enhanced and the bending band of water does not change.....	111
Figure II-38: Schematic of capillary at room temperature.....	112
Figure II-39: Microphotographs of capillary 36. a. before heating, b. after heating in the oven.....	114
Figure II-40: Raman spectra collected on the changes in silica tube.....	114
Figure II-41: Microphotograph of capillary before heating at room temperature.....	116
Figure II-42: Raman spectra of aqueous phase and vapor phase in capillary with solution aqueous of formic acid at room temperature (A. $30\text{s}\times 2$ , B. liquid: $5\text{s}\times 2$ , vapour: $30\text{s}\times 2$ ) .....	116
Figure II-43: Raman spectra of capillary with the solution of formic acid (1m) after heating the capillary. A. in liquid phase, B. in vapor phase.....	117
Figure III-1: Micro-photography of a fluid inclusion in system $\text{H}_2\text{O}$ - $\text{CO}_2$ - $\text{NaCl}$ with the coexisting of vapor phase and liquid phase at temperature.....	121
Figure III-2: Algorithm of program for the calculation of pH.....	133
Figure III-3: Photographs of fluid inclusions in quartz collected from Mokrsko gold deposit in ore-bearing zones.....	136
Figure III-4: Raman spectra collected from liquid phase in fluid inclusion (blue line) and from quartz crystal near inclusion (green line) respectively.....	136
Figure III-5: Relationships between the concentration of $\text{CO}_2$ dissolved in water and the area ratios of bands of $\text{CO}_2$ dissolved in water at $1275\text{cm}^{-1}$ and $1380\text{cm}^{-1}$ obtaining from the analysis of standard capillaries; a. area ratio( $1275/1640$ ); b. area ratio( $1380/1640$ ); c. area ratio( $\text{Total}/1640$ ).....	139

## Listing of tables



Table I-1: Results for the calibration of temperature using synthetic fluid inclusions.....	41
Table I-2: Experimental conditions of fluid inclusions synthesized in simple autoclave heated in oven.....	52
Table I-3: Experimental conditions of fluid inclusions synthesized in high P-T vessel.....	52
Table I-4: Experimental conditions of fluid inclusions synthesized in autoclave for the synthesis of gas-bearing aqueous inclusion.....	53
Table II-1: Assignment of the normal modes of vibration of the bicarbonate ion according to the $C_s(\sigma_h)$ model and the carbonate ion according the $D_{3h}$ point group (from Davis & Oliver, 1972).....	68
Table II-2: Comparison of Eq. II-10 and II-11.....	77
Table II-3: Comparison Eq. II-12 and II-13.....	78
Table II-4: Measurements of volume $V_2$ .....	88
Table II-5: The capillary samples with pure $CO_2$ successfully fabricated in this study.....	93
Table II-6: Results of quantification of $CO_2$ -loading in capillary samples.....	93
Table II-7: Verification of aqueous liquid loaded in silica glass capillary.....	95
Table II-8: The concentration and the quantity of solutions loaded in capillaries.....	97
Table II-9: Measurements of phase volumes in capillary by micrometric stage.....	103
Table II-10: The changes of intensities of bands of Fermi resonance ( $CO_2$ ) on vapour phase and on liquid phase.....	110
Table II-11: The changes of $H_2O$ mole numbers in capillary.....	113
Table II-12: Conditions for heating capillaries of two groups.....	116
Table II-13: Quantity of components in capillary.....	117
Table III-1: Results of microthermometric analysis of fluid inclusions.....	136
Table III-2: Area ratio of bicarbonate band at $1017\text{ cm}^{-1}$ to at $1360\text{ cm}^{-1}$ by using the spectra collected from aqueous phase in standard capillaries.....	138
Table III-3: Area ratio of bicarbonate band at $1017\text{ cm}^{-1}$ to at $1360\text{ cm}^{-1}$ by using the spectra collected from aqueous phase in synthetic fluid inclusion.....	138
Table III-4: Results of calculation through the spectra collected on aqueous phase of fluid inclusions.....	138

## Listing of appendix

Appendix I : The main program for calculating pH of inclusion fluid is presented as follows.....	160
---	-----

# **INTRODUCTION**

## **1. A survey of the main crustal fluids**

Geological fluids, as an essential part in geological and geochemical systems in continental and oceanic crust, play a vital role in all crustal processes. Fluids are a ubiquitous transport medium for heat and matter in and on the Earth. Surface geological fluids transport through the upper mantle and crust are involved in the formation, transportation, deposition, and alteration of mineral assemblages in geological processes. Especially, geological fluids act as solvents for dissolving metals, and as a medium to transport and concentrate them as ores in ore forming processes. Therefore, circulation of fluids is the principal control on the formation of hydrothermal ore deposits. Many textbooks and review articles have addressed the role and diverse aspects of fluids in crustal processes (e.g., Fyfe et al., 1978; Ferry, 1982; Henley et al., 1984; Brimhall & Crerar, 1987; Shmulovich et al., 1995; Thompson, 1995; Green II & Jung, 2005; Kesler, 2005; Liebscher & Heinrich, 2007).

One of the seminal texts, Fyfe et al. (1978), recognized the interest in crustal fluids. Despite the general acceptance of the importance of fluids, most of details on the cycle of fluids were largely unknown and problems related to fluids remained controversial, such as the difficulties to constrain the duration and extent of fluid transport, and to determine the factors of fluids to transport different elements. Geological fluids are the object of this thesis. Normally, upper crustal fluids are rich in water, together with several volatiles (CO<sub>2</sub>, CH<sub>4</sub>, N<sub>2</sub>, etc.) and a variety of dissolved salts, as shown since a long by the analyses of present-day geothermal fluids (e.g., Fyfe et al., 1978; Henley et al., 1984) and fluid inclusions (e.g., Sorby, 1858; Naumov, 1969; Poty et al., 1974; Touret & Dietvorst, 1983; Roedder, 1972). In which geological environments may fluids be strongly involved? And what are the sources of fluids in the crust? The different geologic environments in which crustal fluids may evolve are briefly addressed in the following.

From a global perspective, water-bearing fluids link the different spheres of the Earth in very distinct environments. Water is the main component in geological fluids, and an excellent solvent for salts and polar molecules (e.g., Stumm & Morgan, 1996; Liebscher & Heinrich, 2007). Geological water systems typically consist of numerous mineral assemblages and often include a gas phase in addition to the aqueous phase (Shmulovich et al., 1995;

Stumm & Morgan, 1996). Figure 0-1 shows the surficial water cycle of the Earth. Surficial water is highly mobile and is involved in its cycle by four main processes: evaporation, condensation, precipitation and infiltration (Michard, 1989). About 70% of the earth surface is covered with water. Surface water is on the ground or in a stream, river, lake, wetland and ocean, and most of water is the salt-bearing water in the ocean. Surface water is the most common fluid in the Earth, and is related to groundwater and atmospheric water, and is naturally replenished by precipitation atmosphere and dripping groundwater and naturally lost through discharge to evaporation and sub-surface seepage into groundwater (Michard, 1989). Groundwater is the subsurface water in the Earth and is ubiquitous throughout the crust to depths of at least 15 to 20 km (Taylor, 1990), perhaps deeper in some places.

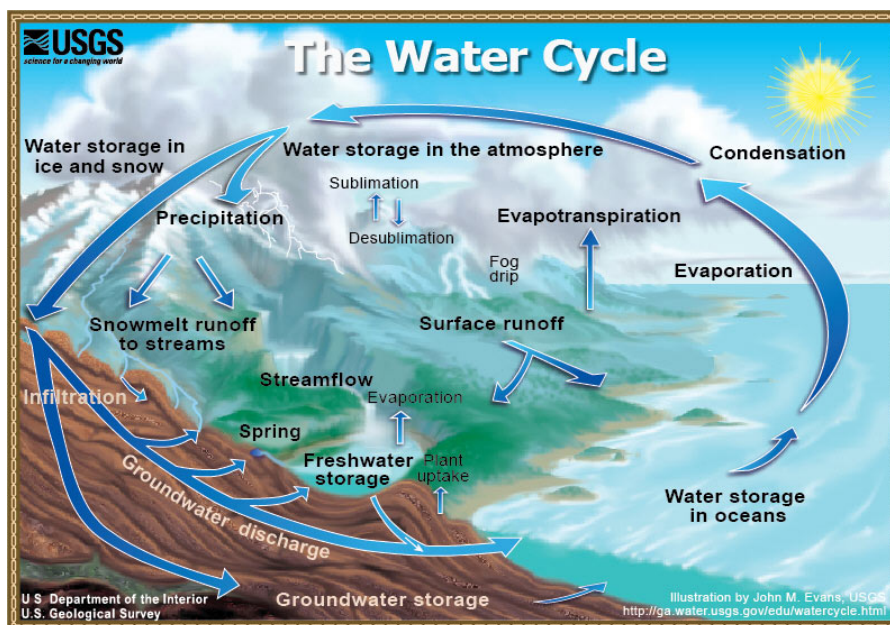


Figure 0-1 Sketch of water cycle (<http://ga.water.usgs.gov/edu/watercycle.html>).

Hydrothermal fluids, hot aqueous fluids, are the main agents for the movement of thermal energy and mass transfer in the crust. Ore-forming hydrothermal systems are common in meteoric, seawater, basinal, magmatic, and metamorphic environments where water is abundant and a process is available to drive fluid flow (Kesler, 2005).

Seawater hydrothermal systems form in submarine crust, usually along mid-ocean and back-arc ridges, but also along faults associated with calderas and rift basins (e.g., Ohmoto & Skinner, 1983; Scott, 1997; Roberts et al., 2003). Ridge and caldera systems are hosted largely by volcanic rocks and form volcanic-hosted massive sulfide (VMS) deposits enriched

in Fe, Cu, and Zn, whereas rift margin systems are hosted by sedimentary rocks and form sedimentary rocks and form sedimentary exhalative (sedex) deposits enriched in Zn and Pb. Seawater hydrothermal systems are largely unconfined and are driven by mafic magma chambers, dikes, and sills (Cathles, 1983). In theory, these systems should form chimneys and mounds where the venting fluid is less dense than seawater, and lens-shaped ponds where it is more dense, although the high salinities necessary to produce bottom-seeking brines at these elevated temperatures might require special settings such as evaporate-contaminated rifts (Scott, 1997; Solomon & Quesada, 2003).

Basinal hydrothermal systems include connate water, as well as water from diagenetic reactions and meteoric recharge (Kharaka & Hanor, 2003). Hydrocarbon fluids are also important parts of basinal systems, but usually play a minor role in the formation of ores. Sedimentary basins form unconfined systems driven by near-surface evaporative brines or topographically high recharge, and confined systems where reservoirs are isolated by burial or deformation (Cathles & Smith, 1983; Garven, 1985; Bethke, 1986; Jones et al., 2002). The most common ores formed by basinal fluids are Mississippi Valley-type (MVT) deposits, which contain Zn and Pb (Leach & Sangster, 1993). Generally similar basinal fluids with different metal contents form unconformity-type uranium and Kupferschiefer-type Cu deposits (Kotzer & Kyser, 1995; Blundell et al., 2003; Richard et al., 2010).

Magmatic hydrothermal systems consisting of fluids released from crystallizing magma are most common around cupolas or other shallow felsic intrusions (Holland, 1972; Burnham, 1997). The systems are probably supplied in part by an underlying magma chamber, are confined by a ductile zone along the margin of the magma, and are surrounded by an unconfined hydrothermal system containing water of meteoric or seawater origin (Norton, 1978; Shinohara et al., 1995; Fournier, 1999). Abrupt release of magmatic fluid results in highly fractured, stockwork zones that host porphyry-type Cu, Mo, and Au deposits (Gustafson & Hunt, 1975; Carten et al., 1988; Muntean & Einaudi, 2001). Skarn deposits form where magmatic fluid intersects carbonate rocks. High-sulfidation epithermal Au-Ag deposits, which form at temperatures of about 200 to 300°C from S-rich, acid fluids, are thought to result from this process (Vennemann et al., 1993; Hedenquist et al., 1998).

Metamorphic hydrothermal systems result from expulsion of water and other fluids from rocks that undergo prograde metamorphism, usually in tectonically stacked zones or

subduction zone (Peacock, 1989; Ferry, 1995; Breeding & Ague, 2002). These fluids consist of mixtures of  $\text{H}_2\text{O}$  and  $\text{CO}_2$ , with eventually  $\text{CH}_4$ ,  $\text{N}_2$ ,  $\text{H}_2\text{S}$  or  $\text{SO}_2$ , the most common fluids released during metamorphic reactions (Powell et al., 1991). Metamorphic hydrothermal systems are largely confined below the brittle-ductile transition and release fluid only when they exceed confining pressure (Sibson et al., 1988). Greenstone or mesothermal Au deposits, which consist of quartz veins in strongly carbonatized wallrock, probably formed from metamorphic hydrothermal fluids with variable contributions of meteoric and magmatic fluid (Burrows et al., 1986; Nesbitt, 1988).

## 2. Parameters controlling mass transport by fluids

Fluids are the medium to transport and deposit the materials as a consequence of fluid-rock reaction, fluid mixing and fluid immiscibility. The transportation and deposition of the materials by fluids are controlled by several parameters. To address the question of transport properties of elements, it is necessary to consider the parameters which control the solubility of phases of these elements. A valuable starting point for the investigation of crustal fluid chemistry is the assumption that, in general, fluids are saturated solutions with respect to minerals of the rocks in which they reside. The concentration of some elements in aqueous crustal fluids is a function of several intensive and extensive parameters. Firstly, pressure and temperature are basic physical parameters. Figure 0-2 shows the phase changes in the system  $\text{Al}_2\text{O}_3\text{-H}_2\text{O}$  as a function of only temperature and  $\text{H}_2\text{O}$  pressure. For more complex systems, when P and T are fixed, the parameters  $f\text{O}_2$ ,  $f\text{S}_2$ ,  $f\text{CO}_2$ ,  $X\text{Cl}^-$ , ....., and pH control the solubility of minerals. Several examples are given in figure 0-3 (phase changes as a function of  $f\text{O}_2$  and  $f\text{S}_2$  in the system  $\text{HCl-H}_2\text{O-(FeO)-O}_2\text{-S}_2$ ), figure 0-4 (phase changes as a function of  $f\text{CO}_2$  in the system  $\text{HCl-H}_2\text{O-(CaO)-CO}_2\text{-H}_2\text{SO}_4$ ), figure 0-5 (solubility of gold in water as a function of  $f\text{O}_2$ ), figure 0-6 (wolframite solubility changed by  $X\text{Cl}^-$ ,  $\text{XF}^-$ , and pH), figure 0-7 and figure 0-8 (mineral phases changes and solution changes of thio-gold complexes as a function of pH, respectively),

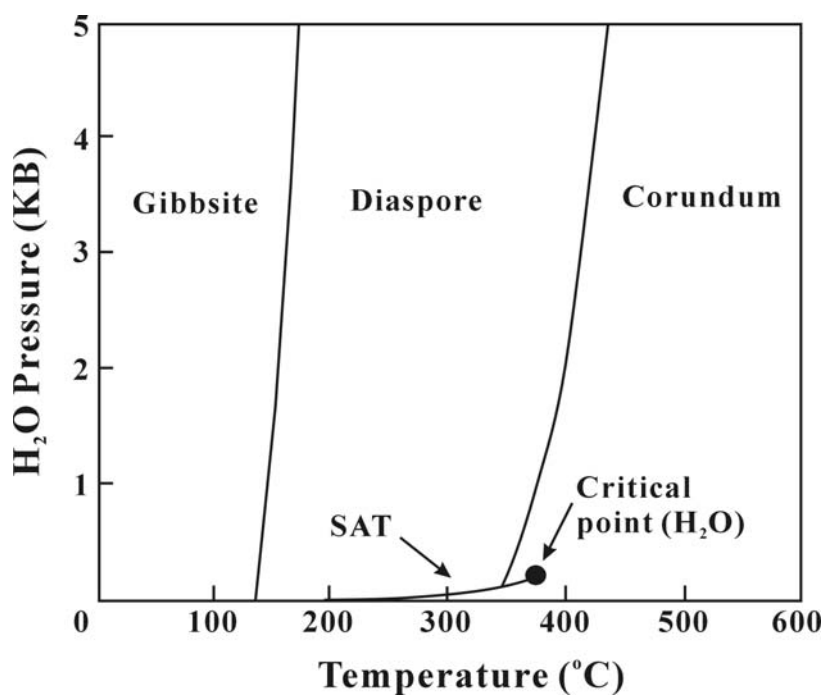


Figure 0-2 Stability fields of gibbsite, diaspore, and corundum in the system  $\text{Al}_2\text{O}_3\text{-H}_2\text{O}$  as a function of temperature and  $\text{H}_2\text{O}$  pressure (Helgeson et al., 1978).

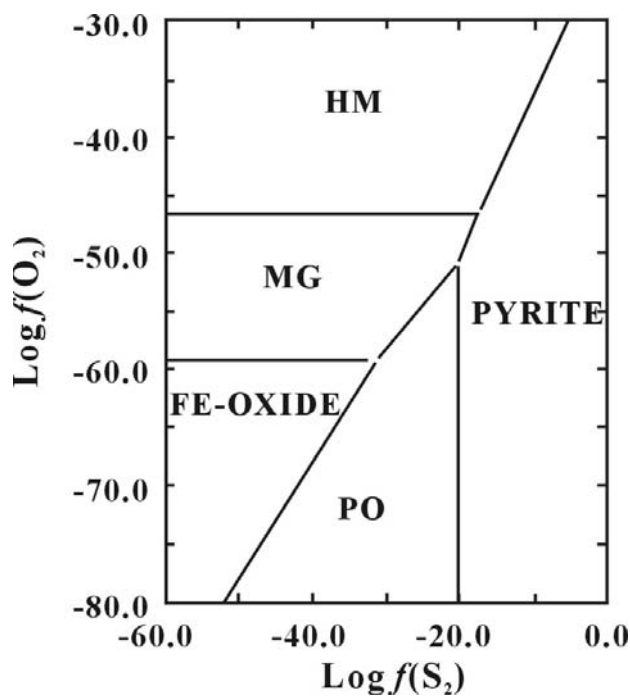


Figure 0-3 Phase relations in the system  $\text{HCl-H}_2\text{O-(FeO)-O}_2\text{-S}_2$  at 150 °C and 3.0 kbar (Bowers et al., 1984).

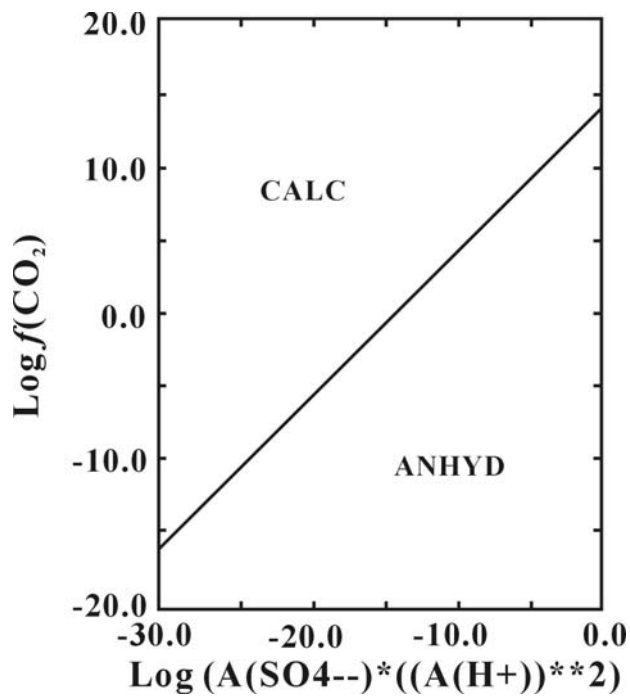


Figure 0-4 Phase relations in the system HCl-H<sub>2</sub>O-(CaO)-CO<sub>2</sub>-H<sub>2</sub>SO<sub>4</sub> at 25 °C and 0.001 kbar (Bowers et al., 1984).

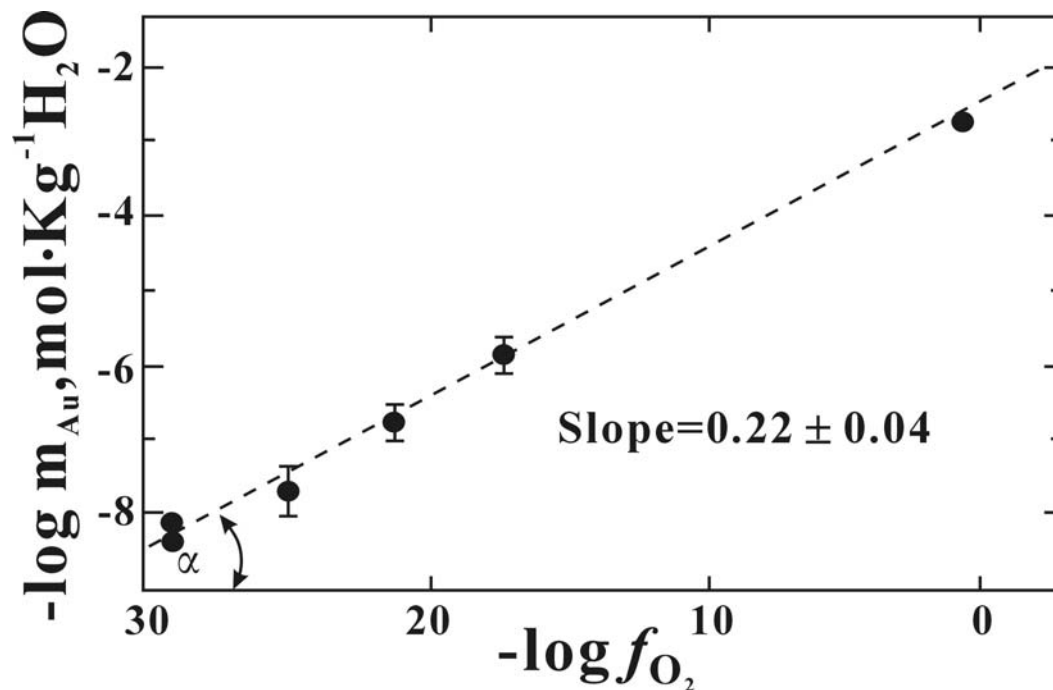


Figure 0-5 Solubility of Au(c) in water as a function of oxygen fugacity at 450 °C and 500 bar (Baranova et al., 1983).



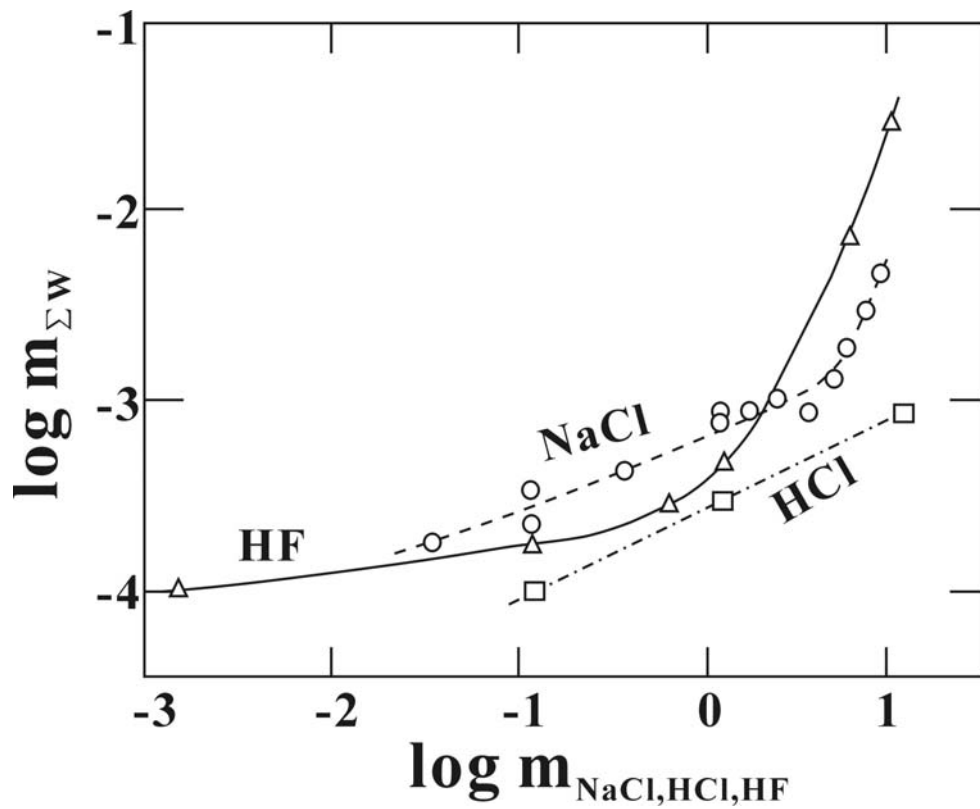


Figure 0-6 Dependence of wolframite solubility as a function of the concentration of NaCl, HCl, and HF at 400 °C, 1 kbar (Zaraisky, 1995).

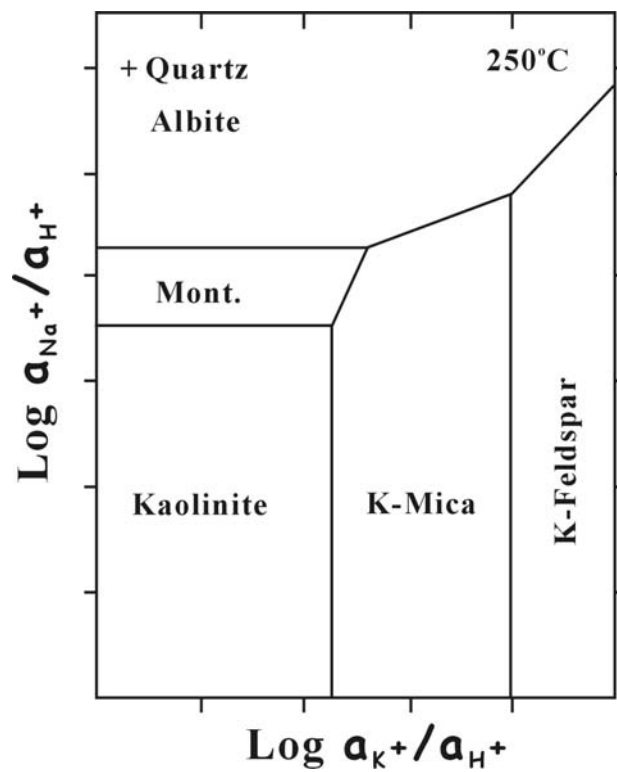


Figure 0-7 Activity diagram for the equilibria of principal mineral phases as a function of pH in the system  $\text{Na}_2\text{O}-\text{K}_2\text{O}-\text{Al}_2\text{O}_3-\text{H}_2\text{O}$  at 250 °C at saturation pressure (Henley et al., 1984).

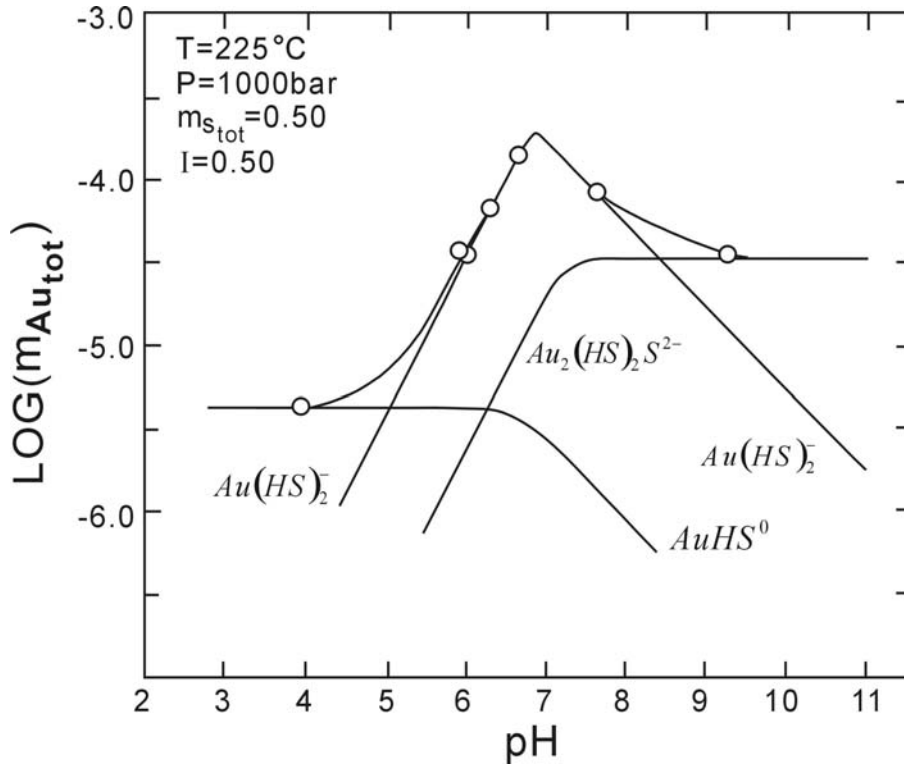


Figure 0-8 Gold solubility and concentration thio-gold complexes as a function of pH at 225 °C and 1 kbar pressure (after Seward, 1973).

### 3. PH of present day geological fluid

#### 3.1. Definition of pH

Several previous diagrams show that pH or proton activity plays a major role in phase equilibria and solubility of metal-bearing phases. PH indicates the sample acidity, or is actually a measurement of the potential activity of hydrogen ions ( $\text{H}^+$ ) in the sample. The original definition of pH (Sørensen, 1909) was

$$\text{pH} = -\log[\text{H}^+] \quad (0-1)$$

Within the infinite dilution concept, pH may be defined in terms of hydrogen ion activity:

$$\text{p}^a\text{H} = -\log\{\text{H}^+\} = -\log[\text{H}^+] - \log f_{\text{H}^+} \quad (0-2)$$

#### 3.2. Main acid-base equilibria

It is the control variable in any acid-base equilibrium. According to the chemical composition of fluids of the upper crust, the main acid-base dissociation equilibria are the following:

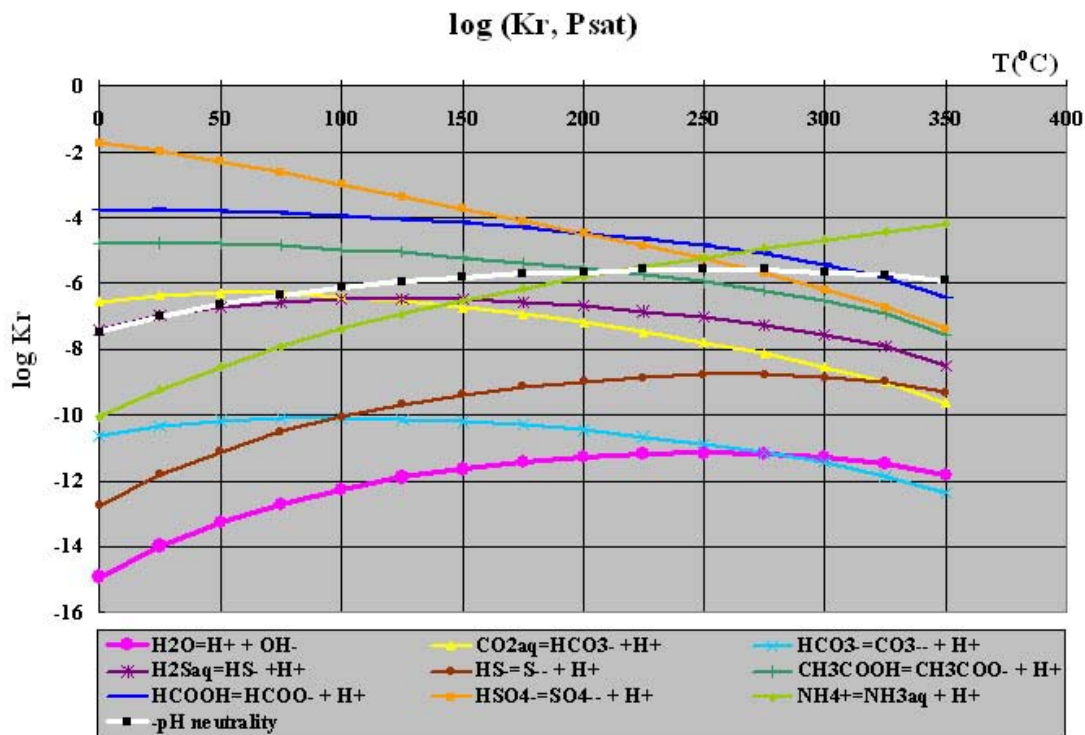
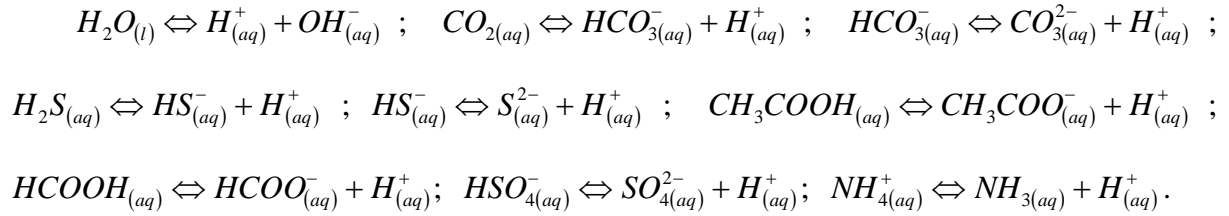


Figure 0-9 Variation of equilibrium constants of acid-base equilibria as a function of temperature along the saturation curve of pure water ( $P = P_{\text{sat}}$  at  $T$ ). Data are calculated from Program OrganoBioGeoTherm (V. 1.52) written by John J. Donovan.

Figure 0-9 shows the variation of the equilibrium constants of acid-base couples in the fluids in the  $P_{\text{sat}}$ - $T$  plane relevant to earth crust conditions. This diagram  $\log K_r$  versus  $T$  at  $P_{\text{sat}}$  shows variation by several orders of magnitude of the equilibrium constants. For instance, the value of the dissociation of pure water ( $\log K_w$ ) varies from -15 at 0 °C to -12 at 350 °C. Therefore, neutral pH (neutral pH =  $-1/2 \log K_w$ ) varies from 7.5 at 0 °C to 5.9 at 350 °C.

This is why the dissociation constants (Kr) of each acid-base equilibrium, more precisely their pKr ( $\text{pKr} = -\log(\text{Kr})$ ) are compared with the neutral pH values of pure water at the same temperature at the saturation pressure. The difference with neutral pH is quantified by calculating the value of the parameter “Delta pH / neutrality” at each T at Psat following the equation:

$$\text{Delta pH / neutrality} = - (1/2) \text{pKw-pKr} \quad (0-3)$$

Results are illustrated in figure 0-10. This diagram shows that fluids with pH equal to the pKr of a given acid-base equilibrium like  $\text{CO}_{2(aq)} \Leftrightarrow \text{HCO}_{3(aq)}^- + \text{H}_{(aq)}^+$  may be acid at room temperature, neutral around 80 °C and basic up to 300 °C with increasing basicity with increasing temperature. Other fluids with pH equal to the pKr of  $\text{HCO}_{3(aq)}^- \Leftrightarrow \text{CO}_{3(aq)}^{2-} + \text{H}_{(aq)}^+$  acid-base equilibrium like remains basic in the 25°C-300°C temperature range. On the other hand, fluids with pH equal to the pKr of  $\text{NH}_4^+ \Leftrightarrow \text{NH}_{3(aq)} + \text{H}_{(aq)}^+$  are basic at low temperature, neutral around 150°C and acid at higher temperature.

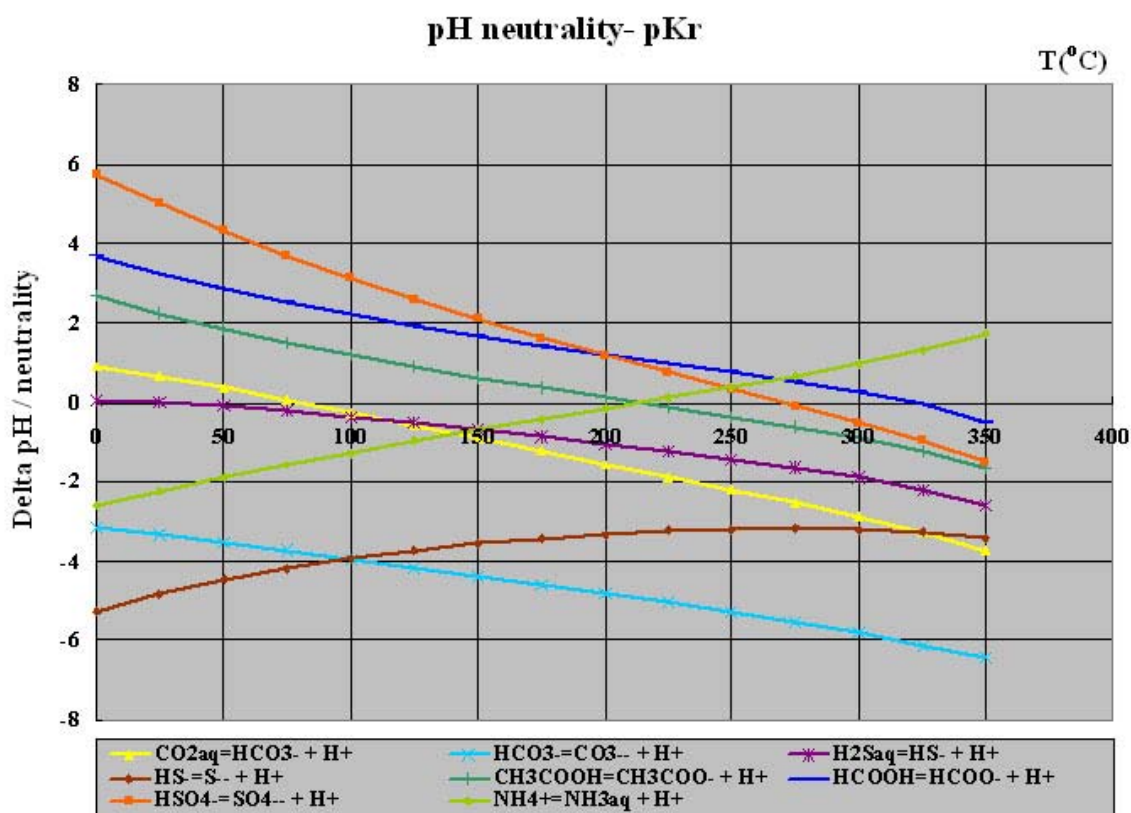


Figure 0-10 Difference of pH of fluids at pH = pKr of different acid-base equilibria versus temperature at water saturation pressure.  $\text{Delta pH / neutrality} = - (1/2) \text{pKw-pKr}$ .

Proton activity plays an important role in the transport and precipitation of ore-forming elements and in the dissolution of mineral phases in geological process because the solubility of minerals and the speciation of metal together with the stability of its main ligand is a function of pH if the other properties of fluids, e.g. P, T, V,  $fO_2$ ,  $fS_2$ ,  $XCl^-$ ,....., are fixed (Henley et al., 1984; Shmulovich et al., 1995). Figure 0-8 shows the existence of thio-complexing of gold and their solution as a function of pH. In a word, it is absolutely necessary to estimate the pH value of geo-fluid in palaeo-circulation for a better understanding of the forming condition of a metal ore deposit.

### **3.3. PH data and pH measurement of present-day geological fluids**

There are two types of geological fluids relevant to Earth crust, modern hydrothermal fluids and ancient fluids.

Hot venting fluids are the modern hydrothermal fluids. Numerous efforts have been made to determine the pH of the hot venting fluids (e.g., Edmond, 1979; Bowers & Taylor, 1986; Ding & Seyfried, 1992; Ding et al., 2005). Direct and indirect measurements of pH of hot venting fluids are developed. Indirect measurement of pH is through sampling fluids by special equipment to determine the pH (Ishibashi et al., 1994). Direct measurement of pH is by using a developed sensor. The measurement of in situ pH of hot venting fluids is available up to 384°C and up to 250 bar (Ding et al., 2005). It is also noted that now there exists in situ sensor which allow pH measurements up to 400°C (Ding & Seyfried, 1996). The variation of pH of hot venting fluids in oceanic ridges is available from less than 3.0 (very rare) to 12.0 (e.g., Ding & Seyfried, 1994; Cipolli et al., 2004; Konn et al., 2009; Nordstrom et al., 2009). Continental geothermal fields or systems are also places of active circulation of hydrothermal fluids. Volcanism, caldera formation, and associated faulting in the area are related to the geothermal system. Hydrothermal fluids are involved in sedimentary basin, corridor, valley or hot spring (e.g., Lewis et al., 1997; Carvalho et al., 2006). The pH of fluids is measured indirectly by sampling fluids or directly by hand-held pH meter. The variation of pH of hydrothermal fluids in these systems ranges from 2 to 9.5 (e.g., Truesdell et al., 1984; Lewis et al., 1998; Carvalho et al., 2006)

### **3.4. PH of palaeo-fluids**

The pH values of ancient fluids in palaeo-circulation remain largely unknown because it can be only estimated from thermochemical equilibria. Palaeo-fluid pH is inferred by combining mineral assemblages and the related fluid inclusions assuming fluid-mineral equilibria (Christie, 1982; Likhoidov et al., 2003). Palaeo-pH can also be evaluated directly from fluid inclusions (Dubessy et al., 1992; Boiron et al., 1999). Another way consists to the indirectly experimental simulation in laboratory (Roberts, 2003; Kolonin & Shironosova, 2002). The difficulty to evaluate the pH of ancient fluids in palaeo-circulation is to obtain representative preserved fluid samples. Fluid inclusions are the vestige of fluids in geological processes (e.g., Sorby, 1858; Roedder, 1962a; Poty et al., 1976). So, fluid inclusions, as remaining of palaeo-circulation, should be an important tool for pH determination. Thus, this thesis is focused on fluid inclusions for the estimation of pH.

#### **3.4.1. Palaeo-fluid and fluid inclusions: a brief summary**

Can the fluids in paleo-circulation be preserved until today? And where are those paleo-fluids? Sorby (1858) showed fluid-, stone- and glass-cavities in artificial and natural crystalline minerals and rocks. These cavities were formed in the process of formation and evolvment of the minerals and rocks. A portion of fluid surrounding them were caught up and enclosed in those cavities. Roedder (1962a) systematically characterized the ancient fluids enclosed in crystals. In his paper, he mentioned that the droplets of fluid preserved in many minerals and rocks were ancient mother liquors and called the minuscule microscopic droplets a “fluid inclusion”. Many techniques and methods have been developed for studying fluid inclusions, such as microthermometry and different microspectroscopies. The data obtained through the analyses of fluid inclusions are useful, because they help determine the physical and chemical properties of inclusion fluids (e.g. P, T, V,  $fO_2$ ,  $fS_2$ ,  $XCl$ , ....., pH), which are necessary to determine the events happened in paleo-circulation, especially to quantify the process of transportation and deposition of material (Poty et al., 1976; Roedder, 1984, 2002; Dubessy et al., 1989; Nyman et al., 1990).

Fluid inclusions, as the vestige in palaeo-circulation, preserve micro-quantity of paleo-fluids, and more and more analytical approaches and techniques applied to measure fluid inclusion have been developed and improved (Poty et al., 1976; Dhamelincourt et al., 1979; Roedder, 1990; Rankin, 2005). The main microanalytical techniques are recalled as following.

- microthermometry, which is firstly applied to the analysis of fluid inclusion and is a technique to determine the inclusion composition and related physical and chemical properties (Roedder, 1962b; Poty et al., 1976; Hollister et al., 1981).

- micro-Raman, which is a non-destructive technique and is applied to identify the gases, polyatomic ions, solid phases, and even solid phase transitions with temperature, and to determine the chlorinity (e.g., Dhamelincourt et al., 1979; Dubessy et al., 1982; Dubessy et al., 1989; Burke, 2001).

- micro-Laser Induced Breakdown Spectroscopy is a destructive technique based on the time resolved optical emission spectroscopy of elements contained in plasma produced by the laser. This technique allows an elemental analysis of major monoatomic cations (alkaline, alkaline earth elements) in individual fluid inclusions (Fabre et al., 2002; Godwal et al., 2008).

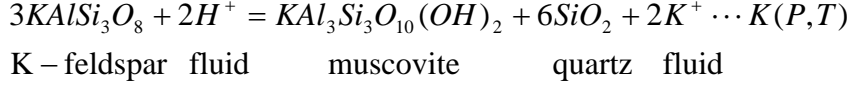
- Laser Ablation Inductively Coupled Plasma Mass Spectrometry (LA-ICP-MS), which is a recent destructive technique to be applied to directly analyze the elements in inclusions, including the major-, minor-, and trace-solute compositions of individual fluid and melt inclusions in minerals (Günther, 1998; Heinrich et al., 2003; Pettke et al., 2004; Allan et al., 2005; Richard et al., 2010).

### **3.4.2. Use of fluid inclusions for palaeo-pH estimation**

Several approaches for the determination of pH in palaeo-circulation from fluid inclusion data can be proposed. According to different cases, two main routes are possible for estimation of pH from fluid inclusion composition.

#### **- Mineral assemblage and fluid chemistry of coexisting fluid inclusions**

The first route is the use of the concentration of an ion, which allows the calculation of pH from the equilibrium between fluid and a mineral phase. For example, if a rock contains potassic-feldspar, muscovite and quartz with a generation of fluid inclusion in quartz as relict of fluid at equilibrium with the three above mentioned minerals, the equilibrium between fluid and minerals is as follows:



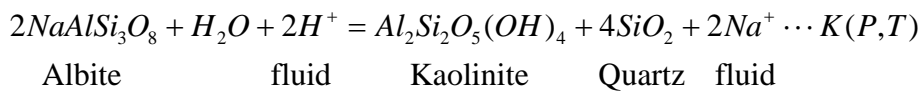
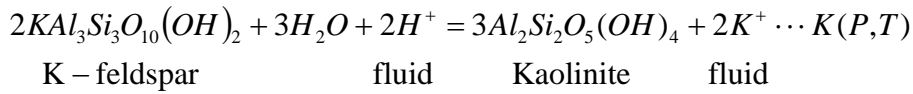
The corresponding equilibrium condition deduced from law mass action is:

$$\left. \begin{aligned} K(P,T) &= \frac{a_{K^+}}{a_{H^+}} \Rightarrow a_{H^+} = \frac{a_{K^+}}{K(P,T)} \\ pH &= -\log a_{H^+} \end{aligned} \right\} \Rightarrow pH = -\log \left( \frac{a_{K^+}}{K(P,T)} \right) \Rightarrow pH = \log K(P,T) - \log a_{K^+}$$

Therefore, pH can be deduced provided the following parameters are known:

- the temperature,
- the pressure to calculate  $K(P,T)$ ,
- the concentration of potassium  $m(K^+)$ , the bulk composition of the fluid and a suitable thermodynamic model for the considered  $P$ - $T$  conditions to calculate the activity coefficient ( $\gamma_i$ ) of potassium in the fluid.

Similar methods of pH determination could also be applied using other mineral alkaline feldspars and kaolinite:



However, the pH determination using this method requires suitable mineral assemblages and to be sure that the analysed fluid inclusions are representative of the fluid which was coexisting and was at equilibrium with the considered mineral phases. This route is not applicable to all natural cases.

#### **- Equilibrium among aqueous species in inclusion fluid**



The second route consists to use the chemical composition itself of fluid inclusion, which permits to calculate the pH from equilibrium among the chemical species of dissociation equilibrium of weak acids in inclusion fluids. This method is just related to acid-base equilibrium in the fluid and does not use equilibrium between fluid and mineral assemblages. Figure 0-11 shows the variation of equilibrium constant as a function of temperature in different equilibrium among the species in natural inclusion fluids.

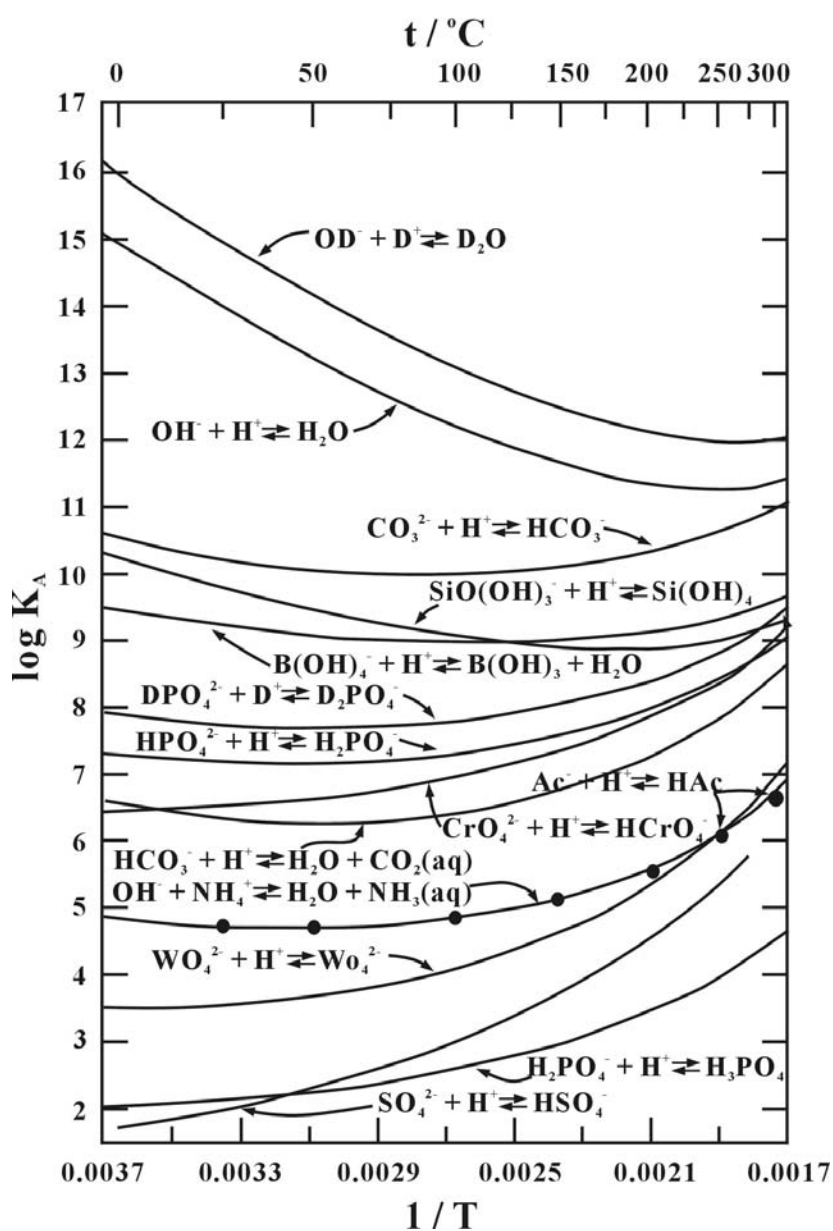
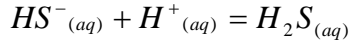
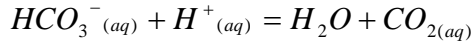
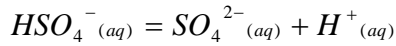


Figure 0-11 Diagram of temperature dependence of the association constants for the formation of weak acids and bases at the saturation vapour pressure of water to 300 °C. (Pitzer, 1991).

For example, three following equilibria are mentioned:



The pH is deduced from the determination of activities of species. Micro-Raman spectrometry is introduced to the quantitative analysis of equilibria controlled by pH between polyatomic ions, which have a Raman spectrum, such as  $HSO_4^-/SO_4^{2-}$ ,  $HCO_3^-/CO_2$  or  $HS^-/H_2S$  (Dubessy et al., 1992). The first equilibrium has been studied in details and successfully applied to natural samples by Dubessy et al. (1992) and Boiron et al. (1999). However, this case is applicable to very acid fluids whose  $pH < 2$  at ambient temperature, which is rare case for geological system, moreover, the presence of sulfate demands quite high oxygen fugacity for the stability of valency VI of sulphur, for instance, in proximity of Hematite-Magnetite buffer. Therefore, many rocks, for instance those containing sulfide minerals, may impose to the fluid a redox state with too low values of oxygen fugacity incompatible with the stability of sulfate in the aqueous phase.

The second equilibrium is a ubiquitous chemical equilibrium, which plays a major role in geological fluid and which is applicable to most of geological fluids with pH such as  $4 < pH < 8$  at ambient temperature.

PH can be estimated from the following equations derived from the law mass actions.

$$K_1 = \frac{a_{CO_2(aq)} \cdot a_{H_2O}}{a_{HCO_3^-} \cdot a_{H^+}} \text{ and } \begin{cases} a_{CO_2(aq)} = m_{CO_2(aq)} \cdot \gamma_{CO_2(aq)} \\ a_{HCO_3^-} = m_{HCO_3^-} \cdot \gamma_{HCO_3^-} \end{cases}$$

$$pH = -\log a_{H^+} = -\log \left( \frac{m_{CO_2(aq)} \gamma_{CO_2(aq)} a_{H_2O}}{K_1 m_{HCO_3^-} \gamma_{HCO_3^-}} \right)$$

$$\Rightarrow pH = \log \left( \frac{m_{HCO_3^-}}{m_{CO_2(aq)}} \right) + \log \left( \frac{\gamma_{HCO_3^-}}{\gamma_{CO_2(aq)}} \right) + \log K_1 - \log a_{H_2O}$$

Most of natural fluids contain carbon dioxide as shown by the identification of carbon dioxide in a variety of natural fluid inclusions from sedimentary basin or hydrothermal

systems. This equilibrium is worth to be studied and the pH can be calculated. It is necessary to obtain concentrations of species ( $\text{HCO}_3^-$  and  $\text{CO}_2$ ) using Raman spectroscopy, thermodynamic values of equilibrium constant, and activity coefficients from a relevant thermodynamic model.

Because of the ubiquitous character of the  $\text{CO}_2\text{-HCO}_3^-\text{H}^+$  subsystem in geological fluids, the development of pH determination using this system is a challenge for fluid geochemistry.

Under these fundamental scientific objectives, this thesis is focused on the pH estimation of paleo-circulation from fluid inclusion in the model system  $\text{H}_2\text{O-Na}^+\text{-Cl}^-\text{-CO}_2\text{-HCO}_3^-$ .  $\text{Na}^+$  and  $\text{Cl}^-$  are considered, not only because they are the most common cation and anion, respectively in natural salt-bearing aqueous fluid inclusions (Roedder, 1972, 1984), but also because  $\text{Cl}^-$  is the main complex anion in hydrothermal solution, making its strong coordination ability with metal cations and its role in the transport of many metals in ore-forming fluids. For determining the pH value of such fluids, the methodology, is based on the combined use of microthermometry and Raman microspectroscopy with thermodynamic modeling. Fundamental methodology on the analysis by Raman spectroscopy and thermodynamic modeling is developed. The application of the methodology on a natural case (such as Au) is also presented in this thesis.

## **CHAPTER I: EXPERIMENTAL METHODS**

The objective of this thesis is the determination of pH of palaeo-fluids found now as fluid inclusions. Therefore, the analytical techniques which will be used are the routinely techniques for fluid inclusions such as microthermometry and micro-Raman spectroscopy. As it will be application later, the methodology developed to achieve pH determination in natural fluid inclusions requires to be calibrated. Calibration can be performed only using standard samples of well known composition. Two kinds of standard samples are produced: synthetic fluid inclusions in quartz crystals and synthetic fluids in pure silica glass capillary following the techniques developed by Chou et al. (2008).

As calibration data are obtained at various temperatures using glass capillaries, their geometry (cylindrical) requires verifying the calibration of temperature measurements using the most relevant heating and freezing stages.

## **I.1. Microthermometric measurements**

Microthermometry is one of non destructive methods to measure the property of the fluid in an inclusion (e.g. Poty et al., 1976; Roedder, 1990; Rankin, 2005). It assumes that the molar volume-composition (v-x) properties of fluid inclusions remain constant during the microthermometric study and are representative of the v-x properties of the initial fluid trapped in the crystal. The aim of microthermometry consists to get information on the main chemical component using temperature of invariant points (triple point, eutectic point), concentration information using temperature monovariant curves (Solid + Liquid + Vapor  $\rightarrow$  Liquid + Vapor) and density information using bubble point curve (Liquid + Vapor  $\rightarrow$  Liquid) or dew point curve (Liquid + Vapor  $\rightarrow$  Vapor). As early as in 1858, Sorby carried out the first microthermometric measurements to attempt to determine components from the melting points of phases in some fluid inclusions. Today, microthermometric measurements of samples are carried out using heating-freezing stage (e.g. Roedder, 1962b; Poty et al., 1976; Hollister et al., 1981). As any analytical device, microthermometric stages need to be calibrated to get accurate molar volume (v) and composition data (x). Such calibration will take into account both the accuracy of the thermocouple and the possible thermal gradient between the sample and thermal sensor and eventually within the sample itself.

In practice, three types of micrometric heating-freezing stages are used in fluid analysis, ChaixMeca stage, Linkam<sup>®</sup> geology stages and USGS gas-flow stage. After some preliminary experiments with capillary, the ChaixMeca stage was not used any more because of the length of the capillary (capillary: 8 to 15 mm long, the diameter of viewing area: 4 mm and 30 mm diameter of the chamber sample). Standard synthetic fluid inclusions or chemical products are chosen to calibrate the stage in terms of the phase change temperatures of interest. Many samples studied in this work are fluid included in silica glass capillaries which have cylindrical geometry (100  $\mu\text{m}$  inner diameter, 8 to 15 mm long). Thus the geometry of the thermal contact between the sample and the heating-freezing elements depends on the geometry of samples which are either silica glass capillary or quartz wafer. It should be noted also that the dimension of the cavity containing the fluid phases inside the capillary is much greater than the one of inside typical fluid inclusions. So it is necessary to check the two geological stages in the application of microthermometric measurement of capillary and to know the advantages and shortcomings of each stage for the measurement of capillary.

### **I.1.1. Linkam geology heating-freezing stage**

Linkam<sup>®</sup> geology heating-freezing stage is widely used in measurement of geological fluid, and it is provided by Linkam Scientific Instruments Ltd., UK (<http://www.linkam.co.uk/>). Two models of MDS600 and THMSG600 are used in two labs (Nanjing and Nancy), and they both include temperature programmer and cooling pump in addition to the main stage (figure I-1a). Electric heating element is used to heat the sample and liquid nitrogen is used to cool the sample, which permits to get the temperature range between -196 °C and 600 °C. The possible heating-freezing rates are between 0.1 °C and 90 °C/minute. Stages are used in conjunction with an optical microscope fitted with high quality long working distance lenses. These allow high resolution observations to be made up to magnifications of  $\times 500$  in this work. Short description of structure of stage is given for well calibration. As shown as in figure I-1b, a pure silver lid - block encloses to form a chamber, to minimize temperature gradients. The sample is put onto sample holder and carrier which is in contact with the silver heating-freezing block and permits to move sample for observation of all the samples. The sample can be observed through the view area only close to the optical

axis of the system determined by the hole of in centre of the silver lid and the optical window in the silver block (1 mm diameter).

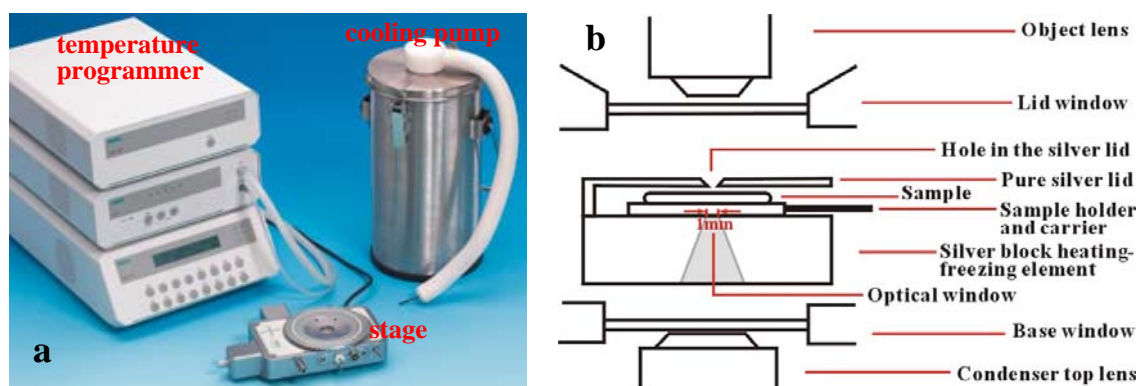


Figure I-1 a. Photograph of the Linkam MDS600 heating-freezing stage; b. the cutaway view of the stage.

The inner diameter (normally 15 mm, figure I-2) of the silver lid determines the maximum dimension of the sample. It is noted that the cylindrical geometry and macro-dimension of capillary sample is different from the chip of quartz wafer (practically, quartz wafers are broken into chips with the appropriate size, usually  $5 \pm 1$  mm). Figure I-2 presents the sample holder and carrier used commonly for the measurements of fluid inclusions (a) and the matched silver lid. Sample holder and carrier must allow optical observation of the capillary along all its length (8 to 15 mm) and must be used with the silver lid to minimize vertical temperature gradient. The shapes of all parts are round for widely observing the sample chip because the part of chip is observed only close to the optical axis of the system determined by the hole in the centre of silver lid and the optical window on the upper part of the heating-freezing block (1 mm diameter). But considering the length of capillary (Length > 8 mm), the size of sample-placed glass (7 mm diameter) matching the sample holder and carrier is not enough to the length of capillary, so larger size of glasses (13 mm diameter and ~ 20 mm diameter) are introduced (figure I-2 b and c). However the large size glasses do not allow to move enough the sample to observe it along its length for the capillary because of the limitations of combination of silver block (20 mm diameter) and silver lid (20 mm outer diameter, 15 mm inner diameter). Therefore the silver lid should not be used with these glasses, which is not suitable for accurate temperature measurements.

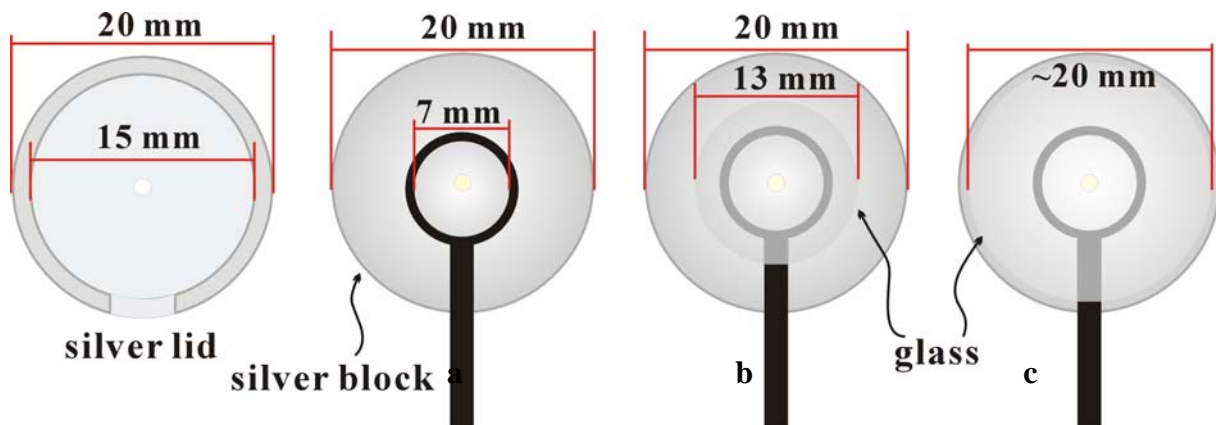


Figure I-2 Sketch of silver lid and sample holder and carrier commonly used in Linkam geology heating-freezing stage. a, b and c are the sample hold and carrier with sample-placed glass in different size.

Considering the cylindrical geometry of capillary, a modified silver lid and sample holder and carrier have been designed by Linkam company. The shape of sample holder is a rectangle (5 mm wide and 14 mm long) and the matched silver lid has two openings (figure I-3), which permits to observe all the capillary with silver lid during the temperature measurements.

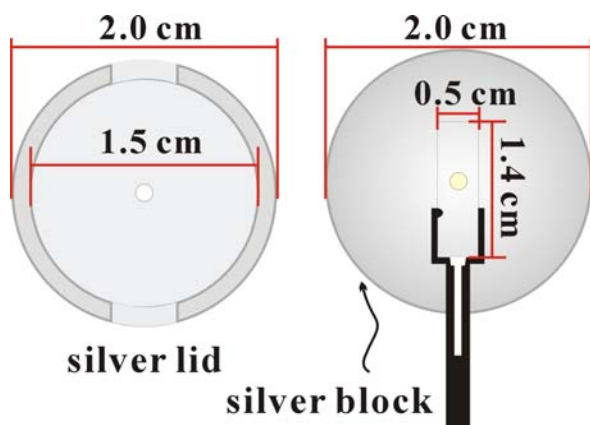


Figure I-3 Sketch of modified silver lid and sample holder and carrier designed for capillary sample.

### I.1.2. USGS gas-flow heating-freezing stage



The USGS gas-flow heating-freezing stage has a larger sample chamber, which is enough for capillary sample. This stage was from Fluid Inc., USA. Apart from the main stage, there are electric heating element, liquid nitrogen tank with gauge-and-regulator unit, variable transformer and gas line with gas flow meter. Figure I-4a shows the stage enclosed by white insulation in conjunction with an optical microscope with high quality long working distance lenses, which also allow high resolution observations to be made up to magnifications of  $\times 500$  in this work. Preheated gas by electric heating element and chilled gas by liquid nitrogen are used to heat and cool a sample over a temperature range  $-195\text{ }^{\circ}\text{C}$  -  $+700\text{ }^{\circ}\text{C}$  and the rate of heating and cooling is changed through adjusting gas flow (cooling mode:  $-100\text{ }^{\circ}\text{C}$  can be obtained in less than 30 seconds; heating mode:  $+300\text{ }^{\circ}\text{C}$  can be obtained in less than 30 seconds) and the reading is to  $0.1\text{ }^{\circ}\text{C}$ . The structure of USGS stage is different from Linkam stage (shown in figure I-4b). The sample chamber is enclosed by several glass chips up and down and by insulation all around. The insulation and the air lays formed by glass chips minimize the vertical thermal gradient. Gas heating-freezing element is placed in cylindrical slot to the left and a thermocouple enters into the sample chamber opposite the gas entry port. The sample is globally observed by moving the whole stage. Figure I-5 gives a view of the details of the sample chamber. The sample chamber is round (23 mm diameter), which is enough for optical observation of capillary up to 20 mm length.

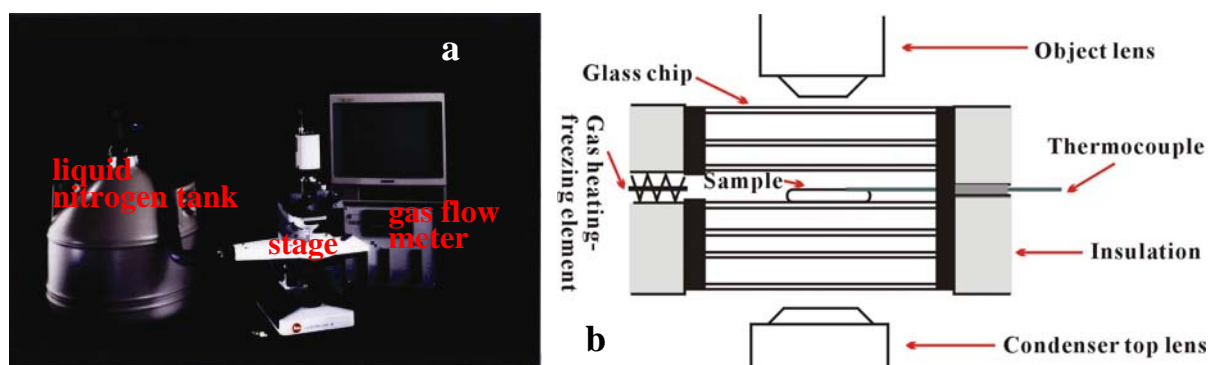


Figure I-4 a. Photograph of the USGS gas-flow heating-freezing stage (taken from Instruction of U.S.G.S. ); b. the cutaway view of the stage.

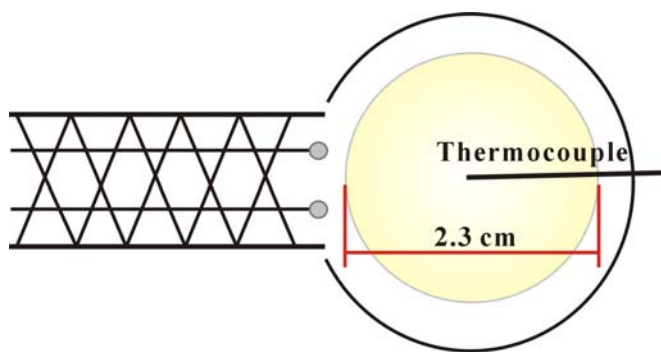


Figure I-5 Sketch of sample chamber of USGS stage.

### I.1.3. Calibration of Linkam and USGS stages

All stages need to be calibrated because of the error of temperature sensor itself and the thermal gradient between the temperature sensor and the sample and also because of the different thermal characteristics of different geometry of the sample. Calibration involves measuring the known temperatures of phase transition of substances. Stages are first calibrated using synthetic fluid inclusions and then using capillary.

System	Texp (°C)				
Pure H <sub>2</sub> O with critical density Tc (374.0 °C)	Position1	374.5	374.4	374.4	Linkam stage
	Position2	374.7	374.8	374.7	Linkam stage
	Position3	374.4	374.4	374.5	Linkam stage
	Position1	376.4	376.3	375.8	USGS stage
	Position2	376.0	375.8	375.7	USGS stage
	Position3	375.0	375.1	375.2	USGS stage
H <sub>2</sub> O-NaOH (salinity is known) Tm (-0.4 °C)	Position1	-0.7	-0.7	-0.7	Linkam stage
	Position2	-0.5	-0.5	-0.5	Linkam stage
	Position3	-0.6	-0.6	-0.6	Linkam stage
H <sub>2</sub> O-CO <sub>2</sub> Tr (-56.6 °C)	Position1	-57.8	-57.8	-57.7	Linkam stage
	Position2	-57.3	-57.4	-57.3	Linkam stage
	Position3	-57.0	-57.1	-57.0	Linkam stage

\*T<sub>exp</sub>: experimental temperature of special phase change; T<sub>c</sub>: critical homogenization temperature; T<sub>m</sub>: final melting temperature of ice; T<sub>r</sub>: temperature of triple point

Table I-1 Results for the calibration of temperature using synthetic fluid inclusions.

The repeatability of the measurements is first checked with a given sample located some positions at the stage. Then, the influence of the sample position is checked. Last experiments consist to use the best position of the capillary for different composition. Table I-1 shows the temperature measurements of synthetic fluid inclusion by Linkam stage have good precision and accuracy, but the ones by USGS stage have low precision and accuracy.

## **I.2. Raman measurements**

Raman microspectrometry is also one of non destructive methods appropriate to the qualitative and quantitative analysis of fluid inclusion (solids, liquids or gases). For example, Dubessy et al. (1982) present the qualitative determination of the electrolytes dissolved in the aqueous phase of fluid inclusions in detail, and Dubessy et al. (1983) gave the excellent result on quantitative determination of sulphate. Dubessy et al. (1989) described the analysis of fluid inclusions by micro-Raman spectrometry in details, including the identification of anions and cations and gases in fluid inclusions. Burke (2001) summarized the application of Raman microspectrometry in analysis of fluid inclusion. This analytical technique is based on the Raman scattering spectroscopy. Coupling Raman spectrometer with an optical microscope makes a Raman microprobe which allows the analysis of samples at the scale of micrometer.

### **I.2.1. Principles of Raman spectroscopy**

Raman spectroscopy is a molecular spectroscopy based on the inelastic Raman scattering of light caused by matter. Raman scattering was discovered by the Indian scientist C. V. Raman who, with K. S. Krishnan, first observed this phenomenon in liquids in 1928. The interaction of the incident light with the vibrational modes in the sample causes the energy exchange between the energy of the exciting incident monochromatic beam and the

vibrational energy of the irradiated sample (solids, liquids or gases). As illustrated as in figure I-6, when the light interacts with the matter, the scattered light consists of two types: the first one named Rayleigh scattering is intense and has the same frequency as the incident beam ( $\nu_0$ ). The intensity of Rayleigh scattering is generally about  $10^{-3}$  of the intensity of the incident exciting radiation. The second type of radiations named Raman scattering, is very weak ( $\sim 10^{-6}$  and lower of the incident beam) and has frequencies  $\nu_0 \pm \Delta\nu$ , where  $\Delta\nu$  is a vibrational frequency of a molecule. The  $\nu_0 - \Delta\nu$  and  $\nu_0 + \Delta\nu$  lines are called the Stokes and anti-Stokes lines, respectively. Thus, in Raman spectroscopy, the vibrational frequency ( $\Delta\nu$ ) is measured as a shift from the incident beam frequency ( $\nu_0$ ). In contrast to IR spectra, Raman spectra can be obtained in UV, visible and Near Infrared (NIR) region. An introduction to Raman effect can be found in the textbook of Long (1977). The application of the theory of Raman scattering to Earth sciences can be found in the review by McMillan & Hofmeister (1988).

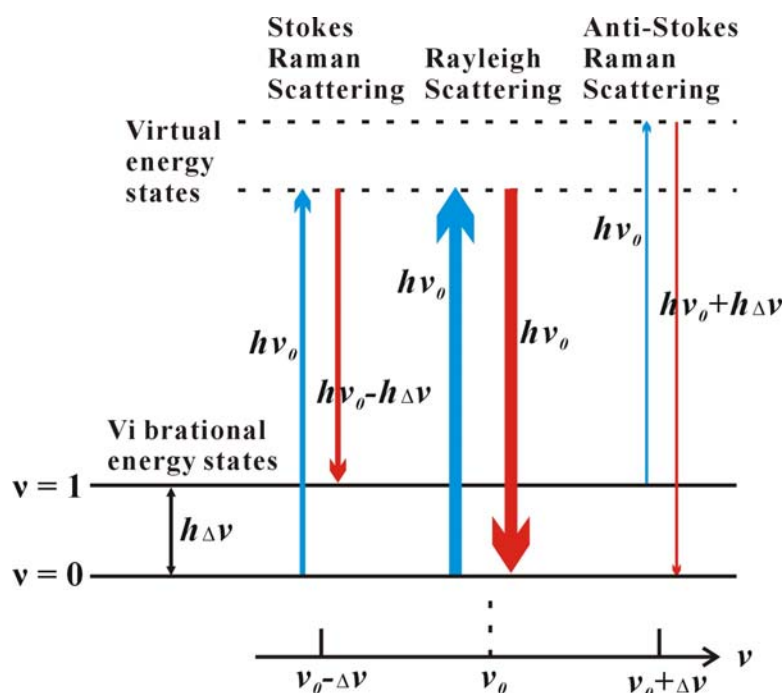


Figure I-6 Diagrammatic representation of an energy transfer model of Stokes Raman scattering, anti-Stokes Raman scattering and Rayleigh scattering.

For predicting whether a molecular vibration is Raman active or not, the classical theory is introduced. Raman scattering phenomena may be described using a classical explanation in terms of the electromagnetic radiation by emitted multipoles induced by the electric field of

the incident radiation. For example, if a diatomic molecule is irradiated by an incident light ( $\nu_0$ ), an electric dipole moment ( $\vec{P}$ ) is induced:

$$\vec{P} = \alpha \vec{E} \quad (\text{I-1})$$

where  $\vec{E}$  is the electric field of the electromagnetic radiation of the incident beam.  $\alpha$  called polarizability is a tensor. According to the classical theory, if the polarizability tensor is not constant during a vibrational normal model

$$\frac{\partial \alpha}{\partial Q} \neq 0 \quad (\text{I-2})$$

then an oscillating dipole radiates light at frequency  $\nu_0 - \Delta\nu$  for the Stokes Raman scattering and at frequency  $\nu_0 + \Delta\nu$  for the anti-Stokes Raman scattering.

A vibrational normal mode is Raman-active, if the polarizability tensor ( $\alpha$ ) changes with a vibrational normal mode. Molecular symmetry is the unifying thread throughout spectroscopy and molecular structure theory. Group theory applied to the symmetry of normal vibrational modes allows the determination of active and inactive vibrational modes. The details on group theory and its application to spectroscopy can be found e.g. Racah (1965).

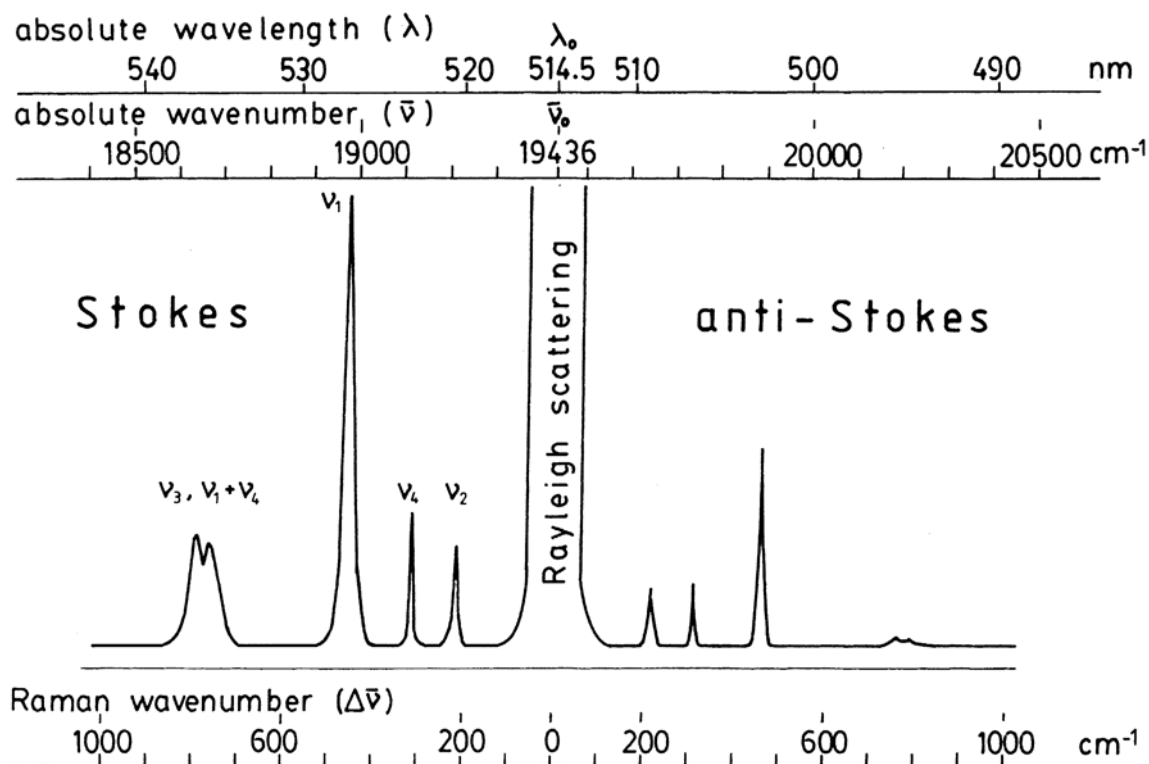


Figure I-7 Rayleigh and Raman spectra of CCl<sub>4</sub> (liquid) excited with 514.5nm laser light (printed from Kerkhof, 1988).

The phenomenon of Raman scattering can be illustrated by Raman spectrum. Figure I-7 presents the spectra of Rayleigh and Raman spectra of carbon tetrachloride (liquid) excited with a monochromatic radiation (wavelength of 514.5 nm) from an argon ion laser and directly recorded. Most photons of the incident light are elastically scattered (Rayleigh scattering) without energy change. Some photons,  $10^{-6}$  to  $10^{-9}$  of the incident photons, gain or lose a small amount of energy by inelastic scattering, resulting in pairs of Raman-shifted lines at higher (anti-Stokes) and lower (Stokes) frequencies. Stokes lines are much more intense, and usually only these are measured.

A Raman spectrum is a plot of the intensity of the scattered radiations (y-axis) versus the energy loss (x-axis), expressed in wave number relative to the source ( $\Delta\nu \text{ cm}^{-1}$ , the Raman shift), i.e., the changes in wave number compared to the exciting radiation. Eq. I-3 allows the calculation of Raman shift in wave number ( $\text{cm}^{-1}$ ) (X is the wavelength of incident light and Y is the wavelength of Raman band obtained with the incident light X expressed in nm):

$$\text{Raman Shift}(\text{cm}^{-1}) = \Delta\bar{\nu} = \left( \frac{10^7}{X(\text{nm})} - \frac{10^7}{Y(\text{nm})} \right) \quad (\text{I-3})$$

The Raman shift of a given vibration is a measurement of the energy of that vibration. As such, it is independent of the laser excitation wavelength used.

### I.2.2. Principles of Raman spectrometers

As Raman effect is very weak but can provide a large amount of information about sample, a Raman instrument needs to detect as many Raman photons from the samples as possible. This property defines the special requirements of Raman instrumentation: 1) an intense monochromatic light source, which is provided by good quality laser; 2) a high luminosity of the spectrometer, which is obtained specially now by the combination of filter (edge on Notch) to remove the intense reflected exciting radiation and Rayleigh radiation and one single grating monochromator for separating the Raman scattering from other light; 3) a detector with low noise and high quantum efficiency, which is now normally equipped with

high signal-to-noise ratios charge-coupled device (CCD) detector cooled at least at  $-100\text{ }^{\circ}\text{C}$ . In addition, the study of microscopic samples requires coupling the spectrometer with an optical microscope. The confocal microscope optics allows performing spatial- and depth-resolved measurements with a resolution at the micrometer scale. This instrument was done for the first time in 1974, in France by Delhaye & Dhamelincourt (1975), and in the USA by Rosasco et al. (1975).

Two micro-Raman spectrometers have been used in this work and are described in the following.

### **I.2.3. Micro-Raman spectrometers used in this work**

#### **I.2.3.1. Labram Raman spectrometer (Dilor/Jobin-Yvon/Horiba, USA)**



Figure I-8 Photograph of Labram micro-Raman spectrometer (Dilor/Jobin-Yvon/Horiba, USA).

In G2R Lab (Nancy-1 University, France), there is a Raman microprobe (figure I-8) from HORIBA Jobin Yvon Inc., United States (<http://www.horiba.com/>). The microprobe is a Labram type (Dilor<sup>®</sup>/Horiba<sup>®</sup>) having 300 mm focal distance with a Edge<sup>®</sup> filter and with a CCD detector cooled at  $\sim -150\text{ }^{\circ}\text{C}$  by liquid  $\text{N}_2$ . The spectrometer is coupled with a BX-41 microscope (Olympus<sup>®</sup>). The spectrometer is coupled with a BX-41 microscope (Olympus<sup>®</sup>).

The exciting radiation at 514.532 nm is provided by an Ar<sup>+</sup> laser cooled by water (type 2020, Spectraphysics®). A grating of 1800 grooves/mm is chosen to combine reasonable spectral resolution (around 2 cm<sup>-1</sup>) with convenient width spectral window around 1500 cm<sup>-1</sup>. The confocal microscope is equipped with the high quality long working distance objectives of ~ 80×. Raman spectra are collected using the LabSpec® software by which cosmic ray strikes can be removed automatically from the spectrum. Raman spectra can be obtained at fixed temperatures between -180 °C to 600 °C using a heating-freezing stage fixed on the microscope of the Raman microprobe.

#### **I.2.3.2. Renishaw Raman spectrometer (Renishaw, UK)**



Figure I-9 Photograph of micro-Raman spectrometer (Renishaw, UK)

In State Key Lab for Mineral Deposit Research (Nanjing University, China), there is a Renishaw® RM2000 type of micro-Raman spectrometer (Figure I-9) from Renishaw plc., United Kingdom (<http://www.renishaw.com/>). This microprobe is equipped with a Notch® filter and with a CCD detector cooled by air and with a confocal research-grade microscope (Leica®) matching the high quality long working distance objectives of ~ 100×. A diffraction grating of 1800 grooves/mm is chosen to combine reasonable spectral resolution (down to 2 cm<sup>-1</sup>). Spectral window is around 1200 cm<sup>-1</sup>. Figure I-10 shows the optical path of this Raman microspectrometer starting from laser light, the exciting radiation at 514.532 nm provided by



an air-cooled  $\text{Ar}^+$  laser (type 5490A, Aiao<sup>®</sup>) and ending to the collection by CCD detector. Raman data are obtained at different temperature using a heating-freezing stage fixed on the microscope and are present through WIRE<sup>™</sup> instrument control software by which cosmic ray strikes can be removed automatically from the spectrum.

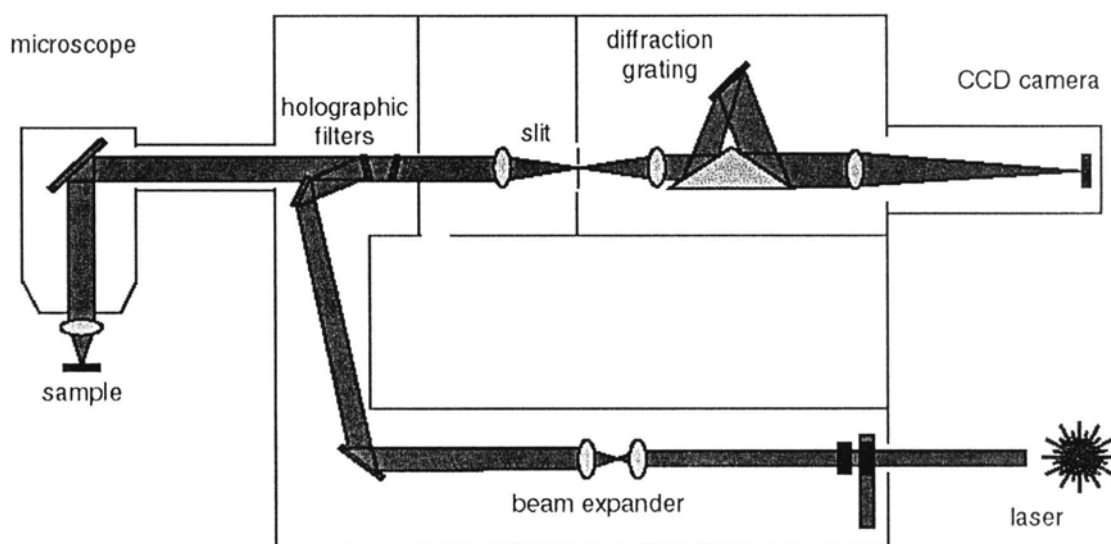


Figure I-10 Optical paths of the Renishaw micro-Raman spectrometer (Renishaw<sup>®</sup>, UK).

### I.3. Synthetic samples

In this study, two types of synthetic samples are introduced, synthetic fluid inclusions, and pure silica glass capillaries, the technique of which have been developed by Chou et al. (2005, 2008). The details of each technique are presented in the following.

#### I.3.1. Synthetic fluid inclusions

It is well-documented that synthetic fluid inclusions can be used to determine P-V-T-X properties and phase relations of fluids, to understand the behaviour of natural fluid inclusions, to calibrate the instruments applied to the analysis of fluid inclusion. Roedder & Kopp (1975) first used the inclusions in synthetic quartz to study interesting problem (errors in measurement of homogenization temperature, errors in calculating pressure corrections, etc.) on fluid inclusion. Shelton & Orville (1980) first documented that synthetic fluid inclusions

trap representative samples of fluids at elevated temperatures and pressures. Sterner & Bodnar (1984) summarized the different compositional types of synthesized fluid inclusions in geologically applicable systems. Bodnar & Sterner (1987) introduced and developed the technique to synthesize fluid inclusions by healing preformed micro-fractures in quartz by the fluid at fixed P-T experimental conditions. Studies related to synthetic fluid inclusions include work with pure fluids, H<sub>2</sub>O and binary and ternary H<sub>2</sub>O-salt systems (e.g. Bodnar et al., 1985; Zhang & Frantz, 1987; Sterner et al., 1988), and work with volatile-bearing fluids, binary H<sub>2</sub>O-volatile systems and ternary H<sub>2</sub>O-volatile-salt volatile systems (e.g. Zhang & Frantz, 1992; Schmidt & Bodnar, 2000; Dubessy et al., 2001). The validity of application of synthetic fluid inclusions have been documented (e.g. Bodnar and Sterner, 1985; Zhang and Frantz, 1987; Sterner and Bodnar, 1991).

#### **I.3.1.1. Autoclaves used for the synthesis of fluid inclusions**

Large volume autoclaves and high P-T vessel are used to synthesize fluid inclusions in this work. These are introduced in the following.

##### **- Large volume autoclaves**

Two types of large volume autoclaves are applied for the synthesis of aqueous inclusions and gas-bearing aqueous inclusions. For the synthesis of aqueous inclusions without gas, a simple autoclave is put in an oven to be heated. Pressure evolves along the saturation curves by the fluid system. Figure I-11a is an illustration of the autoclave, which is made of stainless steel. The fluid sample is isolated from the stainless steel by a golden cup with a gold cover (Diameter of underside of cup: 3 cm, height of cup: 4 cm), which is enclosed in the centre of the autoclave. The autoclave is closed by eight hexagonal bolts (figure I-11b). The maximum temperature is 400 °C for this autoclave.

The autoclave for the synthesis of gas-bearing aqueous inclusion is a little different from the previous one and is made in Hastalloy B2. The experimental fluid is loaded in a Teflon cup covered by a Teflon lid and connected to two tubes (figure I-12). One tube extends into the liquid phase and the second ends at the top of the vapour phase. A CO<sub>2</sub> tank is connected to the tube extending into the liquid phase and air is removed from the system by CO<sub>2</sub>

bubbling into the liquid phase and evacuation is carried out through the second tube. The autoclave is loaded inside cylindrical heating element. The temperature is measured by a thermocouple inserted into the liquid phase. The pressure is measured using a gas pressure gauge in connection with the vapour phase.

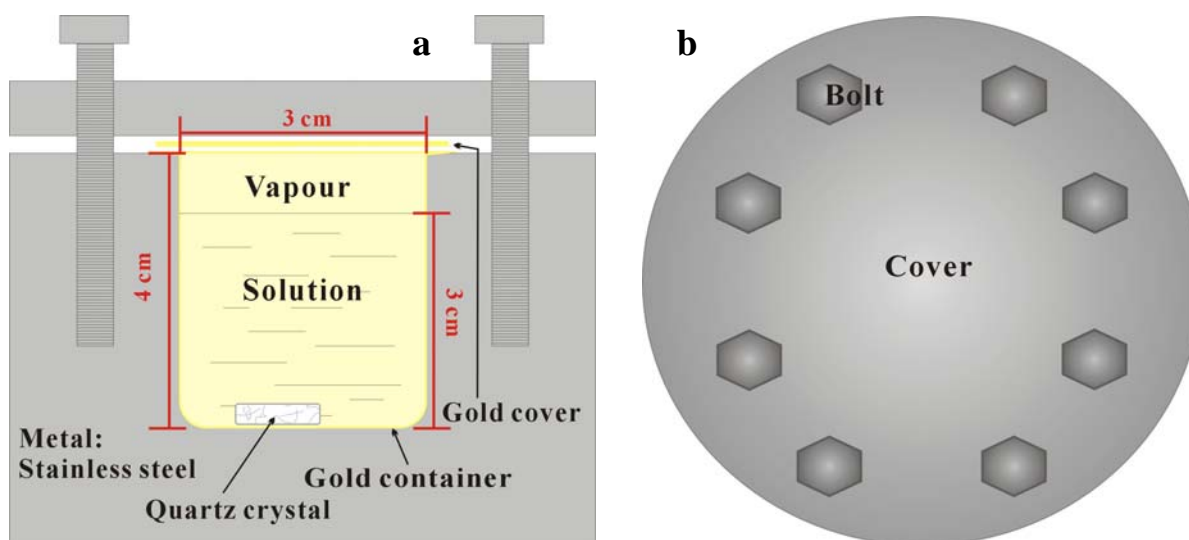


Figure I-11 Sketch of fluid-pressure autoclave (simple autoclave for the synthesis of aqueous inclusion). a and b are section of flank and top of autoclave, respectively.

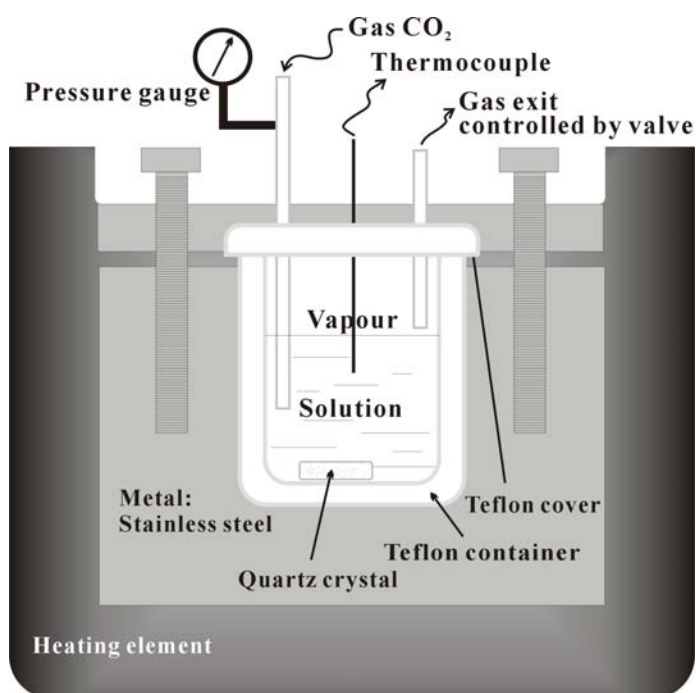


Figure I-12 Sketch of gas-pressure autoclave (autoclave for the synthesis of gas-bearing aqueous inclusion).

### - High P-T vessel

Horizontal cold-seal pressure vessel (RQV type) was used in this work, which can reach a maximum pressure of 2 kbar and a maximum temperature of 900 °C. Quartz crystals are cut into ~ 4mm diameter and 2 ~ 2.5cm long cores. Fractured quartz cores, aqueous solutions and SiO<sub>2</sub> powder are sealed into gold capsule (figure I-13b) which has an outside diameter of 0.5 cm and a wall of 0.15 mm thickness. Sealed capsule is put into the vessel, and a filler rod is loaded after the capsule to fix the position of the capsule and to minimize the thermal difference between the two extremities. Pressure is generated by a compressor to the aqueous fluid inside the autoclave. The vessel is enclosed in an external cylindrical oven. Temperature is measured by a thermocouple penetrating a few millimetres inside the autoclave at a place close to the experimental gold capsule. Figure I-13a presents the structure of vessel. A cold part allows to cool rapidly the gold capsule after the experiment and so to quench it by putting vertically the autoclave removed from the furnace, which makes the gold capsule to fall down in this cold part.

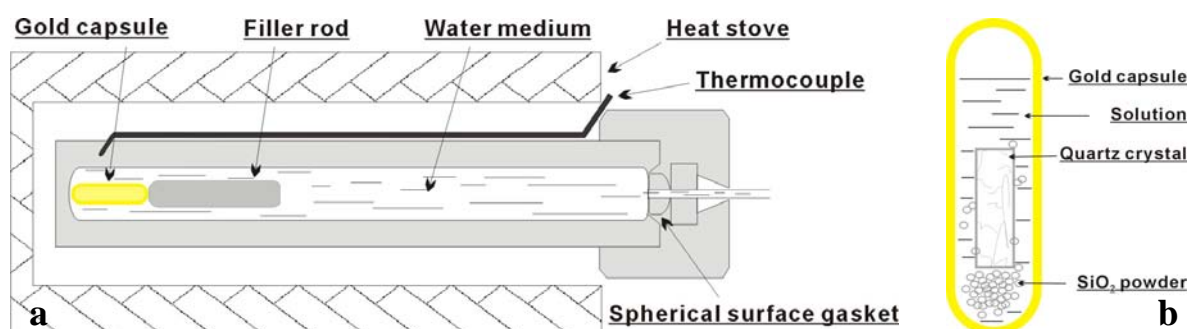


Figure I-13 Sketch of horizontal cold-seal pressure vessel (a) and a sealed golden capsule with samples (b).

#### I.3.1.2. Methods for synthesizing fluid inclusions in cold sealed autoclaves

All inclusions were synthesized by healing preformed micro-fractures in quartz at experimental conditions. Quartz crystal is chosen because it is a transparent mineral, which makes easy to observe the inclusion, and its solubility is weak, and finally because it is a common host mineral for studying natural fluid inclusions geologically. In addition, its mechanical resistance is relatively high, which keep volume of the inclusion relatively

constant if the pressure difference between the inclusion and the host rock is not too high. Natural quartz crystals and inclusion-free synthetic quartz crystals were used in this work. Natural quartz crystals former are first heated in an oven in 5 minutes at 550 °C ( $\alpha$ -quartz is transformed to  $\beta$ -quartz at 573 °C and 1kb) to decrepitate the pre-existing inclusions. Then both types of quartz crystals were prepared to produce micro-fractures by heating them at 350 °C for several minutes and quickly plunged in liquid water (Bodnar & Sterner, 1987). Another method was checked in order to try to form large fluid inclusions. A mini-saw was used to produce some striations on one surface of a 1 mm thick quartz slice. This surface was then put in contact with another quartz slice by binding two slices together with the aim to heal partially the striations and thus to form inclusions in experiment. The second other method consisted to produce some holes (~ several tens  $\mu\text{m}$ ) drilled by laser ablation in one surface of a 1mm thick slice with the aim to heal the holes and so to produce synthetic inclusions. The last two methods did not work.

- Fluid inclusions with  $\text{HCO}_3^-$  aqueous solutions

No.	Solution (molal:molal)	Temperature (°C)	Duration (days)
1*	$\text{KHCO}_3\text{:NaCl}$ (1.0:0.0)	250→220	10→1
2*	$\text{KHCO}_3\text{:NaCl}$ (1.0:1.0)	250→220	10→1
3*	$\text{KHCO}_3\text{:NaCl}$ (0.3:0.0)	250→220	10→1
4*	$\text{KHCO}_3\text{:NaCl}$ (0.3:1.0)	250→220	10→1
5	$\text{KHCO}_3\text{:NaCl}$ (0.1:0.0)	250	10
6	$\text{KHCO}_3\text{:NaCl}$ (0.1:1.0)	250	10

\*At first, 10 days at 250°C, then 1 day at 220°C, and cooling at room temperature rapidly (~ 2 hours). (Samples 5 and 6 10 days at 250°C and then cooling at room temperature rapidly)

Table I-2 Experimental conditions of fluid inclusions synthesized in simple autoclave heated in oven.

No.	Solution (molal)	Temperature (°C)	Pressure (MPa)	Duration (days)
1	$\text{NaHCO}_3\text{:NaCl}$ (0.5:0.0)	350	105	11
2*	$\text{KHCO}_3\text{:NaCl}$ (1.0:0.0)	400	130	14
3*	$\text{KHCO}_3\text{:NaCl}$ (1.0:1.0)	400	110	13

\*2 is by healing the striations in slice; 3 is by healing the holes in slice

Table I-3 Experimental conditions of fluid inclusions synthesized in high P-T vessel.

Aqueous fluid inclusions were synthesized by healing micro-fractures in quartz immersed in monophasic fluids at experimental conditions by using fluid-pressure autoclave or high P-T vessel (details on apparatus were described in section I-3-1-1). Aqueous solutions were prepared first, using analytical reagent chemical products ( $\text{KHCO}_3$ : 99.5% minimum purity,  $\text{NaHCO}_3$ : 99.5% minimum purity,  $\text{NaCl}$ : 99.5% minimum purity) dissolved in deionized water (18 M $\Omega$ ). Fractured quartz crystals, aqueous solutions and  $\text{SiO}_2$  powder which was used to increase healing rate of micro-fractures in the quartz crystal, were sealed into golden cups (simple autoclave heated in oven) and golden capsule (high P-T vessel), respectively. The former experiment is conducted with the changing of pressure and temperature along the isochore curve by heating the autoclave in an oven, and the latter experiment is conducted at pressure generated through water medium in vessel by compressor and temperature generated by an electric oven. Experimental conditions of fluid inclusions synthesized in simple autoclave heated in oven and in high P-T vessel are presented in table I-2 and table I-3, respectively.

#### - $\text{CO}_2$ -bearing fluid inclusions

$\text{CO}_2$ -bearing aqueous fluid inclusions are synthesized in a gas-pressure autoclave (GPA) where the aqueous solution is in equilibrium with a  $\text{CO}_2$ -rich vapour phase (see section I.3.1.1). Fractured quartz crystal, aqueous solution, and  $\text{SiO}_2$  powder are sealed into the Teflon cup (closed into gas-pressure autoclave). At first,  $\text{CO}_2$  gas is injected to flush out the air. Then the pressure of gas is changed slowly for equilibrium of  $\text{CO}_2$  between in vapour phase and in liquid phase during the rising of temperature until it reaches the definite conditions. Experimental conditions of fluid inclusions synthesized in GPA are presented in table I-4.

No.	Solution (molal)	Temperature ( $^{\circ}\text{C}$ )	Pressure (bar)	Duration (days)
1	$\text{NaCl}$ (0.0)	$220 \pm 1$	$50 \pm 5$	6
2	$\text{NaCl}$ (1.0)	$220 \pm 1$	$133 \pm 3$	7

Table I-4 Experimental conditions of fluid inclusions synthesized in autoclave for the synthesis of gas-bearing aqueous inclusion.

At the end of the experiment, heating is stopped and the autoclave is cooled down to room temperature in the air. The quartz sample is made to double-polished wafer for the later analysis of fluid inclusion. This system did not work properly because small leakage have never been eliminated which resulted in a permanent boiling of the liquid phase and thus to the trapping of vapour-rich inclusion but not the liquid end-member of this L-V phase equilibrium.

### I.3.1.3. Samples of synthetic fluid inclusions

Double-polished wafers are first observed using an optical microscope to check the synthetic inclusions. Microthermometric measurements are carried out to verify if the inclusion do have trapped the mother fluid. Then, inclusions are selected for Raman spectroscopy by their study. Figure I-14 shows the microphotograph of synthetic inclusions. Vapour phase and liquid phase coexist in synthetic inclusions at room temperature, and the size of inclusion is enough for the analysis by Raman microspectroscopy.

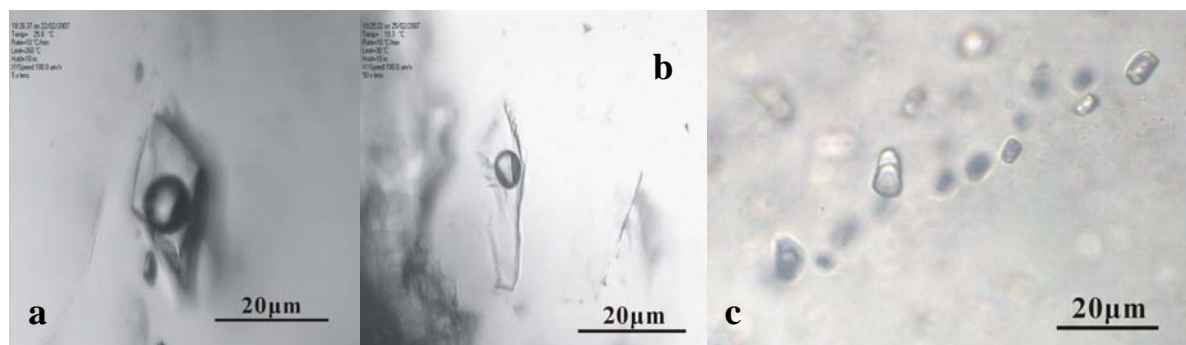


Figure I-14 Microphotographs of synthetic fluid inclusions. a. in the system  $\text{KHCO}_3\text{-NaCl-H}_2\text{O}$  ( $\text{KHCO}_3\text{:NaCl} = 1.0\text{:}0.0$ ), b. in the system  $\text{KHCO}_3\text{-NaCl-H}_2\text{O}$  ( $\text{KHCO}_3\text{:NaCl} = 1.0\text{:}1.0$ ), c. is in the system  $\text{CO}_2\text{-H}_2\text{O}$ .

### I.3.2. Pure silica capillary

This technique was initiated in USA by Chou et al. (2005, 2008), and was adapted in France in G2R (Dubessy et al., 2009). It is documented that sealed pure silica glass capillaries

are similar to the synthetic fluid inclusions and can be applied to the studies of the interest problems related to fluid inclusions and geological fluids (Chou et al., 2008; Dubessy et al., 2009).

### **I.3.2.1. Pure silica capillary tube**

A cylindrical pure silica glass capillary tube is supplied with a polyimide coating (figure I-15, 360  $\mu\text{m}$  outer diameter, 100  $\mu\text{m}$  inner diameter, and 20  $\mu\text{m}$  thick of coating), which is commercially available with Polymicro<sup>®</sup> Technologies, LLC (<http://www.polymicro.com/>). The polyimide coating makes the tube to be flexible and protects it. The coating is easily removed by burning in the cold part of an hydrogen flame. The silica tube without coating provides an optical cell and can be fused using the hottest part of hydrogen flame around 2850 °C. Solids, liquids and gases all can be introduced into the capillary tube. Optical observations and Raman data collections of coexisting phases are carried out using an optical microscope with objectives ( $\times 5$ ,  $\times 10$ ,  $\times 20$  or  $\times 80$  long working distance). Temperatures are controlled using a microthermometric stage. A special heating-freezing stage is under construction with Linkam company (figure I-3). This tube can hold 200 to 300 MPa pressure at room temperature and can be heated at temperature up to 400 °C and at least up to 550 °C for low internal pressures ( $< 50$  MPa).

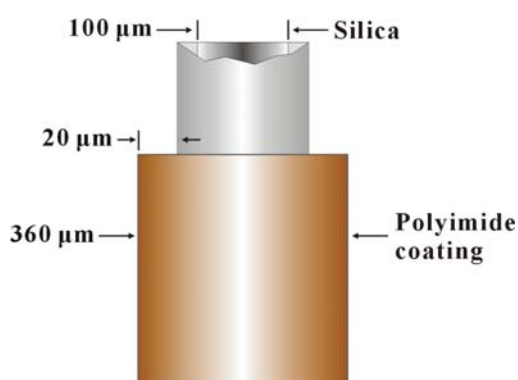


Figure I-15 Sketch of cylindrical of flexible pure silica glass capillary tube coated with polyimide (PolymicroTechnology).

### **I.3.2.2. Adaptation of the system of I-Ming Chou (by J. Dubessy and P. Robert) and general procedure of capillary loading**



Figure I-16 illustrates the adaptation system of I-Ming Chou system, carried out at G2R with Pascal Robert, used for sample loaded in sealed capillaries. All the system is linked by stainless metal tubes (1/16 inch or 1/8 inch) and Swagelok<sup>®</sup> connections and valves. A vacuum pump producing a vacuum down to 0.03 mbar is permanently connected to the stainless steel line heated at 100 °C ~ 120 °C to evacuate any impurity. One-end-sealed silica capillary with or without samples is linked to the system by a special device. Then, air in the sample capillary is evacuated through the metal tubes by vacuum pump. Subsequently, gas samples with triple point temperature higher than the temperature of liquid N<sub>2</sub> (-195.8 °C) are added cryogenically by immersing the sealed end of the capillary in liquid nitrogen, and the gas is condensed or frozen into the sealed end of capillary to a solid for several minutes. The pressure in the system lines is measured by a high precision of pressure detector (~ 0.1 mbar). Because of the limitation of pressure detector (~ 1 bar), the gas tank is linked to the system lines by adding a gas reservoir or a stainless metal tube as a pressure buffer and the large difference of volume between the whole system lines and gas reservoir. Valves which separate the system into several parts, also control the gas pressure in the reference volume. As the capillary is loaded, the capillary is evacuated again and the open end is sealed by melting the silica glass using a hydrogen flame while the loaded material at the other extremity of the capillary is frozen, see figure I-17. The typical length of the capillary ranges is between 8 mm for the shortest ones to 15 mm.

Three devices to link the silica glass capillary to the stainless steel line have been designed and checked. The three following constraints are required for these devices: 1) the lack of leakage at the junction between the silica glass capillary (360 µm external diameter) and the stainless steel line (1/16 inch external diameter); 2) the mobile character of the link between the stainless metal and capillary tube; 3) differences in material of two types of capillary. In this work, three methods have been tried.

The first method designed by I-Ming Chou is illustrated in figure I-18a. A hard plastic tube with two ends closed by amber rubber cap. The cap is elastic and has a hole in the centre, which permits to hold the tube when it is inserted into the hole. Because of the micro-dimension of the capillary tube, the open end of capillary tube is previously inserted inside a glass tube for increasing the quality of imperviousness between the amber rubber and

the tube by a higher diameter dimension. Glue is used to fix the silica glass capillary tube inside the glass tube. This method has two shortcomings, the imperviousness of this junction is not perfect and the use of rubber cap is limited by its fatigue.

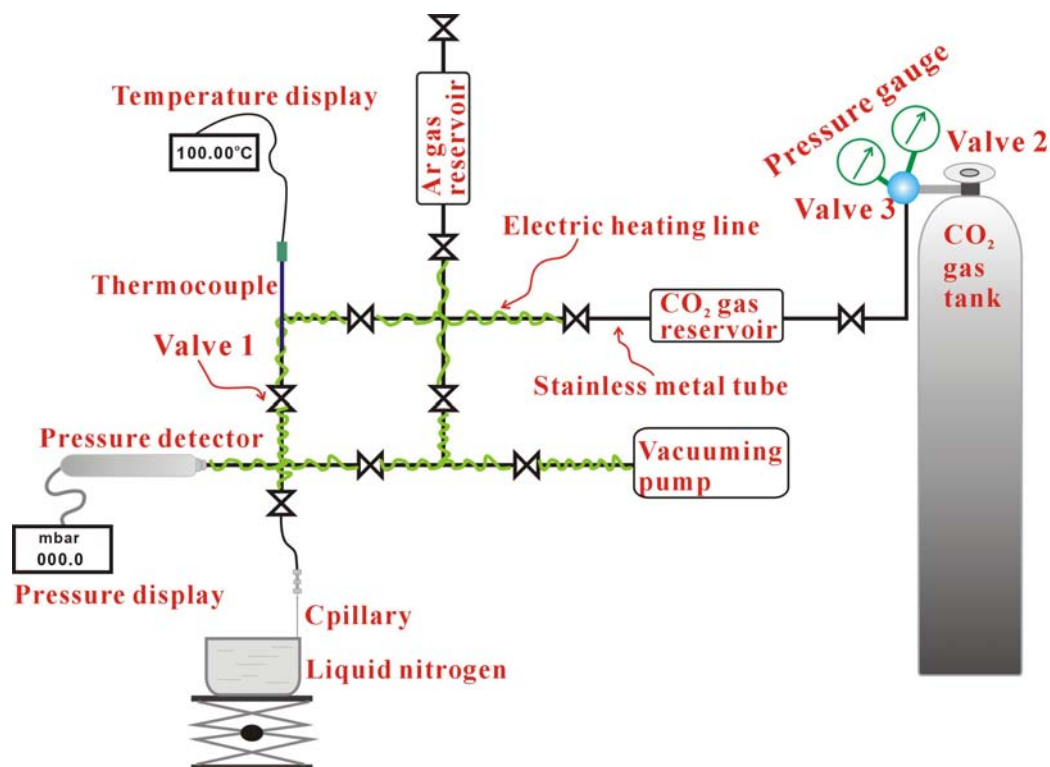


Figure I-16 Schematic diagram showing the adaptation system of Chou I-Ming in G2R lab, France. For details, see text.

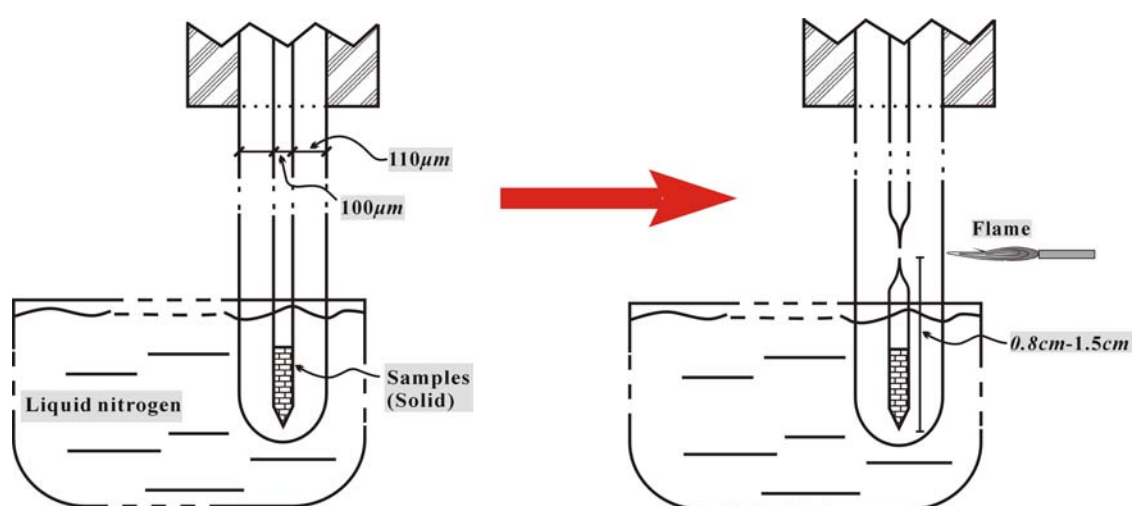


Figure I-17 Silica capillary with samples sealed cryogenically to produce chemical systems in closed capillary.

Figure I-18b shows the second method designed at G2R. One thermoelastic tube is used to connect the silica glass capillary tube with the stainless metal tube by thermal shrinkage (1.2 mm external diameter). The contact between the glass tube and the silica glass capillary is made using glue. The link is neither impermeable between the stainless metal tube and the thermoelastic tube.

Finally, the method designed at G2R illustrated in figure I-18c is applied to the fabrication of silica capillary sample. One special stainless metal connection is used to make the link through engineering closure. Silica capillary tube with its polyimide coating is first inserted into a PEEK<sup>TM</sup> tube (1/16 inch external diameter, 0.015 inch internal diameter), and glue makes the imperviousness of the junction between the two tubes. Figure I-19 gives photographs of this connection. The key point is that a stainless metal nut (in red circle in figure I-19) is inserted before the screw cap is turned to the connection. The silica capillary can be linked with or delinked from this adaptation system and no leakage is measured in more than 10 minutes.

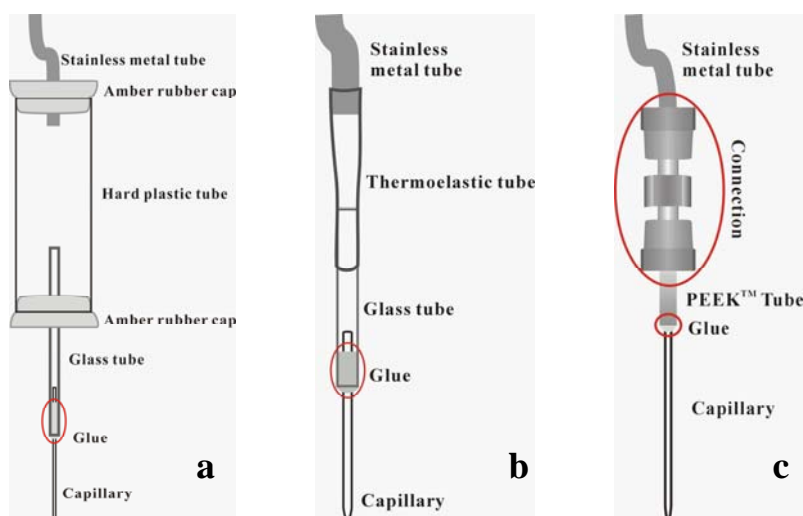


Figure I-18 Three special devices for the link between the stainless steel line (1/16 inch external diameter) and the silica glass capillary.

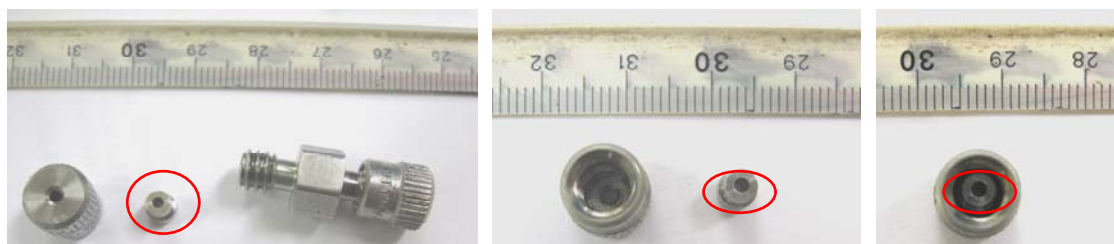


Figure I-19 Photographs of special stainless metal connection.

### I.3.2.3. Procedures for loading silica glass capillary with different gases, liquids and solids

Gases, liquids and solids can be loaded into the silica glass capillary, but the loading methods are different because of their different properties.

- Loading method of solids

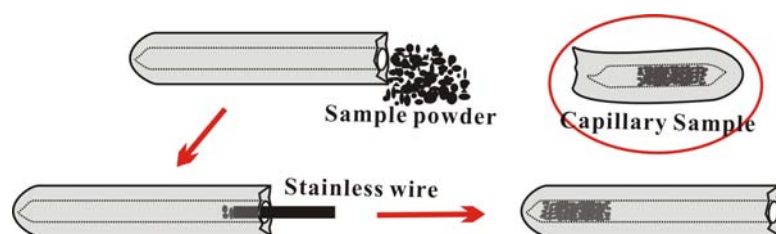


Figure I-20 Schematic diagram showing the procedure 1 to load solid to silica capillary.

Two methods have been used. 1) The solid is ground into powder (~ several tens micron) with the size less than 100  $\mu\text{m}$ . A stainless wire (89  $\mu\text{m}$  diameter, used for syringe needle cleaning) is used to push the powder into the sealed end of silica capillary, as shown in figure I-20. The silica capillary with solid is linked to the adaptation system and is sealed cryogenically under vacuum. This method is not easy and impurities can be loaded with the sample. In addition, the efficiency of this method depends on the electrostatic properties of the solid.

2) Figures I-21 and I-22 show two distinct but similar procedures. The solid is also ground into powder (~ several tens micron) and mixed with a liquid to produce a suspension. The criteria to choose the liquid are the following: i) no chemical reactions between the solid and the liquid; ii) very low solubility of the solid in the liquid; iii) facility for the liquid to evaporate under small heating or no heating. Ethanol is selected in this work.

For the first method, an open silica capillary about 6 cm long is immersed into the suspension which is a mixture of powder and liquid (1). The end is slightly heated with cigarette lighter for separating the powder and liquid (2) and one extremity of the capillary is

sealed using a hydrogen flame (3). Then the tube with the solids and the remaining liquid is centrifuged with a high-speed ( $\sim 14,800$  rpm) Sigma<sup>®</sup> 1-15 Microcentrifuge (4) to move the suspension towards the sealed extremity. The remaining liquid in the capillary tube is evaporated by heating gently the capillary with a hair drier (5). The last step consists to seal the open extremity under vacuum, the capillary being immersed into liquid N<sub>2</sub> (6).

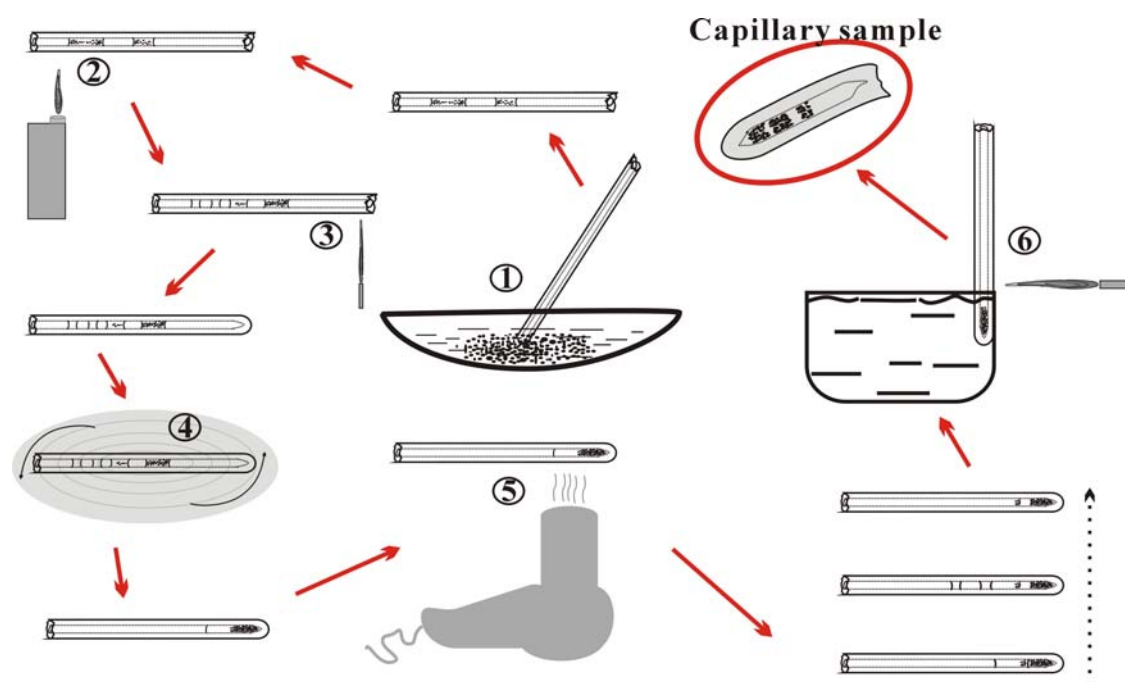


Figure I-21 Schematic diagram showing the procedure 2 to load solid to silica capillary.

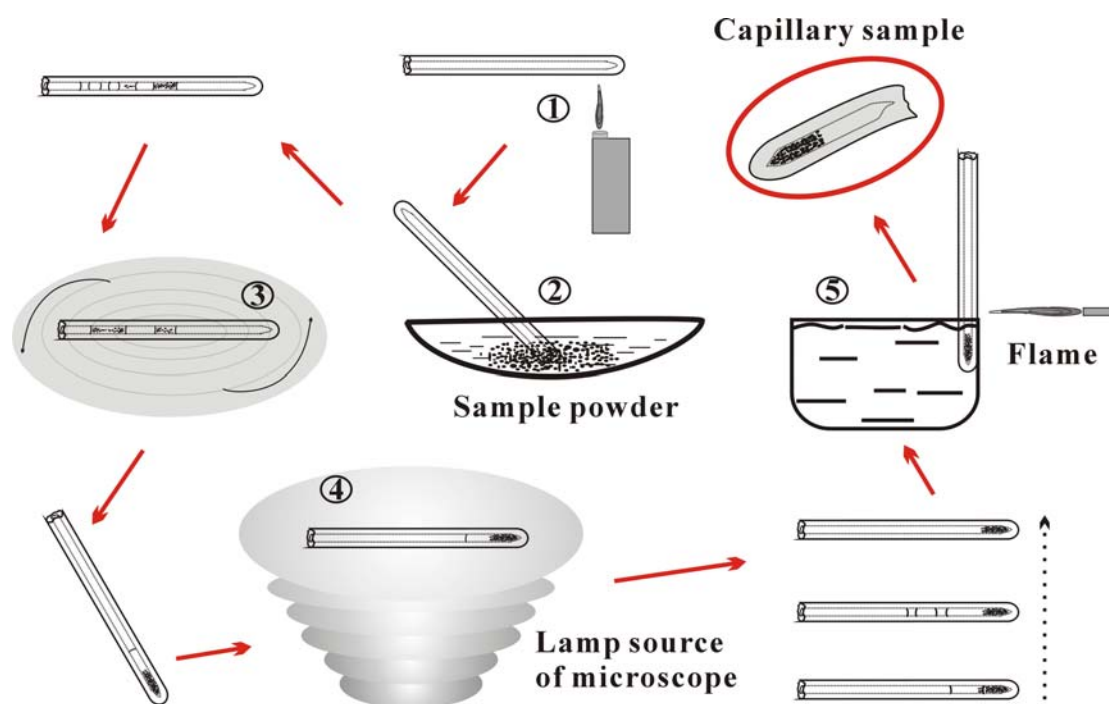


Figure I-22 Schematic diagram showing the procedure 2 to load solid to silica capillary.

3) A slightly modified method of method 2 is present in figure I-22. A 6 cm long capillary is first at one sealed extremity and is gently heated a little by the flame of a cigarette lighter in sealed end (1). This produces an expansion of the inside gas atmosphere towards the atmosphere. Then the opened extremity is quickly immersed into the suspension containing the sample powder as heating is synchronously stopped (2). The resulting rapid decrease of temperature produces a pressure decrease inside the capillary. Pressure equilibrium with external atmosphere is reached by the penetration of the suspension-bearing liquid phase inside the capillary. The suspension in the tube is moved to the sealed end by centrifugation (3). The liquid in the tube is then evaporated using a non infrared filtered lamp source of binocular system (4). This heating procedure is suitable because the liquid evaporates without moving the powder towards the opened extremity. This modified method is more successful to load solid in silica capillary but spends more time (one night for ethanol or water evaporation). To decrease the liquid evaporation time, the tube is first heated by lamp source until the powder is well deposited, then the remaining of liquid is removed under vacuum by linking the tube with stainless steel line (5). Finally, the capillary sample is finished by sealing the open end under vacuum (6), the silica glass capillary being immersed in liquid nitrogen.

- Loading procedure of liquids in the capillaries

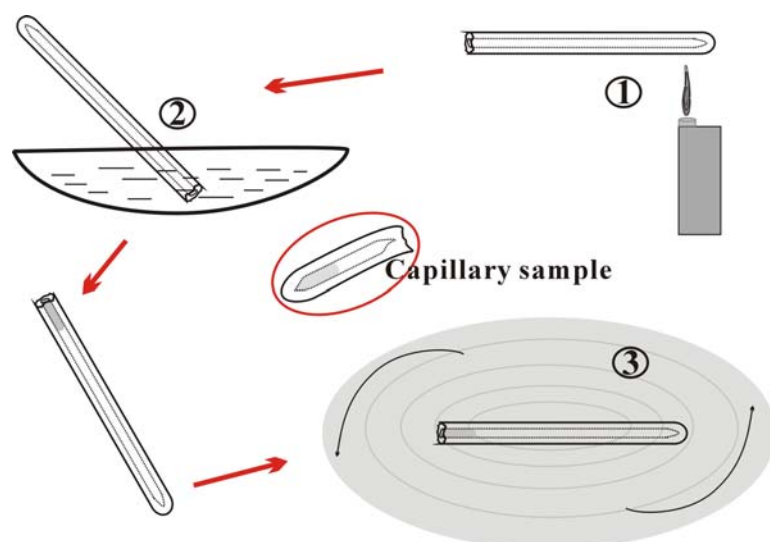


Figure I-23 Schematic diagram showing the procedure to load liquid to silica capillary. For details, see text.

Liquids are easily loaded into the silica capillary. The liquid is sucked into the one end sealed silica capillary with about 6 cm long by the difference of pressure between the interior of capillary and outside atmosphere as described in the first method of solid loading using liquids. Then it is moved to the sealed end using centrifugation, which is illustrated in figure I-23. The tube with liquid sample is sealed cryogenically using vacuum using the stainless steel line.

- Loading procedure of gases in the capillaries

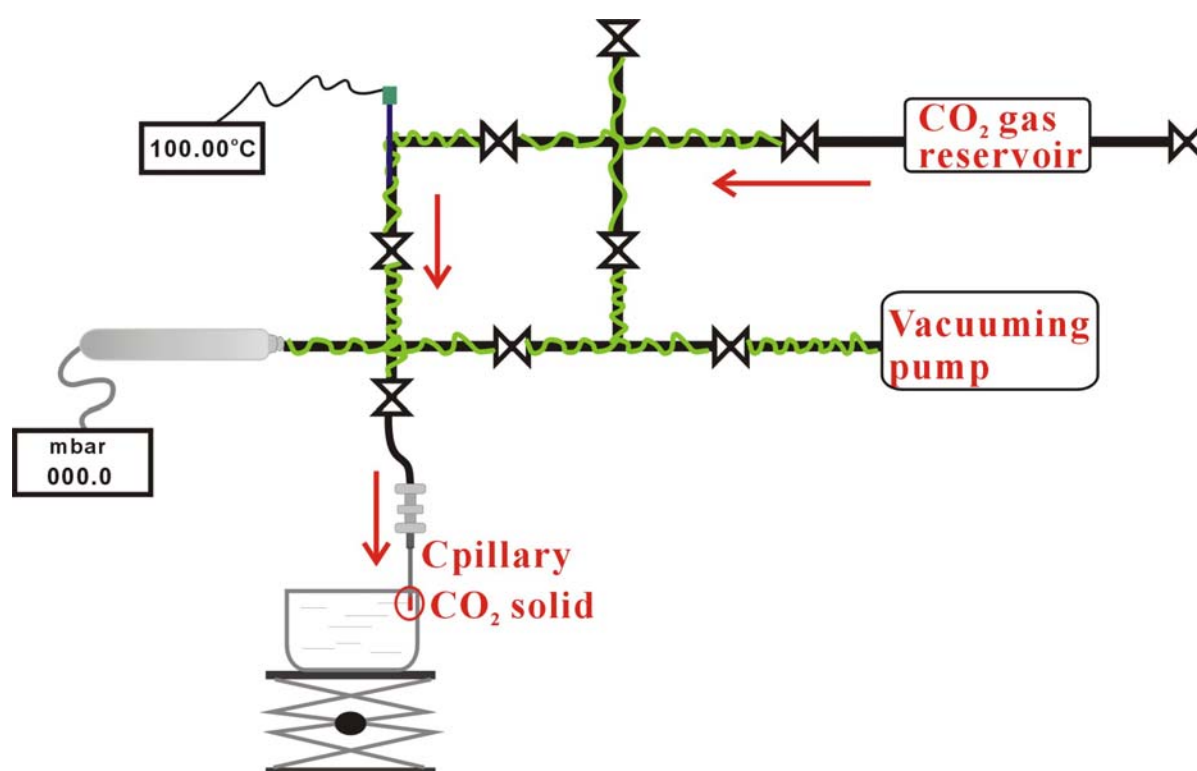


Figure I-24 Schematic diagram showing the procedure of gas loading in silica capillary. For details, see text.

Before gas loading, one end sealed silica tube is linked to the system and air in tube is evacuated. Then gas samples are loaded cryogenically into silica tube through immersing the sealed end of tube in liquid nitrogen, and the gas is condensed or frozen (to a solid) into the



sealed end of the capillary in several minutes (figure I-24). Therefore this method applies to compounds with triple point temperature higher than the liquid nitrogen temperature at one atmosphere:  $N_2$  ( $T_L$ ) = -195.8 °C,  $CO_2$  ( $T_r$ ) = -56.6 °C,  $CH_4$  ( $T_r$ ) = -182.5 °C,  $H_2S$  ( $T_r$ ) = -85.5 °C,  $SO_2$  ( $T_r$ ) = -75.5 °C,  $C_2H_6$  ( $T_r$ ) = -182.8 °C. Therefore  $O_2$ ,  $N_2$ ,  $H_2$ ,  $CO$  cannot be loaded using this method. It is worth noting that the capillary with gas must be sealed cryogenically under very low pressure (< 0.1 mbar), to avoid the capillary explosion which could result from heating the tube at the sealing point by the hydrogen flame (2850 °C). The quantification of gas sealed in capillary sample is deduced from the measurements of pressure change by pressure detector. The methods of quantification of gas in capillary sample are given in details in chapter II.

#### - Loading mixture of aqueous solutions and gases

In this work,  $CO_2$ -bearing aqueous fluids need to be studied, so it is necessary to load capillaries with mixture of aqueous solution and  $CO_2$ . First, the aqueous solution is loaded into the end sealed capillary according to the liquid loading procedure. Then the open end is linked to the system to evacuate the air meanwhile the capillary is immersed inside liquid nitrogen. Then  $CO_2$  is condensed into the capillary (referring to the method of gas loading). Then, the loaded capillary is sealed cryogenically under completely vacuum.

#### I.3.2.4. Capillary samples

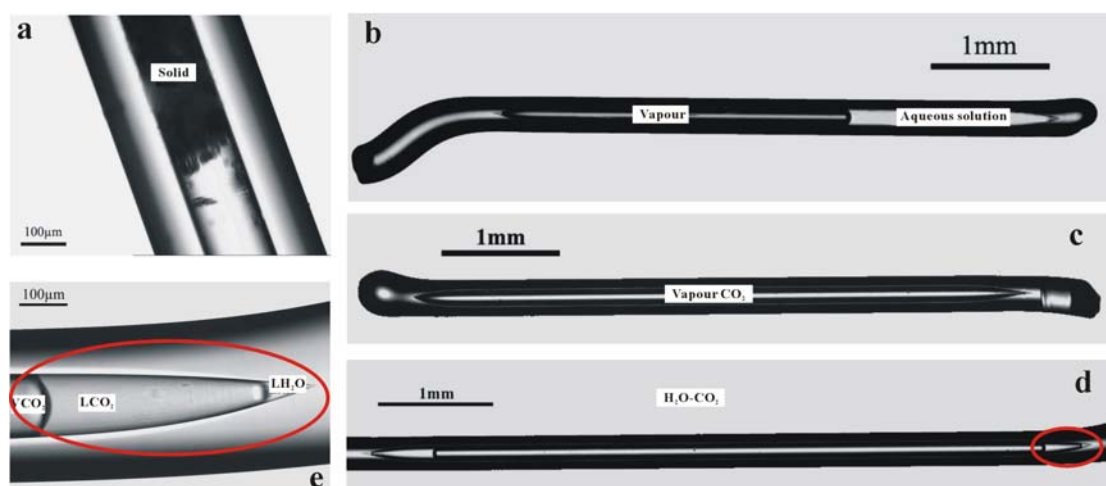


Figure I-25 Microphotographs of capillary samples. a. capillary with solid sample (oxalic acid solid), b. capillary sample in system  $KHCO_3$ - $NaCl$ - $H_2O$  (binary phases: vapour and



aqueous solution), c. capillary in pure CO<sub>2</sub> (monophase), d is capillary in system H<sub>2</sub>O-CO<sub>2</sub> (ternary phases: CO<sub>2</sub> vapour (VCO<sub>2</sub>), CO<sub>2</sub> liquid (LCO<sub>2</sub>), H<sub>2</sub>O liquid (LH<sub>2</sub>O)) and the detail of part in red circle is shown in e.

Silica glass capillary samples are available for optical observation and microthermometric and microspectroscopic analyses. Figure I-25 shows the microphotographs of capillary samples fabricated in this work, capillary sample in oxalic acid solid (a), and binary phase capillary sample in the system KHCO<sub>3</sub>-NaCl-H<sub>2</sub>O (b), and monophase capillary sample in pure CO<sub>2</sub> (c), and ternary phase capillary sample in the system H<sub>2</sub>O-CO<sub>2</sub> (d and e).

It is noted that the volume of capillary sample can be measured by using the micrometric stage equipped with the microscope, shown in figure I-26a and b. Capillary is put on the stage (figure I-26c), and is observed under optical microscope and is measured by moving the stage in X or Y directions. A display (~ 1μm) allows the determination of the coordinates. The reading precision is 1μm and RSD (Relative Standard Deviation) of measurement of capillary is better than 0.5% and RSD of the calculated volume of capillary is better than 1%.

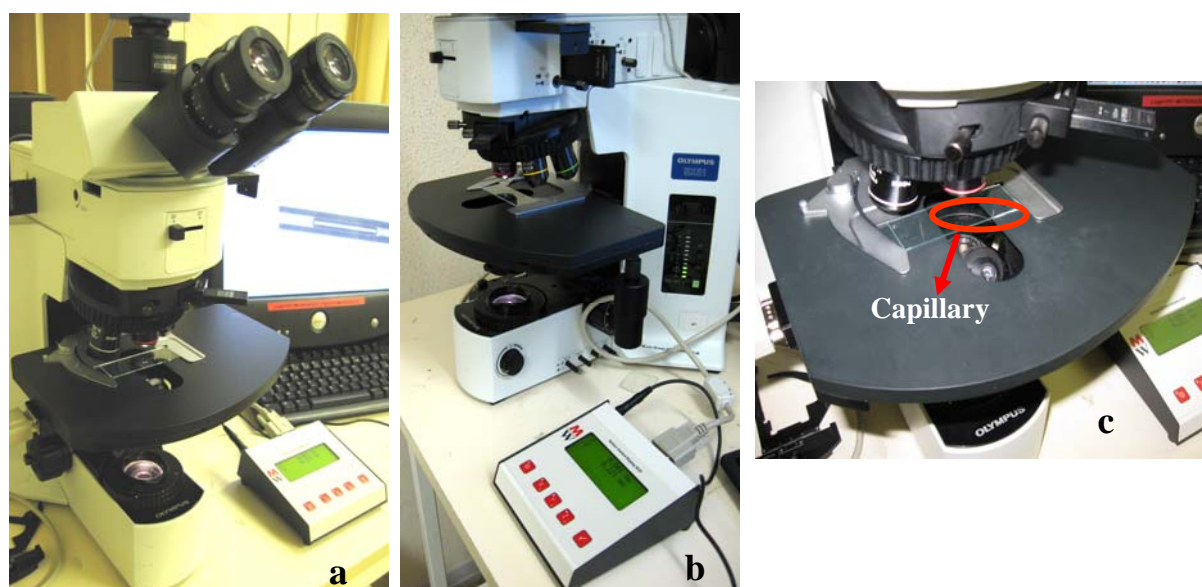
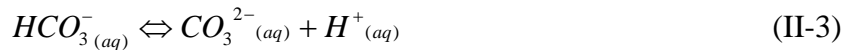
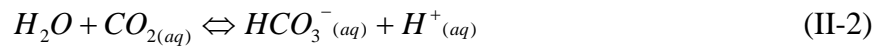


Figure I-26 Photographs of micrometric stage (MW<sup>®</sup>) equipped with microscope. a and b. complete set, c. the capillary sample in stage display.

**CHAPTER II: THE SYSTEM  $\text{H}_2\text{O}-\text{CO}_2-\text{NaCl}-\text{H}^+-\text{HCO}_3^-$ :**  
**RESULTS OF EXPERIMENTS**

## II.1. Objectives of the experimental part

The following chemical equilibria describe the speciation in the  $\text{H}_2\text{O}-\text{CO}_2-\text{H}^+-\text{HCO}_3^-$  system (Eq. II-1, II-2, II-3):



All these species are Raman active except  $\text{H}^+(aq)$ . Therefore, the objective to determine the pH at the conditions of trapping from fluid inclusions analysis requires to get the concentration of the species involved on one of the two acidic-basic chemical equilibria at the P-T conditions of trapping. Therefore, the aim of this part of the thesis is to provide a method for the calibration of the analysis by Raman micro-spectrometry of the concentration of the different chemical species at various temperatures and concentrations. To reach this goal, after summarizing the state of the art of the Raman spectroscopy relative to each chemical species of interest, several experimental methods are described using synthetic fluids. Most of the experimental work is focused on the technique of sealed silica glass capillary first introduced by I-Ming Chou (2008).

## II.2. Calibration of analysis of bicarbonates by Raman spectroscopy

### II.2.1. Vibrational modes and bands of Raman active of related species in $\text{HCO}_3^-$ -bearing aqueous solution

To justify the calibration of the analysis by Raman spectroscopy of each chemical species of the  $\text{H}_2\text{O}-\text{CO}_2-\text{H}^+-\text{HCO}_3^-$  system, there is given a summary of their vibrational modes and the Raman active modes, especially the most intense and thus the most suitable for analytical purpose.

$\text{H}_2\text{O}$  molecule is non-linear with a  $\text{C}_{2v}$  group symmetry. In the gas state, the isolated water molecule has three fundamental modes of vibration: symmetric stretching ( $\nu_1 a_1$ ) at

3655.8  $\text{cm}^{-1}$ , asymmetric stretching ( $\nu_3 b_1$ ) at 3756.7  $\text{cm}^{-1}$  and the symmetric bending ( $\nu_2 a_1$ ) at 1594.6  $\text{cm}^{-1}$ , all of which are Raman active (Brun, 1968; Vergnat, 1974). Liquid water is an associated liquid due to hydrogen bonds between water molecules. Hydrogen bonds strongly modify the vibrational spectrum by strongly increasing the band width at half maximum compared to those from the vapor phase (Walrafen, 1964, 1967, 1970, 1972). By comparison with the vapor phase, the main stretching band in liquid water is shifted to a lower frequency between 3000 and 3800  $\text{cm}^{-1}$  with a dissymmetric profile containing a maximum assumed 3450  $\text{cm}^{-1}$  and a component at lower wavenumber around 3200  $\text{cm}^{-1}$  (Walrafen, 1962). On the contrary, the bending frequency increased ( $\nu_2$ , 1644  $\text{cm}^{-1}$ ) (Venyaminov & Prendergast, 1997).

The vibration spectroscopy of the water varies with temperature as a result of hydrogen bond breaking by thermal agitation. Long before, Walrafen (1964, 1966), Frantz et al. (1993) observed the variations in Raman spectroscopy of water with temperature. We have reproduced the results using the capillary technique. The band of the bending mode  $\nu_2$  does not change significantly with the increase of temperature. Considering the evolution of the O-H stretching band with the increasing of temperature, the maximum peak intensity shifts towards higher wavenumbers and the low wavenumber component decreases in intensity. In the electrolytic solutions, the addition of the salt modifies the water structure by the interaction between the ion and water molecular. Walrafen (1964, 1966) also had presented the evidence on this aspect, which was used by Dubessy et al. (2002) for the analysis of chloride concentration. Interaction between the solvent and the solute, especially anion, modifies strongly the hydrogen bonds between water molecules and thus the stretching Raman band.

-  $\text{HCO}_3^-$

Group theory applied to four possible geometries of the bicarbonate ion predicts nine Raman active bands (Davis & Oliver, 1972). However eight fundamental vibrations are observed since the polarized Raman band at 1684  $\text{cm}^{-1}$  is the first overtone of the weak depolarized line at 840  $\text{cm}^{-1}$  (Davis & Oliver, 1972). Then from polarization consideration,

the authors conclude to the  $C_s(\sigma_h)$  point group for bicarbonate ion in aqueous solution (figure II-1). Wave numbers of the different vibrational modes are given in table II-1.

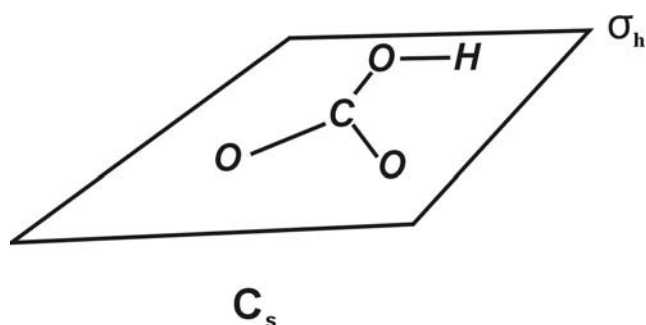


Figure II-1 One possible geometry of bicarbonate ion  $C_s(\sigma_h)$ .

Species	Raman Shift (cm <sup>-1</sup> )	Assignment
Bicarbonate Ion	----	$\nu_9(A'')$ OH torsional vibration
	632	$\nu_7(A')$ (OH) CO bend
	672	$\nu_6(A')$ CO <sub>2</sub> bend
	841	$\nu_8(A')$ CO <sub>3</sub> out-of-plane deformation
	1017	$\nu_5(A')$ C-OH stretching
	1302	$\nu_4(A')$ COH bend
	1360	$\nu_3(A')$ symmetric CO stretch
	1630	$\nu_2(A')$ asymmetric CO stretch
	1684	$(2 \times \nu_8)(A')$
Carbonate Ion	2650	$\nu_1(A')$ OH stretch
	684	$\nu_4(E')$
	880	$\nu_2(A_2'')$
	1064	$\nu_1(A')$
	1380	$\nu_3(E')$
	1436	
	1761	$2 \times \nu_2(A_2'')$

Table II-1 Assignment of the normal modes of vibration of the bicarbonate ion according to the  $C_s(\sigma_h)$  model and the carbonate ion according the  $D_{3h}$  point group (from Davis & Oliver, 1972).

Also, in this study, through the analyses of Raman spectra of the bicarbonate solution, the small amount of  $\text{CO}_3^-$  was proved to be a minor species coexisting with the major  $\text{HCO}_3^-$  species. In the study of Raman spectroscopy of aqueous alkali metal bicarbonate solution of Oliver & Davis (1973), it was demonstrated that at room temperature and pressure the

concentration had no effect on the spectra of the bicarbonate and the alkali metal had little effect on the spectra of the bicarbonate and thus no ion-pairing was evidenced. Frantz (1998) combined Raman spectra with thermodynamic calculations to study the changes in solution speciation for potassium bicarbonate aqueous fluid at elevated temperatures and pressures. In this study, the carbonate concentration increases with increasing temperature but dissolved aqueous carbon dioxide appeared above 300°C and its concentration continued to increase with increasing temperature and decreasing the density.

-  $\text{CO}_3^{2-}$

For the unperturbed carbonate ion, the symmetry point group is  $D_{3h}$  (Davis & Oliver, 1972). Because of the solvation and ion-pairing which perturbs the symmetry of carbonate ion and also slightly some vibrational force constants, the selection rules are not anymore those given by point group  $D_{3h}$  and thus the vibration spectrum of carbonate in aqueous solution is modified (Davis & Oliver, 1972; Oliver & Davis, 1973). Raman-active bands for the carbonate ion dissolved in water at room temperature and pressure are tabulated in table II-1. With increasing temperature, in  $\text{K}_2\text{CO}_3$  solution, Frantz (1998) suggests that the degree of ion paring ( $\text{KCO}_3^-$ ,  $\text{K}_2\text{CO}_3^0$ ) is inhibited by the formation of bicarbonate ion.

-  $\text{CO}_2$

The  $\text{CO}_2$  molecule is linear and of  $D_{\infty h}$  molecular symmetry. It has four modes of vibration, a symmetric stretching mode ( $\nu_1$ ), an anti-symmetric stretching mode ( $\nu_3$ ), and two bending modes ( $\nu_{2a}$  and  $\nu_{2b}$ ). The Raman spectrum displays four bands: two strong  $\text{CO}_2$  lines are as results of Fermi resonance of  $\nu_1$  and  $2\nu_2$  and each is a mixture of the excited  $\nu_1-2\nu_2$  Fermi diad and have the frequencies  $1388 \text{ cm}^{-1}$  (upper band) and  $1285 \text{ cm}^{-1}$  (lower band) respectively (Gordon & McCubbin, 1966; Wienecke et al., 1986; Rosso & Bodnar, 1995). Near the Fermi diad, there are shoulder peaks called hot bands which result from transitions from  $\nu_2$  to levels formed from interactions between  $\nu_1 + \nu_2$  and  $3\nu_2$  (Herzberg, 1945). Davis & Oliver (1972) revealed that the structure of the  $\text{CO}_2$  is unaltered in passing from the gaseous to the aqueous solution state.

## II.2.2. Principles of calibration of $\text{HCO}_3^-$ analysis from Raman spectra at ambient temperature

Referring to the Raman active bands of relative species, the spectra of the aqueous phase in inclusion are collected in two spectrum windows. The first is covering the wavenumber range  $550 - 2150 \text{ cm}^{-1}$ , including bicarbonate bands  $1017 \text{ cm}^{-1}$  ( $\nu_5$  C-OH stretching vibration) and  $1360 \text{ cm}^{-1}$  ( $\nu_3$  symmetric CO stretching vibration) and the bending band of liquid water around  $1640 \text{ cm}^{-1}$ . The second spectral window between  $2800 \text{ cm}^{-1}$  and  $4000 \text{ cm}^{-1}$ , contains the symmetric stretching band of liquid water. The ratio of area bands of bicarbonate with the bending band of liquid water is calculated to calibrate the analysis of concentration of bicarbonate in aqueous solution (Eq. II-4 and II-5).

$$\text{Ratio1} = \frac{\text{Area}(1017 \text{ cm}^{-1})}{\text{Area}(1640)} \quad (\text{II-4})$$

$$\text{Ratio2} = \frac{\text{Area}(1360 \text{ cm}^{-1})}{\text{Area}(1640)} \quad (\text{II-5})$$

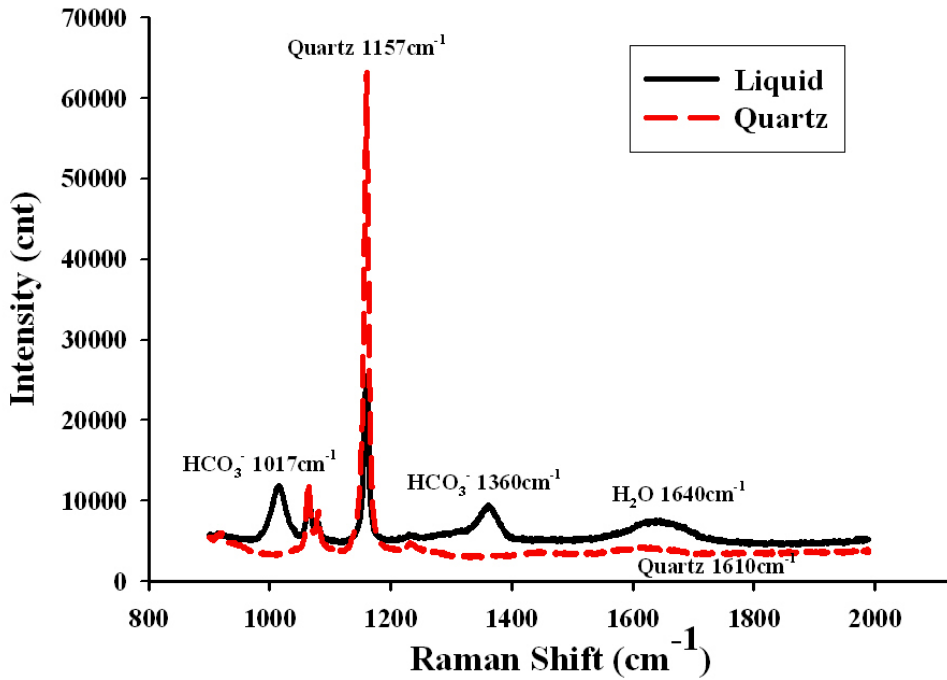


Figure II-2 Spectra collected from the aqueous solution in bicarbonate-bearing inclusion and from quartz near inclusion focusing on the same distance.

In synthetic fluid inclusion in quartz, the signal of quartz is added to the bending band of liquid water (figure II-2), so the true area of bending band of liquid water “*Area*(1640)” is deduced using Eq. II-6 by normalizing the contribution of quartz in the 1550 - 1750  $\text{cm}^{-1}$  spectral region using the intensity of the Raman band of quartz at 1157  $\text{cm}^{-1}$  collected in the fluid inclusion and in quartz crystal near the inclusion (“1” spectrum collected in aqueous solution, “2” spectrum collected in quartz near inclusion focusing on the same distance).

$$Area(1640) = Area1(1640) - Area2(1610) \times \frac{Area1(1157)}{Area2(1157)} \quad (\text{II-6})$$

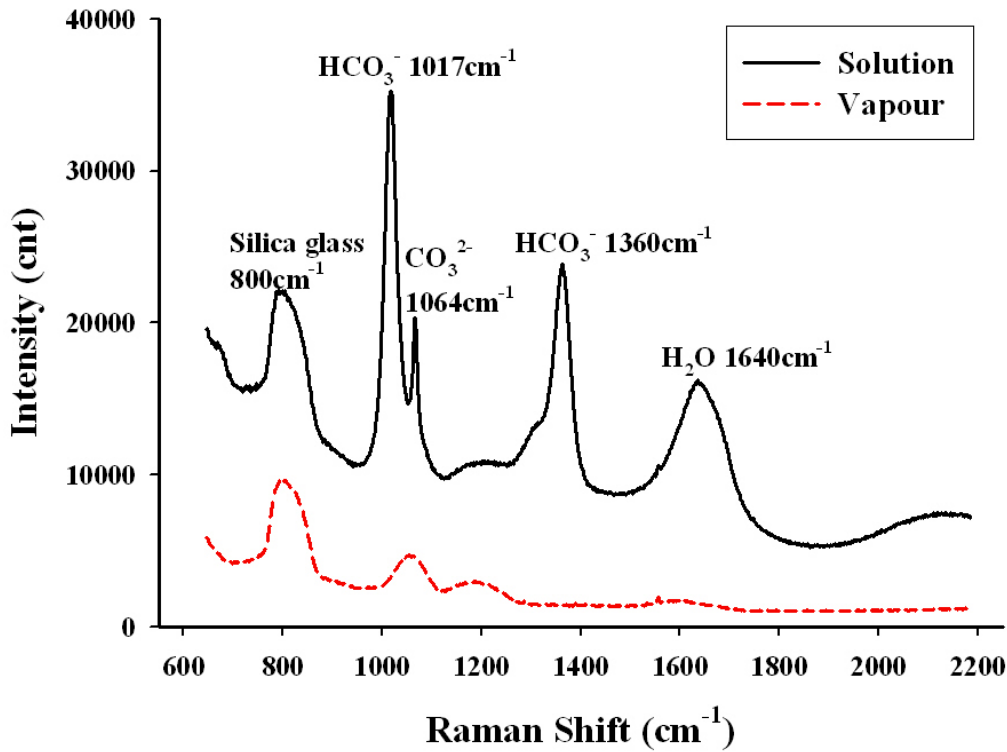


Figure II-3 Spectra collected from the aqueous solution and from the vapour phase in bicarbonate-bearing capillary focusing on the same distance.

For pure silica glass capillary, the signal of silica glass is added to bands of bicarbonate and the bending band of liquid water (figure II-3), so the real area of bands “*Area*(1017)” and “*Area*(1360)” of bicarbonate and bending band of liquid water “*Area*(1640)” are deduced using Eq. II-7, II-8, II-9 by normalizing the contribution of silica glass in the spectral regions



950 - 1150  $\text{cm}^{-1}$ , 1100 - 1300  $\text{cm}^{-1}$  and 1500 - 1750  $\text{cm}^{-1}$  using the intensity of the Raman band of silica glass collected in the aqueous phase and in vapor phase near the aqueous phase in silica glass capillary (“1” spectrum collected in aqueous solution, “2” spectrum collected in vapour phase near solution focusing on the same distance). The band between 720  $\text{cm}^{-1}$  and 920  $\text{cm}^{-1}$  is chosen as reference.

$$Area(1017) = Areal(1017) - Area2(1017) \times \frac{Areal(800)}{Area2(800)} \quad (\text{II-7})$$

$$Area(1360) = Areal(1360) - Area2(1360) \times \frac{Areal(800)}{Area2(800)} \quad (\text{II-8})$$

$$Area(1640) = Areal(1640) - Area2(1640) \times \frac{Areal(800)}{Area2(800)} \quad (\text{II-9})$$

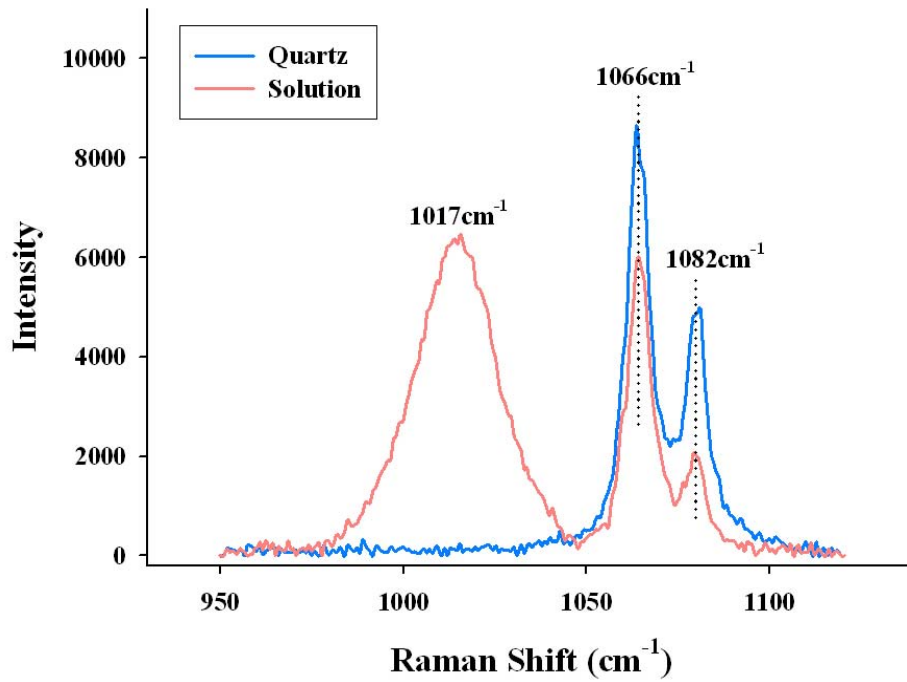


Figure II-4 Two spectra collected from aqueous phase in fluid inclusion and from quartz crystal near inclusion, respectively.

A small complication has to be taken into account in quartz crystal. Figure II-4 presents the spectra respectively collected from aqueous phase in fluid inclusion and from quartz crystal near inclusion at ambient temperature. Two bands at 1066  $\text{cm}^{-1}$  and 1082  $\text{cm}^{-1}$  in two spectra have the same central position. Referring to Davis & Oliver (1972), carbonate band

$\nu_1(A')$  is positioned at  $1064\text{ cm}^{-1}$ , and at the same position there locates quartz band  $E_5$  (at  $1065\text{ cm}^{-1}$ , Krishnan, 1945). The band at  $1082\text{ cm}^{-1}$  is attributed to quartz band  $A_4$  (Krishnan, 1945).

Situation gets clearer when comparison is made with the spectra collected in the aqueous fluid contained in capillary. Figure II-5 presents the spectra collected from aqueous phase in fluid inclusion and in capillary sample at ambient temperature respectively. The positions of bicarbonate in two spectra are the same, at  $1017\text{ cm}^{-1}$  (Davis & Oliver, 1972). In spectrum collected from capillary sample, there is identifiable to the band of carbonate at  $1066\text{ cm}^{-1}$ . Comparing the same range between  $1050\text{ cm}^{-1}$  and  $1100\text{ cm}^{-1}$ , there are two bands at  $1066\text{ cm}^{-1}$  and  $1082\text{ cm}^{-1}$  respectively in spectra from fluid inclusion.

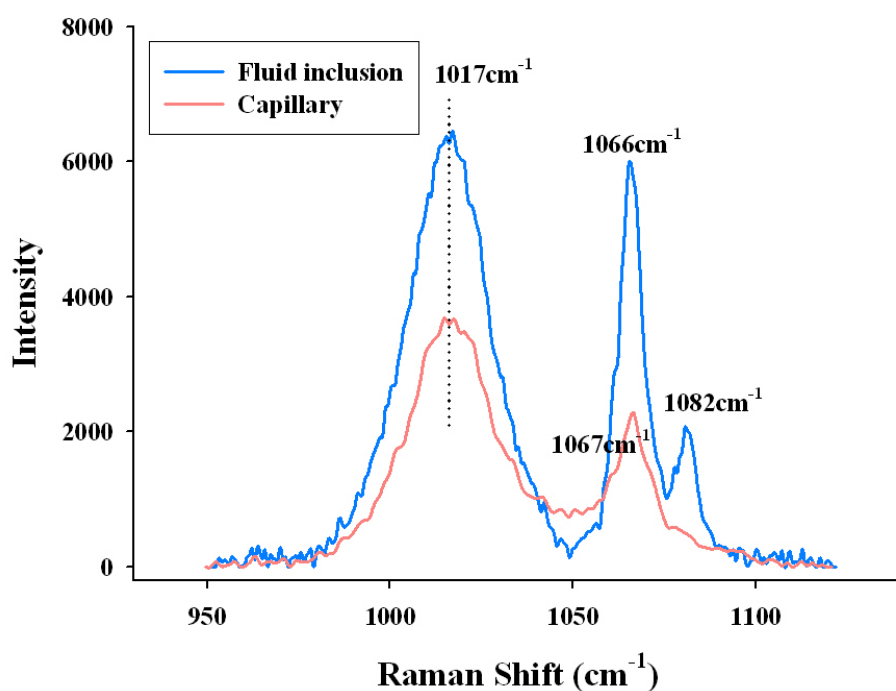


Figure II-5 Raman spectra collected from aqueous phase in fluid inclusion and in capillary, respectively.

Thus, to get in quartz the true intensity of the carbonate band, it is necessary to subtract the contribution of the quartz by normalizing its intensity with respect to the band at  $1082\text{ cm}^{-1}$  obtained in the adjacent quartz.

#### II.2.2.1. Results obtained from synthetic fluid inclusion

Three fluid inclusion samples in system  $\text{KHCO}_3\text{-H}_2\text{O}$  with the concentrations of 0.1m, 0.3m and 1.0m respectively were prepared and analyzed. Figure II-6 presents the relationship between area ratios of bands of bicarbonate with bending band of water and the concentration of bicarbonate calibrated from synthetic fluid inclusions. The area ratios of bicarbonate band at  $1017\text{ cm}^{-1}$  and at  $1360\text{ cm}^{-1}$  with bending band of water are both linear with the concentration of bicarbonate in aqueous solution. The concentration of bicarbonate can be deduced from ratios of bands of bicarbonate with bending band of water by collecting the spectrum of bicarbonate-bearing aqueous phase.  $1017\text{ cm}^{-1}$  band of bicarbonate has better sensitivity than  $1360\text{ cm}^{-1}$  band of bicarbonate.

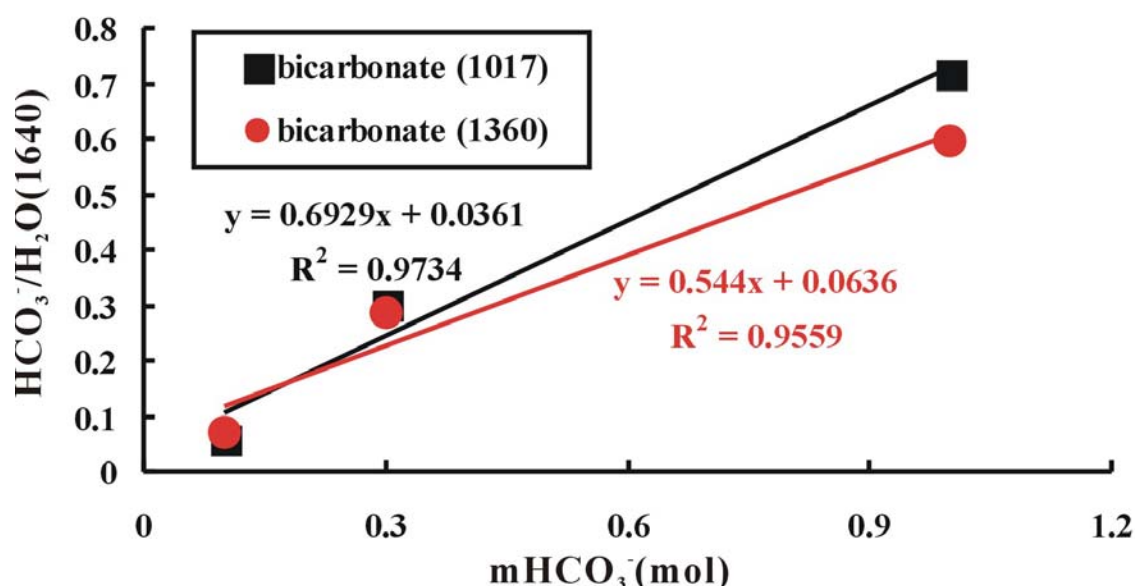


Figure II-6 Linear variations of ratio1 and ratio2 deduced from spectra collected from bicarbonate-bearing synthetic fluid inclusions with the concentration of bicarbonate.

Two samples in system  $\text{KHCO}_3\text{-NaCl-H}_2\text{O}$  (1.0 m NaCl with 0.3 m and 1.0 m  $\text{KHCO}_3$  respectively) are synthesized for checking the influence of anion  $\text{Cl}^-$  which is the most common anion in geological fluid presented in fluid inclusions (Roedder, 1972). The analysis in two samples shows the same trends. The addition of  $\text{Cl}^-$  in solution greatly decreases the area ratio between bands of bicarbonate and bending band of water, as shown in figure II-7. Therefore, it is necessary to consider the influence of  $\text{Cl}^-$  anion for the calibration of  $\text{HCO}_3^-$  analysis at ambient temperature using Raman spectrometry.

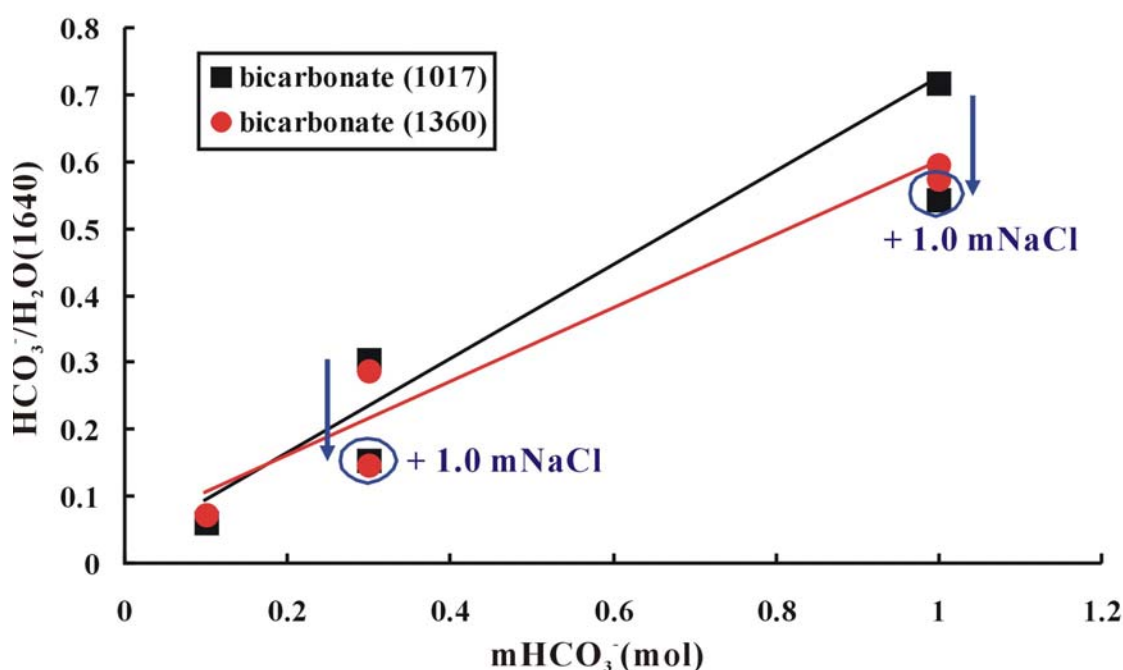


Figure II-7 Influence of the addition of 1.0 m NaCl in bicarbonate-bearing solution to the variations of ratio1 and ratio2. Anion Cl<sup>-</sup> decreases the area ratios between bands of bicarbonate and bending band of water in both inclusion samples.

#### II.2.2.2. Results obtained from silica glass capillaries

For bicarbonate-bearing aqueous solutions in silica glass capillary samples, the equivalent linear relationships of the area ratios of bands of bicarbonate at 1017 cm<sup>-1</sup> and at 1360 cm<sup>-1</sup> to the bending band of water versus the concentration of bicarbonate in aqueous solution are obtained. Figure II-8 shows the results from the analysis of four samples in system KHCO<sub>3</sub>-H<sub>2</sub>O with the concentrations of 0.01m, 0.1m, 0.3m and 1.0m respectively. The bicarbonate band at 1017 cm<sup>-1</sup> has a better sensitivity than the band of bicarbonate at 1360 cm<sup>-1</sup>. Through constructing the relationship between the concentration of bicarbonate and the area ratio of bands of bicarbonate to bending band of water, the concentration of bicarbonate can be obtained by Raman measurement.

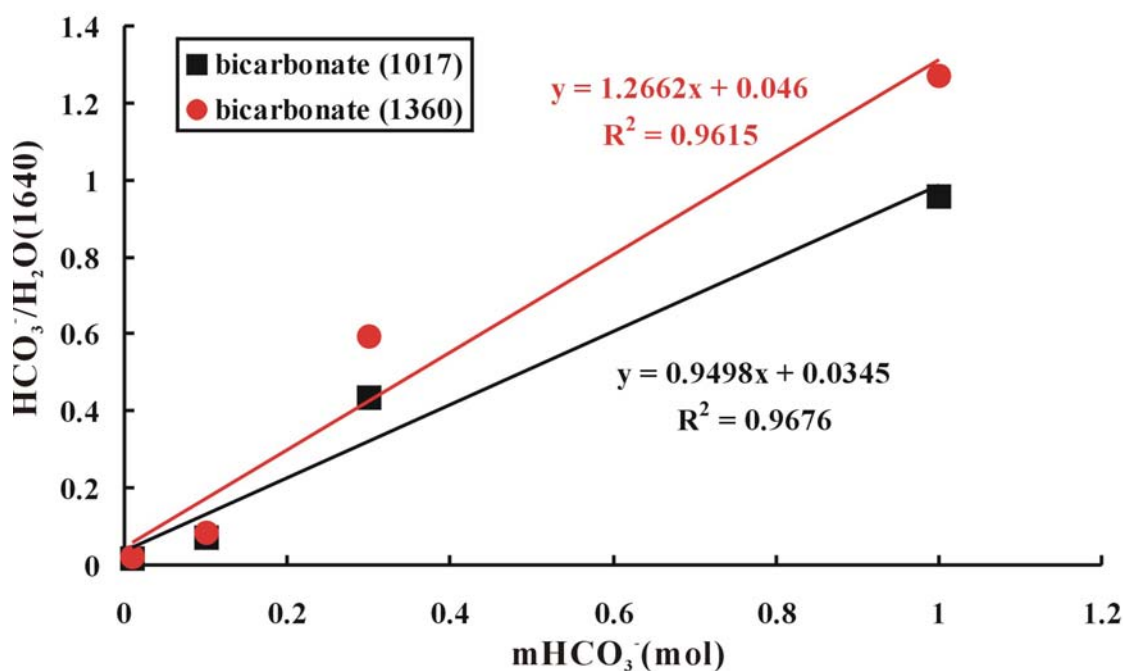


Figure II-8 Variations of ratio1 and ratio2 deduced from spectra collected from bicarbonate-bearing silica glass capillary samples versus concentration of bicarbonate.

For silica glass capillary samples, the influence of anion  $\text{Cl}^-$  to the calibration of concentration of  $\text{HCO}_3^-$  by Raman measurement was also checked. 1.0m NaCl was added to two samples in system  $\text{KHCO}_3\text{-H}_2\text{O}$  (1.0m and 0.3m respectively). Figure II-9 indicates that the addition of anion  $\text{Cl}^-$  decreases the area ratio between bands of bicarbonate and bending band of water at ambient temperature, as well as the analysis for fluid inclusion samples.

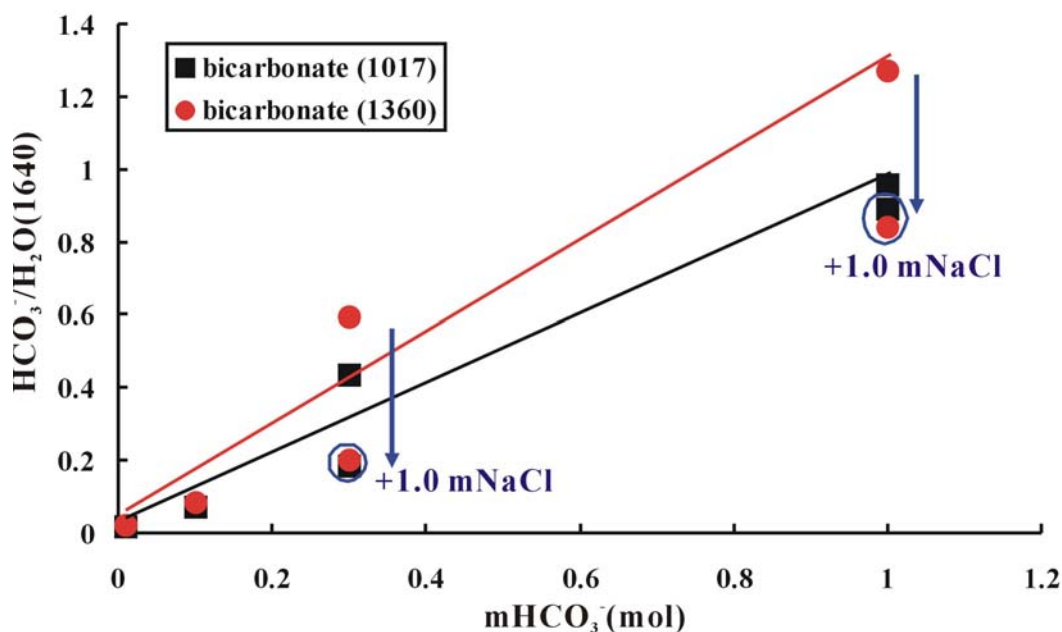


Figure II-9 Influence of the addition of 1.0 m NaCl in bicarbonate-bearing solution to the variations of ratio1 and ratio2. Anion  $\text{Cl}^-$  decreases the area ratios between bands of bicarbonate and bending band of water in both capillary samples.

### II.2.2.3. Comparison between the results from synthetic fluid inclusion and the results from silica glass capillary

Ratio1	Concentration (m)		Difference	((a-b)/a)%
	Inclusion (a)	Capillary (b)		
0.01	-0.037668	-0.0257949	-0.011873	31.5
0.03	-0.008804	-0.0047378	-0.004066	46.2
0.05	0.0200606	0.0163192	0.0037414	18.7
0.1	0.0922211	0.0689619	0.0232592	25.2
0.3	0.380863	0.2795325	0.1013305	26.6
0.5	0.669505	0.4901032	0.1794018	26.8
1.0	1.3911098	1.0165298	0.37458	26.9

Table II-2 Comparison of Eq. II-10 and II-11.

Results from inclusion and capillary samples both show the linear variation between the concentration of  $\text{HCO}_3^-$  and the area ratios of bicarbonate bands to bending band of water. Eq. II-10 and II-11 are the relation between ratio1 and concentration of  $\text{HCO}_3^-$  respectively obtained from inclusion samples and capillary samples.

$$y = (x - 0.0361)/0.6929 \quad (\text{II-10})$$

$$y = (x - 0.0345)/0.9498 \quad (\text{II-11})$$

The concentration of  $\text{HCO}_3^-$  (y) varies with ratio1 (x), area ratio of bicarbonate band at  $1017 \text{ cm}^{-1}$  to bending band of water. The two are not the same. Table II-2 lists some data calculated using the above equations for checking the differences. The data shows that the maximum deviation of data of capillary relative to data of inclusion is 46.2%. Eq. II-12 and II-13 are the relation between ratio2 and concentration of  $\text{HCO}_3^-$  respectively obtained from inclusion samples and capillary samples.

$$y = (x - 0.0636)/0.544 \quad (\text{II-12})$$

$$y = (x - 0.046)/1.2662 \quad (\text{II-13})$$

The concentrations of  $\text{HCO}_3^-$  (y) are calculated from the area ratio of bicarbonate band at  $1360\text{ cm}^{-1}$  to bending band of water (x). Comparison of the deviation of two equations is presented in table II-3. The maximum deviation of data of capillary relative to data of inclusion is 112.6%.

ratio2	Concentration (m)		Difference	((a-b)/a)%
	Inclusion (a)	Capillary (b)		
0.01	-0.098529	-0.02843	-0.0700979	71.1
0.03	-0.061765	-0.01264	-0.0491285	79.5
0.05	-0.025	0.003159	-0.0281591	112.6
0.1	0.066912	0.042647	0.0242645	36.3
0.3	0.434559	0.2006	0.2339586	53.8
0.5	0.802206	0.358553	0.4436527	55.3
1.0	1.721324	0.753435	0.9678881	56.2

Table II-3 Comparison Eq. II-12 and II-13.

The differences between two equations respectively deduced from results of inclusion samples and capillary samples, may have several causes. Firstly, the CCD detector used with the Labram spectrometer at G2R has been changed after the collection of data in synthetic fluid inclusions and before those obtained in silica glass capillary. Secondly, the microscope objectives used to focus the laser beam and to collect the Raman signal are not the same: x 80 for fluid inclusions and x 20 for the signal obtained in the capillary. These objectives have necessarily different depolarization ratios, which combined with the dichroicity of the grating could change the intensity of the band. Thirdly, the birefringence of the quartz, its rotatory power which depends on the orientation of the quartz wafer, may also modify the polarization state of the Raman signal and thus its intensity also as a result of the dichroicity of the grating. This effect was clearly identified by Dubessy et al. (2002) for the determination of the chloride concentration based on the Raman spectra of the OH stretching of water. All these points must be carefully checked for future and precise calibration.

### II.2.3. Calibration as a function of temperature

#### II.2.3.1. Results obtained from synthetic fluid inclusions

Raman spectra of bicarbonate bands ( $\nu_5(A')$  C-O-H [ $1017\text{ cm}^{-1}$  at room temperature] and  $\nu_3(A')$  C-O [ $1360\text{ cm}^{-1}$  at room temperature]) are obtained as a function of temperature (figure II-10). The results of simple data processing are given in the figure II-11 and figure II-12. Wavenumber of the  $\nu_5(A')$  C-O-H and  $\nu_3(A')$  C-O bicarbonate bands decreases slightly and linearly with increasing temperatures. The ratio1 and ratio2 of bicarbonate bands to bending band of water were calculated by analyzing the Raman spectra collected on aqueous phase in fluid inclusion at different temperatures. The results are presented in figure II-12. Ratio1 of the  $\nu_5(A')$  C-O-H band intensity to water bending band intensity decreases with the increasing of temperature, but intensity ratio 2 of the  $\nu_3(A')$  C-O to the bending band of water increases with increasing of temperature.

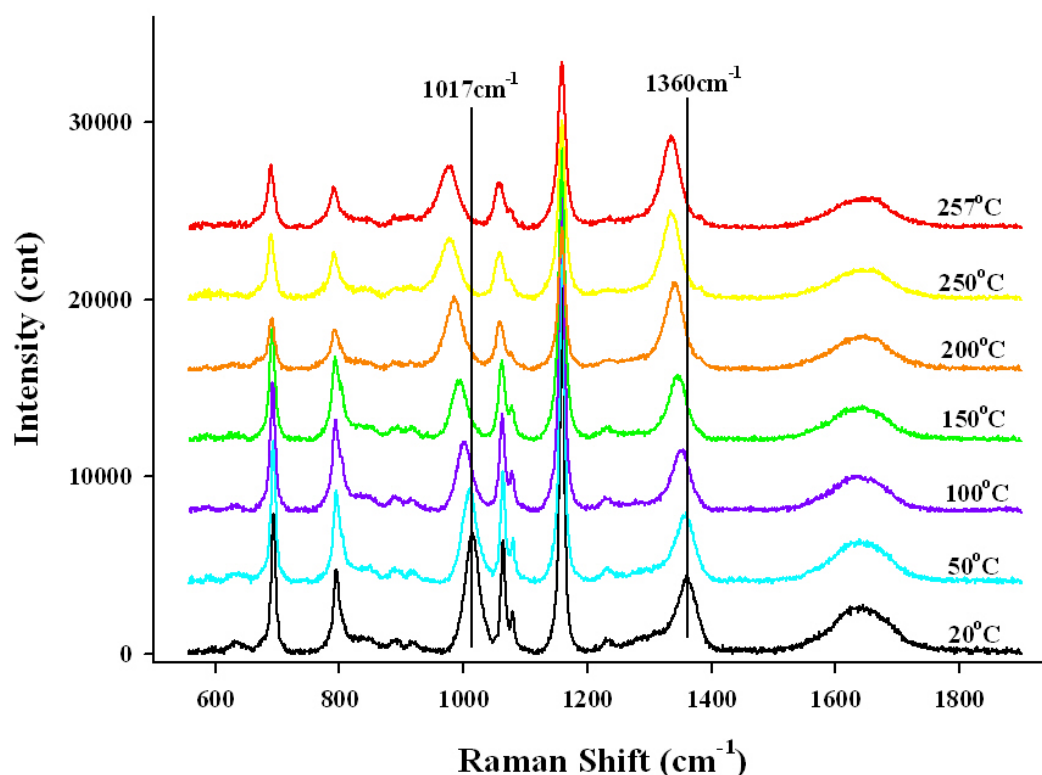


Figure II-10 Spectra collected in the aqueous phase in fluid inclusion at different temperature. This fluid inclusion is homogenized at  $256.6\text{ }^{\circ}\text{C}$  ( $L+V\rightarrow L$ ).



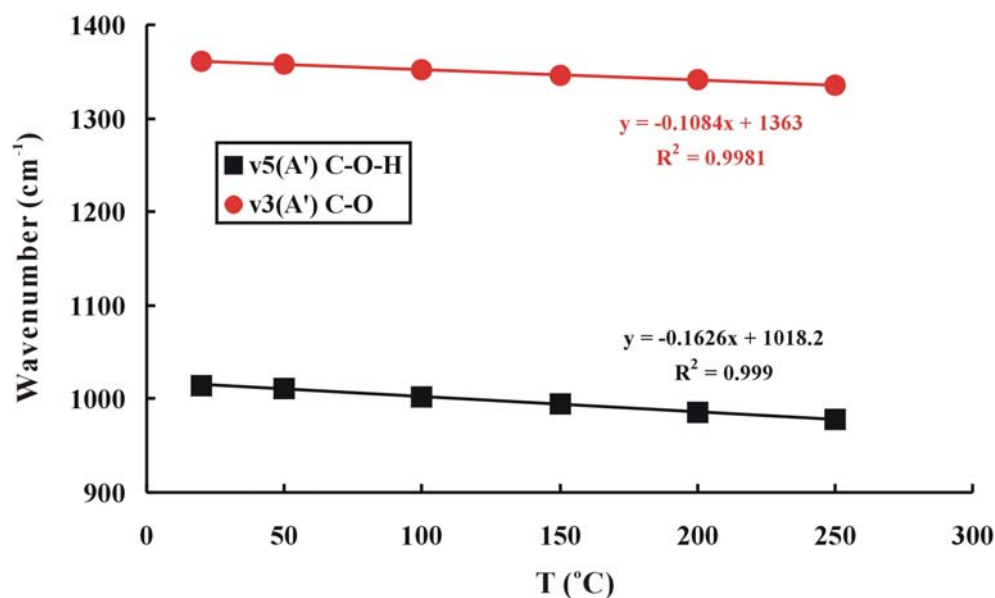


Figure II-11 Variation of  $\nu_5(A')$  C-O-H and  $\nu_3(A')$  C-O wavenumbers versus temperature. Spectra were collected from fluid inclusion.

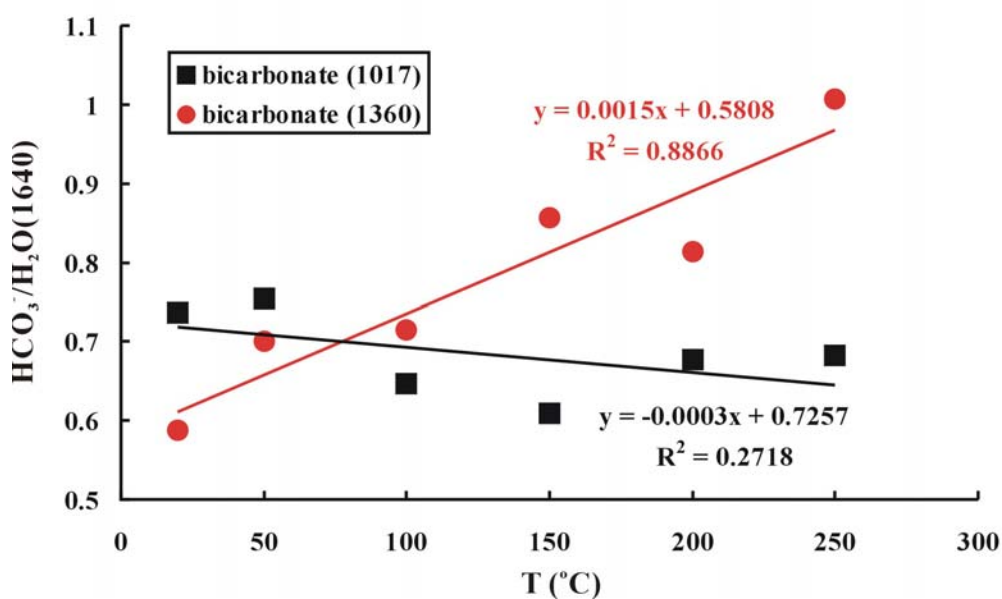


Figure II-12 Variations of intensity ratio1 and ratio2 deduced from spectra collected from bicarbonate-bearing fluid inclusion with the increasing of temperature.

In figure II-13, spectra collected from vapour phase in fluid inclusion are presented. With the increasing of temperature,  $\text{CO}_2$  is detected apparently from 100 °C and the peak of  $\text{CO}_2$  becomes stronger more and more, which is the response of Eq. II-14.



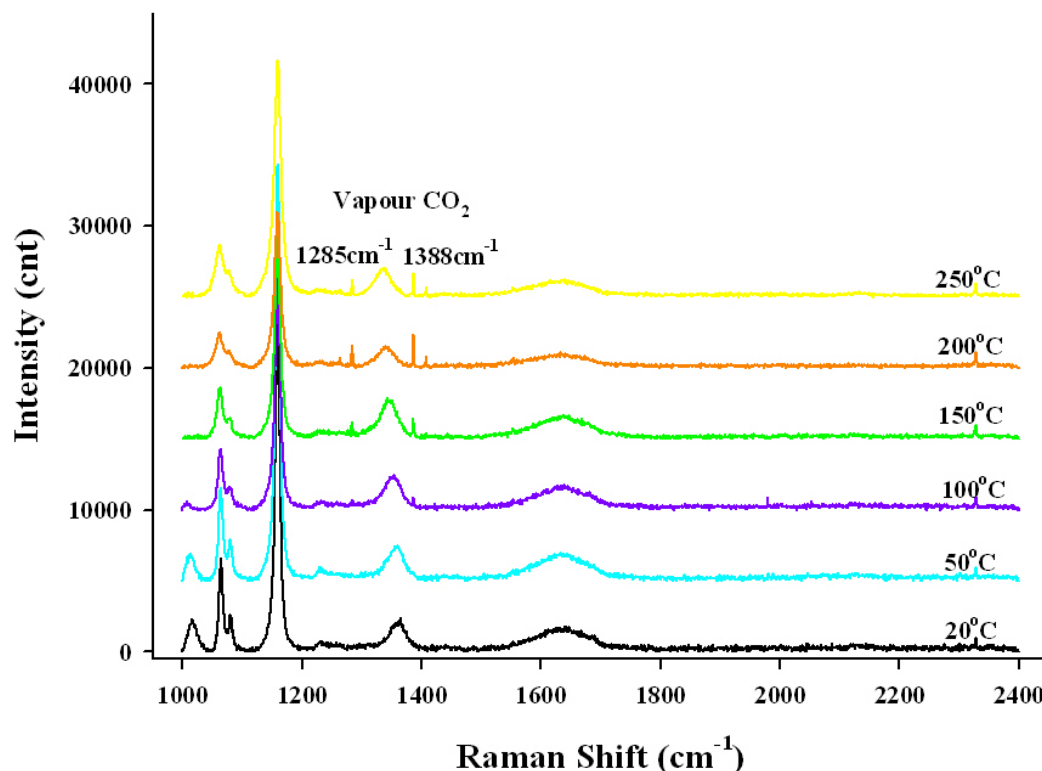


Figure II-13 Spectra collected in the vapor phase in fluid inclusion at different temperature.

The formation of  $\text{CO}_2$  with increasing temperature results from the increase of this equilibrium constant by nearly two orders of magnitude from 25 °C to 250 °C. This is the general law of the decrease the charge of the aqueous species with the increase temperature due to the decrease of the static dielectric constant of the solvent and the solution. However, the results obtained for the bicarbonate bands intensity in figure II-12 are puzzling. First, the evolution of the intensity ratio of the  $\nu_5(\text{A}')$  C-O-H and bending band of water decreases versus increasing temperature. This should indicate a decrease of the concentration of bicarbonate in the molality scale. On the contrary, positive slope of the  $\nu_3(\text{A}')$  C-O band indicates a concentration increase. These contradictory results suggest an additional effect which is probably linked with the Raman scattering of each vibrational mode. Each vibrational band and its related variation of its polarizability tensor are probably sensitive to the molecular environment (solvation, ion-pairing, ...). Thus, the calibration of Raman data with temperature is not straightforward.

### II.2.3.2. Results obtained from capillary samples

As the results obtained from fluid inclusions, the wavenumber of bicarbonate bands ( $\nu_5(A')$  C-O-H and  $\nu_3(A')$  C-O) are shifted to lower wavenumbers with increasing of the temperature (figure II-14). A characteristic band of carbonate ( $\nu_1(A')$ ) at  $1064\text{ cm}^{-1}$  is observed in capillary sample. This band of carbonate becomes stronger relative to the bicarbonate band at  $1017\text{ cm}^{-1}$  above  $100^\circ\text{C}$  and disappears together with the bicarbonate bands when capillary sample homogenized to the vapor phase. In the vapor phase, peaks of  $\text{CO}_2$  are detected from  $100^\circ\text{C}$  and the peak intensity of  $\text{CO}_2$  increases with increasing temperature (figure II-15), as well as in fluid inclusion.

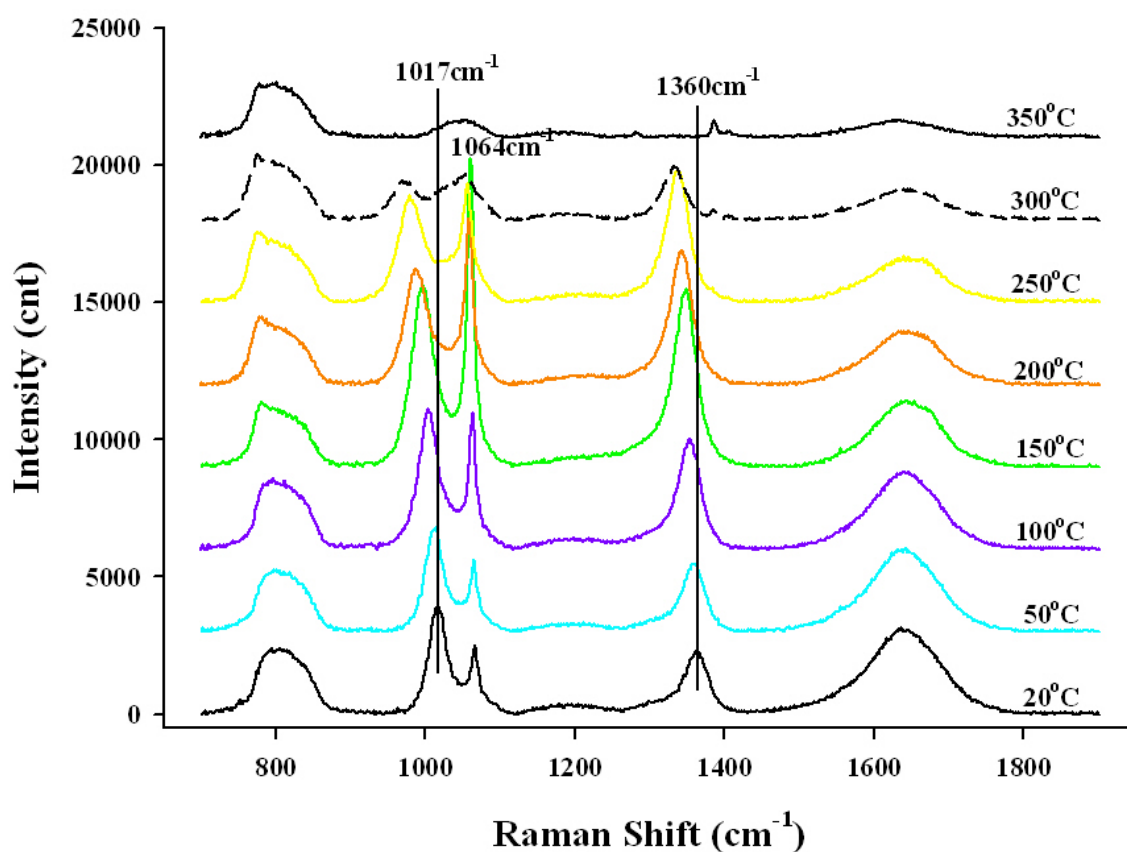


Figure II-14 Spectra collected in the aqueous phase in capillary sample at different temperature. This capillary sample is homogenized as  $L+V \rightarrow V$ .

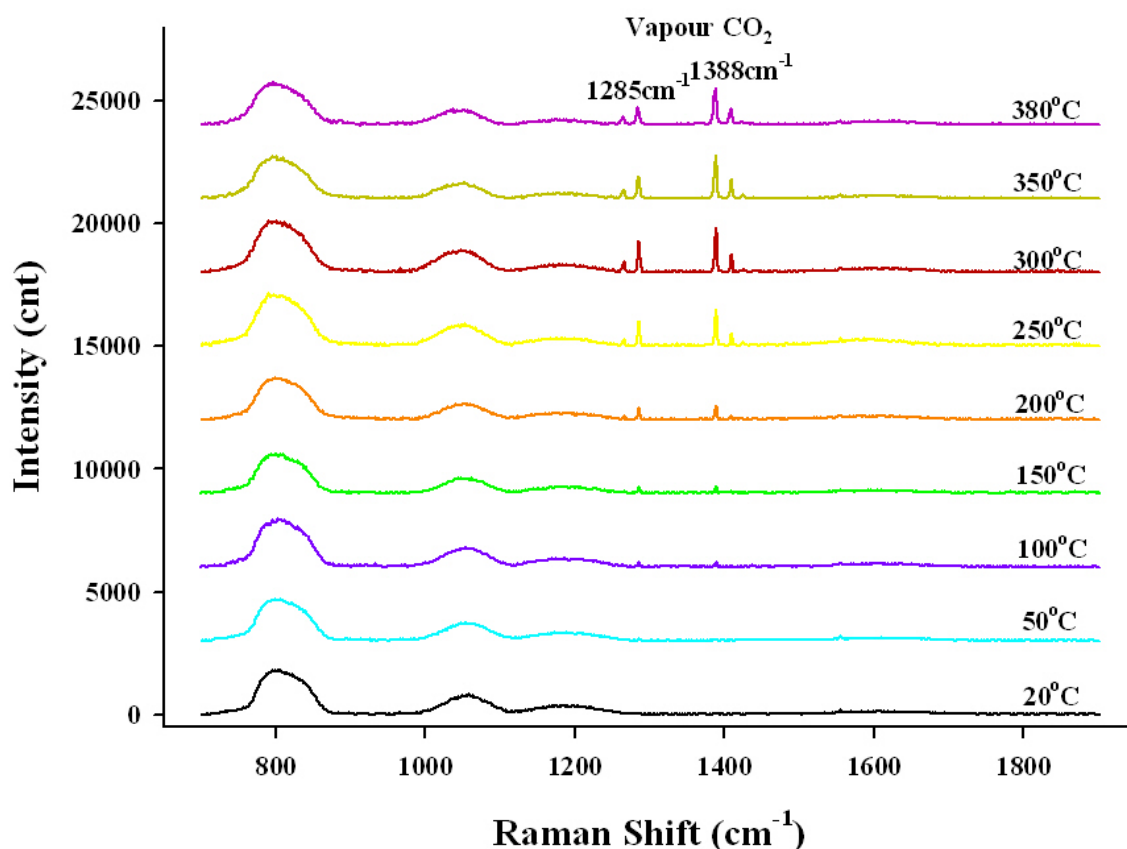


Figure II-15 Spectra collected in the vapour phase in capillary sample at different temperature.

The results of simple data processing are listed in the figure II-16 and figure II-17. The wavenumbers of bicarbonate bands at  $1017\text{ cm}^{-1}$  and  $1360\text{ cm}^{-1}$  are both shifted to the lower wavenumber in linear correlation with the increasing temperature (figure II-16). Figure II-17 presents the relationships between the temperature and ratio1 and ratio2 of bicarbonate bands to bending band of water, which are not distinct that the ratios of bicarbonate band to bending band of water varies with the temperature in linear correlation, but ratio1 of bicarbonate band at  $1360\text{ cm}^{-1}$  to bending band of water also has the trend of increasing with the increasing of temperature as in fluid inclusion. It is noted that ratio1 and ratio2 both decrease suddenly at  $300\text{ }^{\circ}\text{C}$ , which is due to the homogenization of capillary to vapour phase and the signal of bands of bicarbonate becomes weaker in aqueous phase, see the spectrum at  $300\text{ }^{\circ}\text{C}$  (figure II-14).

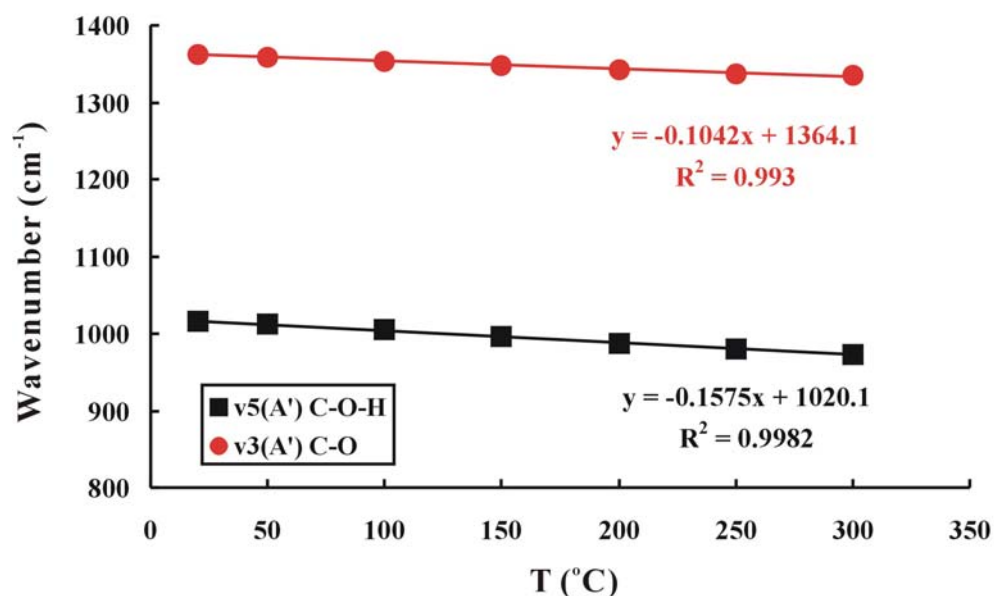


Figure II-16 Variation of v5(A') C-O-H and v3(A') C-O wavenumbers versus temperature. Spectra were collected from capillary sample.

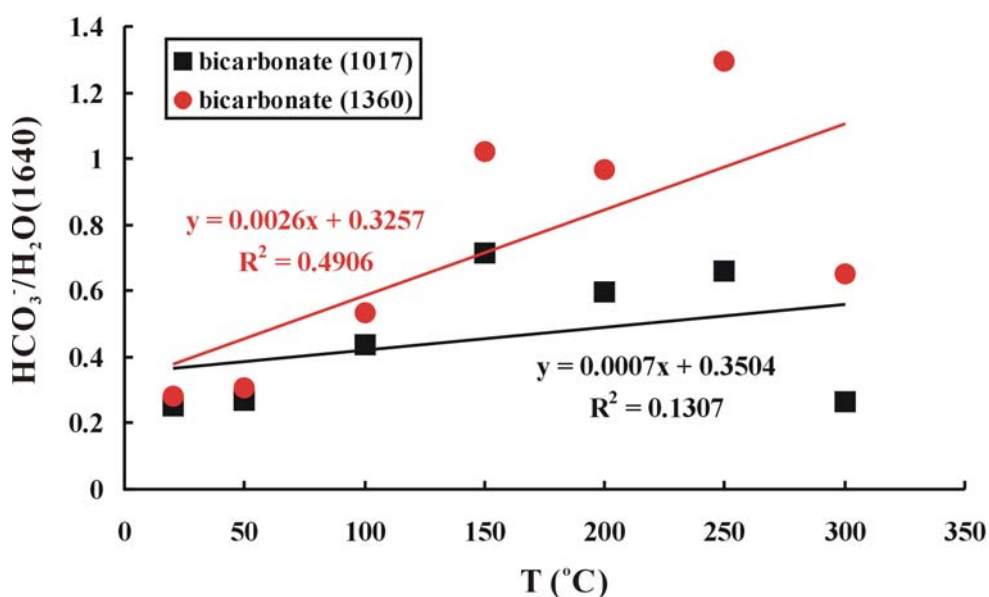


Figure II-17 Linear variations of ratio1 and ratio2 deduced from spectra collected from bicarbonate-bearing capillary with the increasing of temperature.

Interesting features appear with increasing temperature: the coexistence of the three species  $\text{CO}_2$ ,  $\text{HCO}_3^-$  and  $\text{CO}_3^{2-}$ . Indeed, at room temperature the pK of the two equilibria  $\text{CO}_2$ ,  $\text{HCO}_3^-$  and  $\text{HCO}_3^-/\text{CO}_3^{2-}$  differ from 4 log units. This difference is only three log units at 250 °C, which shows that the stability field of  $\text{HCO}_3^-$  with a correlative increase of the stability field of  $\text{CO}_2$  and  $\text{CO}_3^{2-}$ . In addition, the intensity of the symmetric stretching band of

carbonate increases strongly with the increasing temperature. This evolution seems to be contradictory with the law of charge decrease with increasing temperature. However, it should be noted that CO<sub>2</sub> concentration increases also in the vapour phase. Therefore, this suggests that the pH of the aqueous solution would increase as it was modeled in modeling of boiling by Drummond (1981). Another explanation could also be the effect of a slight dissolution of silicate glass which contains O-H radicals. Finally, the homogenization of the capillary towards the vapor phase changes drastically the speciation since ions are not stable in a low density and low static dielectric constant fluid phase. As potassium ion cannot recombine to form a neutral dissolved species, probably precipitation of solid KHCO<sub>3</sub> occurs. However, it was not observed, probably due to its dispersion on the walls capillary.

In order to solve the numerous problems found during these high temperature experiments, it would be necessary to have a system without vapor phase. Experimental set-up connected with a manual pressure pump should be the way to solve this probe by imposing pressure above the saturation line de water, for instance at 500 bar. The second point would be to use an in situ probe: perchlorate ion at low concentration. However, a previous study of its stability should be done. Perchlorate at low concentration (0.01 molal) for instance) would not modify significantly the molecular environments and will provide a reference for intensity measurements. Finally, experiments with higher KHCO<sub>3</sub> concentrations should be done to investigate the steps of homogenization to the vapor phase.

### **II.3. Calibration of the analysis of CO<sub>2</sub> by Raman spectroscopy**

If the amount of aqueous loaded solution in capillary is easy to quantify by measuring the volume of the cavity filled by the aqueous solution, a dedicated protocol should be developed for the determination of the amount of CO<sub>2</sub> loaded in capillary using the condensation method at liquid nitrogen temperature.

#### **II.3.1. Synthesis of fluid from the H<sub>2</sub>O-CO<sub>2</sub>-(NaCl) system in capillary**

##### **II.3.1.1. Method for loading pure CO<sub>2</sub> in silica glass capillary**

CO<sub>2</sub>-loading in capillary is by condensation of CO<sub>2</sub> gas into the capillary when the closed end of capillary is immersed into liquid nitrogen. At first, gas CO<sub>2</sub> is charged inside the reservoir and the CO<sub>2</sub> reservoir is connected with the line. One-end-closed capillary is connected with the system. Then, all the lines are evacuated by connection with the vacuum pump. Then lines are cleaned by a flow of gas CO<sub>2</sub>. Finally, CO<sub>2</sub> gas is condensed into the capillary when its sealed part is immersed into liquid nitrogen. CO<sub>2</sub> vapor above solid CO<sub>2</sub> contained in the silica capillary and in the stainless steel line is evacuated with the vacuum pump. Then capillary is sealed. The change of the pressure is measured by pressure gauge.

### **II.3.1.2. Method for quantifying CO<sub>2</sub> condensed in capillary and the precision of the method**

It is possible to quantify the amount of CO<sub>2</sub> trapped in sealed capillary. When the capillary sample with pure CO<sub>2</sub> is done, it can be quantified by determining the density of CO<sub>2</sub> in capillary and measuring the volume occupies within the capillary. This method has been developed for pure CO<sub>2</sub> and thus, the volume occupied by CO<sub>2</sub> is the total inner capillary volume. Considering that several substances are sealed in capillary at the same time, it is necessary to directly quantify the gas when it is loaded into capillary. This approach is developed to directly estimate the mole number of gas loaded in the capillary using the variation of gas pressure at known temperature and the equation of state of perfect gas. The following describes the approach in detail.

In this study, referring to figure II-18, volume  $V_2$  is filled with gas CO<sub>2</sub> at first, and then gas enters into the lines marked  $V_{cap}$ . After the closed-end of the capillary is immersed into the liquid nitrogen, gas CO<sub>2</sub> is condensed as solid phase in the cold part of the capillary. Before the capillary is sealed, the rest of remaining vapor CO<sub>2</sub> in the volume  $V_{cap}$  is evacuated from  $V_{cap}$  at different steps which are described below. The pressure in each step is measured at each step of evacuation by pressure gauge connected with line  $V_2$ .

The critical point of the procedure consists to know exactly the number of moles of CO<sub>2</sub> contained in volume  $V_2$ . This can be achieved only if pressure  $P$ , volume  $V_2$  and temperature

are known according to the equation of state of perfect gas:  $P \times V_2 = n_{CO_2} \times R \times T$ . As pressure and temperature are measured, the only remaining unknown is  $V_2$ .

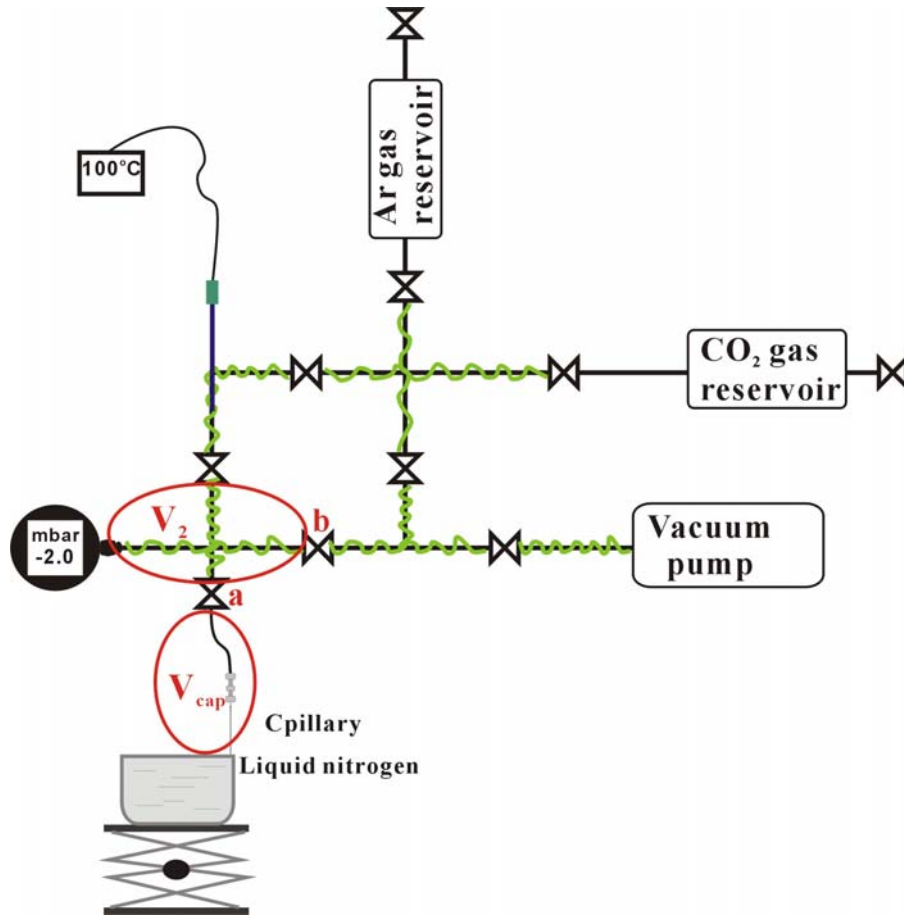


Figure II-18 The line of system for CO<sub>2</sub> loading in silica glass capillary. a and b are two valves.

#### *Calibration of volume $V_2$ .*

$V_2$  is measured using another calibrated standard volume  $V_{std}$  which is connected directly to valve a. This first requires the calibration of this standard volume. It is done by measuring the mass of the empty volume  $V_{std}$  and the mass of the volume  $V_{std}$  filled by liquid water. The value found for  $V_{std}$  is:  $V_{std} = 1.081 \text{ cm}^3 \pm 0.0001$ .

The second step consists to fill  $V_{std}$  and  $V_2$  with CO<sub>2</sub> and to measure pressure  $P_1$ . Then valve a is closed and vacuum is made in volume  $V_2$ . The number of moles of CO<sub>2</sub> in volume  $V_{std}$  is: 
$$n_{CO_2}^{V_{std}} = \frac{P_1 \times V_{std}}{RT}.$$



The third step consists to expand gas CO<sub>2</sub> in volume V<sub>2</sub>. The number of moles of CO<sub>2</sub> is

$n_{CO_2}^{V_2+V_{std}} = \frac{P_2 \times (V_2 + V_{std})}{RT}$  . Because of mass conservation  $n_{CO_2}^{V_{std}} = n_{CO_2}^{V_2+V_{std}}$  , therefore

$P_1 \times V_{std} = P_2 \times (V_2 + V_{std})$  since the temperature is identical. From this equation, V<sub>2</sub> is deduced:

$$V_2 = V_{std} \times \left( \frac{P_1 - P_2}{P_2} \right).$$

The measured values of pressure P<sub>1</sub>, P<sub>2</sub> and calculated volume are given in table II-4.

Then vaules below  $\bar{V}_2 - \sigma$  and above  $\bar{V}_2 + \sigma$  where  $\sigma$  is the standard deviation eliminated. And a new average with new stand deviation value is given:  $V_2 = 1.8860 \pm 0.0008$  cm<sup>3</sup>.

P1(mbar)	P2(mbar)	V2(cm <sup>3</sup> )
224.3	81.7	1.8861
222.6	81.2	1.8824
232.7	84.8	1.8854
231.2	84.2	1.8873
229.4	83.6	1.8853
227.3	82.8	1.8865
225.8	82.2	1.8885
224.0	81.6	1.8865
222.5	81.1	1.8848
220.8	80.4	1.8877
219.7	80.0	1.8877
218.1	79.5	1.8846
216.8	79.0	1.8856
215.3	78.4	1.8876
214.1	78.0	1.8862
212.7	77.5	1.8858
211.6	77.1	1.8858
210.6	76.7	1.8872
209.5	76.3	1.8871
208.4	76.0	1.8832
<b>Average</b>		1.8861
<b>Standard deviation</b>		0.0015
<b>RSD</b>		0.08%
<b>Min</b>		1.8846
<b>max</b>		1.8875

Table II-4 Measurements of volume V<sub>2</sub>.

*Detailed procedure for the quantification of loaded CO<sub>2</sub>.*

- Step 0: Vacuum in volume V<sub>2</sub> and V<sub>cap</sub> to evacuate any traces of gas.

- Step 1: Volume V<sub>2</sub> is filled with gas CO<sub>2</sub> at temperature T(V<sub>2</sub>) (100 °C or 120 °C).

In this state, the total gas CO<sub>2</sub> is just in volume V<sub>2</sub>, its pressure is P<sub>0</sub>. The perfect gas equation of state allows the calculation of mole number of CO<sub>2</sub> in volume V<sub>2</sub>.

$$P_0 \times V_2 = n_{CO_2}^T \times R \times T_{V_2} \quad (II-15)$$

Where  $R$  is gas constant (83144.72 cm<sup>3</sup>·mbar·K<sup>-1</sup>·mol<sup>-1</sup>) and  $n_{CO_2}^T$  is the mole number of CO<sub>2</sub> gas in volume V<sub>2</sub>.

- Step 2: CO<sub>2</sub> gas is expanded in volume V<sub>cap</sub> by opening valve a and CO<sub>2</sub> gas is in the volumes V<sub>2</sub> at temperature T(V<sub>2</sub>) and V<sub>cap</sub> at temperature T (20°C).

The CO<sub>2</sub> gas in system consists of gas CO<sub>2</sub> in volume V<sub>2</sub> and in volume V<sub>cap</sub>. Two relations on mole number of gas CO<sub>2</sub> in system are available.

$$P_1 \times V_2 = n_{CO_2}^{V_2} \times R \times T_{V_2} \quad (II-16)$$

$$P_1 \times V_{cap} = n_{CO_2}^{V_{cap}} \times R \times T \quad (II-17)$$

Where  $n_{CO_2}^{V_2}$  is the mole number of CO<sub>2</sub> gas in volume V<sub>2</sub> and  $n_{CO_2}^{V_{cap}}$  is the mole number of gas CO<sub>2</sub> in volume V<sub>cap</sub>. So the total mole number of gas CO<sub>2</sub> in system verifies the mass conservation Eq. II-18.

$$n_{CO_2}^T = n_{CO_2}^{V_2} + n_{CO_2}^{V_{cap}} \quad (II-18)$$

From this step, V<sub>cap</sub> can be deduced through equations II-15 II-16, II-17 and II-18.

$$V_{cap} = \frac{(P_0 - P_1) \times V_2 \times T}{P_1 \times T_{V_2}} \quad (II-19)$$

- Step 3: Gas CO<sub>2</sub> is in the volumes V<sub>2</sub> (at T(V<sub>2</sub>)) and V<sub>cap</sub> (at T) with the extremity of silica glass capillary is immersed in liquid nitrogen.

As in step 2, the CO<sub>2</sub> in system consists of CO<sub>2</sub> vapor in volume V<sub>2</sub> and in volume V<sub>cap</sub>, but two phases CO<sub>2</sub> coexist in volume V<sub>cap</sub>, CO<sub>2</sub> vapour and solid CO<sub>2</sub>. Solid CO<sub>2</sub> originates from the gas condensation into the capillary when the closed part of the capillary is immersed into liquid nitrogen. This solid CO<sub>2</sub> is the CO<sub>2</sub> loaded in capillary sample and CO<sub>2</sub> pressure measured in volume V<sub>2</sub> decreases to P<sub>2</sub>. The CO<sub>2</sub> mole number in volume V<sub>2</sub> follows Eq. II-20.

$$P_2 \times V_2 = n_{CO_2}^{V_2} \times R \times T_{V_2} \quad (II-20)$$

The budget mass equations relative to CO<sub>2</sub> are the following:

$$n_{CO_2}^T = n_{CO_2}^{V_2} + n_{CO_2}^{V_{cap}} \quad (II-21)$$

$$n_{CO_2}^{V_{cap}} = n_{GCO_2}^{V_2} + n_{SCO_2}^{V_{cap}} \quad (II-22)$$

Where  $n_{CO_2}^{V_2}$  is the mole number of gas CO<sub>2</sub> in volume V<sub>2</sub> at pressure P<sub>2</sub> and  $n_{CO_2}^{V_{cap}}$  is the mole number of total CO<sub>2</sub> in volume V<sub>cap</sub> at pressure P<sub>2</sub>.  $n_{GCO_2}^{V_2}$  is the mole number of gas CO<sub>2</sub> in volume V<sub>cap</sub> and  $n_{SCO_2}^{V_{cap}}$  is the mole number of solid CO<sub>2</sub> in volume V<sub>cap</sub> which must be determined since it corresponds to the CO<sub>2</sub> amount inside the silica glass capillary after the second sealing.

- Step 4: Remaining of CO<sub>2</sub> gas in the volume V<sub>cap</sub> (at T) is evacuated.

The object of this approach is to quantify CO<sub>2</sub>-loading in capillary sample, namely,  $n_{SCO_2}^{V_{cap}}$ . From step 3, it is necessary to determine  $n_{GCO_2}^{V_2}$  for getting  $n_{SCO_2}^{V_{cap}}$ . First, CO<sub>2</sub> gas is evacuated with vacuum pump from only volume V<sub>2</sub> (closing valve a and opening valve b). Then the CO<sub>2</sub> gas of the vapour phase in volume V<sub>cap</sub> is transferred in volume V<sub>2</sub> (valve b is closed). Measured pressure is P<sub>3</sub>. According to Eq. II-23, the amount of CO<sub>2</sub>,  $n_{CO_2}^{V_{cap}}$ , removed from V<sub>cap</sub> can be calculated. This procedure is repeated till pressure P<sub>i</sub> is at the zero of the pressure gauge. Usually the procedure is finished after 4 or 5 steps.

$$P_3 \times V_2 = n_{CO_2}^{V_{cap}} \times R \times T_{V_2} \quad (II-23)$$

$$P_4 \times V_2 = n_{CO_2}^{V_{cap}} \times R \times T_{V_2} \quad (II-24)$$

⋮

$$\sum_{i=3}^n P_i \times V_2 = n_{GCO_2}^{V_{cap}} \times R \times T_{V_2} \quad (II-25)$$

Where  $n_{CO_2}^{V_{cap}}$  is the mole number of CO<sub>2</sub> gas in volume V<sub>2</sub> at each step « i » of expansion of gas in volume V<sub>cap</sub> to V<sub>2</sub> + V<sub>cap</sub> volume.

Now, using the equations presented in above steps, the CO<sub>2</sub>-loading in caillary sample ( $n_{SCO_2}^{V_{cap}}$ ) is deduced.

$$n_{SCO_2}^{V_{cap}} = \frac{(P_0 - P_2) \times V_2}{R \times T_{V_2}} - \frac{\sum_{i=3}^n P_i \times V_2}{R \times T} \quad (II-26)$$

In Eq. II-26, all the parameters to determine  $n_{SCO_2}^{V_{cap}}$  are available when the CO<sub>2</sub>-bearing capillary sample is fabricated.

### II.3.1.3. Validation of the approach and determinations the density of CO<sub>2</sub>

To validate this approach, several capillary samples of pure CO<sub>2</sub> are fabricated. The amount of CO<sub>2</sub> trapped in the capillary can also be quantified by determining the density of CO<sub>2</sub> in the capillary and by measuring the volume of capillary sample. For example, there is a capillary sample in pure CO<sub>2</sub> (see figure II-19), and liquid phase and vapour phase coexist in capillary at ambient temperature. The following parameters are available.

- $T_a$  (K): ambient temperature
- $\rho_L$  (g/cm<sup>3</sup>): density of liquid CO<sub>2</sub> at  $T_a$ ;  $\rho_V$  (g/cm<sup>3</sup>): density of vapour CO<sub>2</sub> at  $T_a$  (Ref.: <http://webbook.nist.gov>)
- $V_L$  (cm<sup>3</sup>): volume of liquid phase in capillary sample at  $T_a$ ;  $V_V$  (cm<sup>3</sup>): volume of vapour phase in capillary sample at  $T_a$ . These volumes are measured using the micrometric stage coupled with an optical microscope (see the corresponding section)
- $T_h$  (K): homogenization temperature (measured using the Linkam heating/freezing stage equipped with microscope)
- $\rho_h$  (g/cm<sup>3</sup>): density of CO<sub>2</sub> in capillary sample at  $T_h$  (Ref.: <http://webbook.nist.gov>)

-  $V_h$  (cm<sup>3</sup>): volume of capillary sample

By using above parameters, the mole number of CO<sub>2</sub> in capillary sample can be deduced by two ways, by Eq. II-27 or by Eq. II-28.

$$n_{CO_2}^1 = \frac{\rho_L \times V_L + \rho_V \times V_V}{M_{CO_2}} \quad (II-27)$$

where  $M_{CO_2}$  is mole mass of CO<sub>2</sub> (44.01 g/mol).  $n_{CO_2}^1$  and  $n_{CO_2}^2$  represent the mole number of CO<sub>2</sub> in capillary sample calculated by two ways, respectively.

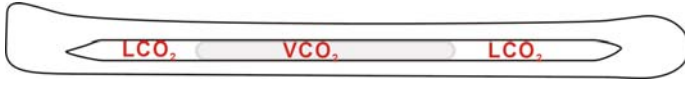


Figure II-19 Sketch of capillary sample in pure CO<sub>2</sub> with two phases at T<sub>a</sub>. LCO<sub>2</sub>: liquid CO<sub>2</sub>; VCO<sub>2</sub>: vapour CO<sub>2</sub>.

Another method to calculate the amount of CO<sub>2</sub> trapped in the capillary consists to use the homogenisation temperature to derive the CO<sub>2</sub> density ( $\rho_h$ ), the whole volume of the cavity ( $V_h$ ), and Eq. II-28.

$$n_{CO_2}^2 = \frac{\rho_h \times V_h}{M_{CO_2}} \quad (II-28)$$

The validation of the approach to quantify CO<sub>2</sub> in capillary sample is realized by comparing  $n_{SCO_2}^{V_{cap}}$  with  $n_{CO_2}^1$  or  $n_{CO_2}^2$ . The differences between  $n_{SCO_2}^{V_{cap}}$  and  $n_{CO_2}^1$  or between  $n_{SCO_2}^{V_{cap}}$  and  $n_{CO_2}^2$  are calculated, referring to Eq. II-29 and II-30.

$$\Delta 1(\%) = \frac{(n_{SCO_2}^{V_{cap}} - n_{CO_2}^1)}{n_{CO_2}^1} \times 100 \quad (II-29)$$

$$\Delta 2(\%) = \frac{(n_{SCO_2}^{V_{cap}} - n_{CO_2}^2)}{n_{CO_2}^2} \times 100 \quad (II-30)$$

#### II.3.1.4. Results and discussion

15 capillary samples in pure CO<sub>2</sub> have been successfully fabricated using the line at G2R according to the procedure described above. The samples are listed in table II-5. These samples are observed in microscope, and some samples are measured and quantified of CO<sub>2</sub>-loading. The results of quantification of CO<sub>2</sub> in capillary samples are listed in table II-6.

No.	Description
2010-2-18-1	Studied
2010-2-18-2	Not studied (the pressure is not precisely noted)
2010-2-18-3	Not studied (the pressure is not precisely noted)
2010-2-18-4	Not studied (the pressure is not precisely noted)
2010-2-25-1	Studied
2010-2-25-2	Studied
2010-2-26-1	Studied
2010-2-26-2	Studied
2010-2-26-3	Not studied (capillary is distorted when it is sealed)
2010-2-26-4	Studied
2010-3-5-1	Not studied (the pressure is not precisely noted)
2010-3-5-2	Not studied (the pressure is not precisely noted)
2010-3-5-3	Not studied (the pressure is not precisely noted)
2010-3-12-1	Not studied (little CO <sub>2</sub> is detected in capillary)
2010-3-15-1	Studied

Table II-5 The capillary samples with pure CO<sub>2</sub> successfully fabricated in this study.

No.	$n_{SCO_2}^{V_{cap}}$ (mol)	$n_{CO_2}^1$ (mol)	$n_{CO_2}^2$ (mol)	$\Delta 1$ (%)	$\Delta 2$ (%)	$T_h$ (°C)
2010-2-18-1	7.963E-07	7.957E-07	7.951E-07	0.075	0.151	30.9 (V)
2010-2-25-1	1.428E-07	1.423E-07	1.643E-07	0.358	-13.06	23.0 (V)
2010-2-25-2	4.802E-07	4.749E-07	4.821E-07	1.11	-0.390	30.9 (L)
2010-2-26-1	2.370E-07	2.328E-07	2.686E-07	1.82	-11.76	24.0 (V)
2010-2-26-2	4.194E-07	4.215E-07	4.212E-07	-0.503	-0.428	30.9 (V)
2010-2-26-4*	3.28E-07	3.187E-07	3.301E-07	2.98	-0.560	30.9 (V)
2010-3-15-1	1.702E-07	1.704E-07	2.087E-07	-0.146	-18.46	27.2 (V)

\*This sample spends more time to be stable in pressure.

Table II-6 Results of quantification of CO<sub>2</sub>-loading in capillary samples.

These samples (2-25-1, 2-26-1, 3-15-1) show an important underestimation of the amount CO<sub>2</sub>. For samples with  $T_h$  very close to the critical point, the density of CO<sub>2</sub> inside the capillary estimated from  $T_h$  is correct (figure II-20) because critical point is a characteristic point of CO<sub>2</sub>.

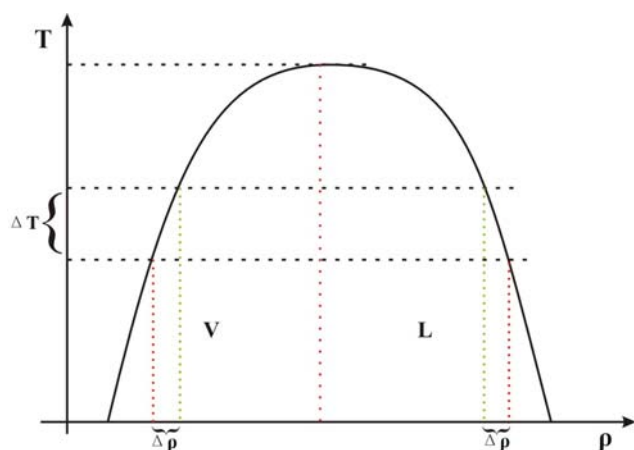


Figure II-20 Sketch of diagram of T- $\rho$  in pure CO<sub>2</sub>.

However, the Linkam stage which is used does not allow verifying whether homogenization has been reached over all of capillary because of the thermal gradients and we are not able to observe the whole capillary: some liquid CO<sub>2</sub> may remain in another part of the capillary. This can be verified using the variation of the Raman intensity with temperature. The intensity of CO<sub>2</sub> peaks changes greatly with a little increasing of temperature near to homogenization temperature.

It is necessary to consider the limitation of maximal density. The density of solid CO<sub>2</sub> is 1.562 g/cm<sup>3</sup>. Thus, if for a 12 mm long capillary 8mm is immersed in liquid N<sub>2</sub> and filled by solid CO<sub>2</sub>, which is a maximum value for sealing the capillary, then the maximum density of CO<sub>2</sub> gas loaded in the capillary will be around 1 g/cm<sup>3</sup>. If the length of the capillary is 20 mm and if 15 mm is filled by solid CO<sub>2</sub>, the maximum resulting density will be near 1.17 g/cm<sup>3</sup>. This high density limit shows that capillary will be suitable for the calibration of water dissolved in dense CO<sub>2</sub> like in deep metamorphic fluids or mantle fluids in xenoliths.

### II.3.1.5. Method for loading CO<sub>2</sub> with H<sub>2</sub>O liquid in silica glass capillary

For the CO<sub>2</sub>-bearing aqueous system, our work also develops the method to load CO<sub>2</sub> with aqueous liquid in the silica glass capillaries. At first, aqueous liquid is loaded into the sealed part of silica glass capillary and is immersed into liquid nitrogen. Then, the open part of silica glass capillary is connected with the system to create vacuum. It is noted that the

vacuum pump is strong enough to sweep all the liquid loaded in silica glass capillary. To avoid to remove the liquid by pumping dynamically, valve b (figure II-18), connecting volume  $V_2$  with vacuum pump, is closed. Then volume  $V_{cap}$  is connected with volume  $V_2$  by switching on valve a (figure II-18). The procedure is repeated two or three times for sweeping off only the air in the silica glass capillary. Finally,  $CO_2$  is loaded in the capillary by condensation of  $CO_2$  gas as the sealed part of silica glass capillary is immersed into liquid  $N_2$  and the silica glass capillary in system  $CO_2$ - $H_2O$ -(NaCl) is sealed under vacuum.

The respective quantifications of  $CO_2$  and aqueous liquid are presented in details as follows.

- Step 1: Quantification of aqueous solution loaded in sealed part of silica glass capillary at room temperature.

$$M_L = \rho_L \times V_L \quad (II-31)$$

where  $M_L$  is the mass of aqueous solution loaded in silica glass capillary,  $\rho_L$  is the density of aqueous solution at room temperature, and  $V_L$  is the volume of aqueous solution loaded in the silica glass capillary using the micrometric stage.

- Step 2: Quantification of  $CO_2$  gas condensed in silica glass capillary (refer to the procedure described in part II.3.1.2.).

The method of quantification of aqueous liquid is verified through measuring the volume of aqueous liquid loaded in silica glass capillary before and after sealing the capillary. Table II-7 shows the results of two samples. The differences between two volumes are calculated as follows.

$$\Delta(\%) = \frac{(V_{H_2O1} - V_{H_2O2})}{V_{H_2O1}} \times 100 \quad (II-32)$$

No.	$V_{H_2O1} (mm^3)$	$V_{H_2O2} (mm^3)$	$\Delta (\%)$
2010-3-15-1	0.015713186	0.016425358	-4.5323226
2010-3-15-2	0.010437933	0.011425031	-9.4568372

$V_{H_2O1}$  and  $V_{H_2O2}$ : Volumes of aqueous liquid loaded in silica glass capillary before and after loading  $CO_2$  and sealing the capillary.

Table II-7 Verification of aqueous liquid loaded in silica glass capillary.



The results indicate that aqueous liquid increases after the condensation of CO<sub>2</sub>. A possible explanation is because of the adherence of H<sub>2</sub>O on the interior surface of the capillary. The metal capillary (1/16 inch inner diameter) and silica glass capillary (100 μm inner diameter) in part V<sub>cap</sub> (figure II-18) are thin. It is very difficult to sweep off H<sub>2</sub>O in these cylindrical capillary at room temperature, but these H<sub>2</sub>O molecules are easily condensed in the silica glass capillary at low temperature when capillary is immersed in liquid nitrogen. The supply of small amount of water during CO<sub>2</sub> filling has been demonstrated during the synthesis of dense CO<sub>2</sub> capillaries. Since, the procedure has been modified after many unsuccessful checks. The final procedure for filling the capillary with CO<sub>2</sub> consisted to connect directly the water-free CO<sub>2</sub> bottle to the stainless steel line and to flow the whole line heated at 120 °C by CO<sub>2</sub>.

### **II.3.2. Synthesis of CO<sub>2</sub>-bearing silica glass capillary by the thermal decomposition of organic acids: oxalic acid and formic acid**

Because of the difficulties of getting quantitative results in the H<sub>2</sub>O-CO<sub>2</sub> system, the use of organic acids decomposing in CO<sub>2</sub> under increasing temperature has been considered. Methods for CO<sub>2</sub>-loading in synthetic fluid inclusions used the thermal decomposition of oxalic acid (H<sub>2</sub>C<sub>2</sub>O<sub>4</sub>) and silver oxalate (Ag<sub>2</sub>C<sub>2</sub>O<sub>4</sub>) (e.g., Holloway et al., 1968; Sterner & Bodnar, 1991; Bakker & Jansen, 1991; Krüger & Diamond, 2001). In our work, formic acid is also used.

#### **II.3.2.1. Oxalic acid as a source of CO<sub>2</sub>**

At ambient temperature, oxalic acid powder is prepared through grinding analytical grade solid H<sub>2</sub>C<sub>2</sub>O<sub>4</sub>. Solutions of oxalic acid at different concentrations are prepared through the analytical-grade H<sub>2</sub>C<sub>2</sub>O<sub>4</sub> (solid) dissolved into pure distilled water, and also the 0.5mol/L oxalic solution is added into the pure distilled water, and another solution is prepared by adding solution of H<sub>2</sub>O<sub>2</sub> (35wt% H<sub>2</sub>O<sub>2</sub> in H<sub>2</sub>O) to the solution of oxalic acid. The addition of H<sub>2</sub>O<sub>2</sub> provides to oxidize CO to CO<sub>2</sub> and to prevent the producing of CH<sub>4</sub>.

Three types of capillaries are fabricated (Table II-8). (1) The oxalic acid powder is directly pushed into the capillary with a thin tungsten rod and sealed into the capillary; (2) The solution of oxalic acid is loaded and sealed into the capillary; (3) The solution of oxalic acid mixed with  $\text{H}_2\text{O}_2$  is loaded and sealed into the capillary in order to oxidize all CO into  $\text{CO}_2$  and  $\text{H}_2$  into  $\text{H}_2\text{O}$ .

No.	Concentration (molality)	Density ( $\text{g}/\text{cm}^3$ )	The capillary before heating				
			$V_l(\text{mm}^3)$	$V_v(\text{mm}^3)$	$M_{oa}(\text{g})$	$n_{oa}(\text{mol})$	$n_w(\text{g})$
3	1.1752m	1.0455	0.01100	0.01975	1.10003e-6	1.22226e-8	1.04008e-5
36	0.5730m	1.0196	0.00964	0.02893	4.81974e-7	5.35526e-9	5.19246e-7
47	0.3000m	1.0110	0.01269	0.02143	3.37208e-7	3.74675e-9	6.93843e-7
48	0.3000m	1.0110	0.01847	0.02724	4.90851e-7	5.45390e-9	1.00998e-6

\* $M_{oa}$  represents the mass of oxalic acid in the capillary;  $n_{oa}$  represents the mole number of oxalic acid in the capillary;  $M_w$  represents the mass of the water in the capillary.

Table II-8 The concentration and the quantity of solutions loaded in capillaries.

In order to obtain the decomposition of oxalic acid, the capillaries firstly are heated in Linkham stage until  $400\text{ }^\circ\text{C}$  during 10-20 minutes and then heated in the oven at  $400\text{ }^\circ\text{C}$  during 10-48 hours. The capillaries are analyzed by microthermometry (Linkham MDS600 heating/freezing stage) and Raman spectroscopy (HORIBA Jobin Yvon LabRAM Raman microprobe).

- The capillary with the powder of oxalic acid

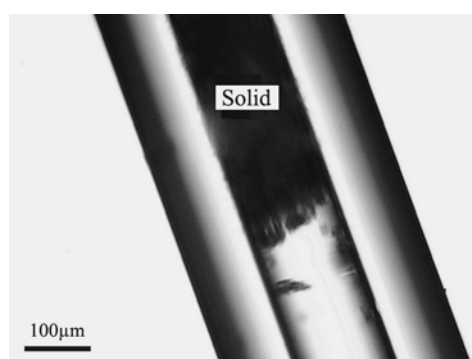


Figure II-21 Microphotograph of the capillary with the oxalic acid solid.

Figure II-21 shows the capillary with the solid of oxalic acid. Firstly, the capillary is heated until 400 °C in Linkam stage in order to decompose the oxalic acid. Secondly, the capillary is heated in the oven at 400°C during 21 hours and at 480°C during 5 hours in order to get complete decomposition of oxalic acid. Three phases are identified under optical microscope in the capillary (figure II-22): two non-colored liquid phases (phase 2 and phase 3) and a vapor phase (phase 1).

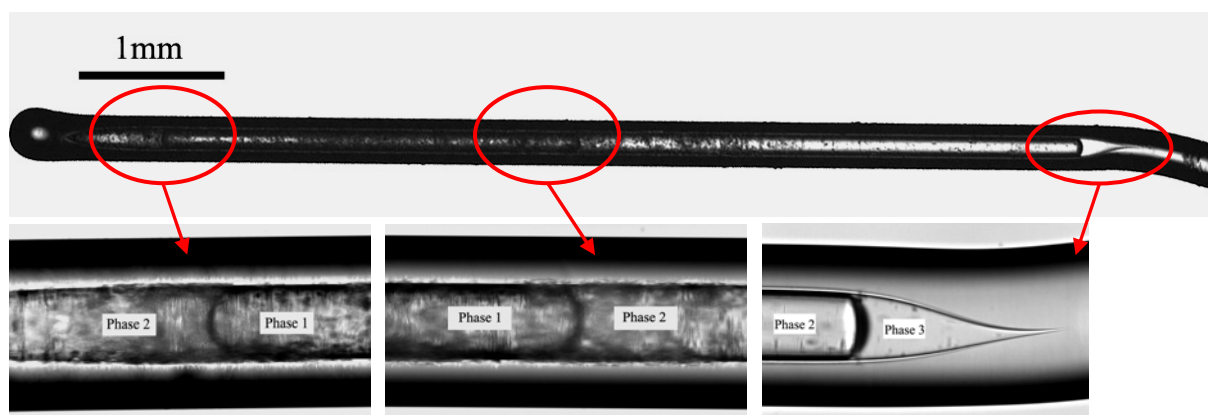


Figure II-22 Microphotographs of the capillary at ambient temperature after heating in the oven. Phase 2 and Phase 3 are two non-colored liquid phases and Phase 1 is vapor phase.

It is worth noting that an unexpected change is observed at the places where solid of oxalic acid was initially located in the capillary before heating. Figure II-23 shows the changes on the interior surface of the capillary. There are clear evidences of corrosion of the glass.

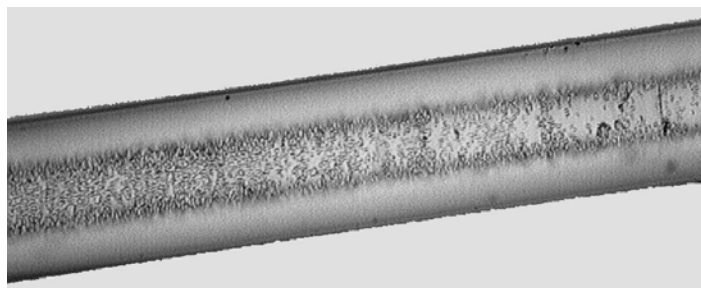


Figure II-23 Changes of interior surface of capillary at ambient temperature after heating in the oven.

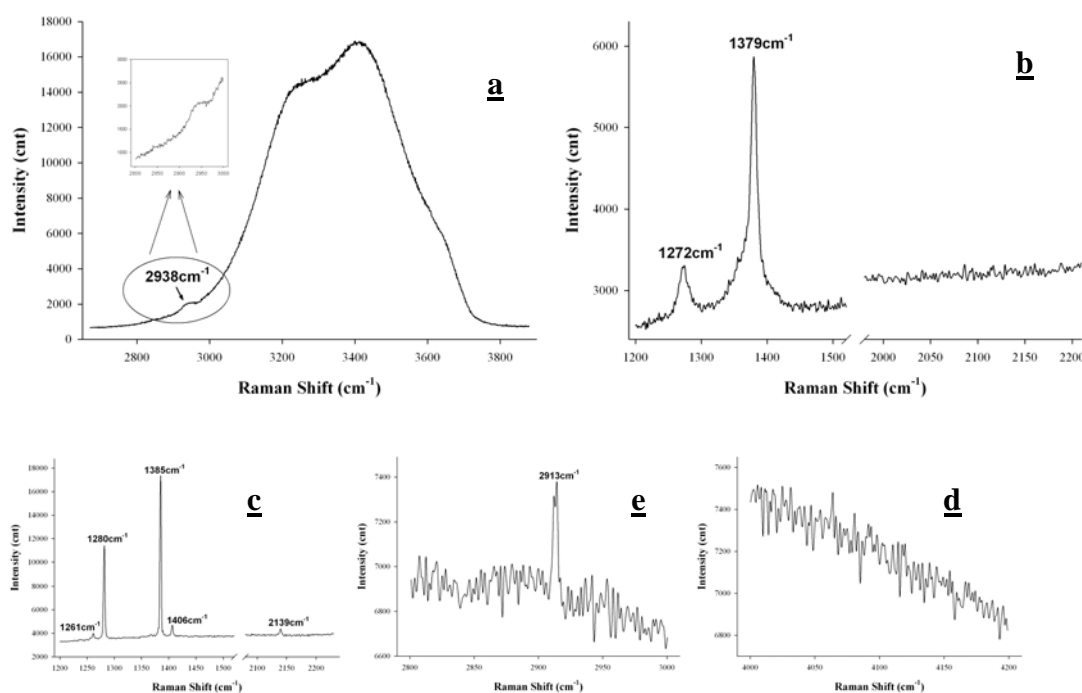


Figure II-24 Raman Spectra collected from the different phases in capillary after heating in the oven. a and b are the spectra of the liquid phase 3; c, d and e are the spectra of the vapor phase1.

Raman spectra are collected for characterizing the co-existing three phases. Figure II-24 (a, b) shows the spectra of the liquid phase 3 with the higher refraction index which is typical of liquid water. In spectral window  $2700 - 3900 \text{ cm}^{-1}$ , there is a broad band between  $3000 \text{ cm}^{-1}$  and  $3700 \text{ cm}^{-1}$  assigned to the stretching vibration band of water and the weak signal ( $2938 \text{ cm}^{-1}$ ) corresponding to CH-stretching vibration (figure II-24a, Walrafen, 1964). This CH stretching band with a rather large width indicates the presence of dissolved hydrocarbon, but it is not defined yet. However there is no evidence of dissolved  $\text{CH}_4$  in the aqueous solution. As the solubility of  $\text{CH}_4$  in water solution decreases with the increase of carbon atom number, this suggests presence of hydrocarbon more soluble than alkane in water. Comparing with the spectra collected on solid of oxalic acid (figure II-25a) and on solution of oxalic acid (figure II-25b) and even on solution of formic acid (figure II-25c), no known reference signal corresponds to the band of  $2938 \text{ cm}^{-1}$ . In the spectral window  $1200 - 2200 \text{ cm}^{-1}$ , there are two notable bands referred to as the  $\nu_1$ - $2\nu_2$  Fermi diad of  $\text{CO}_2$  in aqueous phase with the upper band ( $1379 \text{ cm}^{-1}$ ) and lower band ( $1272 \text{ cm}^{-1}$ ) (figure II-24b, David & Oliver, 1973). Figure II-24 (c, d, e) shows the spectra of the vapour phase 1. In the spectral window  $1200 - 2200 \text{ cm}^{-1}$ ,

there are two intense bands at 1280 and 1385  $\text{cm}^{-1}$  assigned to the  $\nu_1$ - $2\nu_2$  Fermi diad of  $\text{CO}_2$  and two weak bands at 1261 $\text{cm}^{-1}$  and 1406  $\text{cm}^{-1}$  assigned to hot bands of  $\text{CO}_2$  (Dickinson et al., 1929). In addition CO band is identified by its band at 2142  $\text{cm}^{-1}$  (Bergman & Dubessy, 1984; Schrötter & Klöckner, 1979). Spectral widows 2800 - 3000  $\text{cm}^{-1}$  and 4000 - 4200  $\text{cm}^{-1}$  are presented for checking the presence of  $\text{CH}_4$  and  $\text{H}_2$ . The peak (2913  $\text{cm}^{-1}$ ) is assigned to  $\text{CH}_4$  (Schrötter & Klöckner, 1979).  $\text{H}_2$  is not identified. The liquid phase 2 has been also analyzed, but this phase exhibits very high fluorescence under laser excitation preventing to get any Raman signal. By contrast, it is worth noting that spectra collected from solid oxalic acid (figure II-26a) and from dissolved oxalic acid in water (figure II-26b) do not show any fluorescence. This fluorescence indicates the formation at trace level of a highly fluorescent organic compound. By contrasting with the spectra of the vapor phase 1, a low fluorescence level suggests that the fluorescent compounds dissolved in the liquid phase have low volatility and could be heavy hydrocarbons. Finally, as the fluorescent liquid and the vapor homogenize before 30 °C (at 20°C), this liquid phase is probably liquid  $\text{CO}_2$  with some dissolved fluorescent organic compounds.

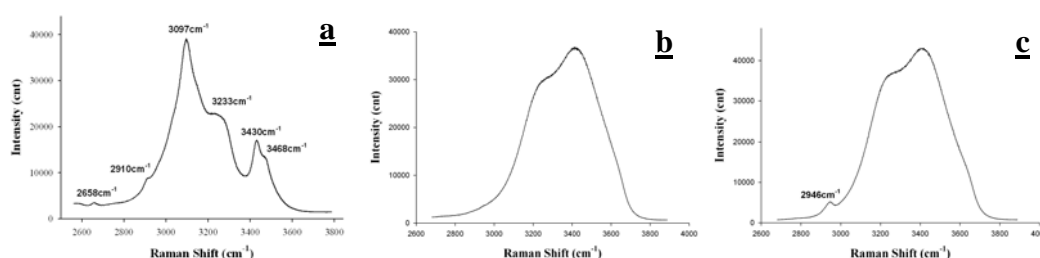


Figure II-25 Raman spectra at ambient temperature in the region of 2600 - 3800 $\text{cm}^{-1}$  collected on (a) solid of oxalic acid and (b) solution of oxalic acid (10g/100ml) and (c) solution of formic acid (1m).

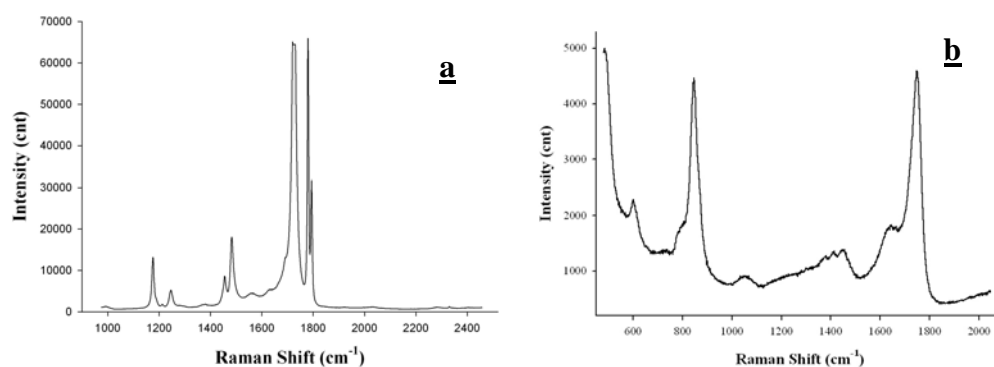


Figure II-26 Raman Spectra in the region of 1000 - 2000  $\text{cm}^{-1}$  collected on solid of oxalic acid (a) and solution of oxalic acid (10g/100ml) (b).

Estimation of the bulk composition of the fluid is carried out considering the volume and density of the aqueous phase and  $\text{CO}_2$  at homogenization temperature. Result is the following:  $\text{H}_2\text{O} = 8$  mole% and  $\text{CO}_2 = 92$  mole%. The thermal decomposition of oxalic acid is described by the reaction:



$\text{H}_2$  is not identified in the vapour phase by Raman spectroscopy. The addition of  $\text{H}_2$  into  $\text{H}_2\text{O}$  produces CO according to the reaction:



The first reaction shows that 1 mole of  $\text{H}_2\text{C}_2\text{O}_4$  gives one mole of  $\text{H}_2$  and 2 moles of  $\text{CO}_2$ . If only  $x$  moles of  $\text{H}_2$  react with  $x$  moles of  $\text{CO}_2$  according to the second reaction, the final composition of the system will be:  $(1-x)$  moles of  $\text{H}_2$ ;  $(2-x)$  moles of  $\text{CO}_2$ ,  $x$  moles of CO and  $x$  moles of  $\text{H}_2\text{O}$ . From the concentration of CO in the vapor phase  $x/(2-x) = 0.07$ , we can deduce  $x$  and thus the  $\text{H}_2\text{O}/\text{CO}_2$  ratio  $= x/(2-x) = 0.075$  which agrees with the measured ratio. Therefore, all the  $\text{H}_2$  produced by the thermal decomposition of oxalic acid did not react with  $\text{CO}_2$ . The explanation of this feature lies in the kinetics of this redox reaction which is not fast enough compared to the  $\text{H}_2$  diffusion out of the capillary through the silica glass. Shang et al. (2009) has demonstrated that  $\text{H}_2$  diffuse very rapidly above 300 °C.

Finally, the corrosion of glass by the acid fluid before the end of the thermal decomposition is not favorable neither for optical observation, neither for Raman analysis. In addition the high fluorescence in the  $\text{CO}_2$  liquid phase is not also favorable for collecting Raman spectra.

#### - Capillary with the oxalic acid aqueous solution

The solutions of the oxalic acid are prepared with the solid oxalic acid (99.99% purity). The concentrations are shown in table II-8. The solutions of oxalic acid are respectively loaded and sealed into the capillaries. The capillaries are heated within the microthermometric stage and in an oven in order to decompose the oxalic acid and liberate  $\text{CO}_2$ . The capillary is

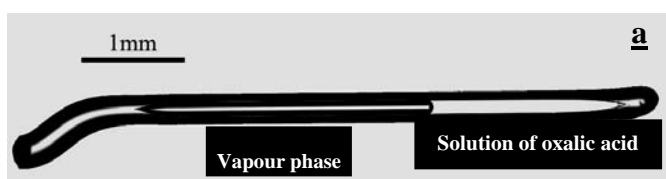
observed under the optical microscope (OLYMPUS<sup>®</sup> petrographic microscope) and the dissociation of the solution of oxalic acid in capillary is analyzed by the combination of the microthermometric stage (Linkam<sup>®</sup> heating/freezing stage) and the Raman microprobe (Jobin Yvon<sup>®</sup>).

## Experiments

The capillary containing the solution of oxalic acid showed in figure II-27a. There is the non-colored liquid phase with the highest refraction index, which is the solution. The quantity of the solution sealed into the capillary is calculated by measuring the volume of the liquid phase in capillary by the microscope equipped with the micrometric stage. The reading is until 1 $\mu$ m and the accuracy of the measurement is identified by the experiments that the total length is less than 1% and the total volume is less than 2% (table II-9). The mass of the solution ( $M$  in g) in capillary is calculated as follows.

$$M = \rho * V \quad (\text{II-35})$$

Where  $\rho$  is the density of the solution in  $\text{g}/\text{cm}^3$  referring to Kandpal et al. (2007) and  $V$  is the volume of the solution in capillary in  $\text{cm}^3$ . The quantities of the solution in capillaries are showed in table II-8. All the capillaries are heated to liberate  $\text{CO}_2$  using a two step procedure. At first, the capillaries are heated in the microthermometric stage from room temperature to 400 $^\circ\text{C}$  and stabilized at 400  $^\circ\text{C}$  during 10-20 min. Figure II-27b shows the capillary after heating in the microthermometric stage, where dark vapor phase and non-colored liquid phase co-exist. Then the capillaries are heated in an oven at 400  $^\circ\text{C}$  during several hours (details given below). A photograph is shown in figure II-27c. No distinct optical differences (color, refractive index, ...) from figure II-27b is observed, where there co-exist vapor phase and liquid phase.



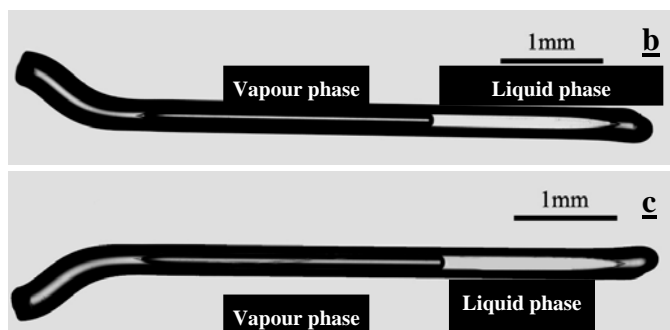


Figure II-27 Microphotographs of the capillary 47 at ambient temperature. a. before microthermometry, b. after microthermometry, c. after heating in the oven at 400 °C lasting 10 hours.

No.	BH				AHMS				AHO				LRSD	VRSD
	LT (mm)	VT (mm <sup>3</sup> )	V <sub>l</sub> (mm <sup>3</sup> )	V <sub>v</sub> (mm <sup>3</sup> )	LT (mm)	VT (mm <sup>3</sup> )	V <sub>l</sub> (mm <sup>3</sup> )	V <sub>v</sub> (mm <sup>3</sup> )	LT (mm)	VT (mm <sup>3</sup> )	V <sub>l</sub> (mm <sup>3</sup> )	V <sub>v</sub> (mm <sup>3</sup> )		
3	4.926	0.03075	0.01100	0.01975	4.949	0.03137	0.01092	0.02045	4.936	0.03162	0.00860	0.02302	0.5%	2.8%
36	5.554	0.03857	0.00964	0.02893	5.563	0.03873	0.00945	0.02928	5.553	0.03870	0.00864	0.03006	0.2%	0.4%
47	4.904	0.03411	0.01269	0.02142	4.910	0.03371	0.01203	0.02168	4.905	0.03400	0.01161	0.02239	0.1%	1.2%
48	6.334	0.04571	0.01847	0.02724	6.345	0.04561	0.01807	0.02754	6.352	0.04582	0.01722	0.02860	0.3%	0.5%

\*BH : “before heating”; AHMS : after heating in the microthermometric stag; AHO : after heating in the oven; LT : total length of phases in capillary; VT: total volume of phases in capillary; V<sub>l</sub>: volume of liquid phase in capillary; V<sub>v</sub>: the volume of vapor phase in capillary; LRSD: the relative difference in length; VRSD is the relative difference in volume.

Table II-9 Measurements of phase volumes in capillary by micrometric stage.



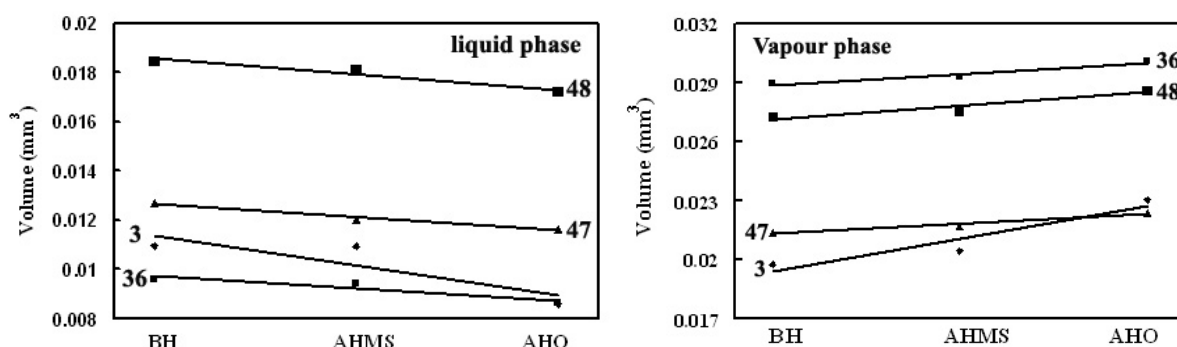


Figure II-28 The changes of volume of each phase in the capillary. The volume of the liquid phase decreases after heating and the volume of the vapour phase increases after heating.

### Raman spectra

- Before heating

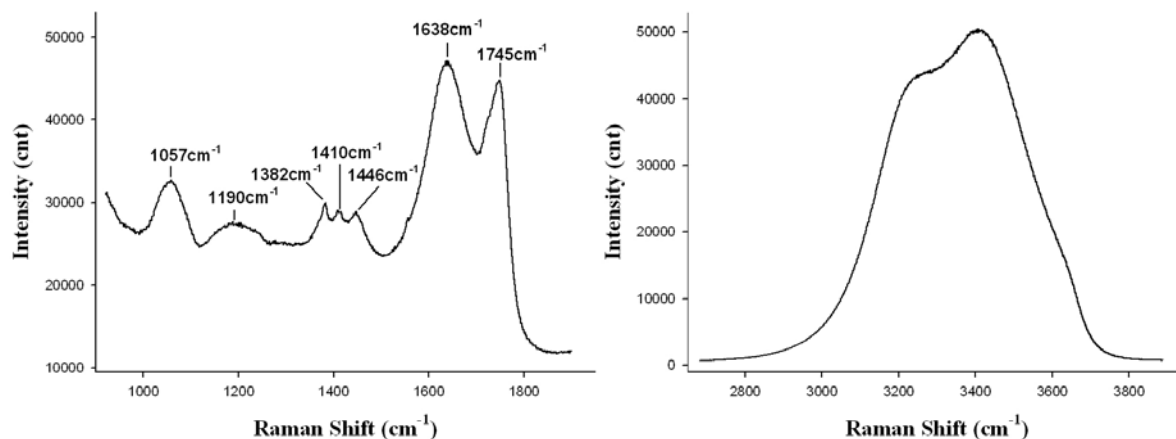


Figure II-29 The Raman spectra of solution of oxalic acid at ambient temperature. 1057 cm⁻¹ and 1190 cm⁻¹: silica glass. 1638 cm⁻¹: H₂O bending mode. 1382 cm⁻¹, 1410 cm⁻¹, 1446 cm⁻¹, and 1745 cm⁻¹: the characteristics of the aqueous oxalic acid. 2800 - 3800 cm⁻¹ region: O-H stretching of molecular H₂O.

At first, Raman spectra are collected from the liquid phase in capillary before heating. For comparing the spectra of the products of the decomposition of the solution of the oxalic acid, the Raman spectra of the 1000 - 4200 cm⁻¹ region are collected. The bands are observed in the Raman spectra of the 1000 - 1900 cm⁻¹ region and of the 2800 - 3800 cm⁻¹ region showed in figure II-29. In the 1000 - 1900 cm⁻¹ region, seven recognizable bands are observed.

The bands  $1057\text{ cm}^{-1}$  and  $1190\text{ cm}^{-1}$  are the characteristics of the silica glass (the capillary tube) (McMillan et al., 1982). The band  $1638\text{ cm}^{-1}$  is assigned to the  $\text{H}_2\text{O}$  bending mode (Walrafen, 1964). The other bands at  $1382\text{ cm}^{-1}$ ,  $1410\text{ cm}^{-1}$ ,  $1446\text{ cm}^{-1}$ , and  $1745\text{ cm}^{-1}$  correspond to the characteristics of the aqueous oxalic acid (referring to study of Raman spectroscopy of natural oxalates by Frost et al., 2003).

In the  $2800\text{--}3800\text{ cm}^{-1}$  region, only the broad band of O-H stretching of molecular  $\text{H}_2\text{O}$  exists (Walrafen, 1964).

- After heating in the microthermometric stage ( $400\text{ }^\circ\text{C}$  during 10-20 mn)

Secondly, Raman spectra of the vapor phase and liquid phase after heating in the microthermometric stage are collected at room temperature. Several clear bands with rather small width are identified in Raman spectra of the  $1000\text{--}4200\text{ cm}^{-1}$  region (figure II-30). In the  $1200\text{--}1500\text{ cm}^{-1}$  region, there exist two strong  $\text{CO}_2$  lines (upper band:  $1387\text{ cm}^{-1}$ , lower band:  $1284\text{ cm}^{-1}$ ) referred to as  $\nu_1\text{--}2\nu_2$  Fermi resonance (Gordon & McCubbin, 1966) and two hot bands of  $\text{CO}_2$  at  $1264\text{ cm}^{-1}$  and  $1408\text{ cm}^{-1}$  (Dickinson et al., 1929) and a very weak band of the isotopic splitting due to the presence of  $^{13}\text{CO}_2$  (Howard-Lock & Stoicheff, 1971). In the  $1000\text{--}4200\text{ cm}^{-1}$  region, except the bands of  $\text{CO}_2$ , there are band  $2141\text{ cm}^{-1}$  which is characteristic of gas  $\text{CO}$  and bands  $4125\text{ cm}^{-1}$ ,  $4143\text{ cm}^{-1}$ ,  $4155\text{ cm}^{-1}$  and  $4161\text{ cm}^{-1}$  which correspond to gas  $\text{H}_2$ . The signals of  $\text{CO}$  and  $\text{H}_2$  are much weaker than the bands of  $\text{CO}_2$ .

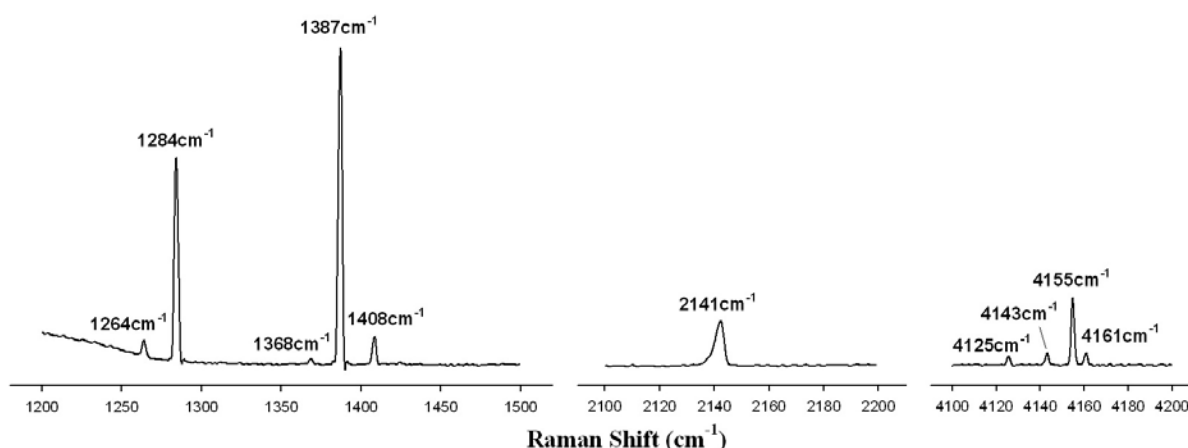


Figure II-30 The Raman spectra of vapour phase in capillary after heating in the microthermometric stage. Bands  $1284\text{ cm}^{-1}$  and  $1387\text{ cm}^{-1}$ :  $\nu_1\text{--}2\nu_2$  Fermi resonance of  $\text{CO}_2$ . Bands  $1264\text{ cm}^{-1}$  and  $1408\text{ cm}^{-1}$ : hot bands of  $\text{CO}_2$ . Bands  $1368\text{ cm}^{-1}$ : the isotopic splitting of

CO<sub>2</sub> due to the presence of <sup>13</sup>CO<sub>2</sub>. Bands 1241cm<sup>-1</sup>: the characteristic of CO. Bands 4125 cm<sup>-1</sup>, 4143 cm<sup>-1</sup>, 4155 cm<sup>-1</sup> and 4161 cm<sup>-1</sup>: the characteristics of H<sub>2</sub>.

The Raman spectrum of the 3000-3800cm<sup>-1</sup> region of the O-H stretching vibration of molecular water collected from the vapor phase at ambient temperature is given in figure II-31. Three overlapped bands are identified in 3500-3800cm<sup>-1</sup> region. Band at 3653 cm<sup>-1</sup> is characteristic of the intramolecular O-H stretching vibration of water in vapor phase. Band at 3672 cm<sup>-1</sup> is suggested to be the SiO-H stretching feature for SiO<sub>2</sub> glass containing water (Hess et al., 1986). Band at 3604cm<sup>-1</sup>, discovered by Hess et al. (1986), is suggested to be one type of OH group with highly symmetric mode present in high-water-content hydrous SiO<sub>2</sub> glass. This indicates that some water diffuses into the glass capillary tube. This could explain the decrease in volume of the liquid phase.

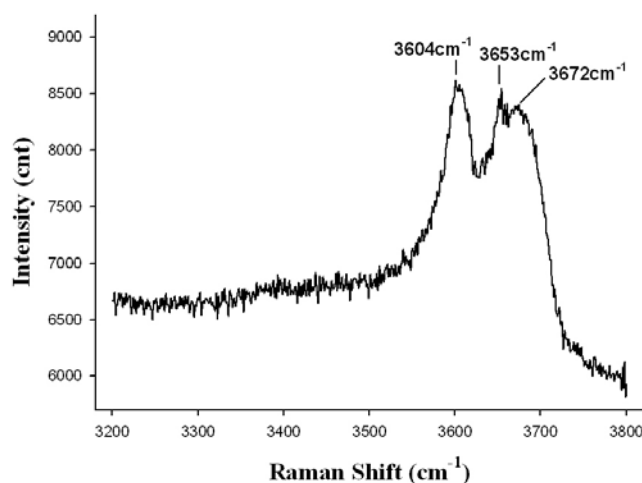


Figure II-31 The Raman spectra of the O-H stretching region of water collected on the vapour phase in capillary after heating in the microthermometric stage. Band at 3653 cm<sup>-1</sup>: intermolecular O-H stretching vibration of water. Band at 3672cm<sup>-1</sup>: SiO-H stretching feature. Band at 3604cm<sup>-1</sup>: one type of OH group.

Figure II-32 shows the Raman spectra of the liquid phase in capillary after heating in the microthermometric stage. In comparison with the Raman spectra of the 1000-4200 cm<sup>-1</sup> region collected on liquid oxalic acid, the bands characteristic of silica glass and water are still present. However, the bands of the aqueous oxalic acid disappear, and two bands at 1272

$\text{cm}^{-1}$  and  $1380\text{ cm}^{-1}$  are observed: they correspond to  $\text{CO}_2$  dissolved in water and indicate the content of  $\text{CO}_2$  in capillary is high.

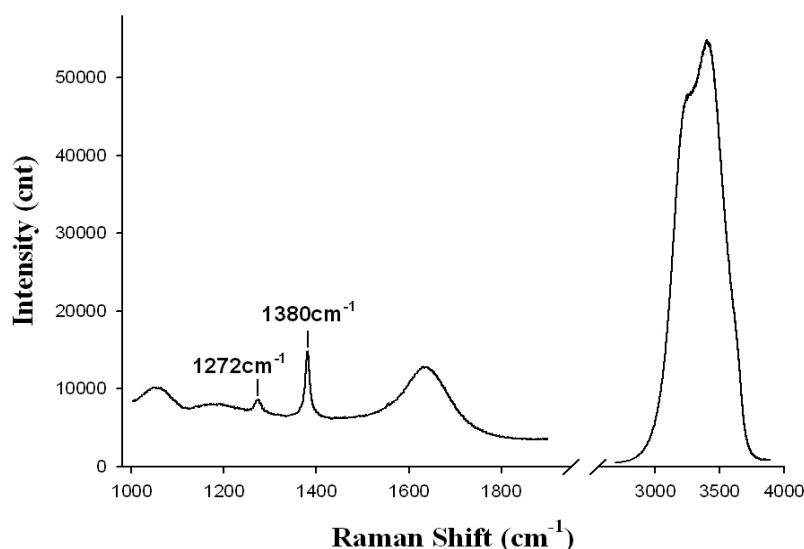
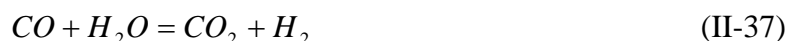
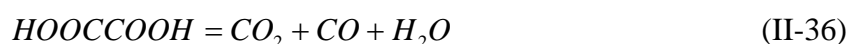


Figure II-32 The Raman spectra collected on the liquid phase in capillary after heating in the microthermometric stage at  $400^\circ\text{C}$  during 10-20 mn. Bands  $1273\text{ cm}^{-1}$  and  $1381\text{ cm}^{-1}$ : characteristic of  $\text{CO}_2$  dissolved in water.  $1500\text{ cm}^{-1}$ - $1800\text{ cm}^{-1}$ : bending mode of water.  $2800\text{ cm}^{-1}$ - $3800\text{ cm}^{-1}$ : stretching mode of water.

The results of Raman analysis of the capillary after heating in the microthermometric stage indicates that no oxalic acid is detected in capillary after heating until  $400^\circ\text{C}$  (10-20 min). Furthermore, the oxalic acid solution is thermally decomposed and  $\text{CO}_2$  is the main product of this decomposition. Reaction (II-36) expresses the decomposition of the oxalic acid. Reaction (II-37) is considered because of the presence of  $\text{H}_2$  and low concentration of  $\text{CO}$ .



- After heating in the oven

Finally, the Raman spectra of the vapour phase and liquid phase in the capillaries are collected at room temperature after heating in the oven at  $400^\circ\text{C}$  for different heating times. The capillaries are heated in the oven at  $400^\circ\text{C}$  lasting different period of time. All the Raman

spectra of the 1000-4200  $\text{cm}^{-1}$  region of the vapor phase show the absence of CO and  $\text{H}_2$  and an intense signal of  $\text{CO}_2$  (figure II-33). Therefore, CO is oxidized to  $\text{CO}_2$  by the reaction (II-37) which is shifted towards the right side by the diffusion out of  $\text{H}_2$  from the fused silica capillary tube (Williams & Ferguson, 1922).

The heating time in the oven is different for the capillaries with different concentrations:

1. The capillaries with low content of oxalic acid (sample 47 and 48) have the Raman spectra without the characteristics of CO and  $\text{H}_2$  after heating in the oven lasting 10 hours.
2. The capillary with modest content of oxalic acid (sample 36) is heated in the oven twice. The duration of the first time is 10 hours and CO and  $\text{H}_2$  are still identified in Raman spectra. The duration of the second time is 36 hours and CO and  $\text{H}_2$  can not be identified in Raman spectra. Figure II-34 shows the changes of the bands of  $\text{CO}_2$ , CO and  $\text{H}_2$  collected from the vapor phase with increasing heating time. The intensity of  $\text{CO}_2$  bands increases, but the intensity of CO and  $\text{H}_2$  decreases, a feature is consistent with reaction (II-37) and the diffusion out of  $\text{H}_2$ . Table II-10 shows the changes of intensities of Fermi resonance bands of  $\text{CO}_2$  of the vapor phase and of the aqueous liquid phase.
3. The capillary with high content of oxalic acid (sample 3) is heated in the oven during 64 hours. Nor CO neither  $\text{H}_2$  are identified in the Raman spectra. A band located at 2918  $\text{cm}^{-1}$  is, assigned to the C-H symmetric stretching band ( $\nu_1$ ) of  $\text{CH}_4$  (figure II-35) blue line). It indicates that the reaction (II-38) took place.



The capillary is heated again in the oven at 400°C, but the signal of  $\text{CH}_4$  is still present after 20 hours (figure II-35 red line).

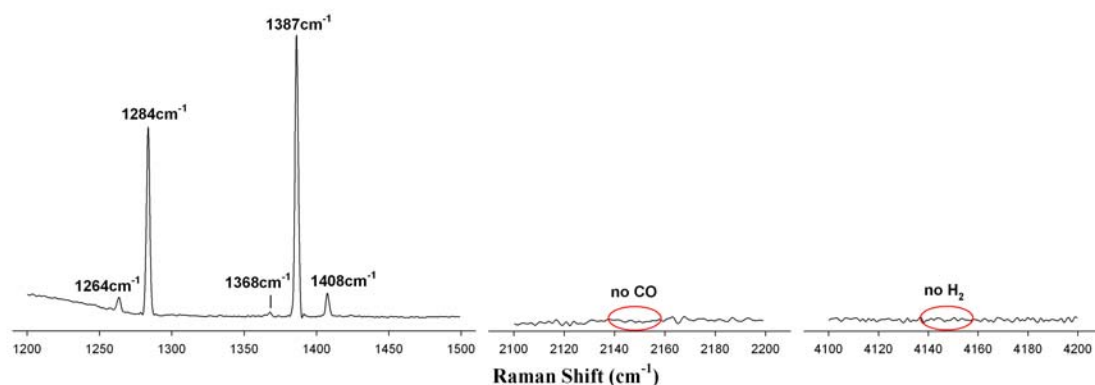


Figure II-33 The Raman spectra collected on the vapour phase in capillary after heating in the oven at 400°C. In 1200-1500 $\text{cm}^{-1}$  region: characteristic of  $\text{CO}_2$ . In 2100-2200 $\text{cm}^{-1}$  region: no characteristic of CO. In 4100-4200 $\text{cm}^{-1}$  region: no characteristic of  $\text{H}_2$ .

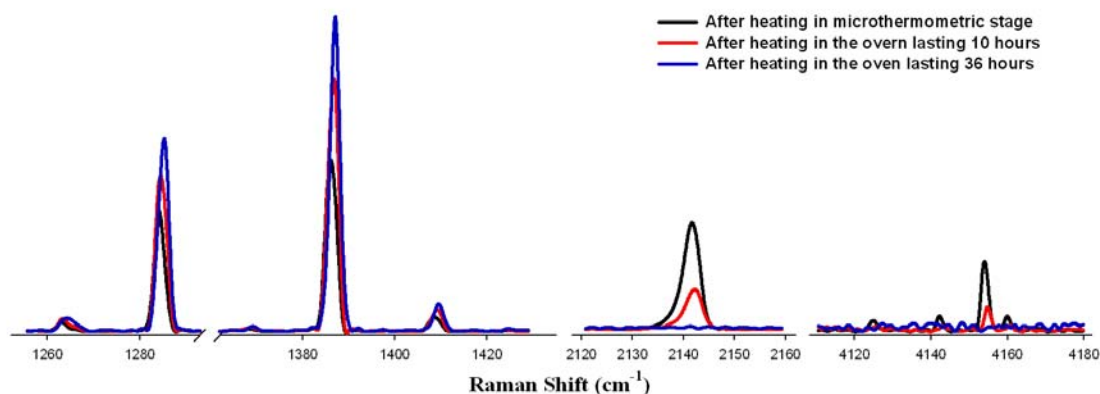


Figure II-34 Raman spectra of the vapor phase in capillary 36 (0.573 molal oxalic acid) after different heating times. With the increasing of heating time, the intensity of  $\text{CO}_2$  bands increases and the intensity of bands of CO and  $\text{H}_2$  (respectively in 2120-2160  $\text{cm}^{-1}$  region and 4110-4180  $\text{cm}^{-1}$  region) decreases versus heating time.

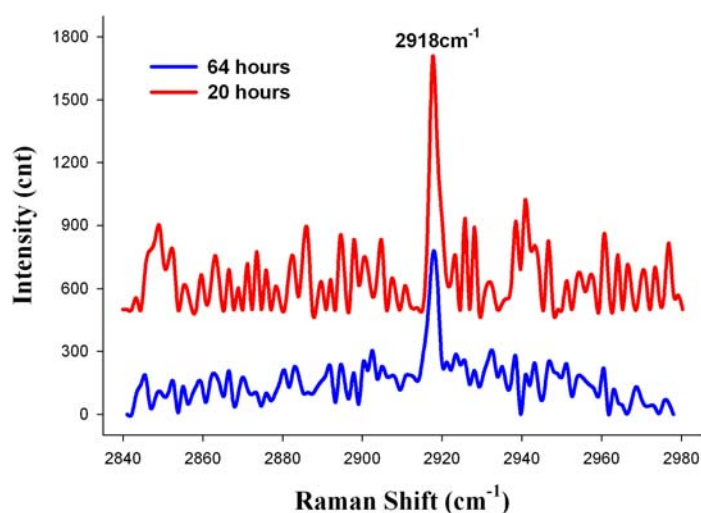


Figure II-35 The Raman spectra of  $\text{CH}_4$  collected at ambient temperature on the vapor phase in capillary 3 (1.175 molal oxalic acid) after heating in the oven. The intensity of band  $\text{CH}_4$  is enhanced with the increasing of heating duration (Blue line: the duration of first heating is 64 hours, red line: the duration of second heating is 20 hours).

Phase	I(BM)/I(AHO36)		I(AHO10)/I(AHO36)	
	1387cm <sup>-1</sup>	1284cm <sup>-1</sup>	1387cm <sup>-1</sup>	1284cm <sup>-1</sup>
Liquid	0.640	0.636	0.823	0.829
Vapour	0.510	0.635	0.778	0.764

\*AHM:After heating in microthermometric stage; AHO10:After heating in the oven lasting 10 hours; AHO36: After heating in the oven lasting 36 hours

Table II-10 The changes of intensities of bands of Fermi resonance (CO<sub>2</sub>) on vapour phase and on liquid phase.

Figure II-36 shows the Raman spectra of the aqueous liquid phase in capillary after heating in the oven. The bands characteristics of CO<sub>2</sub> dissolved in water and liquid H<sub>2</sub>O in the Raman spectra of the 1000-4200 cm<sup>-1</sup> region are identified. The intensities of bands of CO<sub>2</sub> increases versus heating time (figure II-37 and table II-10), which indicates that the quantity of CO<sub>2</sub> increases, that is the advance of the reaction (II-37).

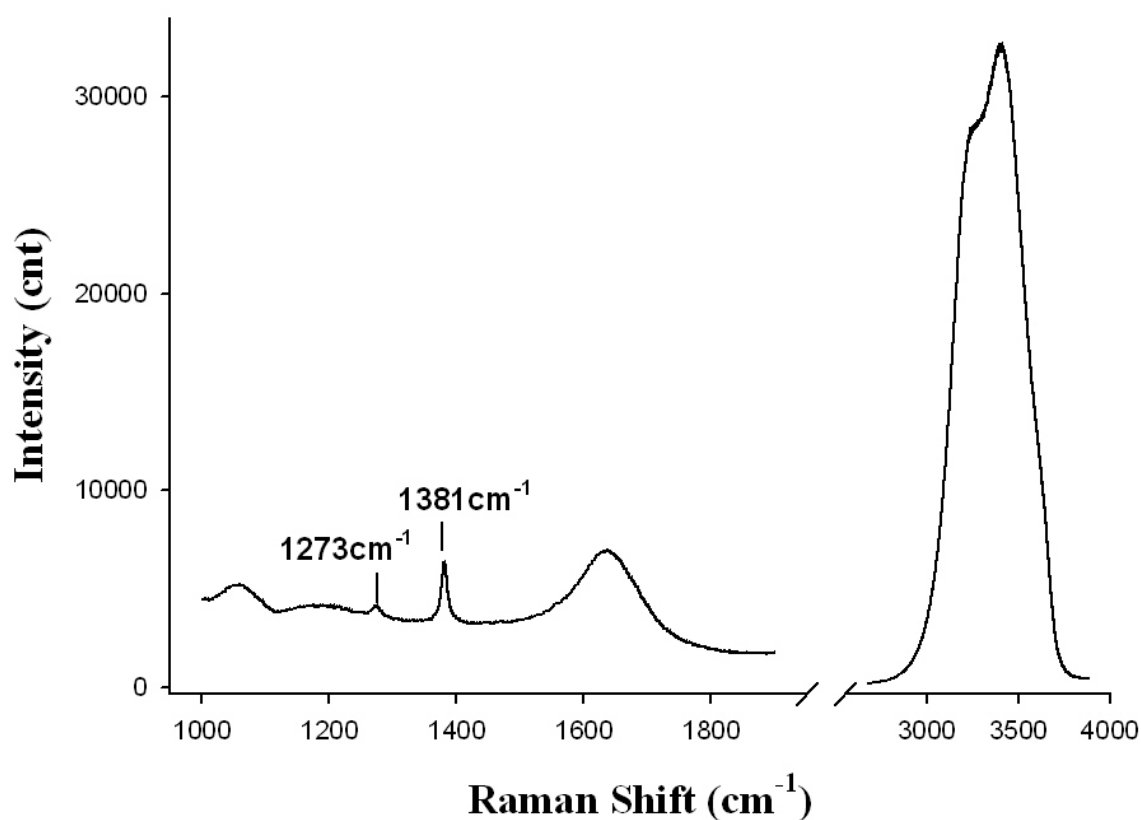


Figure II-36 The Raman spectra collected on the liquid phase in capillary 36 after heating in the oven. Bands  $1273\text{cm}^{-1}$  and  $1381\text{cm}^{-1}$ : characteristic of  $\text{CO}_2$  dissolved in water.  $1500\text{cm}^{-1}$ - $1800\text{cm}^{-1}$ : bending mode of water.  $2800\text{cm}^{-1}$ - $3800\text{cm}^{-1}$ : stretching mode of water.

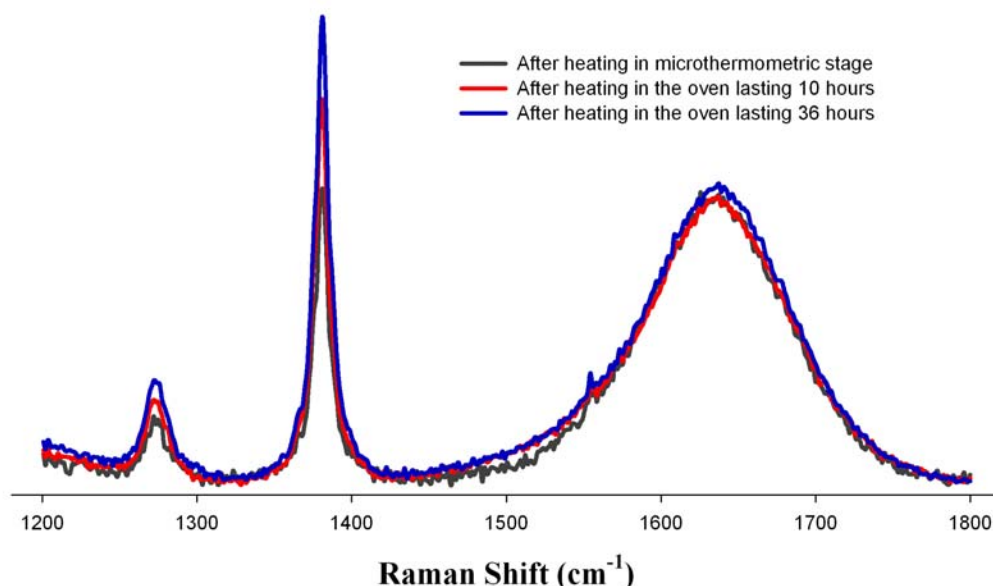


Figure II-37 Raman spectra of the aqueous phase in capillary 36 after different heating times. With the increasing of heating duration, the intensity of bands of dissolved  $\text{CO}_2$  (in  $1260$ - $1420\text{cm}^{-1}$  region) is enhanced and the bending band of water does not change.

Raman analysis of the capillary after heating in the oven indicates the diffusion of  $\text{H}_2$  out of the silica glass tube and the oxidation of  $\text{CO}$  to  $\text{CO}_2$  according to reaction (II-37). The rate of  $\text{CO}$  oxidation is limited both by the diffusion rate of  $\text{H}_2$  and probably also by the kinetics of the reaction itself. The presence of  $\text{H}_2$  at rather high concentration contributes probably to the reduction of  $\text{CO}$  into  $\text{CH}_4$  by reaction (II-38).

#### Quantification of $\text{CO}_2$ and $\text{H}_2\text{O}$ in capillary

- At room temperature

After heating in the oven, the chemistry of the chemical system can be described mainly in the system  $\text{H}_2\text{O}$ - $\text{CO}_2$ . Figure II-38 shows the capillary at room temperature. Two phases



coexist, the aqueous phase with dissolved CO<sub>2</sub> and the vapour phase of approximately pure CO<sub>2</sub>.



Figure II-38 Schematic of capillary at room temperature.

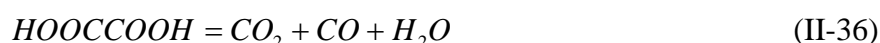
The mole number of CO<sub>2</sub> in capillary includes the mole number of CO<sub>2</sub> in vapor phase and of CO<sub>2</sub> dissolved in aqueous phase. For H<sub>2</sub>O, the mole number of H<sub>2</sub>O in aqueous phase is considered as the mole number of H<sub>2</sub>O because H<sub>2</sub>O in vapor phase is neglectable at room temperature:

$$n_{CO_2} = n_{CO_2}^v + n_{CO_2}^{aq} \quad \text{and} \quad n_{H_2O} = n_{H_2O}^v + n_{H_2O}^{aq} = n_{H_2O}^{aq}$$

1. H<sub>2</sub>O in capillary is able to be quantified as follows.

Two steps are possible for determining the mole number of H<sub>2</sub>O.

i. Provided the oxidation of CO to CO<sub>2</sub> is total, the H<sub>2</sub>O mole number does not change during the decomposition of oxalic acid (see reaction (II-36) and (II-37)) since each mole of produced water is consumed by each mole of produced CO.



Thus, the mole number of H<sub>2</sub>O equals to the mole number of H<sub>2</sub>O in the solution of oxalic acid in capillary before heating.

The mole number of H<sub>2</sub>O in aqueous phase ( $n_{H_2O}^{aq}$ ) can be calculated through the equation (II-39) which is deduced by equations (II-40), (II-41), (II-42) and (II-43), where  $\rho_{oa}$  is the density of solution of oxalic acid,  $V_{(0,aq)}$  is the volume of the solution of oxalic acid in capillary and is measured by micrometric stage,  $M_{H_2O}^{aq}$  is the mass of H<sub>2</sub>O in the solution,

$\overline{M}_{H_2O}$  is the molar mass of H<sub>2</sub>O,  $m_{oa}$  is the molality of solution,  $M_{oa}$  is the mass of solution and  $C_{H_2O}$  is the percentage concentration of H<sub>2</sub>O in solution of oxalic acid.

$$n_{H_2O}^{aq} = \rho_{oa} * V_{(0,aq)} * \frac{1000}{1000 + m_{oa} * \overline{M}_{oa}} * \frac{1}{\overline{M}_{H_2O}} \quad (II-39)$$

$$n_{H_2O}^{aq} = \frac{M_{H_2O}^{aq}}{\overline{M}_{H_2O}} \quad (II-40)$$

$$M_{H_2O}^{aq} = (M_{oa} + M_{H_2O}^{aq}) * C_{H_2O} \quad (II-41)$$

$$M_{oa} + M_{H_2O}^{aq} = \rho_{oa} * V_{(0,aq)} \quad (II-42)$$

$$C_{H_2O} = \frac{1000}{1000 + m_{oa} * \overline{M}_{oa}} * 100\% \quad (II-43)$$

ii. After the decomposition of oxalic acid,  $n_{H_2O}^{aq}$  can be calculated with equation (II-45) which is deduced from equations (II-40) and (II-45)

$$n_{H_2O}^{aq} = \frac{\rho_{H_2O}^{aq} \cdot V_{(1,aq)}}{\overline{M}_{H_2O}} \quad (II-44)$$

$$M_{H_2O}^{aq} = \rho_{H_2O}^{aq} \cdot V_{(1,aq)} \quad (II-45)$$

where  $\rho_{H_2O}^{aq}$  is the density of H<sub>2</sub>O in the aqueous phase at room temperature (refer to <http://webbook.nist.gov/chemistry/fluid/>).  $V_{(1,aq)}$  is the volume of the aqueous phase in capillary and is measured by micrometric stage. Results are provided in table II-11.

No.	BH(mol)	AH(mol)	$\Delta(\%)$
36	5.19e-07	3.45e-07	-40.23
47	6.93e-7	6.21e-7	-11.00
48	1.01e-6	9.090e-7	-10.51

\*BH: Before heating; AH: After heating;  $\Delta$ : Relative variation with respect to initial H<sub>2</sub>O content after heating experiment.

Table II-11 The changes of H<sub>2</sub>O mole numbers in capillary.

Results in table II-11 show that the loss of water during experiments. One possible explanation is that water enters into the silica tube. Figure II-39 is the microphotographs of

capillary 36 before heating and after heating in the oven. There are serious changes on silica tube of capillary 36. The interior surface of silica tube becomes corroded.

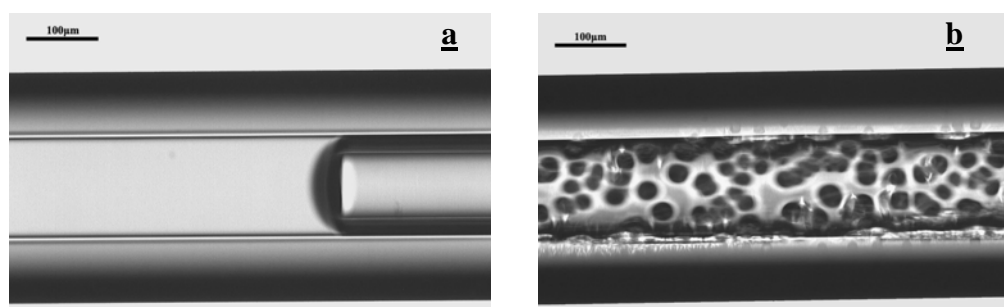


Figure II-39 Microphotographs of capillary 36. a. before heating, b. after heating in the oven.

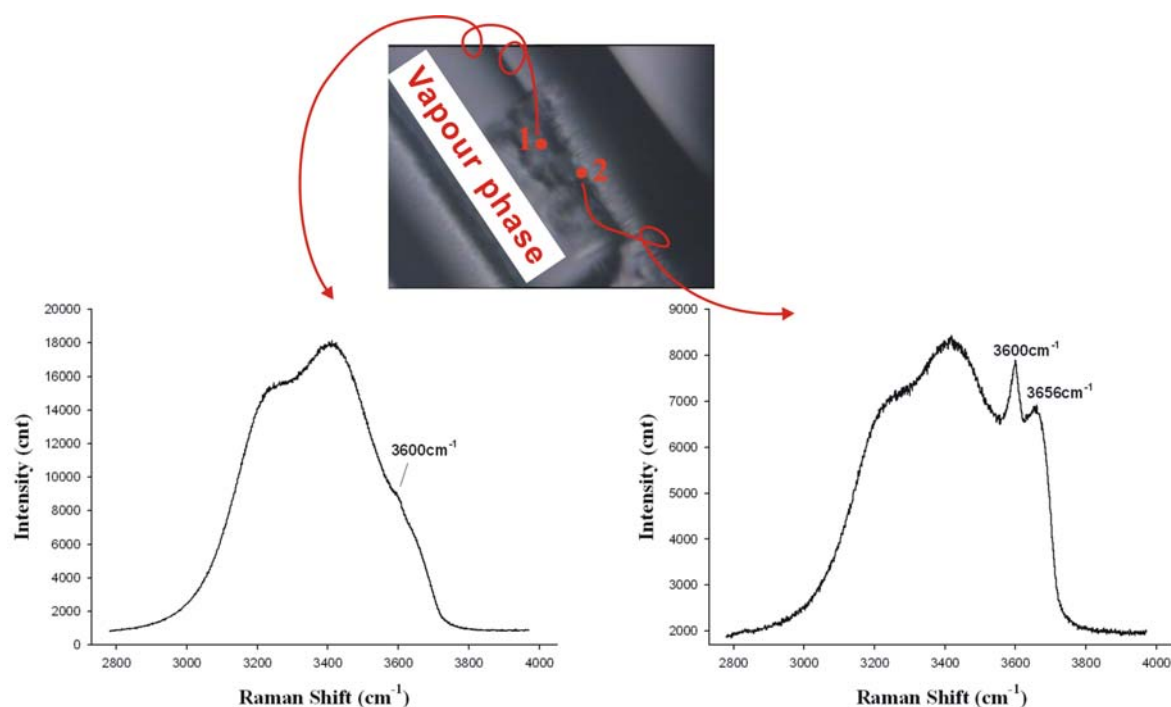


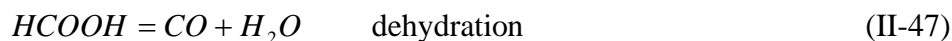
Figure II-40 Raman spectra collected on the changes in silica tube.

Raman spectra of the inner surface of the silica glass tube are collected in order to characterize the evolution of the glass-solution interface (figure II-40). In the 2800-4000  $\text{cm}^{-1}$  region, the O-H stretching vibration of liquid water is identified both a locations 1 and 2. This indicates the presence of a film of liquid water wetting the vapor-glass interface. The spectrum collected in location 2, displays a weaker OH stretching band of liquid water and more importantly a band of 3600  $\text{cm}^{-1}$ , typical of OH stretching in the silica glass. It is worth

noting that shoulder was also noted in the spectrum collected in location 1. Therefore, water diffused into the silica tube.

### II.3.2.2. Formic acid as a source of CO<sub>2</sub>

Formic acid (HCOOH) is the simplest carboxylic acid, the decomposition of which in gas phase and in aqueous phase has been studied both experimentally and theoretically (Blake & Hinshelwood, 1960; Saito et al., 1984; Bjerre & Sørensen, 1992; Yu & Savage, 1998; Akiya & Savage, 1998). Previous studies reported that decarboxylation (II-46) and dehydration (II-47) exist at the same time as the thermal decomposition of formic acid in both phases. At high temperature, CO is oxidized to CO<sub>2</sub> (see the reaction (II-48)) and the gas of H<sub>2</sub> escapes from the capillary. So formic acid is chosen for getting the capillary with CO<sub>2</sub>-bearing system. To obtain full oxidation of CO to CO<sub>2</sub> (see reaction (II-49)), hydrogen peroxide (H<sub>2</sub>O<sub>2</sub>) is added.



### Experimental methods

All the solutions are prepared by 98%wt HCOOH aqueous solution and 35%wt H<sub>2</sub>O<sub>2</sub> aqueous solution and demineralized and deionized water. Additional solutions in system CO<sub>2</sub>-NaCl-H<sub>2</sub>O are prepared by adding the granular white sodium chloride (analytical reagent). The solutions are loaded and sealed into the capillaries. These capillaries are heated in microthermometric stage and in oven and analyzed by Raman microprobe equipped with the microthermometric stage.

### Thermal reactions

- The capillary with the aqueous solution of formic acid

Two groups of capillaries are compared. Each group has two capillaries with the solution of same concentration and these two capillaries are heated with different approach. The conditions are listed in table II-12.

Sample	Concentration (molality)	1		2	
		T(°C)	Heating time (hour/minute)	T(°C)	Heating time (hour/minute)
24	1.0m	400	15h35min	-----	-----
26		300	15h15min	350	21h35min
27	0.3m	400	15h35min	-----	-----
28		300	15h15min	350	21h35min

Table II-12 Conditions for heating capillaries of two groups.

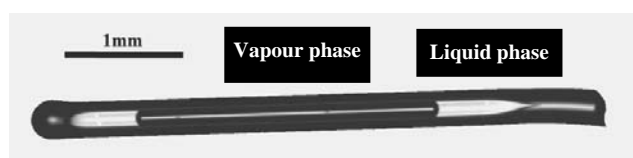


Figure II-41 Microphotograph of capillary before heating at room temperature.

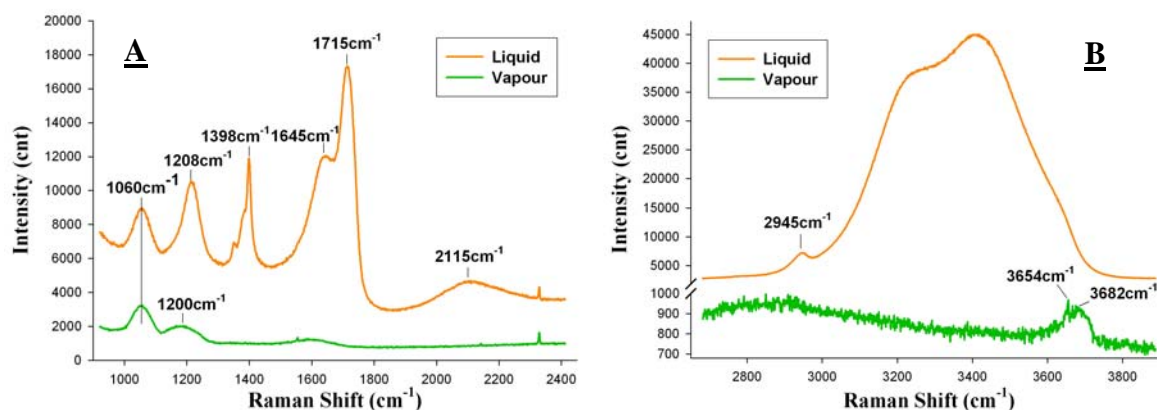


Figure II-42 Raman spectra of aqueous phase and vapor phase in capillary with solution aqueous of formic acid at room temperature (A. 30s×2, B. liquid: 5s×2, vapour: 30s×2).

Before heating, the capillary with aqueous solution has two phases, aqueous phase and vapor phase (figure II-41). The spectra of aqueous phase and vapor phase are showed respectively in figure II-42 A and B. Raman spectra of vapor phase displays only the glass band and a weak band assigned to water vapor at  $3654\text{ cm}^{-1}$  and one band of SiO-H stretching feature of  $\text{SiO}_2$  glass ( $3682\text{ cm}^{-1}$ ). Raman spectra of the aqueous solutions display mainly the

bands of formic acid ( $1060\text{ cm}^{-1}$ ,  $1200\text{ cm}^{-1}$ , Bonner & Kirby-Smith, 1940) and the bands of liquid water (bending band  $\nu_{2A_1}$ :  $1645\text{ cm}^{-1}$ , combination band  $\nu_{L_1}+\nu_{2A_1}$ :  $2115\text{ cm}^{-1}$ , overlapped C-H and O-H stretching bands:  $2800\text{-}3800\text{ cm}^{-1}$ ).

The capillary content is quantified by measuring the volumes of each phase in capillary using micrometric stage. The results are showed in table II-13.

Sample	Concentration (molality)	Vapour phase	Aqueous phase		Calculation	
		H <sub>2</sub> O	HCOOH	H <sub>2</sub> O	CO <sub>2</sub>	H <sub>2</sub> O
24	1.0m	1.34899e-11	1.42423e-8	7.77854e-7	1.42423e-8	7.77868e-7
26		1.91336e-11	1.38865e-8	7.58424e-7	1.38865e-8	7.58443e-7
27	0.3m	1.33902e-11	5.35664e-9	9.60615e-7	5.35664e-9	9.60628e-7
28		1.62334e-11	2.0411e-9	3.66033e-7	2.0411e-9	3.66049e-7

Table II-13 Quantity of components in capillary.

During the Raman measurements, strong fluorescence exists in capillary samples, as shown in figure II-43, which is not further studied in details.

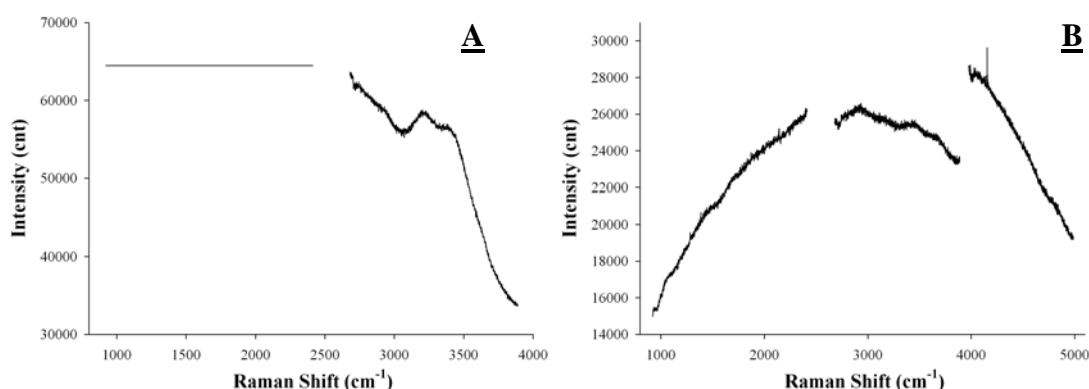


Figure II-43 Raman spectra of capillary with the solution of formic acid (1m) after heating the capillary. A. in liquid phase, B. in vapor phase.

## II.4. Conclusions and perspectives

- This study has shown that the loading procedures of aqueous solutions as well as gas are now well established.

- The calibration procedure for bicarbonate ion of  $\nu_5(A')C-OH$  stretch and  $\nu_3(A')C-O$  stretch Raman bands at room temperature shows that it is necessary to first calibrate the concentration of carbonate ion since it was not possible to get rid of this species due to chemical equilibria. From such independent calibration, the amount of carbonate at equilibrium with bicarbonate could be known and thus the concentration of bicarbonate. Verification using chemical equilibrium calculations could also help the determination of the bicarbonate concentration. Maybe the use of an internal standard, such as perchlorate ion at low concentration (0.01 molal) could help to compare the different calibration curves.
- In natural fluid inclusions contained in quartz, because of the overlapping with a band of quartz, the presence of carbonate ion by the totally symmetric stretching band at  $1064\text{ cm}^{-1}$  must be looked in details. This requires the quantification of the intensity of the quartz contribution by comparing the intensity outside and inside the inclusions of the different bands of the quartz.
- The effect of the crystallographic orientation of the host crystal with respect to the scattering geometry (laser beam, re-scattering) has to be controlled in order to know if the orientation effect is as strong as for the O-H stretching band of water.
- The change of objective (x20 used with the capillary experiments) and (x 80 or x 100) with the fluid inclusions has to be checked.
- The addition of NaCl seems to complicate further the quantification. The reason is probably due to ion-pairing effect. Therefore, the calibration has to be done as a function of the chlorine concentration.
- The effect of temperature on the Raman spectra of bicarbonate and carbonate seems to be very complicated. This problem cannot be addressed using capillary with a vapor phase coexisting with a liquid phase. Therefore, calibration experiments must be done at constant pressure (500 bar for instance) up to  $400\text{ }^{\circ}\text{C}$  in the single liquid phase. The effect of pressure should also be studied. Probably, it will be necessary to start to calibrate using pure carbonate solutions without bicarbonate and following procedure described just above at room temperature. Same experiments must be done using chlorine-bearing solutions. Equilibrium speciation calculations should be done if possible.

- The quantitative loading procedure for pure and dry CO<sub>2</sub> has been established. The quantification by pressure measurements is one method. The density measurement combined with volume measurements are the basis of other methods. Density measurement can be done using one of the four following methods: i) by the measurements of the volume of liquid and vapor CO<sub>2</sub>; by the measurement of the homogenization temperature of the CO<sub>2</sub> phases: this method requires to get a microthermometric stage adapted to the capillary with minimal thermal gradient; iii) by intensity comparison of Raman intensity measurements of a loaded capillary with a CO<sub>2</sub> capillary at a given temperature containing both liquid and vapor CO<sub>2</sub>: first checks have shown precision better than 1%; iv) using the modifications of the Fermi resonance diad (ratio intensity between the two branches; splitting of the two bands and wavenumber shift of each band) with density at fixed temperature.
- The calibration of the analysis of H<sub>2</sub>O-CO<sub>2</sub> mixtures is not straightforward. However, from the experience got during this work, the calibration of the analysis of small amount of water in dominant CO<sub>2</sub> fluids is easy to carry out by measuring first the amount of liquid water and then by introducing known amount of CO<sub>2</sub> deduced from the method described in the previous point. Results could be applied then to CO<sub>2</sub>-dense rich fluid originating from the mantle in xenoliths or the deep continental crust.
- The use of organic products has been demonstrated to be rather complicated due to diffusion of H<sub>2</sub>, corrosion or fluorescence.
- Therefore, the following route is proposed: 1) calibration of the Raman signal of CO<sub>2</sub> dissolved in the aqueous phase using the line at controlled pressure and temperature and previous CO<sub>2</sub> solubility experimental data; 2) use of this calibration for the aqueous liquid phase and application to both ends sealed capillary to deduce the composition of vapor phase.



# **CHAPTER III    METHODOLOGY OF DETERMINATION OF PH APPLICATED TO FLUID INCLUSIONS**

Proton activity (pH) is one of important parameters which controls the transport and deposition of materials by fluids. Fluid inclusions, as the remaining of paleo-fluids, play a key role in the understanding of mass transport and deposition of paleo-circulation. Previous chapter gives the methodology to get the concentration of species in fluids through the routinely analytical techniques for fluid inclusions, microthermometry and micro-Raman spectroscopy. The information of fluids from experimental analyses is applied to the determination of pH of fluids in inclusions. In this part, one numerical model is developed to permit to estimate the paleo-pH in fluid circulations.

### III.1. Determination of pH in fluid inclusions

It is interesting to observe the photography of a fluid inclusion for the repartition of chemical species at different phases of inclusion in system  $H_2O-CO_2-NaCl$  at ambient temperature (figure III-1).

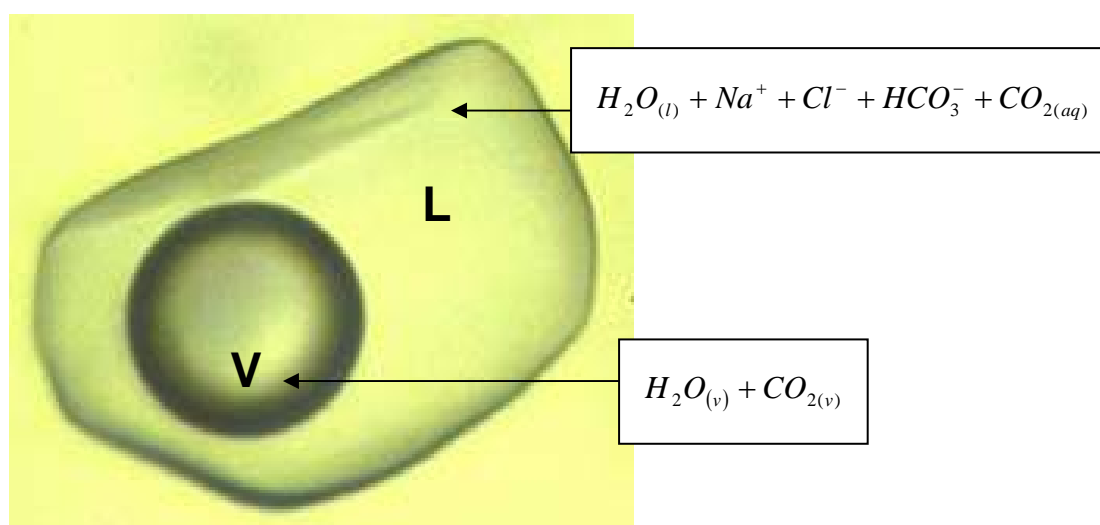


Figure III-1 Micro-photography of a fluid inclusion in system  $H_2O-CO_2-NaCl$  with the coexisting of vapor phase and liquid phase at temperature.

The application of the experimental techniques for the analysis of inclusion in previous parts gives the following information on this type of inclusion:

- microthermometric data, which mainly provides the melting temperature of ice and homogenization temperature of inclusion.

- Raman data, which permits to determine the concentration of  $\text{HCO}_3^-_{(\text{aq})}$  and  $\text{CO}_{2(\text{aq})}$  at different temperature (ambient, homogenization, trapping) through collecting the spectra of inclusion after calibration..
- minerals coexisting and equilibrium with fluid phase, for example which can determine the trapping temperature of fluid.

These experimental known on this system is applied to the estimation of pH.

### **III.1.1. The thermodynamic models**

The thermodynamic model used in this procedure to get the pH is dissymmetric since the activity of components in the liquid and vapor phase are not the same. The Pitzer specific interact model is used to calculate the activity of each dissolved species at the relevant P-T conditions. The fugacity of  $\text{CO}_2$  in the vapor phase is obtained with an equation of state given by Duan. Molar volume of the aqueous liquid phase is also obtained using this model as well as the pressure. A summary of these models is given in the following.

#### **III.1.1.1. Thermodynamic model of the aqueous phase: the Pitzer model**

The base for constructing the numerical modeling is the Pitzer model, which is used to the calculation of the activity coefficient of dissolved species in the aqueous solution. The temperature-pressure range of the application of this model is between 273 K and 523 K and the pressure below 2 kbar. A brief of theory is recalled.

#### Debye-Hückel theory

In 1923, Peter Debye and Erich Hückel published two works which described the method to the calculation of activity coefficients of species in the diluted solutions. These publications are of great advance because they permit to reproduce successfully the solubility of salts which have weak concentration.

Ionic force is one important concept which has permitted the development of the equation of Debye-Hückel. Ionic force is a function of the total concentration of charges

presented in the aqueous solution and is defined by:

$$I = \frac{1}{2} \sum_i m_i z_i^2 \quad (\text{III-1})$$

With the molality  $m_i$  and the charge of ions  $z_i$ .

The equation of Debye-Hückel for the very diluted solution is the following:

$$\log \gamma_i = -A z_i^2 \sqrt{I} \quad (\text{III-2})$$

With the activity coefficient of ion  $i$   $\gamma_i$  and  $A$  is a parameter depends on the density, the dielectric constant and the temperature of pure solvent.

The concentration range for the application of the Debye-Hückel model is very limited since it allows the calculation of the activity coefficients for solutions with very weak concentrations: ionic strength  $I < 0.01$  molal) for the univalent ions and  $I < 0.005$  for the divalent ions. Equation III-2 does not take into account the interactions between the ions of the same charge and the interactions of short range (thermal movement ...) between cations and anions which increase with increasing concentrations. Debye and Hückel considered that the attractive force operates an infinite distance until the maximal distance of approach between two ions of opposing charge.

From this consideration, the extension of the equation of Debye-Hückel has been established:

$$\log \gamma_i = \frac{-A z_i^2 \sqrt{I}}{1 + B a_i \sqrt{I}} \quad (\text{III-3})$$

With  $B$  is a parameter as a function of information the same as  $A$ , and  $a_i$  is a parameter which is sometimes called ionic diameter.

This equation allows the calculation of the activity coefficients for the solution including salts of multi-components having the maximal ionic force to 0.1 mol/ kg H<sub>2</sub>O. However, it is noted that this model does not verify the Gibbs Duhem equation and is not applicable to most of geological fluids of which ionic force greater than 1.

### The Pitzer model

The Pitzer thermodynamic model of the year 1970 is used for the calculation of the activity coefficient in this thesis. It is based partly on the Debye-Hückel theory since it uses

the simplified version of D-H equation to which are added some Viriel type expansion (see next paragraph). It is worth noting that this model verifies the equation of Gibbs-Duhem. The second and third orders of Viriel coefficient model respectively the interaction between 2 ions and the interactions between 3 ions. The superior order of Viriel coefficients are not used to the extremely condensed solutions. The Pitzer model is a model called specific interactions because binary and ternary interaction parameters are specific of the ions involved in the considered interaction. These parameters are obtained from experimental solubility data of minerals. It permits to predict precisely the behavior of solution containing one or more salts of high ionic forces (6 to 8).

Equation of Viriel has been developed to describe the PVT properties of non ideal gas. One example on equation of Viriel is as follows:

$$\frac{PV}{RT} = 1 + \frac{B_2}{V} + \frac{B_3}{V^2} + \dots \quad (\text{III-4})$$

The first term in the left of the equation of Viriel always represents the ideal behavior. In this equation, it represents equation of perfect gas. The second term represents the contribution of interaction between two species, the third is the contribution of three interactions and in this way for the following.

#### III.1.1.2. The equation of state: the Duan model

As it will be seen later, the different steps for pH calculation requires the determination of the fugacity of CO<sub>2</sub> in the vapor phase, of the molar volume of the liquid phase and the pressure along the isochoric line above the homogenization temperature to the aqueous liquid phase.

The equation of state of Duan, Moller and Weare (2003) (see part of “Equation of state based on the terms of contribution and perturbation”) gives an expression of the compressibility factor Z ( $Z = Pv/RT$ ) where P is the pressure in bar,  $v$  is the molar volume and T is the temperature in Kelvin. The general form of this equation is the following:

$$z = \frac{Pv}{RT} = \frac{P_r v_r}{T_r} = 1 + \frac{B}{v_r} + \frac{C}{(v_r)^2} + \frac{D}{(v_r)^4} + \frac{E}{(v_r)^5} + \frac{F}{(v_r)^2} \left( \beta + \frac{\gamma}{(v_r)^2} \right) \exp \left( -\frac{\gamma}{(v_r)^2} \right) \quad (\text{III-5})$$

$$P_r = \frac{P}{P_c}; T_r = \frac{T}{T_c}; v_r = \frac{v}{v_c^*}; v_c^* = \frac{RT_c}{P_c}$$

Where the subscript  $r$  indicates the reduced values defined by the second lines.

This equation was deduced from the perturbation theory. The variables  $P$ ,  $T$  and  $X$  are chosen as be independent.

$$Z = Z^{ref} + Z^{per} \quad (III-6)$$

The perturbation term is a corrective term which is more complicated than the reference system in order to get a better representation of the non ideal behavior. In different studies (Anderko & Pitzer, 1993; Duan et al., 1995), NaCl and H<sub>2</sub>O are considered at temperatures lower 573 K, like the hard spheres with dipolar moment. Molecules like CO<sub>2</sub> and CH<sub>4</sub> are hard spheres with no dipolar moment.

The reference system includes a term of contribution of dure sphere and contribution of interactions between dipoles. The compressibility coefficient can be written as the following form:

$$Z = Z^{hd} + Z^{dip} + Z^{per} \quad (III-7)$$

with  $Z^{hd}$  is calculated from the equation of Boublik (1970)

$Z^{dip}$  is calculated by using the equation of Stell et al. (1972, 1974)

$Z^{per}$  is calculated from Viriel term proposed by Anderko & Pitzer (1973)

#### Equation of state based on the terms of contribution and perturbation

a) The contribution of hard sphere is:

$$Z^{hd} = \frac{1 + \left( \frac{3DE}{F} - 2 \right) \eta_{hd} + \left( \frac{3E^2}{F^2} - \frac{3DE}{F} + 1 \right) \eta_{hd}^2 - \frac{E^3}{F^2} \eta_{hd}^3}{(1 - \eta_{hd})^3} \quad (III-8)$$

Where

$$D = \sum_{i=1}^n x_i b_i^{1/3} \quad (III-9)$$

$$E = \sum_{i=1}^n x_i b_i^{2/3} \quad (III-10)$$

$$F = \sum_{i=1}^n x_i b_i \quad (III-11)$$

$$\eta_{hd} = \frac{\sum_{i=1}^n x_i b_i}{4v} \quad (\text{III-12})$$

With  $b_i$  is the covolume of Van der Waals.

b) The contribution of dipolar:

$$Z_{dip} = \eta \frac{\left(1 - \frac{2A_3}{A_2}\right) \frac{dA_2}{d\eta} + \frac{dA_3}{d\eta}}{\left(1 - \frac{A_3}{A_2}\right)^2} \quad (\text{III-13})$$

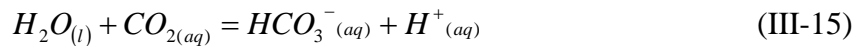
c) The term of perturbation

$$Z_{per} = -\frac{1}{RT} \left( \frac{a}{v} + \frac{acb}{2v^2} + \frac{3adb^2}{16v^2} + \frac{aeb^3}{16v^4} \right) \quad (\text{III-14})$$

The details of dipolar and perturbation terms can be found in the publication of Duan et al. (1995).

### III.1.2. Theoretical principles

It is impossible to directly determine the  $H^+$  activity in inclusion fluid because there is no way to introduce a micro-electrode! However, there exist several chemical equilibria among aqueous species in aqueous phase of inclusion fluid. The following equilibrium (Eq. III-15) is one of common cases for the geological fluids detected in natural fluid inclusions and is the object of this thesis.



Referring to Li & Duan (2007), the above two chemical equilibria (Eq. III-15, III-16) are used. The reaction constants  $K_1$  and  $K_2$  of above two equations depend on the temperature and pressure. The pressure is unknown but is theoretically calculable from the V-X properties of fluid inclusion and the temperature which is supposed to be known from petrological information. For calculating the concentration of  $H^+$  ion, it is necessary to calculate the pressure at homogenization temperature and molar volume.

Before the calculation of pH, it is necessary to determine the concentrations of  $Na^+$  and

Cl<sup>-</sup>. They are the major ions to partly control the activities of other constituents and the isopleths of L-V equilibrium of interested inclusion with its isochore. From this, the pressure at trapping temperature can be deduced. Finally, the pH of inclusion fluid is calculated.

### III.1.2.1. Calculation of the concentration of Na<sup>+</sup> and Cl<sup>-</sup>

The calculation of these concentrations is based on the quantitative interpretation of microthermometric data (freezing point depression) in terms of water activity and the Pitzer equations. In this case, the following information permits to characterize the fluid inclusion chemistry:

- Melting temperature of hexagonal ice coexisting with vapor ( $T_{ice}$ ) which permits to deduce the activity of water as the transition of phase (hexagonal ice + L<sub>(aq)</sub> + V → L<sub>(aq)</sub> + V).
- The activity of water  $a_{H_2O} = f(T_{ice})$  is calculated using the cryometric equation (Pitzer, 1991):

$$\ln a_{H_2O}(T_{ice}) = \frac{\Delta H_f^0}{R} \left( \frac{1}{T^0} - \frac{1}{T_{ice}} \right) + \frac{\Delta C_p}{R} \left[ \ln \left( \frac{T_{ice}}{T^0} \right) + \frac{T^0}{T_{ice}} - 1 \right] \quad (III-17)$$

where  $\Delta C_p$  is the variation of heat capacity of melting ice reaction assumed to be constant in this short temperature range,  $T^0$  is the pure ice melting temperature or water triple point temperature;  $\Delta H_f^0$  is the molar enthalpy of ice melting at triple point temperature.

- The concentrations of HCO<sub>3</sub><sup>-</sup> and CO<sub>2(aq)</sub> obtained from Raman measurements of the aqueous phase;
- The activity of water in the aqueous solution at  $T_{ice}$  is also a function of the solution composition which can be calculated using the Pitzer model (Monnin et al., 2002). Thus we get another equation:  $a_{H_2O} = g(m_{Na^+}, m_{Cl^-}, m_{CO_2}, m_{HCO_3^-})$  which can be simplified to  $a_{H_2O} = g(m_{Na^+}, m_{Cl^-})$  since the concentration of HCO<sub>3</sub><sup>-</sup> and CO<sub>2(aq)</sub> are known. The water activity and this expression can be determined under the help of thermodynamic model of aqueous solution (Monnin et al., 2002), then the following equation is deduced:

$$f(T_{ice}) - g(m_{Na^+}, m_{Cl^-}) = 0 \quad (III-18)$$



- Equation of charge balance:  $m_{Na^+} - m_{HCO_3^-} - m_{Cl^-} = 0$

At low temperature,  $m_{H^+}$ ,  $m_{OH^-}$ ,  $m_{HCO_3^-}$  are neglected. In this equation, there are only two unknown  $m_{Na^+}$  and  $m_{Cl^-}$ .

- Concentrations of  $CO_{2(aq)}$  and  $HCO_3^-(aq)$  as the transition of phase

Thus, a system with two equations and two unknowns is obtained, which is expressed in the following:

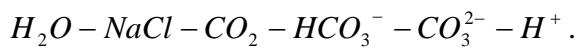
$$\left\{ \begin{array}{l} f(T_{ice}) - g(m_{Na^+}, m_{Cl^-}) = 0 \\ m_{Na^+} - m_{Cl^-} - m_{HCO_3^-} = 0 \end{array} \right\} \quad (III-19)$$

### III.1.2.2. Calculation of bulk composition and density

The next step of these calculations consists to calculate the bulk  $CO_2$  concentration of the fluid inclusion. This is done by combining Raman measurements at bulk homogenization temperature ( $T_h$ ) and modeling the  $CO_2$  solubility at  $T_h$ .

The model developed by Duan & Sun (2003) relevant to the system:  $H_2O - NaCl - CO_2 - HCO_3^- - CO_3^{2-} - H^+$  is chosen because it permits to calculate the solubility of carbon dioxide in pure water and in solution containing  $Na^+$  and  $Cl^-$ . Moreover, it models solubility values close to the experimental measurement (<7% for the solubility of  $CO_2$ ) for the conditions of the temperature between 273 and 533 K and of the pressure between 0 and 2000 bar.

This dissymmetric model is supposed by Viriel extent state equation for describing the vapour phase and by Pitzer model for the liquid phase referring to the system:



To determine the solubility of  $CO_2$  in the aqueous solutions in this method, it is necessary to consider the equilibrium between the vapor and the liquid phase which implies the equality of the chemical potential of each component ( $H_2O$  and  $CO_2$ ) in the vapor and liquid phase, the concentrations of all ionic species being obviously real in the vapor phase:

$$\mu_{CO_2}^l = \mu_{CO_2}^v \quad \text{and} \quad \mu_{H_2O}^l = \mu_{H_2O}^v \quad (III-20)$$

Then, from the equation of the chemical potential in the liquid and vapor phase, the equation

relevant to CO<sub>2</sub> is:

$$\ln \frac{y_{CO_2} P}{m_{CO_2}} = \frac{\mu_{CO_2}^{l(0)}(T, P) - \mu_{CO_2}^{v(0)}(T)}{RT} - \ln \varphi_{CO_2}(T, P, y) + \ln \gamma_{CO_2}(T, P, m) \quad (\text{III-21})$$

where  $y_{CO_2}$  is the fugacity coefficient of carbon dioxide in the vapor phase (obtained using the equation of Duan et al., 1992), molality of carbon dioxide  $m_{CO_2}$  in aqueous phase,  $\gamma_{CO_2}$  is the activity coefficient of CO<sub>2</sub> dissolved in aqueous phase calculated with the Pitzer model with parameters given by Li & Duan (2007).

Equation III-21 has two unknowns, the composition of the vapor phase and the pressure. Therefore, a second equation is required to get the problem solved. Theoretically, this equation is related to the chemical potentials of water:  $\mu_{H_2O}^l = \mu_{H_2O}^v$ . However, because the vapor phase density is low, its composition can be calculated using the Dalton's law:

$$y_{CO_2} = (P - P_{H_2O}) / P \quad (\text{III-22})$$

The fugacity coefficient of CO<sub>2</sub> is calculated using of state of equation of Duan et al. (1992), as well as the molar volume of this phase and the pressure. The activity coefficient  $\gamma_{CO_2}$  of carbon dioxide dissolved in the aqueous phase is calculated using the model of Pitzer and its different binary and ternary interaction parameters of Duan & Sun (2003):

$$\ln \gamma_{CO_2} = 2m_{CO_2} \lambda_{CO_2-CO_2} + 2 \sum_c m_c \lambda_{CO_2-c} + 2 \sum_a m_a \lambda_{CO_2-a} + \sum_c \sum_a m_c m_a \zeta_{CO_2-c-a} \quad (\text{III-23})$$

with c and a respectively correspond to cations and anions.

### III.1.2.3. Calculation of molar volume

In order to calculate the values of the concentration of CO<sub>2</sub> and HCO<sub>3</sub><sup>-</sup> at the P-T conditions of trapping to derive the activity of H<sup>+</sup>, it is necessary to know the pressure at the temperature of trapping and thus the molar volume of the fluid. The principle of the determination of the bulk molar volume is based on the mass conservation of carbon atoms involved in CO<sub>2</sub> and HCO<sub>3</sub><sup>-</sup>. The available information is the following:

- at ambient temperature, the density of CO<sub>2(v)</sub>, and the concentration of CO<sub>2(aq)</sub> and HCO<sub>3-(aq)</sub> are obtained from analysis of Raman:  $\sum C = HCO_3^- + CO_{2,v} + CO_{2,aq}$ .
- the concentrations of Na<sup>+</sup> and Cl<sup>-</sup> (molality scale) are calculated from the melting

temperature of ice as shown before.

- at homogenization temperature, the concentrations of  $\text{Na}^+$  and  $\text{Cl}^-$  (molality scale) are identical to those at ambient temperature.

- Raman analysis permits to know the concentrations of  $\text{CO}_2$  and sometimes  $\text{HCO}_3^-$ . At homogenization temperature:  $\sum C = \text{HCO}_3^- + \text{CO}_2$ .

Thus, the mass conservation equation of carbon atoms between ambient temperature ( $T^0$ ) and homogenization temperature ( $T_h$ ) is the following:

$$\sum_i^3 C_i(T^0) = \sum_i^2 C_i(T_h) \quad (\text{III-24})$$

or written in number of moles of the different chemical species:

$$\left( n_{\text{CO}_2}^v + n_{\text{CO}_2}^{aq} + n_{\text{HCO}_3^-}^{aq} \right)_{T^0} = \left( n_{\text{CO}_2} + n_{\text{HCO}_3^-} \right)_{T_h} \quad (\text{III-25})$$

The following equations describes each term in details:

$$n_{\text{CO}_2}^v = \frac{V_v}{V_v} = \frac{1 - V_{aq}}{V_v} \quad (\text{III-26})$$

$$n_{\text{CO}_2}^{aq} = m_{\text{CO}_2, aq} * \frac{M_{\text{H}_2\text{O}}^{aq}}{1000} \quad (\text{III-27})$$

$$M_{\text{solution}}^{aq} = M_{\text{H}_2\text{O}}^{aq} + \sum M_{i_{\text{dissous}}} \quad (\text{III-28})$$

where  $m$  is the molality,  $M$  is the mass,  $\overline{M}$  is the molar mass,  $V_{aq}$  and  $V_v$  are the volume fractions of the aqueous and vapor phase at room temperature respectively,  $\overline{V}_v$  is the molar volume of the vapor phase.

At room temperature, the mass of the aqueous solution  $M_{\text{solution}}^{aq}$  can be written as:

$$M_{\text{solution}}^{aq} = \rho_{aq} * (1 - V_v) = \rho_{aq} * V_{aq} \quad (\text{III-29})$$

with  $\rho_{aq}$ , the density of aqueous phase provided by Potter & Brown (1977).

$$M_{i_{\text{dissous}}} = m_i^{aq} * \overline{M}_i * \frac{M_{\text{H}_2\text{O}}^{aq}}{1000} \quad (\text{III-30})$$

Then the following equation is deduced:

$$\rho_{aq} * V_{aq} = M_{\text{H}_2\text{O}}^{aq} * \left[ 1 + \frac{1}{1000} * \sum m_i^{aq} * \overline{M}_i \right] \quad (\text{III-31})$$

From this equation, the mass of water can be obtained:

The equation (III-28) is rewritten as the function of the mass of water. The mole number of bicarbonate in the aqueous phase is written as the same method.

$$n_{CO_2}^{aq} = m_{CO_2,aq} * \frac{\rho_{aq} * V_{aq}}{1000 + \sum m_i^{aq} * \overline{M}_i} \quad (III-32)$$

At homogenization temperature where one single phase is present, then:

$$(n_{CO_2} + n_{HCO_3^-})_{Th} = \frac{\rho_{aq} * V_{aq}}{1000 + \sum m_i^{aq} * \overline{M}_i} * \left[ m_{CO_2}^{Th} + m_{HCO_3^-}^{Th} \right] \quad (III-33)$$

With equations III-28, III-30 and III-31, we get one equation with one unknown  $V_{aq}$  is obtained, which allows the calculation of the molar volume of liquid:

$$\overline{V}_{aq} = \frac{V_{aq}}{\sum n_i^{aq}} \text{ and } \sum n_i^{aq} = n_{CO_2}^{aq} + n_{HCO_3^-}^{aq} + n_{Na^+}^{aq} + n_{Cl^-}^{aq} + n_{H_2O} \quad (III-34)$$

From this value, the total density of the fluid inclusion is determined:

$$\rho_{total} = \rho_{aq} V_{aq} + \rho_v (1 - V_{aq}) \quad (III-35)$$

Then the molar volume is deduced:

$$\overline{V}_{total} = \frac{\sum x_i * \overline{M}_i}{\rho_{total}} \quad (III-36)$$

with  $x_i$ , the molar fraction of all the constituents (including water).

#### III.1.2.4. Calculation of pH

Finally, pH is estimated from the previous steps. There are three distinct cases depending on the initial information obtained from fluid inclusion by experimental analysis. Moreover, considering that Pitzer model can be applied only for trapping temperatures  $T_p$  such as  $T_p < 250^\circ\text{C}$ , it would be necessary to use the Helgeson-Kirkham-Flowers (HKF) model if  $T_p > 250^\circ\text{C}$ .

- First case:  $CO_2$  and  $HCO_3^-$  are measured by Raman spectrometry at trapping temperature. As the concentrations of  $HCO_3^-$  and  $CO_2$  at trapping temperature are known, pH calculation is straightforward and can be obtained directly from equation III-37 provided the activity

coefficients are calculated at the trapping pressure:

$$K(P, T) = \frac{a_{H^+} \times a_{HCO_3^-(aq)}}{a_{CO_2(aq)} \times a_{H_2O}} \quad (III-37)$$

The reaction constant is determined in Li & Duan (2007) according to the following equation:

$$\begin{aligned} \ln K = & a_1 + a_2 T + a_3 T^{-1} + a_4 T^{-2} + a_5 \ln T + (a_6 T^{-1} + a_7 T^{-2} + a_8 T^{-1} \ln T)(P - P_s) \\ & + (a_9 T^{-1} + a_{10} T^{-2} + a_{11} T^{-1} \ln T)(P - P_s)^2 \end{aligned} \quad (III-38)$$

Where  $a_1 - a_{11}$  are the parameters and  $P_s$  is equal to 1 bar at temperature lower than 373.15 K and is equal to the saturation pressure of water at temperature higher than 373.15 K. Now, activities of species  $HCO_3^-$  and  $CO_2$  must be calculated.

- Second case:  $CO_2$  and  $HCO_3^-$  are measured by Raman spectrometry at homogenization temperature and  $HCO_3^-$  is not be detected at trapping temperature.

The Pitzer model is always used to resolve this case at temperature lower than 250°C. The unknown concentration of bicarbonate makes the calculation more complicated. The two chemical equilibria (III-15) and (III-16) are considered:  $H_2O_{(l)} + CO_{2(aq)} = HCO_3^-(aq) + H^+(aq)$  and  $H_2O = H^+ + OH^-$ . These equilibria written under the form of the equilibrium condition provide the following equations:

$$(\gamma_{H^+} \gamma_{HCO_3^-}) m_{HCO_3^-} m_{H^+} - K_1 a_{H_2O} a_{CO_2} = 0 \quad (III-39)$$

$$(\gamma_{H^+} \gamma_{OH^-}) m_{H^+} m_{OH^-} - K_2 a_{H_2O} = 0 \quad (III-40)$$

In addition, the charge balance equation provides a third equation:

$$m_{H^+} + m_{Na^+} = m_{Cl^-} + m_{OH^-} + m_{HCO_3^-} \quad (III-41)$$

Thus, we obtain a system of three equations with three unknowns  $H^+$ ,  $OH^-$  and  $HCO_3^-$ . Through substitution, a second degree equation is deduced which permits to determine the concentration of ion  $H^+$ .

### III.1.3. The algorithm of program

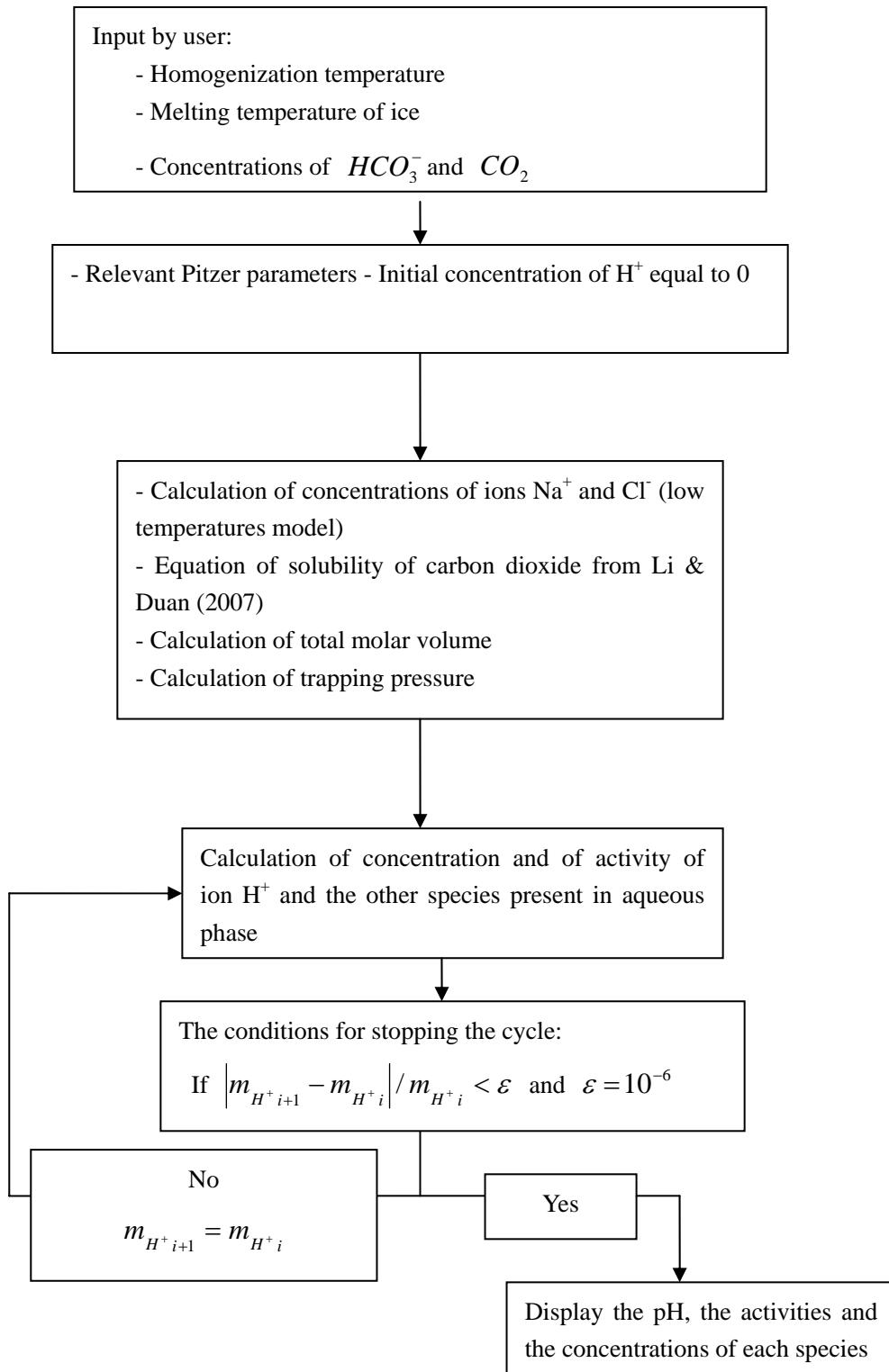


Figure III-2 Algorithm of program for the calculation of pH.

Numerical modeling is obtained using a computer software written in Visual Basic 6.0. Each above parts presents the object of algorithm and program in details. The following object is to perform the method to permit the reality of all the steps of calculation. The

algorithm permitting to the calculation of pH is presented in figure III-2. A final program realizes the all the steps and objects.

The main program for calculating the pH in first case (by Mathieu LEISEN, G2R) is presented in appendix.

## **III.2. Application to natural case**

The methods developed in this work are applied to the largest gold deposit in the Bohemian Massif, Mokrsko gold deposit. This gold deposit is well studied by the groups in G2R lab (Boiron et al., 2001, 2003). Boiron et al. (2001) determined the P-V-T-X conditions of ore fluid migration and determined the relative stages of fluid migration resulting in the ore deposition. In this part, the fluid inclusions in quartz related to Au stage are carried out the microthermometric and micro-Raman analyses, and the results are applied to the estimation of pH of inclusion fluids.

### **III.2.1. Geology background of Mokrsko gold deposit**

The Mokrsko gold deposit is located in central Bohemia and in Jílové belt, approximately 50 km south of Prague. The Jílové belt is 70 km long and 1-7 km wide, and mainly is metaigneous rocks, and is composed of the low-grade Proterozoic and Paleozoic (Barrandian) units and the high-grade metamorphic units of the Moldanubicum. The rocks of Jílové belt were intruded by numerous sets of basic and intermediate dykes during Cadomian and Variscan orogenies. Morávek et al. (1989) indicated that gold-bearing quartz veins and sheeted veinlets are the main types of mineralization in the deposit, which developed in the marginal part of the Variscan granodiorite belonging to the Central Bohemian pluton.

Referring to the Boiron et al. (2001), there are three main stages of fluid migration: Pre-ore stages, Ore stages, and Post-ore stages. The pre-ore stages are characterized by early barren quartz veins, porphyry dykes and ductile deformation patterns. In ore stages, minerals related to gold deposit (arsenopyrite, pyrite and pyrrhotite) were deposited and an important

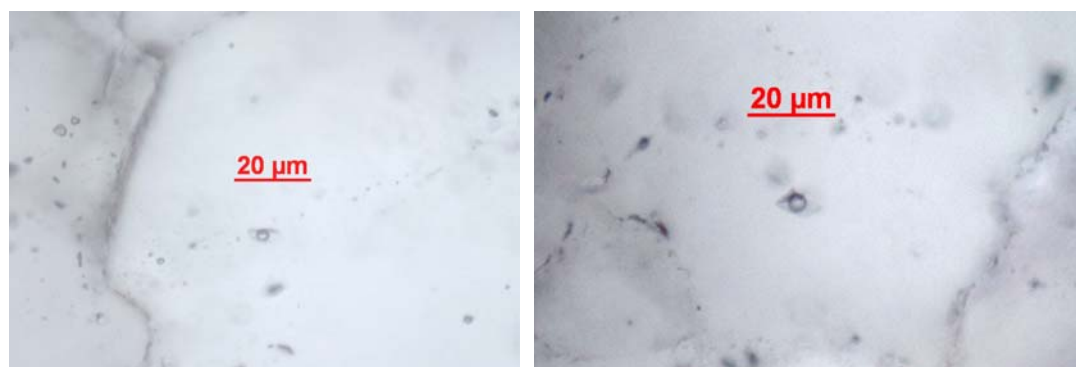
brittle phase of deformation is characterized. The main ore zones occur where exists the densest quartz veinlets resulting from the fracturing and filling events. Our samples were collected from this stage in gold-bearing quartz veinlets. In post-ore stages, early mineral assemblages are kaolinized, but intense kaolinisation is not spatially related to the earlier gold-bearing quartz networks (Morávek et al., 1989).

### III.2.2. Experimental measurements of fluid inclusions

The study of Boiron et al. (2001) on fluid inclusions indicates that CO<sub>2</sub> are identified in volatile-bearing fluid inclusions and aqueous-carbonic fluid inclusions characterized the ore stages.

Fluid inclusions in quartz in ore stages were studied by techniques that included microthermometry, quantitative in-situ analysis by Raman spectroscopy. Microthermometric studies of fluid inclusions were performed on wafers using a Linkam heating-freezing stage. The rate of heating was monitored in order to obtain an accuracy of  $\pm 0.1$  °C during freezing,  $\pm 1$  °C when heating over the 25-300 °C range. In volatile-bearing fluid inclusions, CO<sub>2</sub> was identified by melting of solid below -56.6 °C and by micro-Raman analysis performed on a DILOR X-Y multichannel modular Raman spectrometer. The other volatiles, such as H<sub>2</sub>S, N<sub>2</sub>, are verified by micro-Raman spectrometer.

Figure III-3 illustrates some photographs of fluid inclusions observed in quartz wafer. These inclusions have the coexistence of vapour phase and liquid phase. The size is suitable for the observation of phase change and for the measurement of micro-Raman spectroscopy. Table III-1 presents the results of microthermometric measurements in fluid inclusion. These results indicate the CO<sub>2</sub>-bearing fluid inclusions.





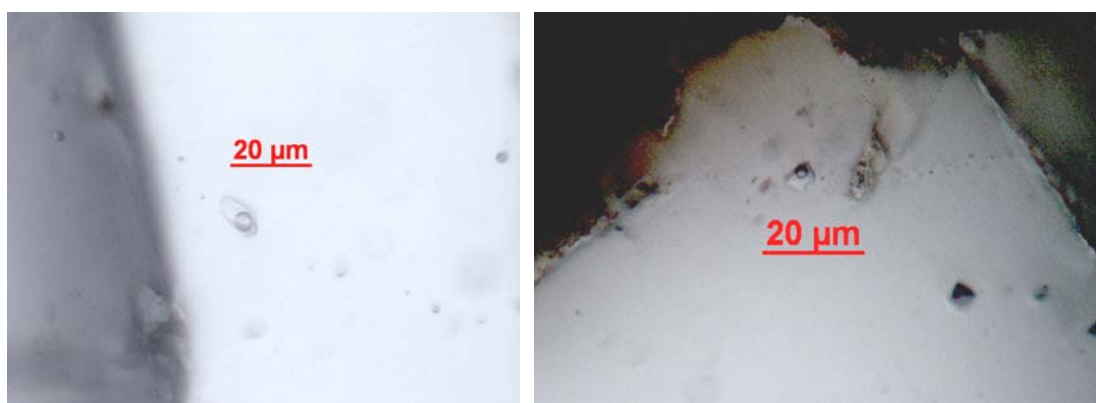


Figure III-3 Photographs of fluid inclusions in quartz collected from Mokrsko gold deposit in ore-bearing zones.

No.	T <sub>m</sub> CO <sub>2</sub> (°C)	T <sub>h</sub> CO <sub>2</sub> (°C)	T <sub>m</sub> Cl. (°C)	T <sub>h</sub> (°C)
1	-58.1	18.2	8.2	> 250
2	-57.4	18.4	6.3	> 250
3	-56.8	19.0	7.5	> 250
4	-57.1	18.2	9.2	> 250
5	-57.7	19.3	8.7	> 250
6	-57.4	18.5	7.8	> 250

T<sub>m</sub>CO<sub>2</sub>: Melting temperature of solid CO<sub>2</sub>; T<sub>h</sub>CO<sub>2</sub>: Homogenization temperature of CO<sub>2</sub>;

T<sub>m</sub>Cl.: Melting temperature of clathrate; T<sub>h</sub>: Total homogenization temperature

Table III-1 Results of microthermometric analysis of fluid inclusions.

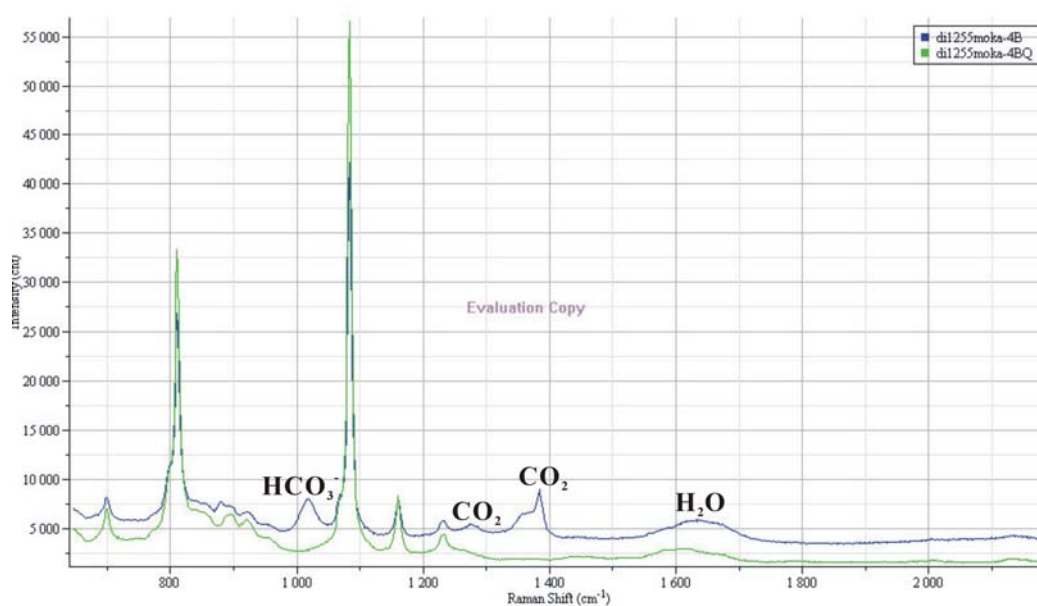


Figure III-4 Raman spectra collected from liquid phase in fluid inclusion (blue line) and from quartz crystal near inclusion (green line) respectively.

Raman spectra collected from liquid phase in fluid inclusion are exemplified in figure III-4. The band of bicarbonate at  $1017\text{ cm}^{-1}$  and bending band of water present apparently in the spectrum of aqueous phase of fluid inclusion. And two bands of aqueous  $\text{CO}_2$  are observed. In the region between  $1300$  and  $1400\text{ cm}^{-1}$ , bicarbonate band at  $1360\text{ cm}^{-1}$  overlaps with one of peak of  $\text{CO}_2$ . Thus, it is difficult to measure the area of  $1360\text{ cm}^{-1}$  band.

### III.2.3. Calculation of pH

Combining the results of experimental analysis with numerical program of calculation of pH, pH of natural inclusion fluids is tried to be estimated.

In spectra collected from aqueous phase in fluid inclusion, there exist bands of bicarbonate at  $1017\text{ cm}^{-1}$  and  $1360\text{ cm}^{-1}$  and bands of aqueous  $\text{CO}_2$  at  $1275\text{ cm}^{-1}$  and  $1380\text{ cm}^{-1}$ . The bicarbonate band at  $1360\text{ cm}^{-1}$  overlaps with the band of  $\text{CO}_2$  dissolved in aqueous phase at  $1380\text{ cm}^{-1}$ . The area ratio of band of  $\text{CO}_2$  dissolved in aqueous phase to bending band of water at  $1640\text{ cm}^{-1}$  is also used to calibrating the concentration of  $\text{CO}_2$  in aqueous phase. Because of the relative weakness of  $\text{CO}_2$  band at  $1275\text{ cm}^{-1}$  to band at  $1380\text{ cm}^{-1}$ , the band at  $1380\text{ cm}^{-1}$  is selected. For subtracting the influence of bicarbonate band at  $1360\text{ cm}^{-1}$ , the area ratio of band  $1017\text{ cm}^{-1}$  to band at  $1360\text{ cm}^{-1}$  collected from standard samples is introduced. The results in table III-2 are from capillaries, which shows that area ratio of band  $1017\text{ cm}^{-1}$  to band at  $1360\text{ cm}^{-1}$  is fixed, but the value changed by the addition of NaCl. Table III-3 illustrates the results from synthetic fluid inclusions, which does not show apparent coincidence of different samples with different concentration of bicarbonate. One of possibilities is that the signal of bands is weak resulting to the error. For natural inclusions, the value obtaining from standard capillaries with the addition of NaCl is used. The results of area ratio of band of  $\text{CO}_2$  dissolved in aqueous phase to bending band of water (“Ratio(1380/1640)”) are presented in table III-4, as well as the area ratio of bicarbonate band at  $1017\text{ cm}^{-1}$  to bending band of water (“Ratio(1017/1640)”).

KHCO <sub>3</sub> :NaCl	Area(1017)/Area(1360)	KHCO <sub>3</sub> :NaCl	Area(1017)/Area(1360)
1.0:0.0	0.75	1.0:1.0	0.89
0.3:0.0	0.73	1.0:0.3	0.89
0.1:0.0	0.85	1.0:0.1	0.86
Mean value	0.78	Mean value	0.88

Table III-2 Area ratio of bicarbonate band at 1017 cm<sup>-1</sup> to at 1360 cm<sup>-1</sup> by using the spectra collected from aqueous phase in standard capillaries.

KHCO <sub>3</sub> :NaCl	Area(1017)/Area(1360)	KHCO <sub>3</sub> :NaCl	Area(1017)/Area(1360)
1.0:0.0	1.20	1.0:1.0	1.07
0.3:0.0	1.05	0.3:1.0	0.95
0.1:0.0	0.90	Mean value	1.01
Mean value	1.05		

Table III-3 Area ratio of bicarbonate band at 1017 cm<sup>-1</sup> to at 1360 cm<sup>-1</sup> by using the spectra collected from aqueous phase in synthetic fluid inclusion.

No.	Ratio(1017/1640)	mHCO <sub>3</sub> <sup>-</sup>	Ratio(1380/1640)	mCO <sub>2</sub>
1	0.52	0.70	0.21	0.031
2	0.67	0.91	0.12	0.023
3	0.51	0.68	0.30	0.040

Table III-4 Results of calculation through the spectra collected on aqueous phase of fluid inclusions.

The relationship between the concentration of bicarbonate and the area ratio(1017/1640) obtaining from the analysis of standard synthetic fluid inclusions (Eq. (II-10): y is the concentration of bicarbonate, x is ratio(1017/1640)) is introduced for calculating the concentration of bicarbonate. The results are shown in table III-4.

$$y = (x - 0.0361)/0.6929 \quad (\text{II-10})$$

The relationship between the concentration of CO<sub>2</sub> dissolved in water and the area ratio(1275/1640) or area ratio(1380/1640) or area ratio(1275+1380/1640) (ratio(Total/1640)) obtaining from the analysis of standard capillaries, which is showed in figure III-5. The area ratio(1275/1640) is chosen because of the highest related correlation coefficient in three relationships. Thus, Eq. (III-42) is introduced for calculating the concentration of CO<sub>2</sub>

dissolved in water, in which  $y$  is the concentration of  $\text{CO}_2$  dissolved in water,  $x$  is ratio(1275/1640)) The results are shown in table III-4.

$$y = (x + 0.1246)/10.606 \quad (\text{III-42})$$

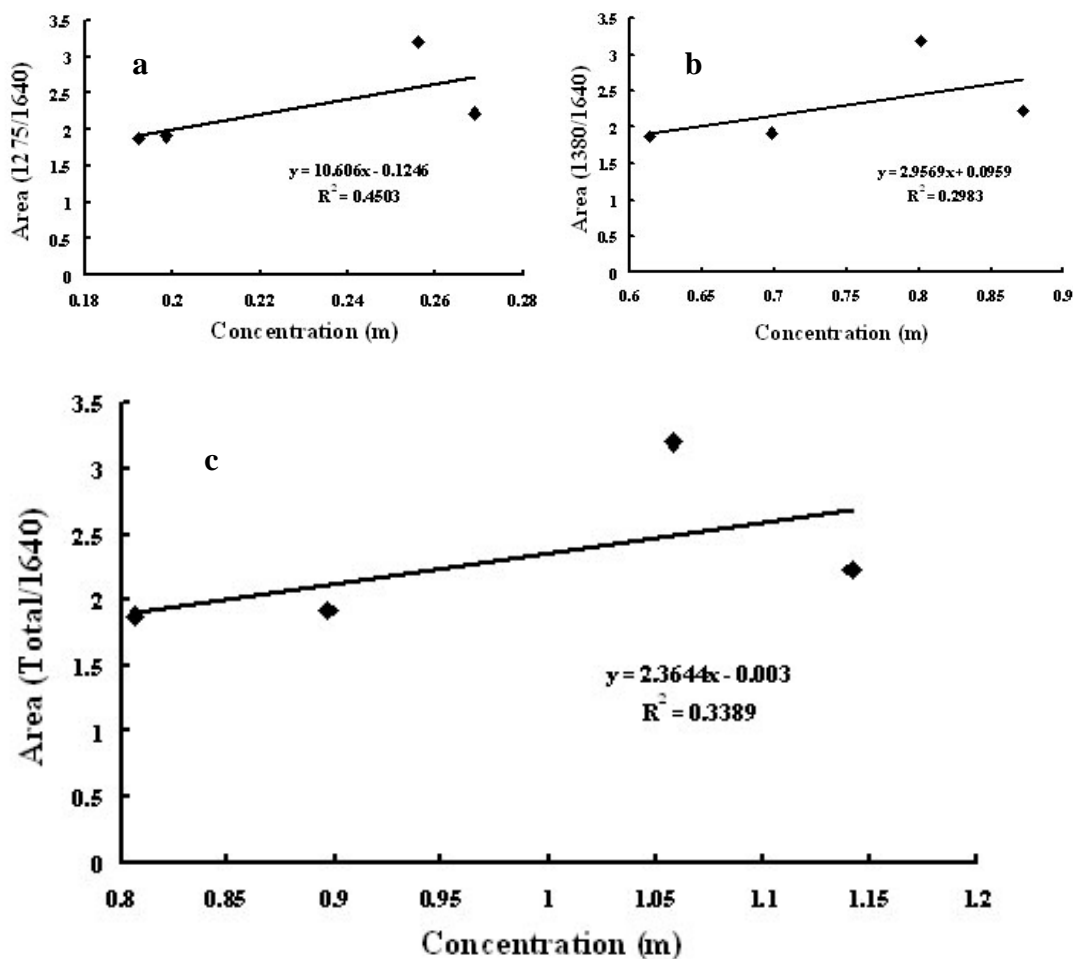


Figure III-5 Relationships between the concentration of  $\text{CO}_2$  dissolved in water and the area ratios of bands of  $\text{CO}_2$  dissolved in water at  $1275 \text{ cm}^{-1}$  and  $1380 \text{ cm}^{-1}$  obtaining from the analysis of standard capillaries; a. area ratio(1275/1640); b. area ratio(1380/1640); c. area ratio(Total/1640).

The homogenization temperature is greater than  $250^\circ\text{C}$ , which makes impossible to use the Duan-Pitzer model to estimate the bulk molar volume and the isochore in the single phase field. Therefore only a pH estimation can be done at  $25^\circ\text{C}$ . If the activity coefficient of dissolved  $\text{CO}_2$  and bicarbonate are respectively around 1.2, and 0.55 (estimations made using the Duan software speciation model for 1 mole NaCl), the pH of the aqueous solution of

inclusions 1, 2 and 3 is respectively 7.35, 7.50 and 7.25. Therefore, the fluid is slightly basic.

In conclusion, the main obstacles which should be overcome for bicarbonate-rich fluids are the followings:

- The lack of experimental data relative to liquid isopleths at equilibrium with a vapor in the system  $\text{H}_2\text{O}-\text{NaHCO}_3-\text{NaCl}-\text{CO}_2$ .
- The lack of P-v-T-X experimental data in the single phase field in the system  $\text{H}_2\text{O}-\text{NaHCO}_3-\text{NaCl}-\text{CO}_2$ . Such data are required to fit experimental data to the “Duan” equation of state of the same type than the one used of  $\text{H}_2\text{O}-\text{NaCl}-\text{CO}_2$ .
- As the Pitzer model does is not reliable above 250 °C, the HKF model should be used for the calculation of speciation and of pH.  $\text{CO}_2$ -rich fluid results in a decrease of the value of the static dielectric constant compared to the value of pure water at the same P and temperature. Consequences are not well known both for the equilibrium constant and the activity coefficients.

## **CONCLUSIONS AND PERSPECTIVES**

## 1. Conclusions

This thesis demonstrates the possibility of the use the equilibrium between fluid species in the  $\text{H}_2\text{O}-\text{CO}_2-\text{HCO}_3^- - \text{NaCl}$  system for the estimation of pH of natural palaeo-fluids trapped as relicts in fluid inclusions. One algorithm of calculation based on Pitzer model has been elaborated in order to interpret the analytical measurement (microthermometry and Raman microspectrometry). Finally, this methodology is applied to a natural case (a gold deposit).

### 1.1. A new method for synthesizing fluid inclusions by sealing material into fused-silica glass capillary tubing

A new method for the synthesis of controlled fluid composition in silica glass capillary is developed using an upgraded line of I-Ming Chou system. This technique permits to seal materials under the three states of matter (solid, liquid or gas) into pure silica glass capillary. The loading materials methodology of solid, liquid or gas phases in silica capillary are presented in this work. In addition, the quantification of liquid and gas loaded into capillary is detailed. This quantitative method based on pressure measurements was first applied to pure  $\text{CO}_2$  fluids and was validated by two independent methods. This demonstrates also the possibility to apply this method to more complex systems such as the  $\text{H}_2\text{O}-\text{CO}_2-\text{HCO}_3^- - \text{NaCl}$  system.

All the methodological developments carried out in this work show that the silica glass capillary techniques can provide standard up to 400 °C and 2 kbar for the study of i) phase equilibria, ii) chemical reactions and eventually their kinetics and intermediate states, iii) speciation and molecular interactions using spectroscopic methods (Raman, infrared,...).

### 1.2. Calibration of the concentration analysis of aqueous species $\text{HCO}_3^-$ and $\text{CO}_2$ using micro-Raman spectroscopy

The relationship between the concentration of aqueous species  $\text{HCO}_3^-$  and  $\text{CO}_2$  and the ratio of relevant Raman active bands of  $\text{HCO}_3^-$  and  $\text{CO}_2$  to the Raman bending band of water

is established using synthetic fluid inclusions and silica glass capillaries as standards. In addition, the influence of addition of NaCl in aqueous phase is also studied. Thus, the concentration of aqueous species  $\text{HCO}_3^-$  and  $\text{CO}_2$  can be deduced through collecting the special spectra on  $\text{HCO}_3^-$ - and  $\text{CO}_2$ -bearing aqueous phase.

### **1.3. Algorithm for the calculation of pH**

One software program for the calculation of pH was constructed. It is based on the Pitzer model. This program can calculate the pH of fluids in system  $\text{H}_2\text{O}-\text{CO}_2-\text{HCO}_3^--\text{NaCl}$  from 273 to 523 K, from 0 to 2000 bars, and from 0 to 5 molality of NaCl just combining the experimental analyses of microthermometry and micro-Raman spectroscopy, which realizes the possibility of calculation of pH of inclusion fluids.

### **1.4. The application on natural case**

One application to natural case (gold deposit) is carried out. The study presents the feasibility of the developed methodology to calculate the pH of natural inclusion fluids. It shows that bicarbonate-rich fluids and slightly base fluids circulated in the Mokrsko gold deposit.

## **2. Perspectives**

Since the new method for fabricating silica glass capillary is still in the period of improvement and exploration, the uncertain difficulties always exist during developing the approaches related to its application to interested studies. There are still many related works to be carried through and to be developed and to be improved.

### **2.1. The calibration of $\text{CO}_2$ amount by controlling the loading materials in system $\text{H}_2\text{O}-\text{CO}_2$ in silica glass capillary**



The problem exists in well controlling the loading materials in system  $\text{H}_2\text{O}-\text{CO}_2$  in silica glass capillary, which is vital for calibrating the analysis of  $\text{CO}_2$  concentration using Raman analytical method  $\text{CO}_2$ . Especially the density of  $\text{CO}_2$  inside capillary at room temperature could be improved using the variation of the frequency of the Fermi resonance bands as a function of density. This requires the use of a spectrometer with a spectral resolution typically around  $0.5 \text{ cm}^{-1}$ . An improved heating and freezing stage adapter to capillary should be used also in order to decrease thermal gradients along the capillary.

## **2.2. The quantification of $\text{CO}_2$ and $\text{H}_2\text{O}$ in system $\text{H}_2\text{O}-\text{CO}_2$ -salts systems should be fully investigated**

The experimental routes to get the calibration of dissolved  $\text{CO}_2$  in pure water at different pressures and temperatures should be carried out using another system for which the pressure is controlled. The calibration could be done using the experimental data of  $\text{CO}_2$  solubility. The same approach should be developed for the calibration of Raman spectrometric analysis of carbonate and bicarbonate dissolved in aqueous solutions. It is worth noting that the solubility of  $\text{CO}_2$  in the  $\text{H}_2\text{O}-\text{CO}_2-\text{HCO}_3^--(\text{NaCl})$  systems is poorly known experimentally. Therefore, the introduction of an internal standard at low concentration could be the way to get also experimental data on  $\text{CO}_2$  solubility in complex aqueous systems.

## **2.3. The liquid-vapor isopleths of bicarbonate-rich fluids**

The liquid-vapour isopleths of bicarbonate-rich aqueous solution in the  $\text{H}_2\text{O}-\text{CO}_2-\text{HCO}_3^--(\text{NaCl})$  system has to be investigated to cover the whole range of fluid composition in which the bicarbonate anion is the major anion.

## **2.4. The use of temperature of relevant phase equilibria other than $T_{m_{ice}}$**

The software program to calculate the chloride concentration is based on the ice melting temperature ( $T_{m_{ice}}$ ) taking into account the bicarbonate concentration. This phase transition gives access to the activity of water in the aqueous solution at this phase transition. However,

if gas-clathrate is present in the inclusion at  $T_{m_{ice}}$ ,  $T_{m_{ice}}$  can not provide the relevant water activity in the bulk aqueous solution since clathrate removes a part of water from the solution and thus increases the salt concentrations. Therefore, relevant phase equilibria should be used to get the right water activity.

## **2.5. Thermodynamic models above 250 °C**

Another difficulty should be solved and concerns the interpretation of chemical and phase equilibria above 250 °C, which is the temperature limit of the application of the Pitzer model. This temperature limit could be probably overcome if it concerns only the modeling of chemical equilibria between  $CO_2$  and  $HCO_3^-$  using the Helgeson-Flowers-Kirkham model. However, a correction of the equilibrium constant due to the decrease of the dielectric constant of the fluid by  $CO_2$  concentration higher than 5 molal should be taken into account. Finally, the interpretation of the bulk homogenization temperature in terms of pressure at this temperature and in terms of bulk molar volume is much more difficult to solve in the absence of a correct thermodynamic model describing the aqueous liquid phase.

## **2.6. More applications to the natural cases are needed for verifying and improving the methodology**

Finally, this thesis shows the difficulties both on the analytical, experimental and modeling aspects. Therefore, natural cases for which the methodology will have been fully established should be chosen. Then, pH deduced from fluid inclusion should be compared with mineral association and the concentration of relevant cations.

## **2.7. Other acido-base equilibria of interest**

Sulfide-bearing systems are widespread in many ore type deposits. Therefore the  $H_2S \rightleftharpoons HS^- + H^+$  equilibrium is another potential route to investigate.

## REFERENCES

- Akiya N. and Savage P. E. Role of water in formic acid decomposition. *AIChE J.*, 1998, 44 (2), 405-415.
- Allan M. M., Yardley B. W. D., Forbes L. J., et al. Validation of LA-ICP-MS fluid inclusion analysis with synthetic fluid inclusions. *American Mineralogist*, 2005, 90 (11-12), 1767-1775.
- Anderko A. and Pitzer K. S. Equation of state representation of phase equilibria and volumetric properties of the system NaCl-H<sub>2</sub>O above 573 K. *Geochimica and Cosmochimica Acta*, 1993, 57, 1657-1680.
- Bakker R. J. and Jansen J. B. H. Experimental post-entrapment water loss from synthetic CO<sub>2</sub> - H<sub>2</sub>O inclusions in natural quartz. *Geochim. Cosmochim. Acta*, 1991, 55, 2215-2230.
- Baranova N. N., Zotov A. V., Bannykh L. N., et al. The effect of redox conditions on the solubility of gold in water at 450°C and 500atm. *Geochemistry International*, 1983, 20 (4), 117-122.
- Bergman S. C. and Dubessy J. CO<sub>2</sub>-CO fluid inclusions in a composite peridotite xenolith: Implications for upper mantle oxygen fugacity. *Contributions to Mineralogy and Petrology*, 1984, 58, 1-13.
- Bethke C. M. Hydrologic constraints on the genesis of the Upper Mississippi Valley mineral district from Illinois basin brines. 1986, *Economic Geology*, 81, 233-256.
- Bjerre A. B. and Sørensen E. Thermal decomposition of dilute aqueous formic acid solutions. *Ind. Eng. Chem. Res.*, 1992, 31, 1574-1577.
- Blake P. G. and Hinshelwood C. The homogeneous decomposition reactions of gaseous formic acid. *Proc. R. Soc. London, A*, 1960, 255, 444-455.
- Blundell D. J., Karnkowski P. H., Alderton D. H. M., et al. Copper mineralization of the Polish Kupferschiefer; a proposed basement fault-fracture system of fluid flow. *Economic Geology*, 2003, 98, 1487-1495.
- Bodnar R. J., Burnham C. W. and Sterner S. M. Synthetic fluid inclusions in natural quartz, III. Determination of phase equilibrium properties in the system H<sub>2</sub>O-NaCl to 1000°C and 1500 bars. *Geochim. Cosmochim. Acta*, 1985, 49, 1861-1873.

- Bodnar R. J. and Sterner S. M. Synthetic fluid inclusions. In: *Hydrothermal Experimental Techniques* (eds. Ulmer G. C. & Barnes H. L.). Wiley-Interscience, New York, 1987, 423-457.
- Boiron M. C., Barakat A., Cathelineau M., et al. Geometry and P-V-T-X conditions of microfissural ore fluid migration: the Mokrsko gold deposit (Bohemia). *Chemical Geology*, 2001, 173, 207-225.
- Boiron M. C., Cathelineau M., Banks D. A., et al. Mixing of metamorphic and surficial fluids during the uplift of the Hercynian upper crust: consequences for gold deposition. *Chemical Geology*, 2003, 194, 119-141.
- Boiron M. C., Moissette A., Cathelineau M., et al. Detailed determination of palaeofluid chemistry: an integrated study of sulphate-volatile rich brines and aquo-carbonic fluids in quartz veins from Ouro Fino (Brazil). *Chemical Geology*, 1999, 154:179-192.
- Boublik T. Hard-Sphere Equation of State. *The Journal of Chemical Physics*, 1970, 53, 471-472.
- Bowers T. S., Jackson K. J. and Helgeson H. C. *Equilibrium activity diagrams for coexisting minerals and aqueous solutions at pressures and temperatures to 5 kb and 600°C*. Springer-Verlag, Berlin, Heidelberg, New York, Tokyo, 1984, 397pp.
- Bowers T. S. and Taylor Jr. H. P. An integrated chemical and stable-isotope model of the origin of mid-ocean ridge hot spring systems. *J. Geophys. Res.*, 1986, 90, 12583-12606.
- Breeding C. M. and Ague J. J. Slab-derived fluids and quartz-vein formation in an accretionary prism, Otago Schist, New Zealand. *Geology*, 2002, 30, 499-502.
- Brimhall G. H., Crerar D. A. Ore fluids: Magmatic to supergene. *Rev. Mineral.*, 17, 1987, 235-321.
- Brun G. Mouvements de libration de la molécule H<sub>2</sub>O dans l'eau, et les solides hydratés. *Rev. Chim. Minér.*, 1968, 5, 899-934.
- Burke E. A. J. Raman microspectrometry of fluid inclusions. *Lithos*, 2001, 55, 139-158.
- Burnham C. W. Magmas and hydrothermal fluids. In: *Geochemistry of hydrothermal ore deposits* (ed. Barnes H. L.), John Wiley, New York, 1997, 63-124.
- Burrows D. R., Wood P. C. and Spooner E. T. C. Carbon isotope evidence for a magmatic origin for Archaean gold-quartz vein ore deposits. *Nature*, 1986, 321, 851-854.

- Carten R. B., Geraghty E. P., Walder B. M., et al. Cyclic development of igneous features and their relationship to high-temperature hydrothermal features in the Henderson porphyry molybdenum deposit, Colorado. *Economic Geology*, 1988, 83, 266-296.
- Carvalho M. R., Forjaz V. H. and Almeida C. Chemical composition of deep hydrothermal fluids in the Ribeira Grande geothermal field (São Miguel, Azores). *Journal of Volcanology and Geothermal Research*, 2006, 156, 116-134.
- Cathles L. M. An analysis of the hydrothermal system responsible for massive sulfide deposition in the Hokuroku Basin of Japan. *Economic Geology Monograph*, 1983, 5, 439-487.
- Cathles L. M. and Smith A. T. Thermal constraints on the formation of Mississippi Valley-type lead-zinc deposits and their implications for episodic basin dewatering and deposit genesis. *Economic Geology*, 1983, 78, 983-1002.
- Chou I-M., Burruss R. C. and Lu W. J. A new optical cell for spectroscopic studies of geologic fluids at pressures up to 100Mpa. In *Advances in High-Pressure Technology for Geophysical Applications* (eds. Chen J., Wang Y., Duffy T. S., et al.). Elsevier, Amsterdam, 2005, 475-485.
- Chou I-M., Song Y. and Burruss R. C. A new method for synthesizing fluid inclusions in fused silica capillaries containing organic and inorganic material. *Geochimica et Cosmochimica Acta*, 2008, 72, 5217-5231.
- Christie A. B. Fluid inclusions, stable isotopes and geochemistry of porphyry copper and epithermal vein deposits of the Hauraki gold-silver Province, New Zealand. *Doctoral Thesis*, Victoria University of Wellington, New Zealand. 1982.
- Cipolli F., Gambardella B., Marini L., et al. Geochemistry of high-pH waters from serpentinites of the Gruppo di Voltri (Genova, Italy) and reaction path modeling of CO<sub>2</sub> sequestration in serpentinite aquifers. *Applied Geochemistry*, 2004, 19, 787-802.
- Davis A. R. and Oliver B. G. A vibrational-spectroscopic study of the species present in the CO<sub>2</sub>-H<sub>2</sub>O system. *Journal of solution chemistry*, 1972, 1(4), 329-339.
- Delhaye M. and Dhamelinourt P. Raman microprobe and microscope with laser excitation. *J. Raman Spectrosc.*, 1975, 3, 33-43.
- Dhamelinourt P., Beny J. M., Dubessy J., et al. Analyse d'inclusions fluides à la microsonde Mole à effet Raman. *Bull. Minéral.*, 1979, 102, 600-610.

- Dickinson R. G., Dillon R. T. And Rasetti R. Raman spectra of polyatomic gases. *Physical Review*, 1929, 34, 582-590.
- Ding K. and Seyfried Jr. W. E. Determination of Fe-Cl complexing in the low pressure supercritical region (NaCl fluid)-Iron solubility constraints on pH of subseafloor hydrothermal fluids. *Geochim. Cosmochim. Acta*, 1992, 56, 3681-3692.
- Ding K. and Seyfried Jr. W. E. Effect of conductive cooling on chemistry of mid-ocean ridge hydrothermal fluids: experimental and theoretical constraints. *Goldschmidt Conference Edinburgh*, 1994, 231.
- Ding K. and Seyfried Jr. W. E. Direct pH measurement of NaCl-bearing fluid with an in situ sensor at 400°C and 40 Megapascals. *Science*, 1996, 272 (5268), 1634-1636.
- Ding K., Seyfried Jr. W. E., Zhang Z., et al. The in situ pH of hydrothermal fluids at mid-ocean ridges. *Earth and Planetary Science Letters*, 2005, 237, 167-174.
- Drummond S. E. Boiling and mixing of hydrothermal fluids: Chemical effects on mineral precipitation. Unpublished Ph.D. dissertation, Pennsylvania State University, USA, 1981, 380 pp.
- Duan Z., Moller N. and Weare J. H. An equation of state for the CH<sub>4</sub>-CO<sub>2</sub>-H<sub>2</sub>O system: I. Pure systems from 0 to 1000°C and 0 to 8000 bar. *Geochimica and Cosmochimica Acta*, 1992, 56, 2605-2617.
- Duan Z., Moller N. and Weare J. H. Equation of state for the NaCl-H<sub>2</sub>O-CO<sub>2</sub> system: Prediction of phase equilibria and volumetric properties. *Geochimica and Cosmochimica Acta*, 1995, 59, 2869-2882.
- Duan Z., Moller N. and Weare J. H. Equations of state for the NaCl-H<sub>2</sub>O-CH<sub>4</sub> system and the NaCl-H<sub>2</sub>O-CO<sub>2</sub>-CH<sub>4</sub> system: Phase equilibria and volumetric properties above 573 K. *Geochimica et Cosmochimica Acta*, 2003, 67, 671-680.
- Duan Z. and Sun R. An improved model calculating CO<sub>2</sub> solubility in pure water and aqueous NaCl solutions from 273 to 573K and from 0 to 2000 bar. *Chemical Geology*, 2003, 193, 257-271.
- Dubessy J., Audeoud D. , Wilkins R. et al. The use of the Raman microprobe mole in the determination of the electrolytes dissolved in the aqueous phase of fluid inclusions. *Chemical Geology*, 1982, 37, 137-150.
- Dubessy J., Boiron M. C., Moissette A., et al. Determination of water, hydrates and pH in

- fluid inclusions by micro-Raman spectrometry. *Eur. J. Mineral.*, 1992, 4, 885-894.
- Dubessy J., Buschaert S., Lamb W., et al. Methane-bearing aqueous fluid inclusions: Raman analysis, thermodynamic modelling and application to petroleum basins. *Chem. Geol.*, 2001, 173, 193-205.
- Dubessy J., Ding J., Robert P., et al. Capillary techniques combined with vibrational spectroscopies applied to fluid inclusions and phase equilibria. Abstract in *European Current Research on Fluids Inclusions*, 2009, 1-2.
- Dubessy J., Geisler D., Kosztolanyi K. et al. The determination of sulphate in fluid inclusions using the M.O.L.E. Raman microprobe. Application to a Keuper halite and geochemical consequences. *Geochimica et Cosmochimica Acta*, 1983, 47, 1-10.
- Dubessy J., Lhomme T., Boiron M. C., et al. Determination of chlorinity in aqueous fluids using Raman spectroscopy of the stretching band of water at room temperature: application to fluid inclusions. *Journal of Applied Spectroscopy*, 2002, 56, 99-106.
- Dubessy J., Poty B. and Ramboz C. Advances in C-O-H-N-S fluid geochemistry based on micro-Raman spectrometric analysis of fluid inclusions. *Eur. J. Mineral.*, 1989, 1, 517-534.
- Edmond J. M., Measures C., McDuff R. E., et al. Ridge crest hydrothermal activity and the balances of the major and minor elements in the ocean: the Galapagos data. *Earth Planet. Sci. Lett.*, 1979, 46, 19-33.
- Fabre C., Boiron M. C., Dubessy J., et al. Advances in lithium analysis in solids by means of laser-induced breakdown spectroscopy : an exploratory study. *Geochimica et Cosmochimica Acta*, 2002, 66 (8), 1401-1407.
- Ferry J. M. Characterization of metamorphism through mineral equilibria. *Reviews in Mineralogy*, 1982, 10, 397pp.
- Ferry J. M. Overview of the petrologic record of fluid flow during regional metamorphism in northern New England. *American Journal of Science*, 1995, 294, 905-988.
- Fournier R. O. Hydrothermal processes related to movement of fluid from plastic into brittle rock in the magmatic-epithermal environment. *Economic Geology*, 1999, 94, 1193-1211.
- Fyfe W. S., Price N. J. and Thompson A. B. *Fluids in the Earth's Crust*. Elsevier, Amsterdam, 1978, 383pp.

- Frantz J. D. Raman spectra of potassium carbonate and bicarbonate aqueous fluids at elevated temperatures and pressures: comparison with theoretical simulations. *Chemical Geology*, 1998, 152, 211-225.
- Frantz J. D., Dubessy J. and Mysen B. An optical cell for Raman spectroscopic studies of supercritical fluids and its application to the study of water to 500°C and 2000bar. *Chemical Geology*, 1993, 106, 9-26.
- Frantz J. D., Zhang Y., Hickmott D. D., et al. Hydrothermal reactions involving equilibrium between minerals and mixed volatiles, 1. Techniques for experimentally loading and analyzing gases and their application to synthetic fluid inclusions. *Chem. Geol.*, 1989, 76, 57-70.
- Frost R. L., Yang J. and Ding Z. Raman and FTIR spectroscopy of natural oxalates: Implications for the evidence of life on Mars. *Chinese Science Bulletin*, 2003, 48(17), 1844-1852.
- Garven G. The role of regional fluid flow in the genesis of the Pine Point deposit, western Canada sedimentary basin. *Economic Geology*, 1985, 80, 307-324.
- Godwal Y., Kaigala G., Hoang V., et al. Elemental analysis using micro laser-induced breakdown spectroscopy (microLIBS) in a microfluidic platform. *Opt Express.*, 2008, 16 (17), 12435-45.
- Gordon H. R. and McCubbin T. K. The 2.8-micron bands of CO<sub>2</sub>. *J. Mol. Spectrosc.*, 1966, 19, 137-154.
- Green II H. W. and Jung H. Fluids, faulting and flow. *Elements*, 2005, 1, 31-37.
- Günther D., Audétat A., Frischknecht R., et al. Quantitative analysis of major, minor and trace elements in fluid inclusions using laser ablation–inductively coupled plasma mass spectrometry. *Journal of Analytical Atomic Spectrometry*, 1998, 13, 263-270.
- Gustafson L. B. and Hunt J. P. The porphyry copper deposit at El Salvador, Chile. *Economic Geology*, 1975, 70, 857-912.
- Hedenquist J. W. Arribas A. and Reynolds T. J. Evolution of an intrusion-centered hydrothermal system: Far Southeast-Lepanto porphyry and epithermal Cu-Au deposits, Philippines. *Economic Geology*, 1998, 93, 373-404.



- Heinrich C. A., Pettke T., Halter W. E., et al. Quantitative multi-element analysis of minerals, fluid and melt inclusions by laser-ablation inductively-coupled-plasma mass-spectrometry. *Geochimica et Cosmochimica Acta*, 2003, 67 (18), 3473-3496.
- Helgeson H. C., Delany J. M., Nesbitt N. W., et al. Summary and critique of the thermodynamic properties of rock-forming minerals. *Am. Jour. Sci.*, 1978, 278A, 1-229.
- Henley R. W., Truesdell A. H., Barton P. B. Jr., et al. Fluid-Mineral equilibria in hydrothermal systems. *Reviews in Economic Geology*, Society of Economic Geologists, BookCrafters, Chelsea, 1984, 1, 267pp.
- Herzberg G. Molecular spectra and molecular structure II. Infrared and Raman spectra of polyatomic molecules. D. Van Nostrand, New York. 1945.
- Hess A. C., McMillan P. F. and O'Keeffe M. Force fields for SiF<sub>4</sub> and H<sub>4</sub>SiO<sub>4</sub>: Ab initio molecular orbital calculations. *J. Phys. Chem.*, 1986, 90, 5661-5665.
- Holland H. D. Granites, solutions, and base metal deposits. *Economic Geology*, 1972, 67, 281-301.
- Hollister L. S., Crawford M. L., Roedder E., et al. Practical aspects of microthermometry: in Short course handbook fluid inclusions: Application to petrology (eds. Hollister L. S. and Crawford M. L.). Mineralogical Association of Canada, 1981, 6, 278-304.
- Holloway J. R., Burnham W. C. and Millhollen G. L. Generation of H<sub>2</sub>O-CO<sub>2</sub> mixture for use in hydrothermal experimentation. *J. Geophys. Res.*, 1968, 73 (20), 6598-6600.
- Howard-Lock H. E. and Stoicheff B. P. Raman Intensity Measurements of the Fermi Diad  $\nu_1$ ,  $2\nu_2$  in <sup>12</sup>CO<sub>2</sub> and <sup>13</sup>CO<sub>2</sub>. *J. Mol. Spectrosc.*, 1971, 37, 321.
- Ishibashi J-I., Grimaud D., Nojiri Y., et al. Fluctuation of chemical compositions of the phase-separated hydrothermal fluid from the North Fiji Basin Ridge. *Marine Geology*, 1994, 116, 215-226.
- Jones G. D., Whittaker F. F., Stuart P. L., et al. Fate of reflux brines in carbonate platforms. *Geology*, 2002, 30, 371-374.
- Kandpal K., Joshi B. K., Joshi S. K., et al. Interaction studies of dilute aqueous oxalic acid. *E-Journal of Chemistry*, 2007, 4 (4), 574-580.
- Kerkhof A. M. van den The system CO<sub>2</sub>-CH<sub>4</sub>-N<sub>2</sub> in fluid inclusions: theoretical modelling and geological applications. PhD Thesis, Vrije Universiteit Amsterdam, The Netherlands, 1988, 206 pp.

- Kesler S. E. Ore-forming fluids. *Elements*, 2005, 1, 13-18.
- Kharaka Y. K. and Hanor J. S. Deep fluids in the continents. I. Sedimentary basins. *Treatise on Geochemistry*, 2003, 5, 499-540.
- Kolonin G. R. and Shironosova G. P. Thermodynamic modeling of possible reasons of REE fractionation with participation of high temperature fluids of complicated composition. *Experiment in Geosciences*, 2002, 10 (1), 77-78.
- Konn C., Charlou J. L., Donval J. P., et al. Hydrocarbons and oxidized organic compounds in hydrothermal fluids from Rainbow and Lost City ultramafic-hosted vents. *Chemical Geology*, 2009, 258, 299-314.
- Kotzer T. G. and Kyser T. K. Petrogenesis of the Proterozoic Athabasca Basin, northern Saskatchewan, Canada, and its relation to diagenesis, hydrothermal uranium mineralization and paleohydrogeology. *Chemical Geology*, 1995, 120, 45-89.
- Krishnan R. S. Raman spectrum of quartz. *Nature*, 1945, 155, 452-453.
- Krüger Y. and Diamond L. W. P-V-T-X properties of two H<sub>2</sub>O-CO<sub>2</sub>-NaCl mixtures up to 850 °C and 500 MPa: a synthetic fluid inclusion study. In: Noronha, F., Dória, A., Guedes, A. (Eds.), XVI ECROFI European Current Research on Fluid Inclusions. Faculdade de Ciências do Porto, Departamento de Geologia, Porto, 2001, 241-244.
- Leach D. L. and Sangster J. F. Mississippi Valley-type lead-zinc deposits. *Geological Association of Canada Special Paper*, 1993, 40, 289-314.
- Lewis A. J., Komninou A., Yardley B. W. D., et al. Rare earth element speciation in geothermal fluids from Yellowstone National Park, Wyoming, USA. *Geochimica et Cosmochimica Acta*, 1998, 62 (4), 657-663.
- Lewis A. J., Palmer M. R., Sturchio N. C., et al. The rare earth element geochemistry of acid-sulphate and acid-sulphate-chloride geothermal systems from Yellowstone National Park, Wyoming, USA. *Geochimica et Cosmochimica Acta*, 1997, 61 (4), 695-706.
- Li D. and Duan Z. The speciation equilibrium coupling with phase equilibrium in the H<sub>2</sub>O-CO<sub>2</sub>-NaCl system from 0 to 250°C, from 0 to 1000 bar, and from 0 to 5 molality of NaCl. *Chemical Geology*, 2007, 244, 730-751.
- Liebscher A. and Heinrich C. A. Fluid-fluid interactions. *Reviews in Mineralogy & Geochemistry*, Mineralogical Society of America Geochemical Society, 2007, 65, 430pp.

- Likhoidov G. G., Plyusnina L. P. and Scheka J. A. Gold solubility in chloride medium interacted with epidote bearing propylites. *Electronic Scientific Information Journal "Herald of the Department of Earth Sciences RAS"*, 2003, 1 (21), 1-3.
- Long D. A. Raman spectroscopy. McGraw-Hill, Inc., New York, 1977, 276. Poty B., Leroy J. and Jachimowicz L. Un nouvel appareil pour la mesure des températures sous le microscope: l'installation de microthermométrie Chaix-Méca. *Bull. Soc. Fr. Minéral. Cristallogr.*, 1976, 99, 182-186.
- McMillan P. F. and Hofmeister A. M. Infrared and Raman spectroscopy. In *Spectroscopic methods in mineralogy and geology* (ed. Hawthorne F. C.). *Rev. Mineral., Mineralogical Soc. Am.*, Washington DC, 1988, 18, 99-159.
- McMillan P. F., Piriou B. and Navrotsky A. A Raman study of glasses along the joins silica-calcium aluminate, silica-sodium aluminate, and silica-potassium aluminate. *Geochimica et Cosmochimica Acta*, 1982, 46, 2021-2037.
- Michard G. *Equilibres chimiques dans les eaux naturelles*. Paris, Editions Published, 1989, 357pp.
- Monnin C., Dubois M., Papaiconomou N., et al. Thermodynamics of the LiCl+H<sub>2</sub>O System. *J.Chem.Eng.Data*, 2002, 47, 1331-1336.
- Morávek P., Janatka J., Pertoldova J., et al. The Mokrsko gold deposit-the largest gold deposit in the Bohemian Massif, Czechoslovakia. *Econ. Geol. Monogr.*, 1989, 6, 252-259.
- Muntean J. L. and Einaudi M. T. Porphyry-epithermal transition; Maricunga Belt, northern Chile. *Economic Geology*, 2001, 96, 743-772.
- Naumov V. B. A thermometric study of melt inclusions in quartz phenocrysts from quartz porphyry. *Geokhimiya*, 1969, 4, 494-498.
- Nesbitt B. E. Gold deposit continuum: a genetic model for lode Au mineralization in the continental crust. *Geology*, 1988, 16, 1044-1048.
- Nordstrom D. K., McCleskey R. B. and Ball J. W. Sulfur geochemistry of hydrothermal waters in Yellowstone National Park: IV Acid-sulfate waters. *Applied Geochemistry*, 2009, 24, 191-207.
- Norton D. Sourcelines, source regions, and pathlines for fluids in hydrothermal systems related to cooling plutons. *Economic Geology*, 1978, 73, 21-29.

- Nyman M. W., Sheets R. W. and Bodnar R. J. Fluid inclusion evidence for the physical and chemical conditions attending intermediate temperature PGE mineralization at the New Rambler deposit, S.E. Wyoming, U.S.A. *Canadian Mineralogist*, 1990, 28, 629-638.
- Ohmoto H. and Skinner B. J. The Kuroko and related volcanogenic massive sulfide deposits. *Economic Geology Monograph*, 1983, 5, 604.
- Oliver B. G. and Davis A. R. Vibrational spectroscopic studies of aqueous alkali metal bicarbonate and carbonate solutions. *Can. J. Chem.*, 1973, 51, 698-702.
- Peacock S. M. Numerical constraints on rates of metamorphism, fluid production, and fluid flux during regional metamorphism. *Geological Society of America Bulletin*, 1989, 101, 476-485.
- Pettke T., Halter W. E., Webster J. D, et al. Accurate quantification of melt inclusion chemistry by LA-ICPMS: a comparison with EMP and SIMS and advantages and possible limitations of these methods. *Lithos*, 2004, 78, 333-361.
- Pitzer K. S. Activity coefficients in electrolyte solutions, CRC Press, USA, 1991, 542pp.
- Poty B., Leroy J. and Jachimowicz L. Un nouvel appareil pour la mesure des températures sous le microscope: l'installation de microthermométrie Chaix-Méca. *Bull. Soc. Fr. Minéral. Cristallogr.*, 1976, 99, 182-186.
- Poty B., Stalder H. A. and Weisbrod A. M. Fluid inclusion studies in quartz from fissures of the western and central Alps. *Schweiz. Mineral. Petrogr. Mitt.*, 1974, 54, 717-752.
- Powell R., Will T. M. and Phillips G. N. Metamorphism in Archean greenstone belts: calculated fluid compositions and implications for gold mineralization. *Journal of Metamorphic Geology*, 1991, 9, 141-150.
- Racah G. Group theory and spectroscopy. Springer Berlin, Heidelberg, 1965, 37, 28-84.
- Raman C. V. and Krishnan K. S. A new type of secondary radiation. *Nature*, 121, 501.
- Rankin A. H. Fluid inclusion. *Encyclopedia of Geology*, Elsevier, 2005, 253-260.
- Richard A., Pettke T., Cathelineau M., et al. Brine-rock interaction in the Athabasca basement (McArthur River U deposit, Canada): consequences for fluid chemistry and uranium uptake. *Terra Nova*, 2010, 22, 303-308.
- Roberts S., Bach W., Binns R. A., et al. Contrasting evolution of hydrothermal fluids in the PACMANUS system, Manus Basin: The Sr and S evidence. *Geology*, 2003, 31, 805-808.
- Roedder E. Ancient fluids in crystals. *Scientific american*, 1962a, 207:38-47.

- Roedder E. Studies of fluid inclusions I: Low temperature application of a dual-purpose freezing and heating stage. *Econ. Geol.*, 1962b, 57, 1045-1061.
- Roedder E. Composition of fluid inclusions. *US Geol. Survey Prof Paper*, 1972, 440JJ, 164.
- Roedder E. Data of Geochemistry. *Geological survey professional paper*, 1972, 440-JJ.
- Roedder E. The fluids in salt. *American Mineralogist*, Mineralogical Society of America, 1984, 69, 413-439.
- Roedder E. Fluid inclusion analysis-Prologue and epilogue. *Geochimica et Cosmochimica Acta*, 1990, 54, 495-507.
- Roedder E. Fluid inclusions. *Encyclopedia of Physical Science and Technology*, Academic Press, 2002, 6, 71-77.
- Roedder E. and Kopp O. C. A check on the validity of the pressure correction in inclusion geothermometry using hydrothermally grown quartz. *Fortsch. Miner.*, 1975, 52, 431-446.
- Rosasco G. J., Roedder E. and Simmons J. H. Laser-excited Raman spectroscopy for nondestructive partial analysis of individual phases in fluid inclusions in minerals. *Science*, 1975, 190, 557-560.
- Rosso K. M. and Bodnar R. J. Detection limits of CO<sub>2</sub> in fluid inclusions using microthermometry and laser Raman spectroscopy and the spectroscopic characterization of CO<sub>2</sub>. *Geochimica et Cosmochimica Acta*, 1995, 59 (19), 3961-3975.
- Saito K., Kakumoto T., Kuroda H., et al. Thermal unimolecular decomposition of formic Acid. *J. Chem. Phys.*, 1984, 80, 4989-4996.
- Schmidt C. and Bodnar R. J. Synthtic fluid inclusions: XVI. PVTX properties in the system H<sub>2</sub>O-NaCl-CO<sub>2</sub> at elevated temperatures, pressures, and salinities. *Geochim. Cosmochim. Acta*, 2000, 64, 3853-3869.
- Schrötter W. and Klöckner H. W. Raman scattering cross-sections in gases and liquids, in "Topics in Current Physics", Springer-Verlag, New York, 1979, Vol. 11, Chapter 4.
- Scott S. D. Submarine hydrothermal systems and deposits. In: *Geochemistry of hydrothermal ore deposits* (ed. Barnes H. L.). John Wiley, New York, 1997, 797-876.
- Seward T. M. Thiocomplexes of gold and the transport of gold in hydrothermal ore solutions. *Geochimica et Cosmochimica Acta*, 1973, 37, 379-399.
- Shang L., Chou I. M., Lu W., et al. Determination of diffusion coefficients of hydrogen in fused silica between 296 and 523 K by Raman spectroscopy and application of fused

- silica capillaries in studying redox reactions. *Geochimica et Cosmochimica Acta*, 2009, 73, 5435-5443.
- Shelton K. L. and Orville P. M. Formation of synthetic fluid inclusions in natural quartz. *American Mineralogist*, 1980, 65, 1233-1236.
- Shinohara H., Kazahaya K. and Lowenstern J. C. Volatile transport in a convecting magma column: implications for porphyry Mo mineralization. *Geology*, 1995, 23, 1091-1094.
- Shmulovich K. I., Yardley B. W. D. and Gonchar G. G. Fluids in the crust. Equilibrium and Transport Properties. London, Glasgow, Weinheim, New York, Tokyo, Melbourne, Madras: Chapman & Hall, 1995, 323pp.
- Sibson R. H., Robert F. and Poulsen K. H. High-angle reverse faults, fluid pressure cycling and mesothermal gold-quartz veins. *Geology*, 1988, 16, 551-555.
- Solomon M. and Quesada C. Zn-Pb-Cu massive sulfide deposits: brine-pool types occur in collisional orogens, black smoker types occur in backarc and /or arc basins. *Geology*, 2003, 31, 1029-1032.
- Sorby H. C. On the microscopic structure of crystals, indicating the origin of minerals and rocks. *Geol. Soc. London Quart. J.*, 1858, 14, 453-500.
- Sørensen S. P. L. Enzymstudien. II: Mitteilung. Über die Messung und die Bedeutung der Wasserstoffionenkonzentration bei enzymatischen Prozessen" (in German). *Biochemische Zeitschrift*. 1909, 21, 131-304.
- Stell G., Rasaiah J.C. and Narang H. Thermodynamic perturbation theory for simple fluids I. *Mol. Phys.*, 1972, 23, 393-406.
- Sterner S. M. and Bodnar R. J. Synthetic fluid inclusions in natural quartz. I. compositional types synthesized and applications to experimental geochemistry. *Geochimica et Cosmochimica Acta*, 1984, 48, 2659-2667.
- Sterner S. M. and Bodnar R. J. Synthetic fluid inclusions. X: Experimental determination of P-V-T-X properties in the CO<sub>2</sub>-H<sub>2</sub>O system to 6 kb and 700 °C. *American Journal of Science*, 1991, 291, 1-54.
- Sterner S. M., Hall D. L. and Bodnar R. J. Synthetic fluid inclusions, V. Solubility relations in the system NaCl-KCl-H<sub>2</sub>O under vapor saturated conditions. *Geochim. Cosmochim. Acta*, 1988, 52, 989-1005.

- Stumm W. and Morgan J. J. Aquatic chemistry: Chemical equilibria and rates in natural waters. New York, Chichester, Brisbane, Toronto, Singapore: John Wiley & Sons, Inc. 1996, 1024pp.
- Taylor H. P. Jr Oxygen and hydrogen isotope constraints on the deep circulation of surface waters into zones of hydrothermal metamorphism and melting. In: The role of fluids in crustal processes (National Research Council, U. S., Geophysics Study Committee), 1990, 185pp.
- Thompson J. F. H. Magmas, fluids, and ore deposits. Mineralogical Association of Canada Short Course Series (ed. Jambor J. L.). Victoria, British Columbia, 1995, 525pp.
- Touret J. and Dietvorst P. Fluid inclusions in high grade anatectic metamorphites. J. Geol. Soc. London, 1983, 140 (4), 635-649.
- Truesdell A. H., Nehring N. L. and Janik C. J. Final Report: Geochemical study of thermal fluids from São Miguel Island, Azores. USGS – USAID Azores Geothermal Project. TA Grant150-001 (BIVD), PASA no. POR-0001-P-IC-2123-00, USDI, Geological Survey, 1984, 16 p.
- Venjaminov S. Y. and Prendergast F. G. Water (H<sub>2</sub>O and D<sub>2</sub>O) molar absorptivity in the 1000-4000 cm<sup>-1</sup> range and quantitative infrared spectroscopy of aqueous solutions. Analytical Biochemistry, 1997, 248, 234-245.
- Vennemann T. W., Muntean J. L., Kesler S. E., et al. Stable isotope evidence for magmatic fluids in the Pueblo Viejo epithermal acid-sulfate Au-Ag deposit, Dominican Republic. Economic Geology, 1993, 88, 55-71.
- Vergnat P. Contribution à l'étude des vibrations transversales et longitudinales de quelques cristaux. Thesis University of Nancy 1, Nancy. 1974.
- Walrafen G. E. Raman spectral studies of the effects of electrolytes on water. The Journal of Chemical Physics, 1962, 1035-1041.
- Walrafen G. E. Raman spectral studies of water structure. The Journal of Chemical Physics, 1964, 40, 3249-3256.
- Walrafen G. E. Raman spectral studies of the effects of temperature on water and electrolyte solutions. The Journal of Chemical Physics, 1966, 44, 1546-1558.
- Walrafen G. E. Raman spectral studies of the effects of temperature on water structure. The Journal of Chemical Physics, 1967, 47, 114-126.

- Walrafen G. E. Raman spectral studies of the effects of perchlorate ion on water structure. *The Journal of Chemical Physics*, 1970, 52, 4176-4198.
- Walrafen G. E. Raman and infrared spectral investigations of water structure. (in *Water: A comprehensive treatise*, Vol. I, Frank F. ed.). Plenum, London. 1972.
- Wienecke P., Finsterholzl H., Schrotter H. W., et al. Raman spectra of carbon dioxide and its isotopic variants in the Fermi resonance region. Part IV: Temperature dependence on Q-branch intensities from 300 K to 650 K. *Appl. Spectrosc.*, 1986, 40, 70-76.
- Williams G. A. and Ferguson J. B. The diffusion of hydrogen and helium through silica glass and other glasses. *J. Am. Chem. Soc.*, 1922, 44, 2160-2167.
- Yu J. and Savage P. E. Decomposition of formic acid under hydrothermal conditions. *Kinetics, Ind. Eng. Chem. Res.*, 1998, 37, 2-10.
- Zaraisky G. P. The influence of acidic fluoride and chloride solutions on the geochemical behaviour of Al, Si and W. In: *Fluids in the crust, Equilibrium and transport properties* (eds. Shmulovich K. I., Yardley B. W. D. and Gonchar G. G.). Chapman & Hall, London, Glasgow, Weinheim, New York, Tokyo, Melbourne, Madras, 1995, 139-162.
- Zhang Y. and Frantz J. D. Determination of the homogenization temperatures and densities of supercritical fluids in the system NaCl-KCl-CaCl<sub>2</sub>-H<sub>2</sub>O using synthetic fluid inclusions. *Chem. Geol.*, 1987, 64, 335-350.
- Zhang Y. G. and Frantz J. D. Hydrothermal reactions involving equilibria between minerals and mixed-volatiles. II) Investigations of fluid properties in the CO<sub>2</sub>-CH<sub>4</sub>-H<sub>2</sub>O system using synthetic fluid inclusions. *Chemical Geology*, 1992, 100, 51-70.



# Appendix

Appendix I The main program for calculating pH of inclusion fluid is presented as follows.

Option Base 1

Dim a(21, 21) As Double

Private Sub Command1\_Click()

'CO<sub>2</sub> et HCO<sub>3</sub><sup>-</sup> mesurés par Raman à la température de piégeage

'On a juste besoin d'utiliser la réaction K1

T = Val(Text1.Text)

P = Val(Text2.Text)

mCO<sub>2</sub> = Val(Text3.Text)

mHCO<sub>3</sub> = Val(Text4.Text)

Tfg = Val(Text5.Text)

mNa = 0.89

mCl = 0.89

'On calcule la valeur de la constante de réaction de K1

a1 = 233.5159304

a2 = 0

a3 = -11974.38348

a4 = 0

a5 = -36.50633536

a6 = -450.8004597

a7 = 21313.18848

a8 = 67.14256299

a9 = 83.93915212

a10 = -4015.441404

a11 = -12.4018735

PcH<sub>2</sub>O = 220.85

TcH<sub>2</sub>O = 647.29

tt = (T - TcH<sub>2</sub>O) / TcH<sub>2</sub>O

CC1 = -38.640844

CC2 = 5.894842

CC3 = 59.876516

CC4 = 26.654627

160

$$CC5 = 10.637097$$

If  $T < 373.15$  Then

$$Ps = 1$$

Else

$$Ps = (PcH2O * T / TcH2O) * (1 + CC1 * (-tt) ^ 1.9 + CC2 * tt + CC3 * tt ^ 2 + CC4 * tt ^ 3 + CC5 * tt ^ 4)$$

End If

$$\begin{aligned} \text{LnK1} = & a1 + a2 * T + a3 * (T ^ -1) + a4 * (T ^ -2) + a5 * \text{Log}(T) + (a6 * (T ^ -1) + a7 * (T ^ -2) + a8 * \\ & \text{Log}(T) * (T ^ -1)) * (P - Ps) + (a9 * (T ^ -1) + a10 * (T ^ -2) + a11 * (T ^ -1) * \text{Log}(T)) * (P - Ps) ^ 2 \end{aligned}$$

$$K1 = \text{Exp}(\text{LnK1})$$

$$pK1 = -\text{Log}(K1) / \text{Log}(10)$$

'Paramètres de pitzer nécessaire aux calculs des coefficients d'activité de CO2 et HCO3

'Paramètre nul d'après Li et Duan 2007

$$a(1, 1) = 0$$

$$a(1, 2) = 0$$

$$a(1, 3) = 0$$

$$a(1, 4) = 0$$

$$a(1, 5) = 0$$

$$a(1, 6) = 0$$

$$a(2, 1) = -0.2739092216$$

$$a(2, 2) = 0.0007399855859$$

$$a(2, 3) = 55.5213285$$

$$a(2, 4) = 0$$

$$a(2, 5) = 0$$

$$a(2, 6) = 0$$

$$a(2, 7) = 0$$

$$a(2, 8) = 0.005683638727$$

$$a(2, 9) = -0.0008009093476$$

$$a(2, 10) = 0$$

$$a(2, 11) = -0.0000174562027$$

$$a(3, 1) = 0.35284$$

$$a(3, 2) = -27.85446$$

$$a(3, 3) = 19.56109$$

'Paramètre pris comme nul dans Li et Duan

$$a(4, 1) = 0$$

$$a(4, 2) = 0$$

$$a(4, 3) = 0$$

$$a(4, 4) = 0$$

$$a(4, 5) = 0$$

$$a(4, 6) = 0$$

'Parmaètre nul, j'ai laissé les formules basse T pour le calcul des ces paramètres car cela m'oblige à tout changer

$$a(5, 1) = 0$$

$$a(5, 2) = 0$$

$$a(5, 3) = 0$$

$$a(5, 4) = 0$$

$$a(5, 5) = 0$$

$$a(5, 6) = 0$$

$$a(6, 1) = 0$$

$$a(6, 2) = 0$$

$$a(6, 3) = 0$$

$$a(6, 4) = 0$$

$$a(6, 5) = 0$$

$$a(6, 6) = 0$$

$$a(7, 1) = 0$$

$$a(7, 2) = 0$$

$$a(7, 3) = 0$$

$$a(7, 4) = 0$$

$$a(7, 5) = 0$$

$$a(7, 6) = 0$$

'Pitzer second virial parameters of NaHCO<sub>3</sub> from Polya et al. (2001)

$$a(8, 1) = 0.0661$$

$$a(8, 2) = 0$$

$$a(8, 3) = 0$$

$$a(8, 4) = 0$$

$$a(8, 5) = 0$$

$$a(8, 6) = 0.0000000375951$$

$$a(8, 7) = 0$$

$$a(8, 8) = 0$$

$$a(9, 1) = -4.116$$

$$a(9, 2) = 0.006309$$

$$a(9, 3) = 924$$

$$a(9, 4) = -52.02$$

$$a(9, 5) = -80.26$$

$$a(9, 6) = 0$$

$$a(9, 7) = 0.0001634$$

$$a(9, 8) = -0.000000139$$

$$a(10, 1) = -0.0914$$

$$a(10, 2) = 0$$

$a(10, 3) = 0$   
 $a(10, 4) = 6.482$   
 $a(10, 5) = 8.048$   
 $a(10, 6) = 0$   
 $a(10, 7) = -0.0000289$   
 $a(10, 8) = 0$

'Pitzer second virial parameters for NaCl(aq) from Pitzer et al. 1984

$a(11, 1) = -656.81518$   
 $a(11, 2) = 24.86913$   
 $a(11, 3) = 0.000053812753$   
 $a(11, 4) = -0.0000000558747$   
 $a(11, 5) = 6.5893263E-12$   
 $a(11, 6) = -4.4640952$   
 $a(11, 7) = 0.011109914$   
 $a(11, 8) = -0.00000026573399$   
 $a(11, 9) = 1.746007E-10$   
 $a(11, 10) = 1.0462619E-14$   
 $a(11, 11) = -0.0000053070129$   
 $a(11, 12) = 8.6340233E-10$   
 $a(11, 13) = -4.1785962E-13$   
 $a(11, 14) = -1.579366$   
 $a(11, 15) = 0.0022022821$   
 $a(11, 16) = -0.00000013105503$   
 $a(11, 17) = -6.3813683E-11$   
 $a(11, 18) = 9.706578$   
 $a(11, 19) = -0.026860396$   
 $a(11, 20) = 0.000015344744$   
 $a(11, 21) = -3.2153983E-09$   
 $a(12, 1) = 119.31966$   
 $a(12, 2) = -0.48309327$   
 $a(12, 3) = 0$   
 $a(12, 4) = 0$   
 $a(12, 5) = 0$   
 $a(12, 6) = 0$   
 $a(12, 7) = 0.0014068095$   
 $a(12, 8) = 0$   
 $a(12, 9) = 0$   
 $a(12, 10) = 0$   
 $a(12, 11) = 0$   
 $a(12, 12) = 0$   
 $a(12, 13) = 0$   
 $a(12, 14) = -4.2345814$   
 $a(12, 15) = 0$   
 $a(12, 16) = 0$   
 $a(12, 17) = 0$

$a(12, 18) = 0$   
 $a(12, 19) = 0$   
 $a(12, 20) = 0$   
 $a(12, 21) = 0$   
 $a(13, 1) = -6.1084589$   
 $a(13, 2) = 0.40217793$   
 $a(13, 3) = 0.000022902837$   
 $a(13, 4) = 0$   
 $a(13, 5) = 0$   
 $a(13, 6) = -0.075354649$   
 $a(13, 7) = 0.00015317673$   
 $a(13, 8) = -0.000000090550901$   
 $a(13, 9) = 0$   
 $a(13, 10) = 0$   
 $a(13, 11) = -0.000000015386008$   
 $a(13, 12) = 8.69266\text{E-}11$   
 $a(13, 13) = 0$   
 $a(13, 14) = 0.35310414$   
 $a(13, 15) = -0.00043314252$   
 $a(13, 16) = 0$   
 $a(13, 17) = 0$   
 $a(13, 18) = -0.091871455$   
 $a(13, 19) = 0.00051904777$   
 $a(13, 20) = 0$   
 $a(13, 21) = 0$

$a(14, 1) = 86.6836498$   
 $a(14, 2) = 0.0848795942$   
 $a(14, 3) = -0.000088878515$   
 $a(14, 4) = 0.000000048809393$   
 $a(14, 5) = -1327.31477$   
 $a(14, 6) = -17.6460172$

'Pitzer parameters from Li et Duan

$a(15, 1) = -0.0145623335$   
 $a(15, 2) = 0$   
 $a(15, 3) = 3.59308925$   
 $a(15, 4) = 0$   
 $a(15, 5) = 0$

$a(15, 6) = 0$   
 $a(15, 7) = 0$   
 $a(15, 8) = 0$

$a(16, 1) = 0.0481363462$   
 $a(16, 2) = 0$   
 $a(16, 3) = -4.05430635$   
 $a(16, 4) = 0$   
 $a(16, 5) = 0$   
 $a(16, 6) = 0$   
 $a(16, 7) = 0$   
 $a(16, 8) = 0$

Pitzer second virial parameters for HCl(aq)

$a(17, 1) = 0.000724$   
 $a(17, 2) = 0$   
 $a(17, 3) = 0$   
 $a(17, 4) = -0.00006072$   
 $a(17, 5) = 0$

$a(18, 1) = 0.1769$   
 $a(18, 2) = -0.0914$   
 $a(18, 3) = 0$   
 $a(18, 4) = -0.0004034$   
 $a(18, 5) = 0.0000062$

$a(19, 1) = 0.2973$   
 $a(19, 2) = 16.147$   
 $a(19, 3) = -0.017631$   
 $a(19, 4) = 0$   
 $a(19, 5) = 0.000072$

$a(20, 1) = -0.01665719188$   
 $a(20, 2) = 0.0000013916186$   
 $a(20, 3) = 0$   
 $a(20, 4) = 0$   
 $a(20, 5) = 0$   
 $a(20, 6) = 0$   
 $a(20, 7) = 0$   
 $a(20, 8) = -0.001873812115$   
 $a(20, 9) = -0.001577400757$   
 $a(20, 10) = 0$   
 $a(20, 11) = 0$

'Paramètre nul d'après Li et Duan 2007

$$\text{LamdaHCO}_2 = a(1, 1) + a(1, 2) * T + a(1, 3) * T^2 + a(1, 4) * T^3 + a(1, 5) / T + a(1, 6) * \text{Log}(T)$$

'The neutral ion parameter of CO2

$$\begin{aligned} \text{LamdaNaCO}_2 = & a(2, 1) + a(2, 2) * T + a(2, 3) / T + a(2, 4) * T^2 + a(2, 5) / (630 - T) + a(2, 6) * P + a(2, 7) \\ & * P * \text{Log}(T) + a(2, 8) * P / T + a(2, 9) * P / (630 - T) + (a(2, 10) * P^2) / ((630 - T)^2) + a(2, 11) * T * \\ & \text{Log}(P) \end{aligned}$$

$$\text{LamdaHco}_3\text{CO}_2 = (a(3, 1) + a(3, 2) / (T - 210) + a(3, 3) / (P - 100)) - \text{lamdaNaCO}_2$$

$$\text{LamdaClCO}_2 = a(4, 1) + a(4, 2) * T + a(4, 3) * T^2 + a(4, 4) * T^3 + a(4, 5) / T + a(4, 6) * \text{Log}(T)$$

'ces paramètres sont nuls d'après Li et Duan 2007

$$\text{Beta0hhco}_3 = a(5, 1) + a(5, 2) * T + a(5, 3) * T^2 + a(5, 4) * T^3 + a(5, 5) / T + a(5, 6) * \text{Log}(T)$$

$$\text{Beta1hhco}_3 = a(6, 1) + a(6, 2) * T + a(6, 3) * T^2 + a(6, 4) * T^3 + a(6, 5) / T + a(6, 6) * \text{Log}(T)$$

$$\text{Chhco}_3 = (a(7, 1) + a(7, 2) * T + a(7, 3) * T^2 + a(7, 4) * T^3 + a(7, 5) / T + a(7, 6) * \text{Log}(T)) / 2$$

'Polya et al.

$$\text{BetaOnahco}_3 = a(8, 1) + a(8, 2) * T + a(8, 3) / T + a(8, 4) / (T - 210) + a(8, 5) / (647 - T) + a(8, 6) * ((T - 443)^3) / 3 + a(8, 7) * (P - 1) + a(8, 8) * ((P - 1)^2) / 2$$

$$\text{Beta1nahco}_3 = a(9, 1) + a(9, 2) * T + a(9, 3) / T + a(9, 4) / (T - 210) + a(9, 5) / (647 - T) + a(9, 6) * ((T - 443)^3) / 3 + a(9, 7) * (P - 1) + a(9, 8) * ((P - 1)^2) / 2$$

$$\text{Cnahco}_3 = (a(10, 1) + a(10, 2) * T + a(10, 3) / T + a(10, 4) / (T - 210) + a(10, 5) / (647 - T) + a(10, 6) * ((T - 443)^3) / 3 + a(10, 7) * (P - 1) + a(10, 8) * ((P - 1)^2) / 2) / 2$$

'Calcul avec les paramètres

$$\begin{aligned} \text{betaOnacl} = & a(11, 1) / T + a(11, 2) + a(11, 3) * P + a(11, 4) * P^2 + a(11, 5) * P^3 + a(11, 6) * \text{Log}(T) + \\ & (a(11, 7) + a(11, 8) * P + a(11, 9) * P^2 + a(11, 10) * P^3) * T + ((a(11, 11) + a(11, 12) * P + a(11, 13) * \\ & P^2) * T^2 + (a(11, 14) + a(11, 15) * P + a(11, 16) * P^2 + a(11, 17) * P^3) / (T - 227)) + ((a(11, 18) + \\ & a(11, 19) * P + a(11, 20) * P^2 + a(11, 21) * P^3) / (680 - T)) \end{aligned}$$

$$\begin{aligned} \text{beta1nacl} = & a(12, 1) / T + a(12, 2) + a(12, 3) * P + a(12, 4) * P^2 + a(12, 5) * P^3 + a(12, 6) * \text{Log}(T) + \\ & (a(12, 7) + a(12, 8) * P + a(12, 9) * P^2 + a(12, 10) * P^3) * T + ((a(12, 11) + a(12, 12) * P + a(12, 13) * \\ & P^2) * T^2 + (a(12, 14) + a(12, 15) * P + a(12, 16) * P^2 + a(12, 17) * P^3) / (T - 227)) + ((a(12, 18) + \\ & a(12, 19) * P + a(12, 20) * P^2 + a(12, 21) * P^3) / (680 - T)) \end{aligned}$$

$$\begin{aligned} \text{Cnacl} = & (a(13, 1) / T + a(13, 2) + a(13, 3) * P + a(13, 4) * P^2 + a(13, 5) * P^3 + a(13, 6) * \text{Log}(T) + \\ & (a(13, 7) + a(13, 8) * P + a(13, 9) * P^2 + a(13, 10) * P^3) * T + ((a(13, 11) + a(13, 12) * P + a(13, 13) * \\ & P^2) * T^2 + (a(13, 14) + a(13, 15) * P + a(13, 16) * P^2 + a(13, 17) * P^3) / (T - 227)) + ((a(13, 18) + \\ & a(13, 19) * P + a(13, 20) * P^2 + a(13, 21) * P^3) / (680 - T))) / 2 \end{aligned}$$

'Aphi est un terme provenant de Debye hückel donc on prend les valeurs existantes

'Demander à Jean si c'est bien comme cela

$$\text{Aphi} = a(14, 1) + a(14, 2) * T + a(14, 3) * T^2 + a(14, 4) * T^3 + a(14, 5) / T + a(14, 6) * \text{Log}(T)$$

$$\begin{aligned} \text{Psihnacl} = & a(15, 1) + a(15, 2) * T + a(15, 3) / T + a(15, 4) * \text{Log}(T) + a(15, 5) / (T - 263) + a(15, 6) * (T^2) \\ & + a(15, 7) / (680 - T) + a(15, 8) / (T - 227) \end{aligned}$$

$$\text{Tetahna} = a(16, 1) + a(16, 2) * T + a(15, 3) / T + a(16, 4) * \text{Log}(T) + a(16, 5) / (T - 263) + a(16, 6) * (T ^ 2) \\ + a(16, 7) / (680 - T) + a(16, 8) / (T - 227)$$

'Calcul des paramètres

'Calcul de la densité de l'eau po. Comme l'on connaît P et T , on utilise l'équation d'état de Duan ET WEARE 1993 pour calculer le volume molaire puis po

$$aa1 = 0.086444922$$

$$aa2 = -0.396918955$$

$$aa3 = -0.0573334886$$

$$aa4 = -0.000293893$$

$$aa5 = -0.00415775512$$

$$aa6 = 0.0199496791$$

$$aa7 = 0.000118901426$$

$$aa8 = 0.000155212063$$

$$aa9 = -0.000106855859$$

$$aa10 = -0.00000493197687$$

$$aa11 = -0.00000273739155$$

$$aa12 = 0.00000265571238$$

$$\alpha = 0.00896079018$$

$$\beta = 4.02$$

$$\gamma = 0.0257$$

$$P_c = 220.85$$

$$T_c = 647.29$$

$$P_r = P / P_c$$

$$T_r = T / T_c$$

$$R = 83.1447 * 0.000001$$

$$R = 83.1447 \text{ cm}^3/\text{bar}$$

$$V_c = (R * T_c) / P_c$$

$$B = aa1 + aa2 / (T_r ^ 2) + aa3 / (T_r ^ 3)$$

$$CC = aa4 + aa5 / (T_r ^ 2) + aa6 / (T_r ^ 3)$$

$$D = aa7 + aa8 / (T_r ^ 2) + aa9 / (T_r ^ 3)$$

$$E = aa10 + aa11 / (T_r ^ 2) + aa12 / (T_r ^ 3)$$

$$F = \alpha / (T_r ^ 3)$$

If P < 400 Then

If T < 300 Then  $V_r = (2.5 * 10 ^ {-5})$  Else  $V_r = (2.5 * 10 ^ {-5}) / V_c$

Else:  $V_r = (2.5 * 10 ^ {-5}) / V_c$



End If

'Le calcul de Vr de l'eau nécessite une résolution par la méthode de Newton Raphson

$$fcVr1 = ((Pr * Vr) / Tr) - (1 + B / Vr + CC / (Vr ^ 2) + D / (Vr ^ 4) + E / (Vr ^ 5) + F * (beta + gamma / (Vr ^ 2))) * \exp(-gamma / (Vr ^ 2)) / (Vr ^ 2)$$

$$fcVr2 = (Pr / Tr) - (-B / (Vr ^ 2) - 2 * CC / (Vr ^ 3) - 4 * D / (Vr ^ 5) - 5 * E / (Vr ^ 6) - F * (beta / (Vr ^ 2)) * 2 * \exp(-gamma / (Vr ^ 2)) + F * (beta / (Vr ^ 5)) * gamma * 2 * \exp(-gamma / (Vr ^ 2)) - 4 * F * (gamma / (Vr ^ 5)) * \exp(-gamma / (Vr ^ 2)) + F * 2 * ((gamma ^ 2) / (Vr ^ 7)) * \exp(-gamma / (Vr ^ 2)))$$

$$Vri = Vr - fcVr1 / fcVr2$$

Do Until Abs((Vri - Vr) / Vr) < 0.0001

$$Vr = Vri$$

$$fcVr1 = ((Pr * Vr) / Tr) - (1 + B / Vr + CC / (Vr ^ 2) + D / (Vr ^ 4) + E / (Vr ^ 5) + F * (beta + gamma / (Vr ^ 2))) * \exp(-gamma / (Vr ^ 2)) / (Vr ^ 2)$$

$$fcVr2 = (Pr / Tr) - (-B / (Vr ^ 2) - 2 * CC / (Vr ^ 3) - 4 * D / (Vr ^ 5) - 5 * E / (Vr ^ 6) - F * (beta / (Vr ^ 2)) * 2 * \exp(-gamma / (Vr ^ 2)) + F * (beta / (Vr ^ 5)) * gamma * 2 * \exp(-gamma / (Vr ^ 2)) - 4 * F * (gamma / (Vr ^ 5)) * \exp(-gamma / (Vr ^ 2)) + F * 2 * ((gamma ^ 2) / (Vr ^ 7)) * \exp(-gamma / (Vr ^ 2)))$$

$$Vri = Vr - fcVr1 / fcVr2$$

Loop

$$V = Vc * Vri$$

$$MMH2O = (15.9994 + 2 * 1.0079) * 0.001$$

$$po = (MMH2O / V)$$

'po est calculé avec les densités de eau pure à des températures T pressions particulières (Holmes et al.1987)

$$Chcl = (a(17, 1) + a(17, 2) * \log(po / 997) + a(17, 3) * (po - 997) + a(17, 4) * (T - 298.15) + a(17, 5) * (P - 1)) / 2$$

$$Beta0hcl = a(18, 1) + a(18, 2) * \log(po / 997) + a(18, 3) * (po - 997) + a(18, 4) * (T - 298.15) + a(18, 5) * (P - 1)$$

$$Beta1hcl = a(19, 1) + a(19, 2) * \log(po / 997) + a(19, 3) * (po - 997) + a(19, 4) * (T - 298.15) + a(19, 5) * (P - 1)$$

$$XiNaClCO2 = a(20, 1) + a(20, 2) * T + a(20, 3) / T + a(20, 4) * T ^ 2 + a(20, 5) / (630 - T) + a(20, 6) * P + a(20, 7) * P * \log(T) + a(20, 8) * P / T + a(20, 9) * P / (630 - T) + (a(20, 10) * P ^ 2) / ((630 - T) ^ 2) + a(20, 11) * T * \log(P)$$

$$\alpha = 2$$

$$B = 1.2$$

$$P_{\text{sinahhco3}} = 0$$

'Second virial term

$$P_{\text{ihco3cl}} = 0.0359$$

$$P_{\text{ihna}} = T_{\text{etahna}}$$

$$P_{\text{sihhco3na}} = 0$$

$$P_{\text{sinahco3cl}} = -0.0143$$

$$P_{\text{sihclhco3}} = 0$$

$$\alpha = 2 \quad \text{'pour le electrolytes 1:1, 1:2 ou 2:1}$$

$$P_{\text{hiprimhco3cl}} = 0$$

$$P_{\text{hiprimnah}} = 0$$

$$m_{\text{H}} = 0.000000001$$

$$M_{\text{i}} = m_{\text{HCO3}} + m_{\text{Cl}} + m_{\text{Na}} + m_{\text{H}} + m_{\text{CO2}}$$

$$Z = m_{\text{HCO3}} + m_{\text{Cl}} + m_{\text{Na}} + m_{\text{H}}$$

$$I = (1/2) * (m_{\text{HCO3}} + m_{\text{Cl}} + m_{\text{Na}} + m_{\text{H}})$$

$$G = 2 * (1 - ((1 + \alpha * I^{(1/2)}) * \text{Exp}(-\alpha * I^{(1/2)}))) / ((\alpha * I^{(1/2)})^2)$$

$$B_{\text{hhco3}} = B_{\text{eta0hhco3}} + B_{\text{eta1hhco3}} * G$$

$$B_{\text{nahco3}} = B_{\text{eta0nahco3}} + B_{\text{eta1nahco3}} * G$$

$$B_{\text{nacl}} = B_{\text{eta0nacl}} + B_{\text{eta1nacl}} * G$$

$$B_{\text{hcl}} = B_{\text{eta0hcl}} + B_{\text{eta1hcl}} * G$$

$$B_{\text{phiNaCl}} = B_{\text{eta0nacl}} + B_{\text{eta1nacl}} * \text{Exp}(-\alpha * I^{(1/2)})$$

$$B_{\text{phiNaHCO3}} = B_{\text{eta0nahco3}} + B_{\text{eta1nahco3}} * \text{Exp}(-\alpha * I^{(1/2)})$$

$$B_{\text{phiHCl}} = B_{\text{eta0hcl}} + B_{\text{eta1hcl}} * \text{Exp}(-\alpha * I^{(1/2)})$$

$$B_{\text{phiHHCO3}} = B_{\text{eta0hhco3}} + B_{\text{eta1hhco3}} * \text{Exp}(-\alpha * I^{(1/2)})$$

$$g_{\text{g}} = -2 * (1 - ((1 + \alpha * I^{(1/2)} + 0.5 * (\alpha * I^{(1/2)})^2) * \text{Exp}(-\alpha * I^{(1/2)}))) / ((\alpha * I^{(1/2)})^2)$$

$$B_{\text{primhcl}} = B_{\text{eta1hcl}} * g_{\text{g}} / I$$

$$B_{\text{primhhco3}} = B_{\text{eta1hhco3}} * g_{\text{g}} / I$$

$$B_{\text{primnacl}} = \beta_{\text{a1nacl}} * gg / I$$

$$B_{\text{primnahco3}} = \beta_{\text{a1nahco3}} * gg / I$$

'Calcul de l'activité de l'eau

$$Phia = 1 + (2 / Mi) * ((-A_{\text{phi}} * I^{(3/2)}) / (1 + B * I^{(1/2)})) + m_{\text{Na}} * m_{\text{Cl}} * (B_{\text{phiNaCl}} + Z * C_{\text{nacl}}) + m_{\text{Na}} * m_{\text{HCO3}} * (B_{\text{phiNaHCO3}} + Z * C_{\text{nahco3}}) + m_{\text{H}} * m_{\text{Cl}} * (B_{\text{phiHCl}} + Z * C_{\text{hcl}}) + m_{\text{H}} * m_{\text{HCO3}} * (B_{\text{phiHHCO3}} + Z * C_{\text{hhco3}})$$

$$Phib = m_{\text{Na}} * m_{\text{H}} * (Phihna + m_{\text{HCO3}} * P_{\text{sihhco3na}} + m_{\text{Cl}} * P_{\text{sihnacl}}) + m_{\text{HCO3}} * m_{\text{Cl}} * (Phihco3cl + m_{\text{Na}} * P_{\text{sinahco3cl}} + m_{\text{H}} * P_{\text{sihclhco3}})$$

$$Phic = m_{\text{Na}} * m_{\text{CO2}} * \lambda_{\text{NaCO2}} + m_{\text{H}} * m_{\text{CO2}} * \lambda_{\text{HCO2}} + m_{\text{HCO3}} * m_{\text{CO2}} * \lambda_{\text{Hco3CO2}} + m_{\text{Cl}} * m_{\text{CO2}} * \lambda_{\text{ClCO2}} + m_{\text{Na}} * m_{\text{Cl}} * m_{\text{CO2}} * X_{\text{NaClCO2}}$$

$$Phi = Phia + Phib + Phic$$

'Affiner un peu la masse molaire de l'eau

$$MM_{\text{H2O}} = 18$$

$$aw = \exp((-MM_{\text{H2O}} * Phi * Mi) / 1000)$$

'calcul des coefficients d'activité

$$\ln_{\text{coefco2}} = 2 * (m_{\text{H}} * \lambda_{\text{HCO2}} + m_{\text{Na}} * \lambda_{\text{NaCO2}} + m_{\text{HCO3}} * \lambda_{\text{Hco3CO2}} + m_{\text{Cl}} * \lambda_{\text{ClCO2}}) + m_{\text{Cl}} * m_{\text{Na}} * X_{\text{NaClCO2}}$$

$$\text{coefco2} = \exp(\ln_{\text{coefco2}})$$

$$aco2 = m_{\text{CO2}} * \text{coefco2}$$

$$FF = -A_{\text{phi}} * ((I^{(1/2)}) / (1 + B * I^{1/2}) + (2 / B) * \log(1 + B * I^{(1/2)})) + m_{\text{H}} * m_{\text{Cl}} * B_{\text{primhcl}} + m_{\text{H}} * m_{\text{HCO3}} * B_{\text{primhhco3}} + m_{\text{Na}} * m_{\text{Cl}} * B_{\text{primnacl}} + m_{\text{Na}} * m_{\text{HCO3}} * B_{\text{primnahco3}} + m_{\text{Na}} * m_{\text{H}} * P_{\text{hiprimnah}} + m_{\text{Cl}} * m_{\text{HCO3}} * P_{\text{hiprimhco3cl}}$$

$$\ln_{\text{coefhco3}} = FF + m_{\text{H}} * (2 * B_{\text{hhco3}} + Z * C_{\text{hhco3}}) + m_{\text{Na}} * (2 * B_{\text{nahco3}} + Z * C_{\text{nahco3}}) + m_{\text{Cl}} * (2 * P_{\text{hihco3cl}} + m_{\text{Na}} * P_{\text{sinahco3cl}} + m_{\text{H}} * P_{\text{sihclhco3}}) + m_{\text{Na}} * m_{\text{H}} * P_{\text{sinahhco3}} + m_{\text{H}} * m_{\text{Cl}} * C_{\text{hcl}} + m_{\text{Na}} * m_{\text{Cl}} * C_{\text{nacl}} + m_{\text{HCO3}} * m_{\text{Na}} * C_{\text{nahco3}} + m_{\text{H}} * m_{\text{HCO3}} * C_{\text{hhco3}} + 2 * m_{\text{CO2}} * \lambda_{\text{Hco3CO2}}$$

$$\text{coefhco3} = \exp(\ln_{\text{coefhco3}})$$

$$ah_{\text{CO3}} = m_{\text{HCO3}} * \text{coefhco3}$$

$$ah = K_1 * (aw * aco2) / ah_{\text{CO3}}$$

$$\ln_{\text{H}} = FF + m_{\text{Cl}} * (2 * B_{\text{hcl}} + Z * C_{\text{hcl}}) + m_{\text{HCO3}} * (2 * B_{\text{hhco3}} + Z * C_{\text{hhco3}}) + m_{\text{Na}} * (2 * P_{\text{hihna}} + m_{\text{Cl}} * P_{\text{sihnacl}} + m_{\text{HCO3}} * P_{\text{sihhco3na}}) + m_{\text{Cl}} * m_{\text{HCO3}} * P_{\text{sihclhco3}} + m_{\text{Na}} * m_{\text{Cl}} * C_{\text{nacl}} + m_{\text{Na}} * m_{\text{HCO3}} * C_{\text{nahco3}} + m_{\text{H}} * m_{\text{HCO3}} * C_{\text{hhco3}} + m_{\text{H}} * m_{\text{Cl}} * C_{\text{hcl}} + 2 * m_{\text{CO2}} * \lambda_{\text{Hco3CO2}}$$

$$\text{coefH} = \exp(\ln_{\text{H}})$$

$$m_{\text{Hn}} = ah / \text{coefH}$$

Do Until (Abs(mHn - mH) / mH) < 0.0000001

mH = mHn

'Calcul de l'activité de l'eau

Phia = 1 + (2 / Mi) \* ((-Aphi \* I ^ (3 / 2)) / (1 + B \* I ^ (1 / 2))) + mNa \* mCl \* (BphiNaCl + Z \* Cnacl) + mNa \* mHCO3 \* (BphiNaHCO3 + Z \* Cnahco3) + mH \* mCl \* (BphiHCl + Z \* Chcl) + mH \* mHCO3 \* (BphiHHCO3 + Z \* Chhco3)

Phib = mNa \* mH \* (Phihna + mHCO3 \* Psihhco3na + mCl \* Psihnacl) + mHCO3 \* mCl \* (Phihco3cl + mNa \* Psinahco3cl + mH \* Psihclhco3)

Phic = mNa \* mCO2 \* LamdaNaCO2 + mH \* mCO2 \* LamdaHCO2 + mHCO3 \* mCO2 \* LamdaHco3CO2 + mCl \* mCO2 \* LamdaClCO2 + mNa \* mCl \* mCO2 \* XiNaClCO2

Phi = Phia + Phib + Phic

'Affiner un peu la masse molaire de l'eau

MMH2O = 18

aw = Exp((-MMH2O \* Phi \* Mi) / 1000)

Lncoefco2 = 2 \* (mH \* LamdaHCO2 + mNa \* LamdaNaCO2 + mHCO3 \* LamdaHco3CO2 + mCl \* LamdaClCO2) + mCl \* mNa \* XiNaClCO2

coefco2 = Exp(Lncoefco2)

aco2 = mCO2 \* coefco2

Mi = mHCO3 + mCl + mNa + mH + mCO2

Z = mHCO3 + mCl + mNa + mH

I = 1 / 2 \* (mHCO3 + mCl + mNa + mH)

FF = -Aphi \* ((I ^ (1 / 2)) / (1 + B \* I ^ 1 / 2) + (2 / B) \* Log(1 + B \* I ^ (1 / 2))) + mH \* mCl \* Bprimhcl + mH \* mHCO3 \* Bprimhhco3 + mNa \* mCl \* Bprimnacl + mNa \* mHCO3 \* Bprimnahco3 + mNa \* mH \* Phiprimnah + mCl \* mHCO3 \* Phiprimhco3cl

Lncoefhco3 = FF + mH \* (2 \* Bhhco3 + Z \* Chhco3) + mNa \* (2 \* Bnahco3 + Z \* Cnahco3) + mCl \* (2 \* Phihco3cl + mNa \* Psinahco3cl + mH \* Psihclhco3) + mNa \* mH \* Psinahhco3 + mH \* mCl \* Chcl + mNa \* mCl \* Cnacl + mHCO3 \* mNa \* Cnahco3 + mHCO3 \* mH \* Chhco3 + 2 \* mCO2 \* LamdaHco3CO2

coefhco3 = Exp(Lncoefhco3)

ahCO3 = mHCO3 \* coefhco3

ah = K1 \* (aw \* aco2) / ahCO3

LnH = FF + mCl \* (2 \* Bhcl + Z \* Chcl) + mHCO3 \* (2 \* Bhhco3 + Z \* Chhco3) + mNa \* (2 \* Phihna + mCl \* Psihnacl + mHCO3 \* Psihhco3na) + mCl \* mHCO3 \* Psihclhco3 + mNa \* mCl \* Cnacl + mNa \* mHCO3 \* Cnahco3 + mH \* mHCO3 \* Chhco3 + mH \* mCl \* Chcl + 2 \* mCO2 \* LamdaHco3CO2

$$\text{coefHn} = \text{Exp}(\text{LnH})$$

$$\text{mHn} = \text{ah} / \text{coefHn}$$

Loop

'Calcul de tous les coefficients

$$\text{mH} = \text{mHn}$$

$$\text{Lncoefco2} = 2 * (\text{mH} * \text{LamdaHCO2} + \text{mNa} * \text{LamdaNaCO2} + \text{mHCO3} * \text{LamdaHco3CO2} + \text{mCl} * \text{LamdaClCO2}) + \text{mCl} * \text{mNa} * \text{XiNaClCO2}$$

$$\text{coefco2} = \text{Exp}(\text{Lncoefco2})$$

$$\text{aco2} = \text{mCO2} * \text{coefco2}$$

$$\text{Mi} = \text{mHCO3} + \text{mCl} + \text{mNa} + \text{mH} + \text{mCO2}$$

$$\text{Z} = \text{mHCO3} + \text{mCl} + \text{mNa} + \text{mH}$$

$$\text{I} = 1 / 2 * (\text{mHCO3} + \text{mCl} + \text{mNa} + \text{mH})$$

$$\text{FF} = -\text{Aphi} * (\text{I}^{1/2} / (1 + \text{B} * \text{I}^{1/2}) + (2 / \text{B}) * \text{Log}(1 + \text{B} * \text{I}^{1/2})) + \text{mH} * \text{mCl} * \text{Bprimhcl} + \text{mH} * \text{mHCO3} * \text{Bprimhhco3} + \text{mNa} * \text{mCl} * \text{Bprimncl} + \text{mNa} * \text{mHCO3} * \text{Bprimnahco3} + \text{mNa} * \text{mH} * \text{Phiprimnah} + \text{mCl} * \text{mHCO3} * \text{Phiprimhco3cl}$$

$$\text{Lncoefhco3} = \text{FF} + \text{mH} * (2 * \text{Bhhco3} + \text{Z} * \text{Chhco3}) + \text{mNa} * (2 * \text{Bnahco3} + \text{Z} * \text{Cnahco3}) + \text{mCl} * (2 * \text{Phihco3cl} + \text{mNa} * \text{Psinahco3cl} + \text{mH} * \text{Psihclhco3}) + \text{mNa} * \text{mH} * \text{Psinahhco3} + \text{mH} * \text{mCl} * \text{Chcl} + \text{mNa} * \text{mCl} * \text{Cncl} + \text{mHCO3} * \text{mNa} * \text{Cnahco3} + \text{mHCO3} * \text{mH} * \text{Chhco3} + 2 * \text{mCO2} * \text{LamdaHco3CO2}$$

$$\text{coefhco3} = \text{Exp}(\text{Lncoefhco3})$$

$$\text{ahCO3} = \text{mHCO3} * \text{coefhco3}$$

$$\text{ah} = \text{K1} * (\text{aw} * \text{aco2}) / \text{ahCO3}$$

$$\text{LnH} = \text{FF} + \text{mCl} * (2 * \text{Bhcl} + \text{Z} * \text{Chcl}) + \text{mHCO3} * (2 * \text{Bhhco3} + \text{Z} * \text{Chhco3}) + \text{mNa} * (2 * \text{Phihna} + \text{mCl} * \text{Psihnacl} + \text{mHCO3} * \text{Psihhco3na}) + \text{mCl} * \text{mHCO3} * \text{Psihclhco3} + \text{mNa} * \text{mCl} * \text{Cncl} + \text{mNa} * \text{mHCO3} * \text{Cnahco3} + \text{mH} * \text{mHCO3} * \text{Chhco3} + \text{mH} * \text{mCl} * \text{Chcl} + 2 * \text{mCO2} * \text{LamdaHco3CO2}$$

$$\text{coefHn} = \text{Exp}(\text{LnH})$$

$$\text{'mHn} = 1.865 * 10^{-4}$$

$$\text{'Z} = \text{mHCO3} + \text{mCl} + \text{mNa} + \text{mHn}$$

$$\text{'I} = 1 / 2 * (\text{mHCO3} + \text{mCl} + \text{mNa} + \text{mHn})$$

$$\text{'F} = -\text{Aphi} * (\text{I}^{1/2} / (1 + \text{B} * \text{I}^{1/2}) + (2 / \text{B}) * \text{Log}(1 + \text{B} * \text{I}^{1/2})) + \text{mHn} * \text{mCl} * \text{Bprimhcl} + \text{mHn} * \text{mHCO3} * \text{Bprimhhco3} + \text{mNa} * \text{mCl} * \text{Bprimncl} + \text{mNa} * \text{mHCO3} * \text{Bprimnahco3} + \text{mNa} * \text{mHn} * \text{Phiprimnah} + \text{mCl} * \text{mHCO3} * \text{Phiprimhco3cl}$$

$$\text{IncoeffCl} = \text{FF} + \text{mNa} * (2 * \text{Bncl} + \text{Z} * \text{Cncl}) + \text{mH} * (2 * \text{Bhcl} + \text{Chcl}) + \text{mHCO3} * (2 * \text{Phihco3cl} + \text{mNa} * \text{Psinahco3cl} + \text{mH} * \text{Psihclhco3}) + \text{mNa} * \text{mH} * \text{Psihnacl} + \text{mNa} * \text{mCl} * \text{Cncl} + \text{mNa} * \text{mHCO3} *$$

$C_{\text{NaHCO}_3} + m_{\text{H}} * m_{\text{HCO}_3} * C_{\text{Hhco}_3} + m_{\text{H}} * m_{\text{Cl}} * C_{\text{Hcl}} + 2 * m_{\text{CO}_2} * \text{LamdaHco}_3\text{CO}_2 + 6 * m_{\text{CO}_2} * m_{\text{Na}} * X_{\text{NaClCO}_2}$

$\text{coeffCl} = \text{Exp}(\ln\text{coeffCl})$

MsgBox coeffCl

$\text{pK1} = -\text{Log}(\text{K1}) / \text{Log}(10)$

MsgBox pK1

MsgBox aco2

MsgBox coefco2

MsgBox ahCO3

MsgBox coefhco3

MsgBox mHn

MsgBox ah

MsgBox coefHn

$\text{pH} = -\text{Log}(\text{ah}) / \text{Log}(10)$

MsgBox (pH)

MsgBox aw

End Sub